# PROCEEDINGS OF THE XIX$^{th}$ ANNUAL MEETING OF THE SOCIEDADE ASTRONÔMICA BRASILEIRA

(AUGUST 1993)

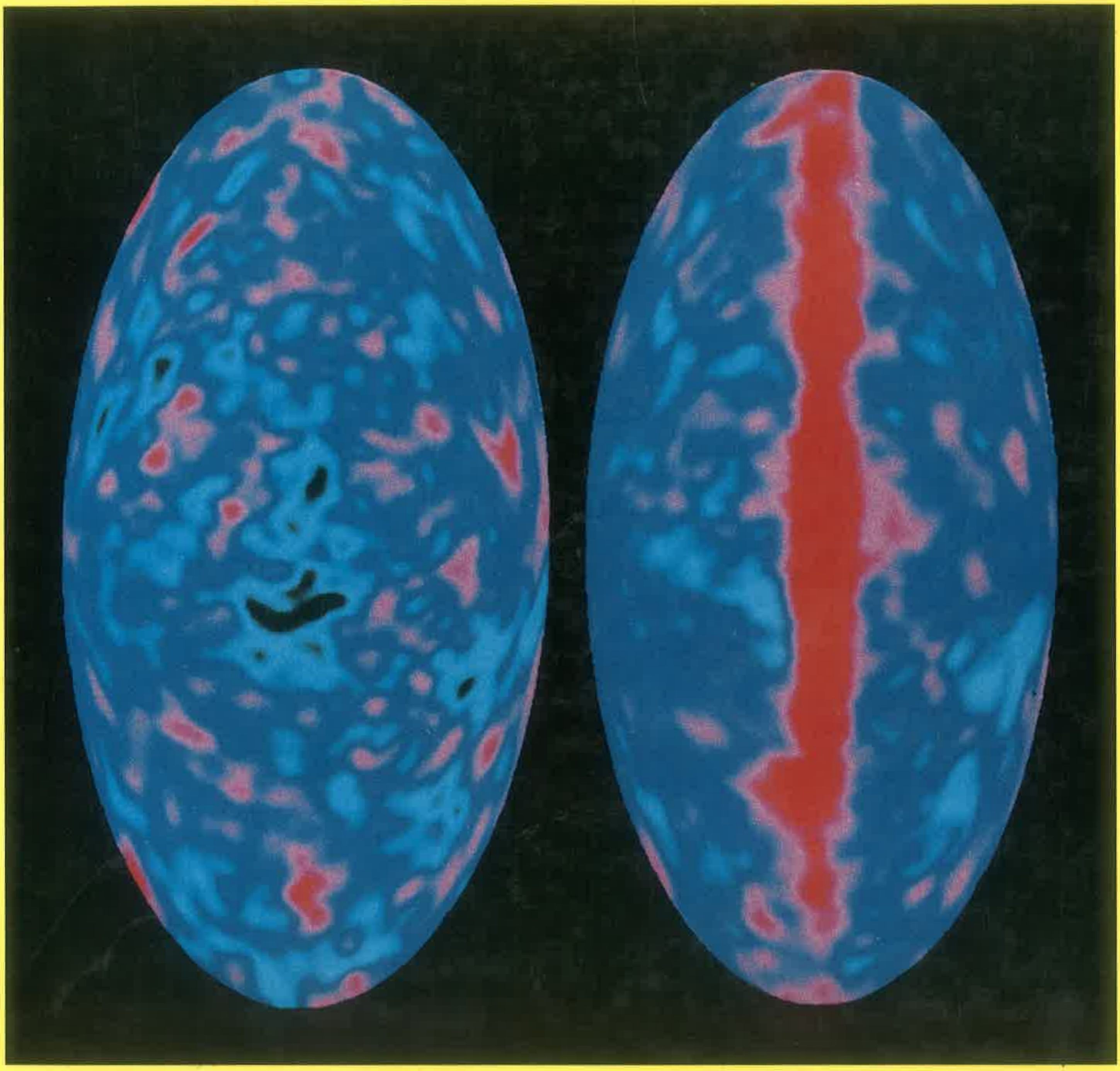

EDITED BY J. BRAGA, B. BARBUY AND N. V. LEISTER

ISSN: 0104-6071

# PROCEEDINGS OF THE XIX$^{\text{th}}$ MEETING OF THE BRAZILIAN ASTRONOMICAL SOCIETY

August 1 – 4, 1993
Caxambu, MG, Brazil

S A B

Edited by

**João Braga**,
Instituto Nacional de Pesquisas Espaciais
C. P. 515, S. J. Campos, SP 12201-970, Brazil

**Beatriz Barbuy** and **Nelson V. Leister**
Instituto Astronômico e Geofísico – USP
C. P. 9638, São Paulo, SP 01065-970, Brazil

Ficha catalográfica

Sociedade Astronômica Brasileira
Proceedings of the XIX$^{th}$ meeting of the Brazilian Astronomical Society
220 páginas.

Contribuições de conferencistas. 1994.
I. Título: Proceedings of the XIX$^{th}$ meeting of the Brazilian Astronomical Society

ISSN: 0104-6071

Distribuição:

Instituto Astronômico e Geofísico - USP
Av. Miguel Stefano, 4200 - Parque do Estado
04301-902 - São Paulo - SP

# FOREWORD

This volume contains the proceedings of the XIXth Meeting of the Brazilian Astronomical Society ("Sociedade Astronômica Brasileira – SAB), held at *Hotel Glória*, in the city of Caxambu, state of Minas Gerais, Brazil, on August 1 – 4, 1993. This is the first time that the proceedings of a SAB meeting are published as a separate volume. Only the invited talks given at the conference are included, but the meeting also had a large number of poster presentations, whose abstracts, as usual, have been published in a special number of the Bulletin of the Brazilian Astronomical Society.

We decided to alter the traditional format of the annual SAB meetings so that all the contributed papers were presented in the form of posters, whereas the oral presentations consisted solely on invited talks with durations ranging from 15 to 45 minutes. We think that in this way the discussion over specific research topics were improved inasmuch as the authors have had more time to explain their paper at different levels during the poster sections, while the talks could cover broader subjects and reach most of the audience.

We believe that the meeting has been very fruitful owing to the excellent contributions of many invited speakers and to the large number of poster presentations. The meeting has clearly shown that numerous new and exciting results are to be expected from the brazilian astronomers in the years to come, most of which by virtue of strong international collaboration.

We are very grateful to Fundação de Amparo à Pesquisa do Estado de São Paulo (FAPESP), Conselho Nacional de Desenvolvimento Científico e Tecnológico (CNPq) and IBM for financial support.

João Braga
Beatriz Barbuy
Nelson V. Leister

# Section 1:

# The Sun and the Solar System

XIX REUNIÃO ANUAL S.A.B.
HOTEL GLÓRIA CAXAMBÚ AGOSTO 93

# Table of Contents

Foreword ........................................................................ 1

**Section 1 : The Sun and the Solar System** ...................... 3

Is There a Planet Around $\beta$-Pictoris ?
– *D. Lazzaro* ........................................................... 5

Residuals from Catalog Comparisons
– *A. H. Andrei* ........................................................ 17

MHD Waves in the Solar Atmosphere
– *V. Jatenco-Pereira* .................................................. 33

**Section 2 : Stars and the Interstellar Medium** ............... 41

Stellar Seismology
– *E. J. Pacheco* ........................................................ 43

Doppler Tomography of Polars: Indirect Imaging of VV Pup
– *M. Diaz & J. E. Steiner* ............................................ 63

On the Rotation of Evolved Stars
– *J. R. Medeiros* ....................................................... 73

Towards a New Source of $^7$Li in the Galaxy
– *R. de la Reza & L. da Silva* ....................................... 81

**Section 3 : The Galaxy and the Magellanic Clouds** ......... 87

The Delayed Formation of the Galactic Bulge
– *M. Rich* ............................................................... 89

Electron Densities of HII Regions in The Magellanic Clouds
– *M. V. F. Copetti* .................................................... 99

Astronomy with the Space Shuttle: the Astro-1 Observatory
– *A. M. Magalhães* ................................................... 107

A Spectroscopic Study of Galactic Planetary Nebulae
– *R. D. D. Costa & J. A. F. Pacheco* .............................. 125

**Section 4 : Extragalactic Astrophysics** ........ 131

Chemical Abundances and Morphology of the Narrow Line Region in Low-Activity Galactic Nuclei
– *T. Storchi-Bergmann* ........ 133

Automatic Classification of Galaxies by Artificial Neural Networks
– *L. Sodré* ........ 151

Progress Report of the Redshift Survey on the Declination Strip +9° to +15°
– *M. Maia* ........ 157

Primordial Perturbations and the Global Properties of Elliptical Galaxies
– *R. E. Souza* ........ 165

**Section 5 : Software, Modeling and Instrumentation** ..... 173

Deterministic Restoration Of Hubble Space Telescope Images
– *I. Busko* ........ 175

GAUSSFIT: A Simple Way for Robust Estimate
– *J. L. Kohl* ........ 185

3-D Simulations of Continuous and Pulsed Astrophysical Jets
– *E. G. Dal Pino* ........ 195

The Imminent Aurora of Gravitational Wave Astronomy
– *O. D. Aguiar & N. S. Magalhães* ........ 199

An International Antarctic Observatory
– *V. V. Burdyuzha* ........ 207

The TIMAX Project
– *J. Braga* ........ 209

HIPPARCOS Mission
– *R. Teixeira* ........ 219

# IS THERE A PLANET AROUND $\beta$-PICTORIS?

Daniela Lazzaro

*Observatório Nacional, Dep. de Astrofísica, 20921 Rio de Janeiro, Brasil*

**Abstract** - Observations show that a large number of young stars are surrounded by circumstellar disks where the planetary evolution is supposed to begin. We will concentrate our attention to the $\beta$-Pictoris disk; first going through a brief review of the observations and then showing that the observed inner clearing zone can be due to the presence of a planet. We present a numerical and analytical modelization of the evolution of a dust grain under the gravitational attraction of a central mass, the gravitational perturbation of a planet, the radiation pressure and the Poynting-Robertson drag. Using the numerical parameters of $\beta$-Pictoris system we show that a planet with a mass of the order of Uranus can confine the inner edge of the disk through resonance trapping.

## 1. Introduction

The study of circumstellar regions may give clues to understand the formation and evolution of planetary systems, in particular, of our Solar System. Due to the increasing quality of observations the interest on these regions has arisen and new structures are beginning to be revealed. The first important result is that circumstellar disks are not unusual objects in the universe. According to recent statistics based on observations, more than 50% of young stellar objects do have proto-planetary disk.

The first evidence was obtained from the IRAS data, from which nearly 30 nearby stars were selected as good candidates to have circumstellar disk based mainly on its strong infrared (IR) excess which indicates the presence of cold material. Of these, only one, $\beta$-Pictoris, has a confirmed protoplanetary disk while is highly probable in other three, $\alpha$-Lyrae, $\alpha$-Piscis Austrini and $\epsilon$-Eridani.

More recently the Hubble Space Telescope (HST) reported the discovery of nearly 15 young stars in the Orion Nebulae with a dusty disk. Unlike previous observations HST has observed newly formed stars, less than a million years old, which are still contracting out of primordial gas. Hubble's images provide direct evidence that dust surrounding a newborn star has too much spin to drawn into the collapsing star. Instead the material spread out into a broad flattened disk (O'Dell et al., 1993). These discoveries confirm more than a century of conjectures and theory about the genesis of our Solar System from a flattened disk around the newborn Sun.

In what follows we will first give a brief overview of the observational data available on the $\beta$-Pictoris disk, then modelize the dynamical problem of the perturbation of a planet on a circumstellar disk and, finally, describe the numerical results obtained when we incorporate the data of $\beta$-Pictoris' disk in the above physical model.

## 2. The $\beta$-Pictoris disk

The $\beta$-Pictoris ($\beta$-Pic) star is belived to be a young A5 dwarf of nearly $2 \times 10^6$ years old (Paresce, 1991) and the disk around it is, so far, the best known of such objects. First selected due to its high IR excess, the presence of the disk was confirmed by Smith and Terrile, in 1984, through optical images. Since then the disk has been observed in a wide range of wavelenghts going from the ultraviolet (UV) through the visible into the infrared (IR). We shall now describe briefly the main results of each kind of observation.

The UV spectroscopic observation of $\beta$-Pic are very interesting as they reveal the presence of strong, narrow resonance absorption lines of MgII, FeII and AlII and of metastable FeII caused by a circumstellar shell of gas. These lines can be decomposed into a steady component and a time variable component. The most amazing aspect of the time variable component is that it is always redshifted, typically by $\sim$ 100-400 Km s$^{-1}$ (Lagrange-Henry et al., 1988). These events are highly variable in time with time-scale from some hours to some months and this gas could be produced by cometary-like objects vaporized as they fall onto the star.

The optical spectroscopic observations of $\beta$-Pic have identified both CaII K- and NaI D -lines in absorption due to a gaseous shell (Hobbs et al., 1985). The NaI may be located in the outer region and the CaII in an inner region of the disk. We can suppose a power law model for the density fall off of the gas with radius as $r^{-n}$, with $n$ between 0 and 1. The outer edge of such a model is supposed to be at 400AU and the inner edge at 0.5-1 AU where the CaII is expected to be present. Again are observed transient events in the CaII but with typical redshifts of the order of 40 km s$^{-1}$.

Optical observations with a coronograph, first obtained by Smith and Terrile (1984) show a nearly-edged-on-disk with an extension of more than 1000 AU and asymmetric at large distances from the star. Paresce and Burrows (1987) also obtained photometrical images of the disk in the optic and near IR from which they established its colour in the range between B and I bands. The scattering is found to be independent of wavelength, indicating that the scattering particles have a characteristic size of the order of micron. This limit is extremely important in order to assert that particle agglomeration has already occoured, or is occouring (Norman and Paresce, 1989). The intesity distribution of the scattered light from the disk has been determined to be of the form $I(r) \sim r^{-3.6}$ (Paresce and Burrows, 1987).

Recent observations of the inner region of the disk with an anti-blooming CCD, clearly indicate a cleared zone around $\beta$-Pic. Moreover, these observations seem to show that the disk colour drops down in the blue with a factor 4 from 75 AU to 30 AU when the disk colour is neutral in V, R and I (Vidal-Madjar et al., 1992). This result is very interesting as it seem to indicate that the nature of the grains is changing when moving inward. A change in the grain size could not explain such result since greater grains should induce no colour variation while smaller ones should favour the blue. This effect can be more probably attributed to a variation in the surface albedo, as for example, icy material getting more and more covered with dust. This seem to be the first direct indication that a different situation prevails in the inner region of $\beta$-Pic disk, where planets are possibly forming (Vidal-Madjar et al., 1992).

The IR data also indicate a cleared zone around the star. But, if its existence is certain, the size of this zone is very model dependent and varies between 5 and 30 AU. Coronographic images do not give much informations on the very inner part of the disk where the IRAS data, at wavelenghts smaller than 160 $\mu$m, are sensitive. Therefore the comparison between IRAS and optical data is quite difficult, but it allows to derive that the most probable particle population is medium sized, 1-30 microns in radius with high albedo (Artimowich et al., 1989). The disk has a thickness of 30-50 AU and such a large thickness could be due to an stirring by comet-like objects.

### 3. The hypothesis of a planet

If the observations clarly involve a hole near the star this depletion poses a dynamical problem: the dust grains are submitted to the Poynting-Robertson drag and should fall very rapidly onto the star filling the depletion. This depletion zone could be due to the sublimation of the particles, if the grains are made of pure ice. Another hypothesis to explain this inner edge is the existence of one (or several) planet that revolves inside the disk and confines the inner edge.

Analyzing the physical forces acting on a dust grain of a circumstellar disk evolving under the influence of a central star and a planet we note that they can be separated in two classes: gravitacional and non-gravitacional. The former due to the gravitacional attraction of the central star and perturbation by the planet and the latter due to colletive phenomena or/and physical properties of the star. Let's briefly discuss each one separately.

(a) - *Non-gravitational* forces (Burns, Lamy and Soter, 1979);

- **Radiation Pressure** - The impact of photons on a dust grain. Photons carry energy and momentum, hence when a dust grain is hitten by photons it feels a pressure due to the momentum carried by photons. This acceleration is proportional to the radiation flux from the star which decreases as $\frac{1}{r^2}$, where $r$ is the distance to the star. As a result, the dust grain feels the gravitacional attraction exerted by the central star reduced by a factor of $(1-\beta)$, where $\beta$ is the ratio betweem the radiation pressure and the gravitational attraction of the central mass. The value of $\beta$ depends mainly on the particle's size and on its chemical composition. For particles of micron size, as in the case of the disk of $\beta$-Pictoris, $\beta$ has values of the order 0.1.
- **Poynting-Robertson drag** - A dust grain absorbs anisotropically the photons from the star. Since the grain is in thermal equilibrium, the absorbed energy is reradiated isotropically. The reradiated photons carry momentum. As a consequence of the anisotropic gain and isotropic loss of momentum the grains's orbit looses momentum and it spiral slowly onto the central star. An important aspect of this effect is that it is velocity dependent. The Poynting-Robertson effect is, as the radiation pressure, stronger for smaller particles. Around $\beta$-Pic, a 3 $\mu$m grain will fall from 30 AU onto the star in less than $\approx 10^6$ years.
- **Magnetic field** and **stellar wind** - Interactions of the dust grain with the stellar wind induces a drag comparable to the Poynting-Robertson and induces a Coulomb pressure for charged grains. The magnetic field also affects strongly the motion of charged particles. Eventhou is reasonable to suppose that young star should have strong stellar wind and/or a magnetic field, so far we do not have any observational constraints on this point.
- **Gas drag** - The gas drag is a result of the negative radial pressure gradient; the gas does not have Keplerian orbit around the central star as do the grains. This causes a friction and a decay in the grain's orbit. The presence of a strong gas component in a circumstellar disk could strongly perturb its dynamical evolution, however, the $\beta$-Pic

disk has only a weak gaseous component (hydrogen density of $10^4 cm^{-3}$ at 400 AU) which is negligible.

- **Evaporation** - The evaporation of particles occours at a distance from the star that depends on its composition. For most of the material, except ices, the melting temperature is in the range of 1000-1500 K. Hence evaporation is important at a distance of few radii from the star. Pure ice are predicted to evaporate at 170 K. In the Solar System ice particles are known to evaporate at heliocentric distance of 3 AU while in the $\beta$-Pic system should evaporate around 7 AU.
- **Collisions** - Mutual collisions between particles depend strongly on the impact velocity The $\beta$-Pic disk's thickness induces a typical encounter velocity of nearly 1 km s$^{-1}$, which would destroy particles. The collision frequency estimated from the optical thickness (0.007 at radii where the grain temperature is 95$\sim$115 K) gives a typical life time of less than $2 \times 10^4$ years. It is important to note that this value can be ten times greater or smaller, due to the uncertanities on the optical thickness. This time scale is very short and a replenishing source for the dust is necessary, anyway.

(b) - *Gravitacional* forces due to the perturbing planet;

- **Close encounters** - Close encounters of a dust grain with the planet can lead to planet-grain accretion, to an ejection of the grain or a drastic change in the grain's orbit. Such an effect could explain the existence of an inner cleared zone if a large portion of the infalling grains have a close encounter with the planet. This occours if the grains fall through the planet's influence zone on a timescale longer than one planetary revolution and if the particle has an inclination $i$ of the order of $\frac{m}{M} \approx \frac{i^3}{3}$, where $M$ and $m$ are the masses of the star and the planet, respectively. In the $\beta$-Pic disk a Earth-like planet ($3 \times 10^{-6} M$) should be sufficient to scatter-off a disk of particles with inclinations smaller than 1 degree. However, a disk with an opening angle of 5 degree would need a greater mass, of the order of $2 \times 10^{-4} M$.
- **Resonance trapping** - Another effect of the planet is the long term perturbation involving mean-motion resonances between the planet and the grains. As a grain spirals toward the central star due to some drag effect, it crosses the geometrical place of mean-motion resonances with the planet. This is the location where the mean motion of the two bodies are in a ratio of small, integer numbers. If a particle is in a resonance the perturbation of the planet has a systematic effect at every synodic period. When the resonance is exterior and the grain revolves slower than the planet, the effect is a

secular transfer of momentum from the planet to the grain. The gain of momentum from the planet would then balance the loss due to the drag effect. The timescale of this equilibrium depends on the physical/dynamical parameters of the planet and grain. This is the particular case of a more general phenomenon which tends to push the particle away from the planet orbit as soon as some collective or irreversible effects are introduced in the system, the so-called *shepherding mechanism* (Sicardy et al, 1993; Goldreich and Tremaine, 1982).

In cooperation with B. Sicardy, F. Roques, H. Scholl and R. Greenberg (Scholl et al., 1993; Roques et al., 1993; Lazzaro et al., 1993) we alleged the existence of a planet in the $\beta$-Pic disk in order to explain the depletion zone observed. The problem focoused is then the decay of circumstellar grains due to the Poynting-Robertson drag and their possible capture into mean motion resonances with an hypothetical planet orbiting the star. For this approach to be valid we assumed that the gas from the proto solar nebula has already been cleared and that the optical thickness of the disk is small enough so that mutual collisions do not play an important role. These assumptions, as discussed above, are quitely in accordance to the data derived from the observations of $\beta$-Pic.

## 4. The model

The physical model considered is basically a restricted three body problem defined by the star, the planet and the grain dust and under the influence of the radiation pressure and Poynting-Robertson drag. We have two possible ways to describe the evolution of a grain dust: numerical or analytical. We shall analyze the results of both of them in what follows.

### 4.1 Numerical approach

The exact equations of motion of the above physical model were implemented in a Connection Machine where the parallel architecture of the computer allows to simulate the evolution of a disk of 8192 test particles. The great number of particles makes then visible any collective pattern driven by the alleged planet.

The Connection Machine used, CM-2/8k, can be briefly described as a sample of microcomputers which all execute simultaneously the same instruction of a code and which can exchange data on a very rapid network. A total of 8192 simple data processor can handle 8192 data element in parallel.

Each of the 8192 data processor was associated to a grain and the evolution analyzed over a time interval of 10000 planetary revolutions. It was used a 4th order variable time-step

Runge-Kutta integrator which is a relatively fast integrator on a massively parallel computer. It is important to note that due to the special configuration of this kind of computers we have a serius compromise between the best step-size for each particle and the optimization of the computation time. This problem was overcame in our case, defining an independent proper time for each grain since we assumed no mutual interaction between the grains.

Various simulations were done varying the parameters of the model, namely the planetary mass, the eccentricity of the planetary orbit, the radiation pressure (reflected in the parameter $\beta$) and the initial orbital elements of the grains. The mass of $\beta$-Pic was taken as 1.5 solar masses and the semi-major axis of the planetary orbit set equal to 20 AU. The osculating orbital elements of the grains were randomly distributed in the following ranges: 30 to 40 AU the semi-major axis, 0 to 8 degrees the inclinations, and 0 to 360 degrees the angular variables. Finally, the parameter $\beta$ was set between 0.1 and 0.3 which corresponds to grains with radii $\approx 2.7$ to 20 $\mu$m, depending on the assumed chemical composition.

The general feature of the evolution of a grain is that the semi-major axis of its orbit begins to decay due to the Poynting-Robertson drag. As it reaches the geometrical location of a resonance the semi-major axis stops to decrease while the eccentricity is pumped up. Depending on the parameters of the simulation, or the grain remains *trappped* at this location and its orbit becomes more and more excentric or it *escapes* and the semi-major axis keep up decreasing until it reaches another resonance and the process of trapping/escape starts over again. The main results of all the simulations are:

- For a planetary mass of the order of $10^{-6}$ star masses ($M_\star$), i.e. nearly half of the Earth's mass, all the grains fall onto the star on a timescale of $\sim 10^6$ years;
- There exists a critical planet mass of $\sim 10^{-5} M_\star$, i.e. about 5 Earth masses, above which trapping into resonance is very efficent;
- It was not observed any permanent trapping into resonances. However, the trapping time scale is comparable to the PR drag decay time scale, resulting in an accumulation of grains just outside the planet orbit;
- Once a grain escapes from the resonance, it readly fall onto the star, due to its enhanced eccentricity at that time;
- A moderate, $10^{-2}$, planet orbital eccetricity can create large scale azimutal (arc-like) asymmetries in the disk;
- The protection mechanism associated to the resonances also creates a void region just outside the planet and corototating with it.

In figure 1 we show a pole-on view of the simulated circumstellar dust disk after 8000 planet's revolutions, i.e. $5.84 \times 10^5$ years. The dotted line is the orbit of the planet at 20 AU from the star and with an eccentricity of 0.01. The planet mass is of $10^{-4} M_*$, the $\beta$ factor is 0.3 and the initial inclinations of the grain's orbits are set equal to zero. We can note clearly the arc-like structures in the disk and the void near the planet's position (cross).

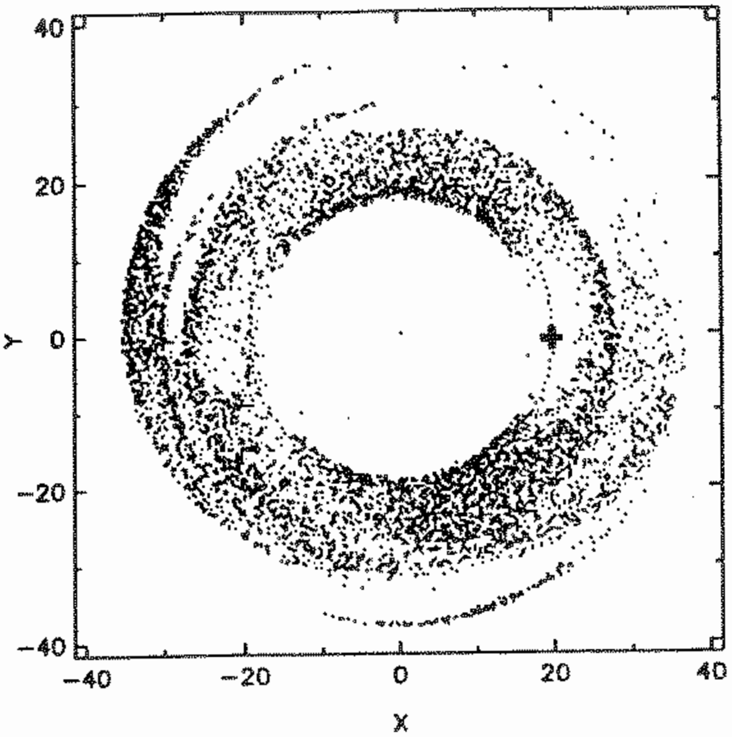

Figure - 1

### 4.2 Semi-analytical approach

The numerical simulations revelead some interesting structures. In order to understand their origin, we should resort to an analytical approach. Essentially we would like to answer to questions as: (a), what would be a *minimum* planetary mass necessary to trap a grain in a resonance?; (b), there exists *equilibrium* orbits in which a grain could be trapped permanently?; (c), the trapping could be *long enough* to explain a statistical accumulation of grains even if not permanent?; (d), what should be the *probability* of capture given some initial distribution of orbital elements?

Analytically our model can be described by the Hamiltonian system of the restricted three body problem plus an additional non-conservative drag force proportional to the velocity. When this drag term is zero the equations reduce to the classical equations of the perturbed motion in a conservative system and their solution in the presence of resonances are well studied (Henrard and Lemaitre, 1983; Ferra-Mello, 1985). These equations are then canonically transformed in variables more suitable to the study of resonances (Brower and Hori, 1966; Ferraz-Mello, 1992) and are finally averaged over short period terms.

Our approach was semi-analytical in the sense that we first derived the averaged equation of motion and then numerically integrated the resulting set of differential equations. The advantage of such a procedure are two: first, it is much faster in a computational point of view than the integration of the exact equations of motion and, second, the averaged equations keep only the relevant terms of the perturbing function allowing to better seperate local behaviour from global trends which will have statistical effects on the disk structure.

The price to pay is that the perturbing function must be truncated at some order in eccentricity, which invalidate its use at high eccentricities. Thus our aim was restricted to the better understanding of the *entrance* into the resonance. The principal results of our analysis were:

- the topological interpretation of the resonance effect is biven by two surfaces, a "Mexican hat" and a plane, steadly evolving in the phase space under the effect of dissipation;
- only external Lindblad resonances allow the existence of equilibrium orbits;
- the grain must have a conjunction with the planet after it has passed its apoapse but before it has reached its periapse. This ensures that the satellite *provide* energy to the grain to counteract the effect of dissipation;
- the eccentricity will increase as $\sqrt{t}$, where $t$ is the time, when trapped in a resonance;
- the final equilibrium eccentricity is *independent* of the damping coefficient. This result is the same as the "universal eccentricity" derived by Weidenschilling and Davis (1985) and by Beaugé and Ferraz-Mello (1993) in the case of gas drag;
- there exists a limiting value for the planetary mass in function of the star's mass, in order for trapping to be possible. This value is $\approx 4 \times 10^{-6}$ to $4 \times 10^{-7}$ depending on the resonance and for a $\beta$ coefficient of 0.3. Physically it means that if the dissipation is too strong, or if the planet mass is too small, not enough enegy is transferred to the grain to balance the dissipation;

- the crossing of a resonance is *non-adiabatic* for typical grains of the $\beta$-Pic disk. In this case the time of libration is not much smaller than the evolution time of the grain.

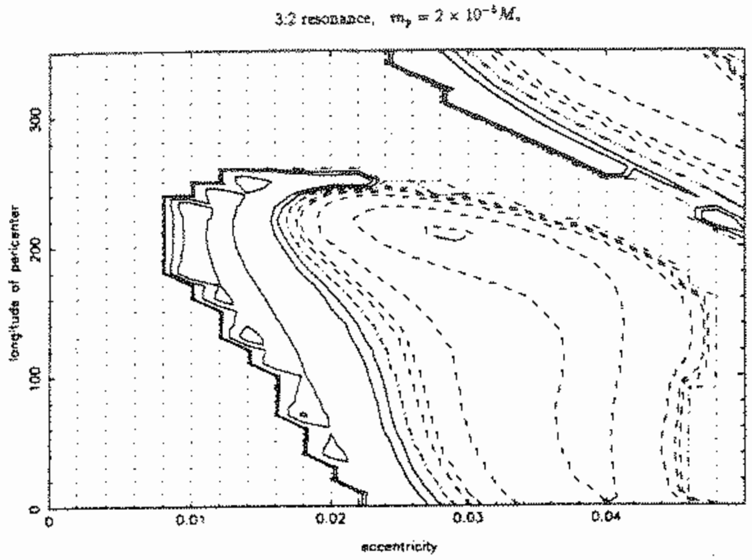

Figure - 2

In order to study the probability of capture we performed many integration and plotted the result of the resonance crossing (escape or capture) in a grid with the initial values of the longitude of pericenter in one axis and the eccentricity on the other axis. Such maps yield the probability of capture for a given resonance, planetary mass and $\beta$ coefficient. In figure 2 we show one of these maps where the dotted regions correspond to capture while solid level curves link points corresponding to the same net *increase* of eccentricity and dasched lines show points corresponding to the same *decrease* of eccentricity. We can readly note the smooth boundary between the capture and escape regions, but also the absence of obvious symmetries or regularities in the shapes of these regions. We thous suspect that the shapes of these regions cannot be derived analytically being impossible to have an expression for the probability of capture.

## 5. Conclusions

We have described the main results of the investigation of an alternative process in which a planet can induce large scale structures in a circumstellar dust disk. These structures, essentially a cleared zone near the star, match with the observations of the $\beta$-Pic disk.

Several questions remain open, however. From a purely dynamical point of view the problem of the escape from a resonance at high eccentricities should be better investigated. Also, some numerical intergration method that describes accurately the close encounters should be used to clarify whether particles are preferentially ejected outside or inside the planet orbit.

Another problem concerns with the collisional time scale of the particles trapped in a resonance. If this time is of the order of $10^4$ years in the most dense part of $\beta$-Pic, while the time scale for creating accumulation of material is in the range $10^5 - 10^6$ years. If so, the structures created by the resonances should be continuosly eroded. This point need to be carfully studied.

In spite of the very symplified model adopted and some problems left for a better solution, the results presented here are quite interesting since they point out a new way to confirm the presence of a planet of Earth-size in the disk of $\beta$-Pictoris. The detection of this (or *these*) planet not being by direct imaging of it but through the distribution analysis of the disk. As shown in figure 1 the trapping in resonances would create asymmetries and also a void in the disk around the planet. And this would be an indirect confirmation of the presence of a planet!

### References

Artymowicz, P., Burrows, C., Paresce, F.: 1989, *Astrophy. J.* **337**, 494.

Beaugé, C., Ferraz-Mello, S.: 1993, *Icarus* , in press.

Beust, H., Lagrange-Henry, A.M., Vidal-Madjar, A., Ferlet, R.: 1990, *Astron. Astrophys.* **236**, 202.

Burns, J.A., Lamy, P.L., Soter, S.: 1979, *Icarus* **40**, 1.

Ferraz-Mello, S.: 1985, *Celest. Mech.* **35**, 209.

Ferraz-Mello, S.: 1992, in Physics and Dynamics of Small Bodies of the Solar System, D. Benest and Cl. Froeschlé *(Eds.)*, Ed. Frontières, 45.

Goldreich, P., Tremaine, S: 1982, *Ann. Rev. Astron. Astrophys.* **20**, 249.

Henrard, J., Lemaitre, A.: 1983, *Celest. Mech.* **30**, 197.

Hobbs, L.M., Vidal-Madjar, A., Ferlet, R., Albert, C.E., Gry, C.: 1985, *Astrophys. J.* **239**, L29.

Lagrange-Henry, A.M., Vidal-Madjar, A., Ferlet, R.: 1988, *Astron. Astrophys.* **190**, 275.

Lazzaro, D., Sicardy, B., Roques, F., Greenberg, R.: 1993, *Icarus* , submitted

Norman, C.A., Paresce, F.: 1989, in The formation and Evolution of Planetary Systems, H.A. Weaver and L. Danly *(Eds.)*, Cambridge University Press, 151.

O'Dell, C.R., Zheng, W., Xi-Hai, H., Hester, J.: 1993, *Astrophys. J.* , in press.

Paresce, F.: 1991, *Astron. Astrophys.* **247**, L25.

Paresce, F., Burrows, C.: 1987, *Astrophys. J.* **319**, L23.

Roques, F, Scholl, H., Sicardy, B., Smith, B.: 1993, *Icarus* , submitted.

Scholl, H., Roques, F., Sicardy, B.: 1993, *Celest. Mech.* **56**, 395.

Smith, B., Terrile, R.J.: 1984, *Science* **226**, 1421.

Sicardy, B., Beaugé, C., Ferraz-Mello, S., Lazzaro, D., Roques, F.: 1993, *Celest. Mech.* , in press.

Vidal-Madjar, A., Lecavelier des Etangs-Levallois, A., Perrin, G., Ferlet, R., Sevre, F., Colas, F., Arlot, J.-E., Buil, C., Beust, H., Lagrange-Henry, A.-M., Lecacheux, J.: 1992, *The Messenger* **69**, 45.

Weidenschilling, S.J., Davis, D.R.: 1985, *Icarus* **62**, 16.

# Residuals from Catalogues Comparisons

A. H. Andrei ; CNPq / Observatório Nacional - Brasil
E-mail : oat1@on.br ; oat1@lncc.bitnet

**Abstract:** A number of large, precise catalogues, both in the optical and radio wavelengths, have been issued in the last decade. However, the comparison between the catalogues in the two bands shows disagreements larger than $10^{-1}$ arcseconds. Strategies to superseded this outfit are examined. On a test case, a model is applied, which uses the systematic deviations regarding the employed reference systems.

The FK5 minus FK4 systematic deviations, referred to the J2000.0 epoch and equinox, are calculated and analyzed. The methods of analysis include those used in the FK5 preparation (Schwan, 1985, 1988; Brosche, 1966). Also the angles of relative orientation between the two catalogues are calculated. Residual corrections ranging 0".05 appear for some regions as well as magnitude terms.

## I) Introduction

The Supplement to the Astronomical Almanac 1984, as well as a substantial number of authors (e.g. Standish, 1982; Aoki et al, 1983) recommended the use of J2000.0 referred corrections for transformations from the FK4 system to the FK5 system. Owing mainly to proper motions, the set of the corresponding B1950.0 referred corrections is not adequate for this purpose. The J2000.0 set is calculated, following the method presented by Schwan (1985, 1988), and analyzed.

Initially, the major optical and extragalactic astrometric catalogues are reviewed. Their adherence to the FK5 system at the epoch of place J2000.0 can improve the understanding of the sizeable, systematic mismatching between the equatorial systems defined by the different techniques.

Then, the optical minus radio positions of 17 stars, from Johnston et al, 1985, article are compared with the AGK3 minus FK4 region deviations, as an example of the usefulness of such residual corrections for works of higher precision.

## II) Review

From the mid eighties, a number of instrumental enhancements, theoretical improvements and enlarged requirements for precision, claimed for a better representation of the inertial frame. This is meant by an equatorial reference system which, in turn, is materialized by astrometric position catalogues.

In the optical side, gathered from various astrographic and transit catalogues, some compilations were published. Also, an out of the atmosphere effort, onboard the satellite HIPPARCOS, shall in due course supply an internally very precise catalogue. Stated below, the main all sky such catalogues are briefly commented.

_ The Fifth Fundamental Catalogue / FK5 : It is the successor to the FK4 (Fricke et al, 1963) and contains the classical fundamental stars used to define the latter system. It contains 1535 stars (about one per 25 square degrees), most of them brighter than the seventh magnitude. The average mean errors are 0".02 for positions and 0".05/cy for proper motions. It results from the determination of systematic and individual corrections to the mean positions and proper motions of the FK4, brought from the mean epochs of the revising catalogues to the FK4 zero points. Accordingly, the systematic differences, in the sense FK5 minus FK4, are defined at the epoch and equinox B1950.0 . Then the error in the FK4 equinox and the elliptical terms were eliminated and the 1976 IAU System of Astronomical Constants were introduced, in order to take the FK5 at the epoch of place J2000.0 (Fricke et al, 1988).

_ The FK5 Extension / FK5 Ext. : It contains 3117 stars, extending the FK5 system to fainter reaches, ranging from magnitude 5.5 up to about 9.5 . Its stars are selected from the FK4 Sup. (Fricke, 1963) and from the IRS (Corbin, 1991) on the basis of their history of observation. The accuracy of their positions and proper motions is significantly inferior to those of the basic fundamental stars (in average 0".08 for positions and 0".4/cy for proper motions) (Fricke, Schwan and Corbin, 1991).

_ The International Reference Stars Catalog / IRS : It contains 36027 stars, with a 81% more accurate core (just short of one star per square degree, therefore). It was compiled by matching 122 meridian circle catalogues with the AGK3R (Corbin, 1977) and SRS (Smith et al, 1990), retaining the stars on basis of the observational history, to provide the data base. Its magnitudes range from 6.5 up to 9.5 . Special care was taken to place it onto the FK4 System, epoch and equinox B1950.0 and then to FK5 system, at the equinox and epoch of place J2000.0, using the coefficients of H. Schwan (1988), fitting for the magnitude equation. The accuracy equals that of the FK5 Ext (Corbin, 1991).

_ Astrographic Catalogue of Reference Stars / ACRS : The downgrade of the SAO, which present accuracy is of the order of one arcsecond, caused a great demand for a high-density catalogue of astrometric positions and proper motions. The ACRS, as the PPM reviewed below , was designed to attend this goal. It contains

320211 stars, with a 78% core of higher precision (about 10 stars per square degree). The magnitude range is from the 6th to the 12th. It is based on the AGK3 (Dieckvoss et al, 1975) in the north and on the CPC2 (de Vegt et al, 1989) in the south. These two catalogues were matched with many astrographic and circle meridian catalogues for redundancy, and then reduced to a combination of the FK4 and FK4 Sup. systems, attaining average mean errors of 0".12 in positions and 0".5/cy in proper motions (Corbin and Urban, 1991).

_ The Catalogue of Positions and Proper Motions / PPM : Presently, it is the larger of the compiled catalogues, possessing 326518 stars. It is based on the AGK3 in the north and on the FOKAT (Bystrov et al, 1993) in the south. Accounting for the natural discrepancy of ways between two independent teams, it shares with the ACRS most of the aims and methods of compilation and reduction. The PPM, however, has some intrinsic differences in its northern and southern parts. In the south, the precisions are 0"12 for positions and 0".35/cy for proper motions, the magnitudes range from the 6th to 11th, peaking at the 9th. In the north the accuracies are 0".28 for positions and 0".45/cy for proper motions, the magnitudes extending from the 6th to 13th, peaking at the 10th. There is a high precision subset of the northern PPM, with 31841 stars, for which the accuracy matches that of the southern portion (Roeser and Bastian, 1989).

_ High Precision Parallax Collecting Satellite catalog / HIPPARCOS: Launched in mid 1989, the HIPPARCOS satellite failed to reach its intended geostationary orbit. The pessimistic prospects at that time had, however, been superseded by successful redesigning of onboard and remote attitude controls, in such a way that around 90% of the scheduled mission shall be achieved (Van der Ha, 1992). The HIPPARCOS satellite has a field of view of little less than one square degree, covered by a grid of parallel slits with a period of 1".2 . On the field two regions, 58 degrees apart in the sky, are brought together, by a mirror. The orbital and revolutioning movements of the satellite enable every star to be observed against different parts of the sky ( Ratier et al , 1992 ) . This way

118000 stars are being observed and final accuracies of 0".002 for positions and 0".2/cy are to be reached, 87% are brighter than magnitude 11 and 4% are fainter than 12. The distribution over the sky is homogeneous, still with a slight concentration along the galactic plane (Turon et al, 1992). The very precise system so obtained will require a further link to the FK5 system, the radio reference system and the dynamical reference system. To this purpose practically all the FK5 and IRS stars, about 200 selected radio stars and about 200 selected link stars are in the input list (Jahreiβ et al, 1992), as well as 48 minor planets and two natural satellites are observed (Bec-Borsenberger, 1992).

In the radio band, no coherent catalog of radio emitting stars have been issued. There are, in opposition, three independent list of radio quasars, all from VLBI consortia. They are presented following.

_ Jet Propulsion Laboratory / JPL : It contains 127 point extragalactic radio sources (a point source being defined by it compactness below $10^{-2}$ arcseconds). The sources are distributed uniformly northern of -40 degrees of declination. The VLBI sessions have been carried out with six antennas of the NASA's Deep Space Network in Spain, California and Australia. Near equator sources observed only from the Spain-Australia baseline present a much larger error in declination. There is also a reduction in precision for those sources observed only at 2.3 GHz (S band), as the effects of the ionosphere cannot be adequately removed. For most of the sources however, north-south baselines were included and dual frequency observations, including the 8.4 GHz / X band, and therefore the position accuracies are below 0".005. The equatorial coordinates are referred (non-explicitly) to the equator and equinox J2000.0. Declinations are absolute and right ascensions are tied to the conventional value for 3C273B, **RA** = $12^h$ $29^m$ $06^s.6997$ (Fanselow et al, 1984).

_ National Geodetic Survey / NGS : This is the less numerous of the lists, just containing 26 compact extragalactic sources (defined as above). It is a subset of the POLARIS/IRIS space navigation and earth rotation VLBI projects. The distribution of the sources is fairly even in the northern celestial hemisphere. In this, it is not fully independent of the GSFC list reviewed next. All observations have been carried out at the S and X bands, being therefore free from ionosphere effects. The observations were made using the Mark III system, which more adequately handles tropospheric effects. Four stations participate of the observations: Haystack/Massachusetts, Onsala/Sweden, Miami and Bavaria/Germany. The reductions procedures conformed those recommended by the IAU, except by corrections to the standard nutation series, with a quasi-annual period of amplitude ranging 0".005. Positions are referred to the equator and equinox J2000.0 and the quoted precision is below 0".001 in average (Robertson, Fallon and Carter, 1986).

_ Goddard Space Flight Center / GSFC : This is the largest of the catalogues, presently containing 274 extragalactic radio sources. It is an well distributed all sky catalogue, aiming to reach 400 sources. Starting with the Mark I VLBI system (Ma et all, 1986), it now uses the Mark III system, dual frequency observations and 28 stations, providing accuracies consistently below one milli arcsecond. Sixteen of the stations are in North America (one in Alaska), six in Europe (the southern in Spain), two in South Africa, three in the Pacific (one in Japan) and one in Australia. This is the first program planned towards establishing a global radio/optical reference frame. The right ascension origin is fixed by the average of 28 sources, which optical counterparts are tied to the FK5 System. The sources are re-observed, to improve the positions as well as to monitorize the development of structures (Ma et all, 1990; Russel et al, 1991; Russel et al, 1992).

## III) Comparison of Optical and Radio Positions

The VLBI extragalactic system, therefore, is the primary celestial reference system for its accuracy and stability over time. The average internal accuracy of this system is better than one milli-arcsecond, as shown by comparisons between independent realizations (Arias, Feissel and Lestrade, 1988). The precision is comparable to the 2 milli-arcsecond precision expected for the internal consistency of the Hipparcos optical reference frame. A link between these two reference frames is important to unify the optical and radio coordinate systems for registration of images at both wavelengths and to stop the global rotation of the Hipparcos frame for dynamical studies.

On the other hand, the present standard celestial reference frame is materialized by the FK5. The zero points of the VLBI and Hipparcos frames must be referred to those of the FK5. Finally, the matching between the FK5 and the extragalactic system is required to halt the complex residual rotation that the FK5 system can still possess. The low star density of the FK5 makes it needed to extend its system (and the improvements to it) onto the denser catalogues.

The optical and radio reference frames may be related by measuring the positions of objects that display both optical and radio emission. Stars, small solar system bodies and compact extragalactic objects have all been proposed to this link. All have peculiar advantages and difficulties, and probably a combination of them will at some stage be required. The details of such ongoing programs are out of the scope here, suffice to say that special programs of optical observation of quasars and stars are being pursued at the CNPq/Observatório Nacional, the latter in a joint effort with the IAG/USP and the Observatório do Valongo/UFRJ .

The analysis of the differences between the optical and the radio system has shown a systematic nature. The differences range 0".2 and are illustrated by figures 1 and 2, from Johnston et al (1985). It has to be stressed that these trends have been repeatedly found by most of the authors publishing on the subject.

The offsets can have three origins: 1) accidental or systematic errors tied to one or another technique; 2) a displacement between the centroids at one or other frequency; 3) a misalignment between the two reference systems.

In the following, the third hypothesis is examined. To do so, the systematic differences between the FK4 (origin reference system of the optical catalogues) and the FK5 (materialization of the celestial frame) are calculated at the equinox and equator J2000.0 (epoch of place of the VLBI catalogues)

## IV) Obtaining the FK5 minus FK4 Offsets at J2000.0

In Schwan method, the systematic differences between two catalogues are represented by series of functions, which terms are normalized products of Hermite and Legendre polynomials and Fourier terms. They represent, respectively, the declination, magnitude and right ascension dependencies. Adopting Schwan's notation a systematic difference is represented by:

$$\Delta = \sum_j b_j \; Y_j \tag{1}$$

$$Y_j = R_{pnml} \; H_p(y(m)) \; L_n(x(\delta)) \; F_{ml}(\alpha) \tag{2}$$

$\mathbf{R_{pnml}}$ is a normalizing factor and $\mathbf{b_j}$ is the free coefficient to be determined.

The most significant $\mathbf{Y_j}$ , that is combinations of **H** , **L** and **F**, are selected through an F-test.

In the present work, all possible $\mathbf{Y_j}$ were formed from the following range of variations: **p** from 0 to 2 ; **n** from 0 to 30 ; **m** from 0 to 4 ; **l** assumes the values +1 or -1, meaning sinus or cosinus functions of the right ascension. All $\mathbf{Y_j}$ were separately tested with the F-test and those significant at 10% level were retained. This limit was chosen for reasons of computation and it ensured that more functions are retained than in the original analysis on the two catalogues.

The retained functions were then adjusted by Least Squares, to determine the coefficient $\mathbf{b}_j$ . Only those functions for which $\mathbf{b}_j$ were found larger than one standard deviation are kept in the final set. All effects of borders' steepness are removed this way.

The representative functions found in this way are used to calculate a detailed table of differences, in the fashion presented in the Fifth Fundamental Catalogue Explanations (Andrei, 1993). Also the usual equatorial coordinates offsets between the catalogues, assorted per right ascension and declination zones, were calculated, as they reveal the unsmoothed trend of the systematic differences (Andrei, 1992).

In general, the trends of the systematic differences, in the sense FK5 minus FK4, at the epoch of place B1950.0, repeat themselves at J2000.0 , for which all our results are placed. There are two sets of such systematic differences, one including (set **D**) and one without including (set **WD**) the B1950.0 systematic differences.

The transformations from B1950.0 to J2000.0 were performed according the algorithm given on page B42 of the Explanatory Supplement for the Astronomical Almanac, 1984. The procedures of Schwan method used the software from that author and were checked along the lines suggested in Schwan (1988). As a final test, we reobtained the J2000.0 IRS coordinates, from the B1950.0 ones, for the stars below the 7th magnitude in that catalogue. All computations were performed in double precision and all tests had succesfull outcomes. As a remark, it could be noted that the results from the series representation differs only by about 0".01 from those obtained by the interpolation of the FK5 tables of differences.

## V) Conclusions and Final Remarks

For two thirds of the fundamental stars, individual J2000.0 , FK5 minus FK4 differences in right ascension and in declination are larger than 0".05, after correcting for the B1950.0 systematic differences between the catalogues. These individual differences are randomly distributed in the major part of the sky. However , southern of $\delta = -35°$ and in some few other regions the averages have significant departures from the quoted precision of the FK4.

When non considering the B1950.0 FK5 minus FK4 systematic effects, set **WD** therefore, there is a significant (0".034   0".005) clockwise rotation along an equatorial axis perpendicular with the equinox direction. Those effects considered, set **D**, still a small residual rotation of the same kind remains (0".007   0".004). Also interesting is the rapid variation of values between neighboring regions and the markedly worsening southwards (Andrei, 1992).

In what concern the equatorial coordinates, the systematic differences for set **WD** are enlarged pictures of those referred to B1950.0. On the other hand, for both the proper motions there is not such enlargement, rather a quasi-coincidence.

The major features in set **D** are that pure declination dependencies vanish, that is declination dependencies appear instead as cross functions of right ascension and magnitude. A strong magnitude equation subsists for right ascensions, reaching $0^{s}.015$ for the brighter southern stars. The right ascension dependencies are only important on the southern sky. Very much the same happens for the corresponding proper motions.

The picture that emerges shows residual systematic differences upon the equatorial coordinates (ranging 0".05), which are consistent with the residual differences in proper motions.

This way, a further J2000.0 , FK5 minus FK4 set of corrections (set **D** , in this paper) would be useful when transforming FK4 referred positions to the FK5 system, with the highest precision.

An independent illustration of the effect of such systematic local differences is here drawn from a forthcoming work (Andrei et al, in preparation). From the series articles published in 1985 by Johnston, deVegt, Florkowsky and Wade a table of optical minus radio positions of 17 northern stars is extracted. After converting the FK5 onto the B1950.0 , FK4 orientation, we calculated the AGK3 minus FK5(B1950) average differences for $30^0$ x $30^0$ regions around each of those stars, at the mean epochs of observation. The correlations between the two sets of differences is found at the levels of confidence of 0.88 for right ascensions and 0.96 for declinations. There is no attempt to correct the right ascensions differences for a magnitude equation, this accounts, in part, for the worse right ascension result. On the other hand, if the first two stars, which optical positions have not been established in the same way of the rest, are removed and only stars for which the AGK3 minus FK5(B1950) coordinates differences are equal or smaller than 0".07 are used for the averages, then the correlations are found at the levels of confidence of 0.95 for right ascensions and 0.94 for declinations.

## VI) Acknowledgements

The author would like very much to thank to Dr. H. Schwan for his analysis software and a reference paper gently sent. Many thanks go also to Dr R. Martins, Dr C. H. Veiga and M. Assafim from the Observatório Nacional / Brasil and Dr. B. Elsmore and Dr. N. Argue from Cambridge/UK for their encouragement in different steps of this work.

## VII) References

_ Andrei, A.H.; 1992; "Compilação de Posições de Rádio Estrelas"; XVIII Reunião Anual da SAB.

_ Andrei, A.H.; 1993; "Resíduos em Comparações de Catálogos"; XIX Reunião Anual da SAB.

_ Aoki, S., Sôma, M., Kinoshita, H. and Inoue, K.; 1983; Astron. Astrophys., **128**, 263.

_ Arias, E.F., Feissel, M. and Lestrade, J.-F.; 1988; Astron. Astrophys., **199**, 357.

_ The Astronomical Almanac; 1984; The Nautical Almanac Office, U.S. Naval Observatory and H.M. Nautical Almanac Office, Royal Greenwich Observatory.Florkowski, D.R., Johnston, K.J., Wade, C.M. and Brosche, P.; 1966; Veröff. Rechen-Institut, **17**.

_ Bec-Borsenberger, A.; Astron. Astrophys., **258**, 94.

_ Corbin, T.E.; 1991; International Reference Stars Catalog; Washington, U.S. Naval Observatory.

_ Corbin, T.E.; 1978; in IAU Coll. 48, "Modern Astrometry", p505; ed F.V. Prochazka and R.H. Tuckerms, Inc.

_ Corbin, T.E. and Urban, S.E.; 1991; "Astrographic Catalogue Reference Stars; Doc. No. NSSDC/WDC-A-R&S 91-10, Greenbelt, USA.

_ deVegt, C.; 1985; Astron. Jour., **90**(11), 2381.

_ deVegt, C., Florkowski, D.R., Johnston, K.J. and Wade, C.M.; 1985; Astron. Jour., **90**(11), 2387.

_ deVegt, C., Zacharias, N., Murray, C.A. and Penston, M.J.; 1989; in "Star Catalogues: A Centenial Tribute to A.N. Vyssotsky", p45; Schenectady, L. Davis Press.

_ Dieckvoss, W., Kox, H., Guenther, A. and Brosterhus, E.; 1975; "AGK3, Star-Catalogue of Positions and Proper Motions North of -2.5 Declination"; Hamburg-Bergedorf.

_ Fanselow, J.L., Sovers, O.J., Thomas, J.B., Purcell Jr, G.H., Cohen, E.J., Rogstad, D.H., Skjerve, L.J. and Sptizmesser, D.J.; 1984;, Astron. Jour., **89**, num. 7, 987.

_ Fricke, W., Schwan, H., Lederle, T., Bastian, U., Bien, R., Burkhardt, G., duMont, B., Hering, R., Jährling, R., Jahreiβ, H., Röser, S., Schwerdtfeger, H.M., and Walter, H.G.; 1988; "Fifth Fundamental Catalogue (FK5)"; Veröff. Rechen-Institut, **32**.

_ Fricke, W., Kopff, A., Gliese, W., Gondolatsch, F., Lederle, T., Nowacki, H., Strobel, W. and Stumpff, P.; 1963; "Fourth Fundamental Catalogue (FK4)"; Veröff. Rechen-Institut, **10**.

_ Fricke, W., Schwan, H. and Corbin, T.; 1991; "Fifth Fundamental Catalogue (FK5), Part II. The FK5 Extension."; Veröff. Astron. Rechen-Institut, **33**.

_ Jahreiβ, H., Réquième, Y., Argue, A.N., Dommanget, J., Rousseau, M., Lederle, T., Le Poole, R.S., Mazurier, J.M., Morrison, L.V., Nys, O., Penston, M.J., Périe, J.P., Prévot, L., Tucholke, H.J. and deVegt, C.; 1992; Astron. Astrophys, **258**, 82.

_ Johnston, K.J., deVegt, C., Florkowski, D.R. and Wade, C.M.; 1985; Astron. Jour., **90**(11), 2390.

_ Ma, C., Clark, T.A., Ryan, J.W., Herring, T.A., Shapiro, I.I., Corey, B.E., Hinteregger, H.F., Rogers, A.E.E., Whitney, A.R., Knight, C.A., Lundqvist, G.L., Shaffer, D.B., Vanderberg, N.R., Pigg, J.C., Shupler, B.R. and Ronnang, B.O.; 1986; Astron. Jour., **92**, num. 5, 1020.

_ Ma, C., Shaffer, D., deVegt, C., Johnston, K.J., and Russel, J.L.; 1990; Astron. Jour., **99**, num. 4, 1284.

_ Ratier, G., van Katwijk, K., Fade, G. and Perryman, M.A.C.; 1992; ESA Bulletin, **69**, 27.

_ Robertson, D.S., Fallon, F.W. and Carter, W.E.; 1986; Astron. Jour., **91**, num. 6, 1456.

_ Roeser, S. and Bastian, U.; 1989; in "Star Catalogues: A Centenial Tribute to A.N. Vyssotsky", p31; Schenectady, L. Davis Press.

_ Russel, J.L.,, Johnston, K.J., Ma, C., Shaffer, D. and deVegt, C.; 1991; Astron. Jour., **101**, num. 6, 2266.

_ Russel, J.L., Jauncey, D.L., Harvey, B.R., White, G.L., Reynolds, J.E., Ma, C., Johnston, K.J., Nothnagel, A., Nicolson, G., Kingham, K., Hindsley, R., deVegt, C., Zacharias, N. and Malin, D.F.; 1992; Astron. Jour., **103**, num. 6, 2090.

_ Schwan, H.; 1985; Astron. Astrophys., **149**, 50.

_ Schwan, H.; 1988; Astron. Astrophys., **198**, 363.

_ Smith, C.A., Corbin, T.E., Hughes, J.A., Jackson, E.S., Krutskaya, E.V., Polozhentsev, A.D., Polozhentsev, D.D., Yagudin, L.I. and Zverev, M.S.; 1990; in IAU Symp. 141, "Inertial Coordinate System on the Sky", p457; ed J.H. Lieske and V.K. Abalakim, Dordrecht, Reidel.

_ Standish, E.M.; 1982; Astron. Astrophys., **115**, 20.

_ Turon, C., Gómez, A., Crifo, F., Crézé, M., Perryman, M.A.C., Morin, D., Arenou, F., Nicolet, B., Chareton, M. and Egret, D.; 1992; Astron. Astrophys, **258**, 74.

_ Van der Ha, J.; 1992; ESA Bulletin, **69**, 9.

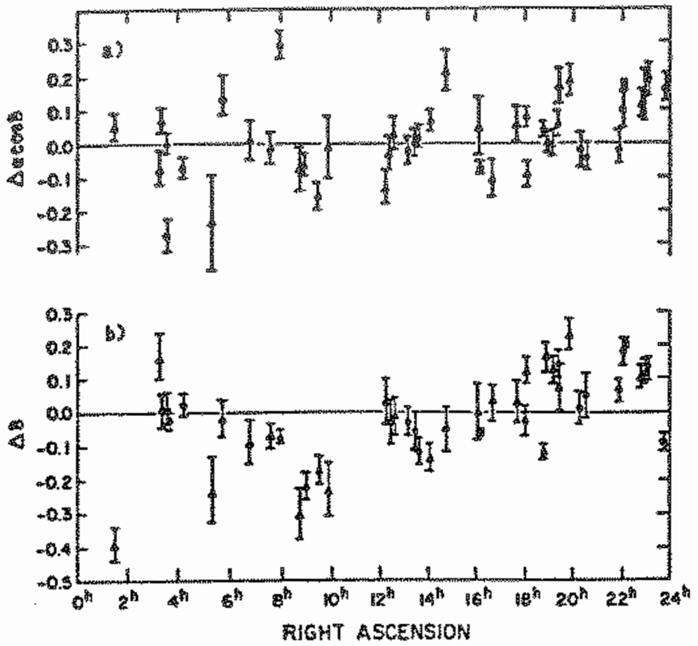

FIG. 1. Difference between optical – radio position for $\Delta\alpha \cos\delta$ versus right ascension. (b) The corresponding difference in declination. Units are tenths of an arcsecond.

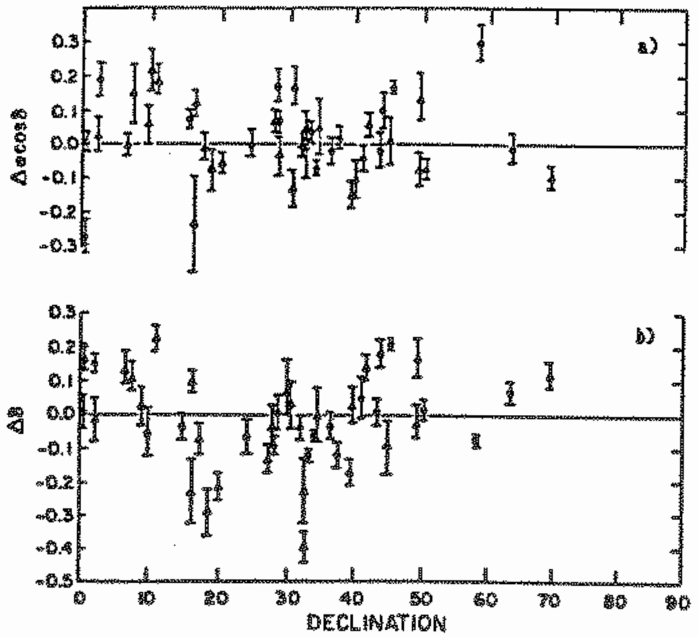

FIG. 2. (a) Difference between the optical – radio positions versus declination for $\Delta\alpha \cos\delta$. (b) The corresponding optical – radio difference in declination. (⊕) denote stars, (△) extragalactic sources. Only sources in the northern hemisphere are shown. Units are tenths of an arcsecond.

# MHD WAVES IN THE SOLAR ATMOSPHERE

**Vera Jatenco-Pereira**
Instituto Astronômico e Geofísico - Universidade de São Paulo
Av. Miguel Stéfano, 4200, CEP 04301-904, São Paulo, SP, Brazil

### Abstract

We discuss the solar magnetic activity and the role of a nonthermal mechanism in heating the corona as well as heating and accelerating the solar wind. In particular, we present a solar wind coronal hole model driven by Alfvén waves which reproduce the observational data of temperature and velocity profiles of the wind. We also discuss the model with a frequency-dependent flux of Alfvén waves.

## 1 Introduction

The solar atmosphere consists basically of photosphere, chromosphere and corona. Above the photosphere and into the chromosphere and corona, the density falls rapidly from $10^{17}\,cm^{-3}$ through $10^{11}\,cm^{-3}$ to $10^9 - 10^8\,cm^{-3}$, while the temperature increases slightly from $\sim 6000\,K$ to $10^4\,K$ and them suddenly jumps through a narrow transition layer to $\sim 2 \times 10^6\,K$. The solar wind is an extension and a super-sonic expansion of the solar corona into interplanetary space (Priest 1985).

Magnetic fields introduce structuring into the atmosphere. At the photospheric level, the field is found to occur in magnetic clumps or flux tubes, which are isolated from their neighbours. The field strengths are high, generating a hierarchy ranging from $\sim 1.5\,kG$ in intense flux tubes to $\sim 3\,kG$ in sunspots. Above the photospheric layers, in the low chromosphere, the isolated flux tubes rapidly expand to merge with their neighbours, completely filling the chromosphere and corona with magnetic field. An H$\alpha$ photograph of the chromosphere shows a bright active region surrounding a sunspots group, in which a flare occasionally takes place. Also, thin dark structures called filaments or prominences meander across the disc. At times of solar eclipse the corona is revealed with plasma structures outlining the magnetic field. There are closed regions, where the magnetic field is strong enough to contain the plasma. Soft X-rays images from Skylab reveal dark regions of open magnetic field, called coronal holes, along which the fast solar wind is escaping (Priest 1985).

The nuclear energy released in the solar interior is transported outward as flux of *thermal* energy by conduction, convection, and radiation. The existence of a hot corona implies in a *nonthermal* outward energy flux to maintain it. Some form of macroscopic motion, either oscillatory or quasistatic, is needed to transport this nonthermal energy. The first hypothesis and by far the most completely studied is that propagating waves, generated by motions in the hydrogen convective zone, provide this energy flux. As they propagate through the atmosphere, these waves produce, in addition to heating, nonthermal broadening and Doppler shifts of spectral lines.

There are three principal kinds of wave generation mechanisms, corresponding to each of the three conservation laws (mass, momentum and energy) that govern fluid motions. These mechanisms are applied to three kinds of waves: acoustic, gravity, and Alfvén waves. These are not the only kinds that can exist, but they give some idea of the range of wave types, at least for low frequencies where plasma effects are unimportant. They are pure cases, distinguished by their different restoring forces: pressure for acoustic waves, buoyancy for gravity waves, and magnetic tension for Alfvén waves (Stein and Leibacher 1981).

According to the theory developed over the past several decades, sound waves rise from the photosphere, steepen into shocks, and dissipate into heat, with a suitably fraction of the waves reaching into the corona before dissipation. The result is an essentially uniform heating of the lower corona, which if difficult to reconcile with the observations of loop structure. On the other hand, the theory that the corona is heated by hydromagnetic waves is of interest because it naturally fits into a scheme explicitly involving coronal structure, and it also implies a suitable source of momentum for the solar wind.

We have direct evidence for Alfvén waves in the solar wind. Waves are observed with large perturbations in the magnetic field, with negligible density perturbations, indicating the presence of Alfvén waves. A proton temperature higher than electron temperature, and a proton temperature perpendicular to the magnetic field higher than the temperature parallel to the magnetic field, indicate ion-cyclotron heating, which is the high-frequency limit of Alfvén waves.

We will concentrate here in a coronal hole solar wind model driven by Alfvén waves (Jatenco-Pereira and Opher 1989), and the extention of this model including a frequency dependent flux of Alfvén waves (Jatenco-Pereira, Opher and Yamamoto 1991, 1992).

## 2 The Model

In various solar wind models Alfvén waves are included as a major mechanism of the wind acceleration (e.g. Hollweg 1978; Jatenco-Pereira and Opher 1989 (JPO)). The nonthermal energy flux is deposited in the region of supersonic flow in order to explain: (1) the observed high asymptotic flow speed $u_\infty \geq v_{e0}$ (where $u_\infty$ is the terminal velocity and $v_{e0}$ is the surface escape velocity) and (2) the low mass-flow density. It is known that coronal holes are the source of the high-speed solar wind streams at the Earth's orbit (e.g. Neupert and Pizzo 1974). The measurement of particle fluxes mapped back to coronal holes implies mass fluxes at the base of a coronal hole which are $5-10$ times as great as the mass flux obtained by assuming a spherically symmetric solar wind (Hundhausen 1977) (i.e., implying coronal holes occupying an area $10\,\%-20\,\%$ of the solar surface).

The model of JPO is based on our knowledge of the magnetic structure of the Sun. At the surface, we observe coronal holes in which the opening solid angle ($\Omega_o$) changes to $\approx 7\Omega_o$ going from $r=R_\odot$ to $r=3R_\odot$. Beyond $3R_\odot$ the edges of the coronal holes are radial and a net non-radial expansion factor of $F\equiv\frac{\Omega}{\Omega_o}=7.26$ for ($r>3R_\odot$) is found (Munro and Jackson, 1977).

We assume for studying the effects of a diverging geometry in coronal holes, the following initial conditions $(a)-(d)$:

$(a)$ We simulate the possible geometry of a coronal hole considering that $i)$ initially the geometry is radial up to $r_t$, with $A(r)=A(r_o)(\frac{r}{r_o})^2$, where $A(r)$ is the cross-section of the geometry at a radial distance $r$, $r_o$ is the initial radius; $ii)$ after which, the geometry is rapidly divergent up to $r_T$ ($\sim 2R_\odot$), with $A(r)=A(r_o)(\frac{r_t}{r_o})^2(\frac{r}{r_t})^S$; and $iii)$ after $r_T$ the geometry is again radial, with $A(r)=A(r_o)(\frac{r_t}{r_o})^2(\frac{r_T}{r_t})^S(\frac{r}{r_T})^2$. $S$ a parameter that determines the divergence of the geometry (see Fig. 1).

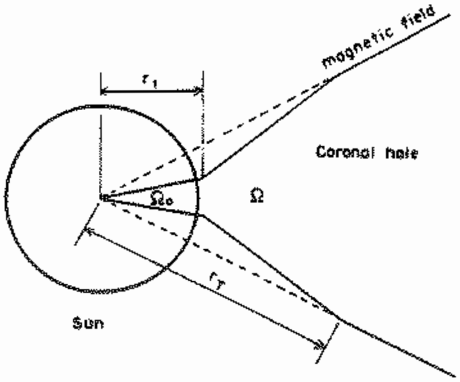

Figure 1: The model studied.

$(b)$ In order to satisfy the observational data near the base of the solar corona, we use in our model two average values for the base pressure: $(nT)_o=2.0\times10^{14}$ and $(nT)_0=4.0\times10^{14}\,cgs$, where $n$ is the electron or proton density (e.g. Mariska 1978). We begin our calculations at the temperature $T_o=5\times10^4\,K$.

($c$) Coronal holes are believed to cover a fraction $g \sim 10\% - 20\%$ of the area of the Sun. Using the observational mass-loss rate of the Sun, $\dot{M} \sim 2 \times 10^{-14} M_\odot\, yr^{-1}$, we have the initial velocity $u_0 = \dot{M}/4\pi R_\odot^2 \rho_o g$. We note, in general, that in previous calculations $u_o$ is left as a free parameter, adjusted in such a way that the solution goes through the critical point. In our study, $u_o$ is a boundary condition, required to satisfy observations, and $r_t$ is adjusted in such a way that the solution goes through the critical point.

($d$) We use a flux of Alfvén waves ($\phi_M \sim 10^6\, erg\, cm^{-2}\, s^{-1}$) generated near the solar surface (possibly by the annihilation of twisted magnetic fields) as a mechanism of heating and acceleration of the solar wind, with an average damping length $\bar{L}$, which in principle may cover the possibility that the various dissipation processes, discussed in the literature, may act jointly. We use an initial magnetic field $B_o = 8.25\, G$, which is consistent with the solar wind magnetic field at $1\, AU$.

We use the equation of state for fully ionized hydrogen and the equations for mass, momentum, and energy conservation.

The equation of motion (e.g., eq. [52] of Holzer, Fla and Leer 1983; eq. [16] of JPO) is

$$\frac{1}{u}\frac{du}{dr} = \frac{Z}{r}\frac{N}{D},$$

where $u$ is the ejected velocity at the radius $r$, $Z = 2$ for $r \le r_t$ and $r > r_T$, and $Z = S$ for $r_t \le r \le r_T$. $N$ and $D$ are given by

$$N \equiv v_T^2 \left(1 - \frac{r}{v_T}\frac{dv_T}{dr}\right) + \frac{1}{4}\left(\frac{1+3M_A}{1+M_A}\right)\langle \delta v^2 \rangle + \frac{1}{4}\frac{r}{L}\langle \delta v^2 \rangle - \frac{1}{2Z} v_e^2,$$

$$D \equiv u^2 - v_T^2 - \frac{1}{4}\left(\frac{1+3M_A}{1+M_A}\right)\langle \delta v^2 \rangle,$$

where $M_A \equiv u/V_A$ ($V_A$ is the Alfvén velocity), $L$ the damping length, $v_T$ the ion thermal velocity, $v_e$ the escape velocity, and $\langle \delta v^2 \rangle$ the energy density of the Alfvén waves divided by the local mass density.

We have from conservation of energy that at all points the sum of the Alfvén flux ($\phi_M$), the conductive flux ($\phi_C$), the radiative flux ($\phi_R$), and the wind flux ($\phi_W$) is a constant.

We start our integration at the radius $r_o$ (which is slightly larger than the photospheric value of the solar radius $R_\odot$). We found that by varying $r_t$ we obtain the requirement of $D$

and $N$ passing through zero at approximately the same point (the critical point) and obtain resonable values of $u$ and $T$. We continued the calculations until $10R_\odot$ taking into account the thermal conductivity becoming collisionless at larger distances from the Sun. We show in Fig. 2 the results of $T$, $u$, $\phi_M$, $\phi_W$ and $\phi_C$ as a function of distance.

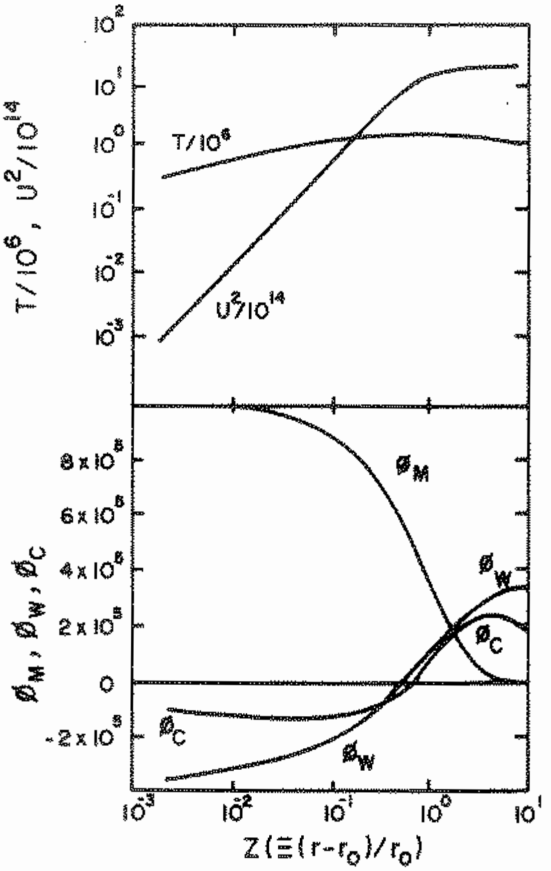

Figure 2: Dependence of $T$, $u$, $\phi_M$, $\phi_W$ and $\phi_C$ with the distance.

On the other hand, the in situ observations of the solar wind in the interplanetary medium show a spectral break in the power density spectra. Bavassano (1990) showed that near the Sun most of the fluctuations are propagationg outward with respect to the Sun indicating that the fluctuations observed originate from the Sun.

Tu et al. (1989, 1990) studied the observed ($r \sim 0.3\,AU$) power spectrum in the frequency range ($6\times10^{-6}-6\times10^{-3}\,Hz$). They fitted two power law indices for low and high frequencies. In the present model we try to explain the break in the frequency spectrum. We use the solar wind model of JPO driven by Alfvén waves, modifying it for a frequency-dependent flux of Alfvén waves. We also assume that initially (up to $r \sim 2R_\odot$) we have appreciable heating and momentum deposition by network activity (Parker 1991).

The initial Alfvén wave flux,

$$\phi_{Mo} = \phi_{Mo\nu}\left(\frac{\nu}{\bar{\nu}}\right)^{-\alpha} \quad erg\, cm^{-2}\, s^{-1}\, Hz^{-1} \ .$$

is described by a power law with $\bar{\nu}$ the mean frequency in the observed power density spectra and $\alpha = 0.6$ obtained from the low frequency part of the observed power density spectra (e.g. Tu et al. 1989).

For this study, we assume the same initial conditions $(a)-(d)$ with $(nT)_o = 4.0 \times 10^{14}\, cgs$ and a flux of Alfvén waves jointly with network activity as a mechanism of heating and acceleration of the solar wind. Surface Alfvén waves appear whenever exist a discontinuity which can extract energy from the existing waves near this region. In the present work, we assume that only a fraction of the Alfvén waves will be in the surface region and will be damped by the ressonant damping mechanism (Jatenco-Pereira, Opher and Yamamoto 1991, 1992). We solved autoconsistenly the equations of mass, momentum and energy conservation. We evolved the calculations from $r_o$ until $r = 64 R_\odot$ to obtain the results of frequency distribution, velocity and temperature profiles.

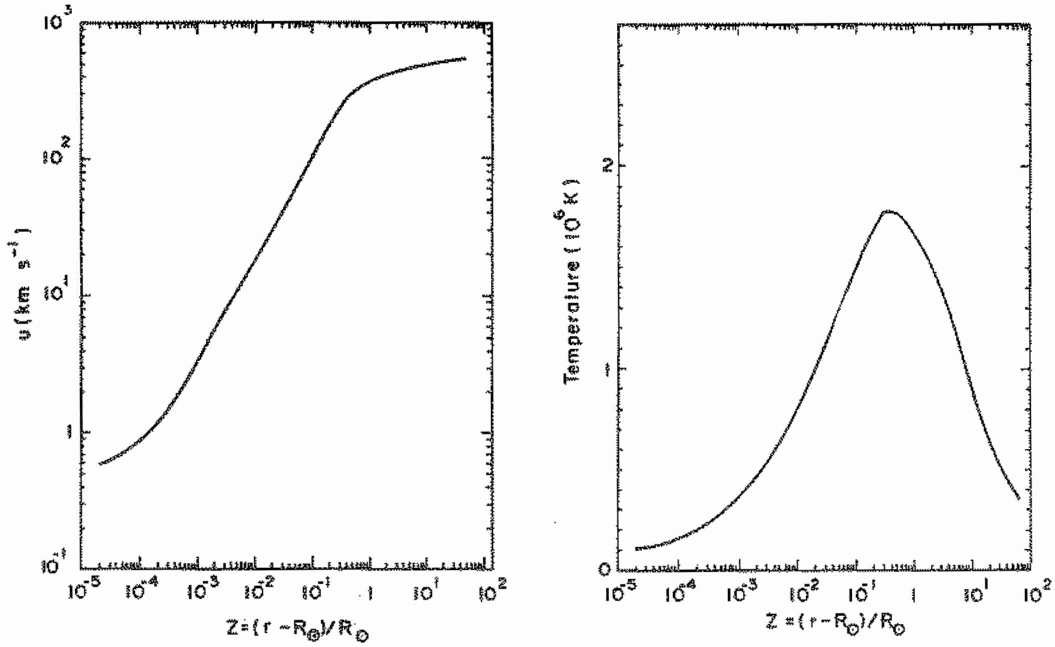

Figure 3: The velocity and temperature as a function of distance.

We show in Fig. 4 the evolution of $< \delta v^2 >_\nu$, the power density of Alfvén waves as a function of frequency with a spectral break compatible with observations. Curves show the evolution with distance.

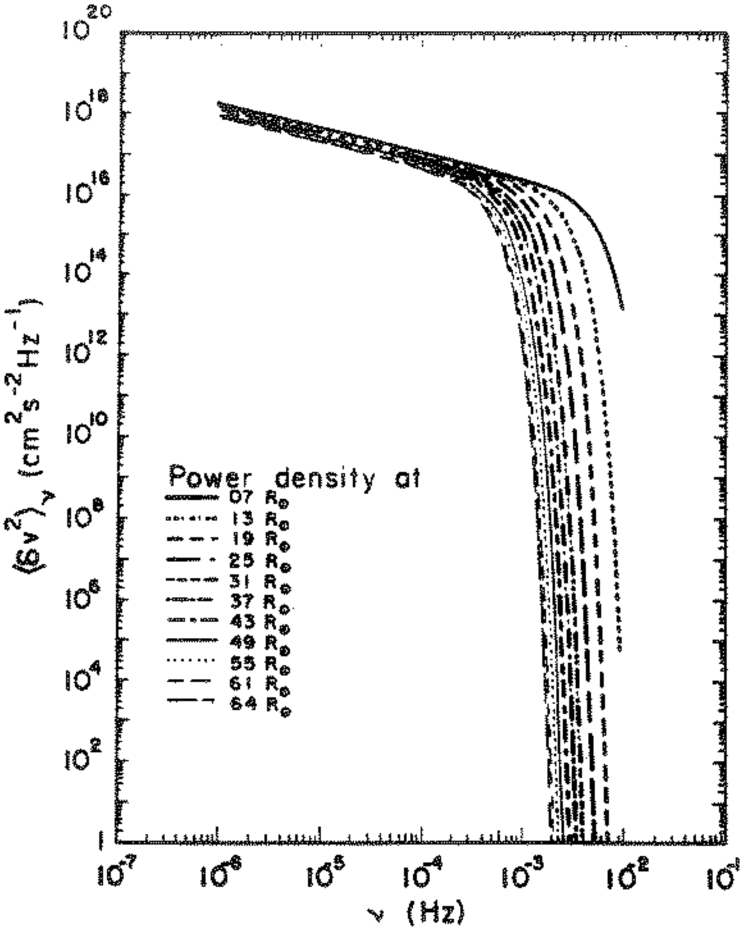

Figure 4: The power density spectrum $< \delta v^2 >_\nu$ as a function of frequency.

# 3 Conclusions

We presented a coronal hole solar wind model where to reproduce the solar observational data and Alfvén wave deposition, we need a combination of both a slow divergence in a coronal hole up to a height $r_t$, and a rapid divergence thereafter for the magnetic field. We obtained, for the parameters studied, $r_t - r_o$ in the range $0.01 - 0.1 R_\odot$, followed by a rapid divergence up to a height $\sim 1 R_\odot$.

In a sense, our results are very reasonable and are what might be expected if the open field lines of coronal holes are radial in the transition region, and are still approximately radial in the lower corona. The origin of the solar wind and the Alfvén waves is then in a region where the magnetic field is still approximately radial. In another sense, our results are very surprising, in that such small values of $r_t - r_o$ can change qualitalively the types of wind solutions that are obtained.

We also modified the model to introduce a frequency dependent flux of Alfvén waves to obtain the power density evolution of an Alfvén wave flux in the interplanetary medium up to $0.3\,AU$. Using a total nonthermal flux, $\phi_M = 1.0 \times 10^6\, erg\, cm^{-2}\, s^{-1}$, composed by Alfvén waves flux and network activity energy flux, we reproduce the observed temperature profile of the corona and the observed total magnetic fluctuations at $0.3\,AU$. The resultant velocity is that of a fast wind, $\sim 600\, km\, s^{-1}$.

**Acknowledgements**

The author would like to thank the brazilian agency CNPq for partial support.

## References

Bavassano, B. 1990, Nuovo Cimento, **13**, 79

Hollweg, J.V. 1978, Rev. Geophys. Space Phys., **16**, 689

Holzer, T.E., Fla, T. and Leer, E. 1983, ApJ, **275**, 808

Hundhausen A.J. 1977, Coronal Holes and High Speed Wind Streams, Ed. J.B. Zirker, Colorado: Associated University Press

Jatenco-Pereira, V. and Opher, R. 1989, ApJ, **344**, 513

Jatenco-Pereira, V., Opher, R. and Yamamoto, L.C. 1991, Proceedings of the First Brazilian Congress of Plasma Physics, 100

Jatenco-Pereira, V., Opher, R. and Yamamoto, L.C. 1992, Proceedings of V Latin American Workshop on Plasma Physics, 112

Mariska, J.T. 1978, ApJ, **225**, 252

Munro, R.H., Jackson, B.V. 1977, ApJ, **213**, 874

Neupert, W.M. and Pizzo, V. 1974, J. Geophys. Res., **79**, 3701

Parker, E.N. 1991, ApJ, **372**, 719

Priest, E.R. 1985, Ed. Solar System Magnetic Fields, D. Reidel

Stein, R.F. and Leibacher, J.W. 1981, The Sun as a Star, Ed. S. Jordan, NASA SP-450

Tu, C.Y., Marsch, E. and Rosenbauer, H. 1990, Geophys, Res. Letters, **17**, 283

Tu, C.Y., Marsch, E. and Thieme, K.M. 1989, J. Geophys. Res., **94**, 11739

# Section 2:

# Stars and the Interstellar Medium

# STELLAR SEISMOLOGY

EDUARDO JANOT PACHECO - IAG/USP

## I - Introduction

In the early sixties, up-and-down oscillations with a period of about 5 min were discovered in the Sun. It has became clear in the seventies that they were the result of the interference between more than $10^7$ resonant modes of non radial pulsations (NRP). Many of them are observed to be coherent over the entire, spatially-resolved surface of the Sun. Just as geologists can investigate the Earth's interior by analysing seismic (non radial) waves that reach the surface of our planet, so astrophysicists can study stellar interiors. Our knowledge of the Sun's interior through this technique is remarkable. Until recently, the only information about the central part of stellar interiors came to us from the (difficult) detection of neutrinos produced by core nuclear neactions. It is know possible to probe the inside of a star in much more detail through seismological analysis. Studies of the kind for stars other than the Sun have started recently (e.g. Winget et al., 1991)

In the Sun, oscillations arise from randon motions due to turbulence in the outer parts of the solar convection zone. Analysis of surface oscillation patterns led to studies of the radial variation of quantities such as the sound speed, density and angular velocity in the solar interior. Consequently, constraints could be put to the Sun's overall Helium abundance, to the neutrino production and to the thickness of the convection zone (see section III).

## II - Theoretical Sketch

The amplitudes of solar oscillations are small, and can be treated as perturbations about spherical equilibrium states. The oscillations can thus be separated into normal modes, which are described by:

$$\delta\vec{r}(r,\Theta,\varphi,t) = R_e\left[\xi_r(r)Y_l^m\vec{\partial}_\gamma + \xi_h(r)(\frac{\partial Y_l^m}{\partial\Theta}\vec{\partial}_\Theta + \frac{1}{Sin\Theta}\frac{\partial Y_l^m}{\partial\varphi}\vec{\partial}_\varphi)\right]e^{-iwt} \qquad (1)$$

Where $\delta\vec{r}$ is the displacement vector, $\xi_\gamma$ and $\xi_h$ are the radial and horizontal eigen functions, respectively, Y are spherical harmonics, $\vec{\partial}_r$ and $\vec{\partial}_h$ are the radial and horizontal unit vectors, respectively and $\omega$ is the angular frequency. Each oscillation mode is characterized by three wave numbers or quantumm numbers:

n $\equiv$ radial order ($\sim$ number of zeros in $\xi_x$),

l $\equiv$ degree

m $\equiv$ azimuthal order ($m = -l$, ...o, +l).

In a condition of spherical symmetry the m states are degenerate; degeneracy disappears in the presence of rotation or of a magnetic field, in wich case there will be a splitting of the m modes, forming a multiplet for each l.

Figure 1 shows how different individual modes might appear to an observer. The complex, NRP oscillations can be more easily understood in terms of their l and m values. At any given instant of time, the pattern of Doppler velocities of an individual mode is one of alternating regions of approaching (clear areas) and receding (hatched areas) flow (see the Figure caption).

A feeling of the basic properties of oscillations can be obtained by looking at results of calculations of eigen frequencies and eigen functions. Results from a "standard solar model" (that is, a model computed under traditional assumptions of solar evolution theory) are shown in Figure 2; frequencies with like values of n are connected with straight lines. In all cases $\vartheta$ increases with l at fixed n. The f mode is a kind of intermediate case between p and g modes: it is essentialy a surface gravity wave. Note that in the upper right part of Figure 2, the eigen frequencies of two theoretical solar models (Y = 0.25; Y = 0.19) are superposed on the ridges of the power spectrum of Doppler data. The fit is better for the Y = 0.25 model (see section III). This example illustrates the way in which stellar properties can be derived from the observed pulsation frequencies.

The principal restoring forces responsable for solar and, presummabily, stellar oscillations are pressure and buoyancy. Their relative importance depends largely on frequency and to a lesser extent on wavelength. Pressure fluctuations dominate at high frequency, producing acoustic waves (called p modes). At low frequency, buoyancy dominates, producing internal gravity waves (g modes). Radial pulsations correspond to l

$= 0$ p modes.

Waves propagating through a star do not travel in straight lines. The increasing speed of sound toward the star's center ($c_s \alpha T^{1/2}$) refracts in ward-travelling waves outwards, whereas the stellar surface reflects outward-travelling waves back in (Fig. 3). Waves are thus confined in a a cavity of deepness.

$$\frac{r}{c_s(r)}\alpha \left[l(l+1)\right]^{1/2} \tag{2}$$

A resonant mode of oscillation is the result of constructive interference between such internal reflected waves, in a way analogous to standing waves in an organ pipe. As in an organ, resonance can occur only at particular frequencies, which depend on conditions in the cavity. A sound wave can thus cross the star in one pulsation period (fundamental) or in two periods (first harmonic), or three, and so on. Indeed, stars are often observed to pulsate in the fundamental or in the first harmonic, or in both. In fact, motions in a star are three-dimensional, and a better analogy than the one-dimensional organ pipe is a combination of an organ pipe and a bell: stellar pulsations are really sound waves that must fit with their radial motion as in an organ pipe, but must also fit on to a great circle around the star, as on a bell. Figure 4 shows one possible mode of oscillation seen through out the Sun (Wentzel, 1991).

It can be shown that, for large n, the spacing between the observed frequencies, $v_{ne}$ (e.g., in Figs. 2 and 3), is $1/2v_a$:

$$v_{nl} \sim v_o(n + l/2 + constant), \tag{3}$$

$$v_o = (2\int_o^R \frac{dr}{c_s})^{-1} \tag{4}$$

Where $c_s$ is the sound speed.

In the presence of rotation, the splitting of the m modes can be written as

$$v_{nlm} \simeq v_{nlo} + m\Delta v_{nlm}, \tag{5}$$

$$\Delta v_{nlm} \simeq \frac{\bar{\Omega}(r,\Theta)}{(2\Pi)}$$

Where $v_{nl0}$ is the frequency without rotation, $v\gamma_{nlm}$ is the rotational splitting and $\Omega$ is the mean angular velocity of the Sun.

Equations (1) through (5) are used in the so called inversion problem, that is, in deducing physical properties of the Sun from the observed oscillation frequencies of p and g modes.

## III - **Helioseismology**

Besides the mandatory reference on NRP by Unno et al. (1989), the reader is urged to read one of the comprehensive, prolific papers by Christensen-Daalsgaard and collaborators (e.g. IAU Symposium 123, 1988) on this fertile research field. We present here some results on the thickness of the convective zone, on the Helium abundance, on the neutrino abundance and on solar rotation

The so-called "5-min oscillations" are composed of many modes in the 2,5-11 min interval. A sample of these oscillations and the corresponding power spectrum are shown in Figures 5 and 6 (Wentzel, 1991). This kind of observations allows the determination of physical characteristics of the solar interior:

### III - a) Helium abundance and neutrino production -

Acoustic modes of low and intermediate degree indicate typically $Y= 0.25 \pm 0.02$ and a high (as predicted by current stellar models) neutrino flux. This strengthens the case for searching for a physical, as opposed to an astrophysical, solution of the neutrino problem. Indeed, neutrino pulsations have recently been argued as a possible explanation for the low flux of such particles measured on Earth (Lippari, 1993). The internal sound speed can also be deduced from the above-referred p modes. This is illustrated in Figure 7. It also led to a precise location of the Sun's convective zone.

### III - b) The thickness of the convective layer -

The base of the convection zone occurs when the second derivative of the temperature, that is sound speed, changes abruptly. It is located at $r/R \simeq 0.71$ (see Fig. 7). Typical solar models place the bottom of the convection zone at a depth between 0.20 - 0.30 solar radii. Helioseismology contributed to the adoption of $\sim 0.3$ R in more recent calculations.

III - c) Solar rotation -

Acoustic modes (concentrated near the surface) and gravity modes (more deeply penetrating) altogether furnish a detailed map of the radial dependence of solar rotation. As seen in Figure 8, the most intriging feature is the inward declive of $\Omega$ in regions outside the Sun's core. Braking due to the solar wind in the outermost layers should led to an increase in $\Omega$ with depth. Only the core appears to be rotating more rapidly, but why is it surrounded by a region of relatively slow rotation? Another question posed to theorists by helioseismology.

## IV - **Asteroseismology**

Stars other than the Sun are also observed to pulsate non-radially, although for them we cannot see the richness of detail that can be obtained for the spatially-resolved solar disk. Non-radial (and sometimes, radial) pulsations were discovered practically all over the HR diagram (see Figure 9). Besides the classical pulsation variables (Cepheids and $\delta$ Sct stars) and solar like GB stars, NRPs have also (and some what unespectedly) been detected in the Ap, yellow and O-B giants and supergiants, and in WDs. Such a variety of objects indicate that different physical mechanisms can drive NRPs in stars. For the Ap stars, the strong magnetic field is responsible for the splitting of the m modes, where as in Be stars, there could be a cause-and-effect relation between high rotation velocity, mass loss and NRPs (Kambe et al., 1993). We give below some examples of stellar studies based in NRP analysis. More information can be found in Unno et al. (1989).

IV - a) White Dwarf Stars (e.g. Nather & Winget, 1992) -

The WD types noted in Fig. 9 (DO, DB, DA) form in fact an evolutionary sequence which starts with planetary-nebula nuclei. As the star moves toward lower right in the HR diagram, it passes through four zones of instability, that is, places where a layer of material below the star's surface acquires such a degree of opacity as to modulate the energy flow from its interior, causing the stellar pulsation. Oscillations in WDs are much larger than solar ones. As much as 30% of the total light can be modulated! Understanding the cooling process of WDs, in particular, how long they take to reach the different phases, would enable us to investigate the detailed history of star formation and population evolution in the galaxy and to measure the ages of the disk and halo in a self-consistent way. For this, it is essential determining the basic physical parameters of WDs, which can be done with astounishing efficiency by seismological analysis. The amount of physical information we can get from NRPs is a sensitive fuction of the number of fully resolved pulsation modes. From a single observing site, interruptions due to day light and to bad weather produce alias frequencies and side lobes in the Fourier transforms of the time-series data which renders impossible to determine the real stellar periodicities (see Fig. 10). This problem has been solved by the set of an observing cooperative called Whole Earth Telescope (WET). It consists of many observers at longitudes spaced around the planet (Fig. 11). This interactive network of photometric observers provide essentially continuous coverage of a target. From Brazil, Kepler S. Oliveira and collaborators participate in this operation. Results of 6.5d of continuous by photometric observations of the DO star PG 1159-035 by WET (Winget et al., 1991) are presented schematically below: (see in Fig. 10 a part of the power spectrum)

- 101 g modes detected;
- n $\simeq$ 2, $l$ = 1,2, m splitting (see eq. 1)
- $\Delta v$ at interior of multiplets $\longrightarrow \vec{B} < 6.000G$
- $l, \Delta v \longrightarrow \mathrm{P}^{WD}_{rotation} = 1.38 \pm 0.01d$
- relative intensity of various m peaks $\longrightarrow i \sim 60^o$
- multiplet spacing $\longrightarrow$ M $= 0.586 \pm 0.003M_\odot$
- relative multiplet spacing $\longrightarrow$ pulsation layer composition of $\mathrm{H/H_e}$ + C,O

A considerable increase in our knowledge about the evolutionary process of WDs is thus being provided by seismological studies. It will have important consequences for establishing the age of the galaxy and of the Universe.

IV - b) Solar-mass stars - (e.g. IAU Symp. 123)

Solar-like oscillations have also been discovered in $\sim 1M_\odot$ stars in the solar neighborhood (MS-GB stars). High-precision photometric measurements are required to detect such weak variations. Important informations concerning physical parameters of the objects have been obtained from seismological analysis. Three examples are given below:

- $\alpha$ Cen A (G2V): this almost solar twin shows 3.5-8.5 min oscillations with amplitude up to ten times as great as the Sun's. The derived star's radius and mass ($R \simeq 0.93\ R_{\odot}$, $M \simeq 1\ M_{\odot}$) differ substantially from the well-established values ($R \simeq 1.23\ R_{\odot}$, $M \simeq 1.1\ M_{\odot}$) calculated from spectroscopic data. So, $\alpha$ Cen A is in fact younger than previously thought.

- $\alpha$ CMi (Procyon, F5V): 10-25 min oscillations were found as expected. The deduced Procyon's radius ($1.87\ R_{\odot}$) is in agreement with theory, suggesting that the star is near the end of its main- sequence phase. The observed frequency intervals $\Delta v$ points to Rossby waves as the driving mechanism for the NRPs.

- $\xi$ Eri (K2V): observed oscillations near 10 min allowed the estimation of physical parameters for this star. In particular, its chemical composition was found to be $Y = 0.26$, $X = 0.73$.

### IV - c) Be stars

These are fast-rotating, B-type stars that show in their spectra Balmer emission lines formed in an asymetrical (equatorially-concentrated) circumstellar envelope. The cause for the rapid rotation and the abnormall mass loss is yet unknown, but NRPs could share a part of responsibility in the so-called "Be phenomenon". In deed, since the early 80's, moving bumps (~ 1% of the continuum) were observed to cross the spectral lines from blue to red (Vogt & Penrod, 1983). They could be explained by a corrugation travelling across the stellar surface such as a small number of sectorial NRP modes would produce (see Figures 12, 13). In Be stars, rapid rotation furnishes a powerful tool for resolving the stellar surface through the Doppler effect. If sectorial modes are really predominant, the splitting of modes due to rotation can be measured: indeed, m can be determined by counting the number of moving bumps crossing the line center. It can be shown that

$$|m| \simeq 2\Pi V sini/a\Delta t$$

Where a is the acceleration of the bumps at the line center and $\Delta$ t is the time interval between successive bump crossings. An example is given in Figure 13, for the star $\eta$ Cen.

Subsequent studies have shown that O-B stars in deed show a limited number of NRP modes (e.g. Baade, 1991).

We have started in Brazil, in 1990, a campaign of seismological studies of Be stars through high resolution ($\lambda/\Delta\lambda \geq 30.000$), high signal-to- noise ratio ($S/N \geq 300$) spectroscopic observations. For optimal reasons, the HeI $\lambda$ 667.8nm line was selected and spectra were taken at the coudé focus of the 1.6m L.N.A. telescope equipped with a CCD camera and a 1,800 l/mm grating. A dozen bright ($V \leq 3.5$) southern Be stars have been observed so far (Table 1). We detected the presence of moving bumps in several active stars, and found for instance $l = |m| = 14 \pm 4$ for $\eta$ Cen (Figure 15) and $l = |m| = 10 \pm 1$ for $\alpha$ Eri (Leister et al., 1993; Janot-Pacheco & Leister, 1993). We are now engaged in a long-term follow-up of certain objects in order to search for correlation between NRPs and mass ejection phases of Be stars.

## V - Prospects for the Near Future

Stellar seismology is expected to acquire the status of a leading field in astrophysics in the near future. This status will be attained with the help mainly of the GONG and SOHO projects.

GONG is an acronym for Global Oscillation Network Group, an international project under the leadership of the american National Solar Observatory. Six identical instruments are being installed around the world to observe the Sun with as little interruption as possible for at least three years. The scientific goal of the project is to measure extremely precisely the vibrations of the Sun and to use these measurements to understand quantitatively the physical conditions in the solar interior. It is estimated that the network will be able to observe the Sun 93% of the time during the operation period. High precision in the identification of pulsation frequencies will be secured by avoiding the gaps in the measurements. Enormous progress will be attained, for instance, in our understanding of: 1) the detailed dynamics of convection and of the dynamo mechanism; 2) the detailed geometry of the Sun's magnetic field; 3) the solar activity cycle; 4) the stellar evolution as a whole, by observing other stars - difference in pulsation frequencies could constitute the first direct stellar age measurements.

The Solar and Heliospheric Observatory (SOHO) is an ESA Satellite planned to be launched in late 1994. It will carry three instruments: the High Resolution Spectrometer (HRS) that will furnish high-precision radial velocity measurements, allowing long-period studies of low $\underline{l}$ modes; the SIM (Solar Irradiance Monitor) that will measure $\frac{\Delta I}{I} \leq 10^{-6}$ at several wavelenghts simultaneously, and the Solar Oscillations Imager, which will furnish two-dimension velocity images with 2 x 2 arcsec resolution, allowing detection of modes with $0 < l < 600$.

These two projects will not simply answer questions, but point out new problems we were not even able to imagine yet.

Finally, the enormous success of the WET network has stimulated the planning of other world networks for continuous observations of many type of stars in the next years. The Be-group of IAG-USP will participate in such a global campaign starting in February, 1994.

Stellar seismology will render possible, in a near future, to see through the glass clearly, in the field of stellar structure and evolution.

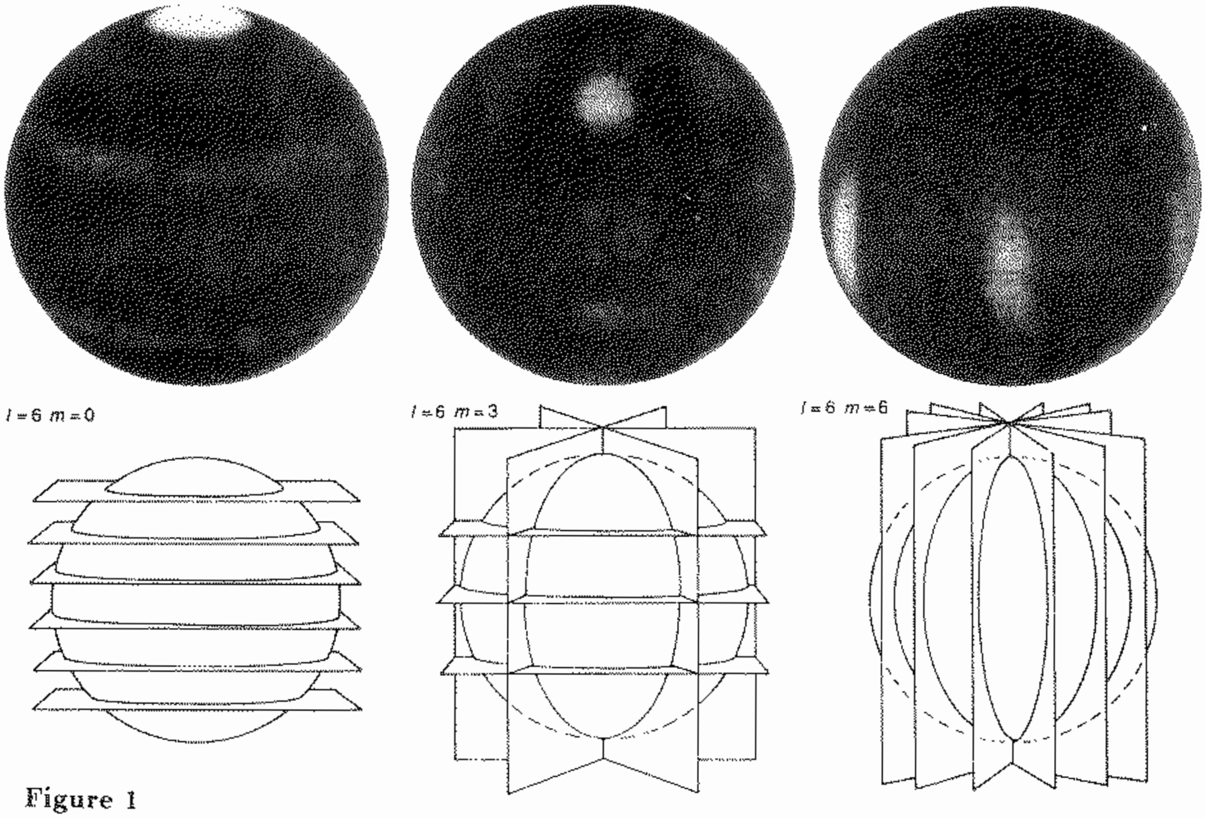

**Figure 1**

Solar oscillations can be very complex, but are more easily understood when classified by their $l$ and m values. These parameters represent the number of nodes (stationary points) belonging to each oscillation. A simple vibrating violin string, for example, has (a minimum of) two nodes, one at each end. The $l$ parameter represents the total number of nodal planes slicing the Sun's surface. The m value gives the number of planes cutting perpendicular to the equator. The computer-generated images corresponding to the sketches show how various parts of the solar surface would move if the Sun were oscillating with an $l$-value of six and various values of m. The dark regions in the images are the nodes, while the yellow areas can be thought of as moving toward us and the green portions moving away. At left, there are no nodal planes perpendicular to the equator so m is zero. At center, six planes still cut the Sun, but because three are oriented vertically m is three. At right, the $l$ value remains six, but as all the planes are vertical, m is also six.

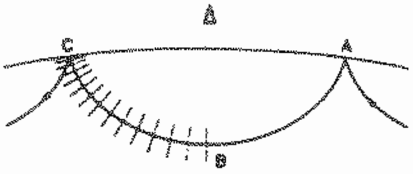

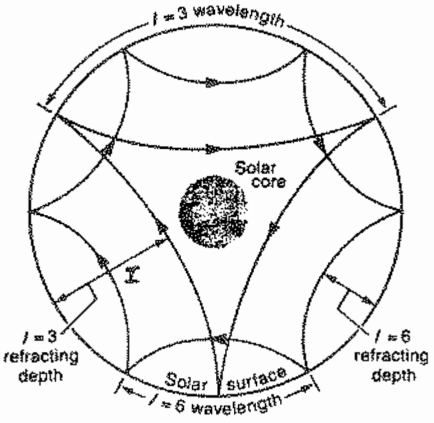
ℓ = 3 wavelength
Solar core
r
ℓ = 3 refracting depth
ℓ = 6 refracting depth
Solar surface
ℓ = 6 wavelength

Sound waves in the Sun, like seismic disturbances in the Earth, do not travel in straight lines. The increasing speed of sound toward our star's center refracts inward-traveling waves outwards, whereas the Sun's surface reflects outward-traveling waves back in.

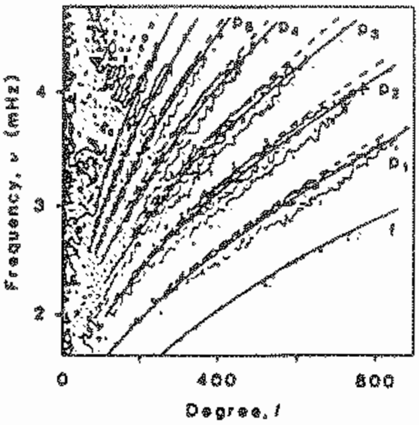

$$\frac{r}{c(r)} \propto \{\ell(\ell+1)\}^{1/2}$$

$$c \propto T^{1/2}$$

$$\nu_{n,\ell} \sim \Delta\nu_0 (n+\ell/2+cte.)$$

$$1/\Delta\nu_0 = 2\int_0^R dr/c$$

Figure 2

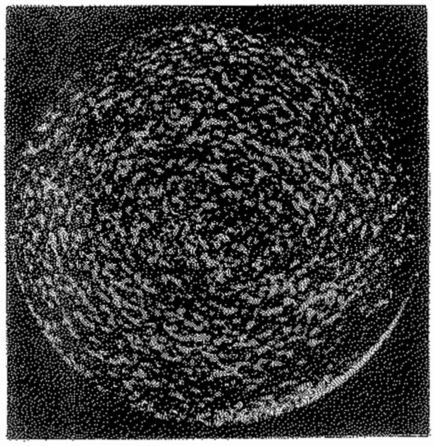

The Sun's surface is in constant up and down motion as this "velocity image" shows. Regions moving toward us are light and those receding are dark. The mottled appearance is due to the combined effect of millions of different oscillation modes and random motions. Photograph courtesy Big Bear Solar Observatory.

Figure 3

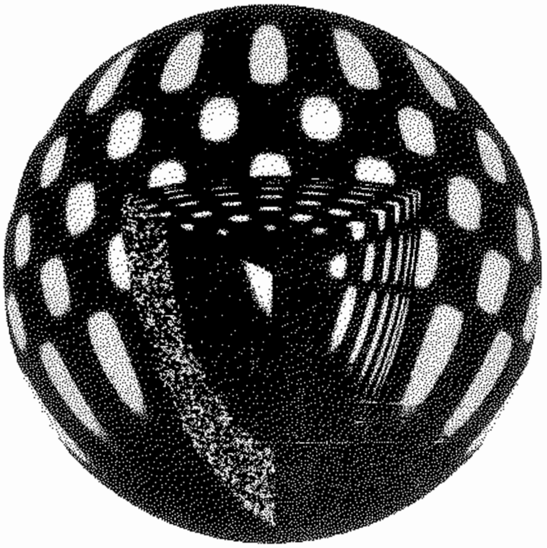

**Figure 4** *Patterns of motion throughout the Sun associated with one possible mode, or tone, of solar oscillations. White implies radially outward motions, dark inward. The directions of all the motions reverse after about 2.5 minutes, hence the name five-minute oscillations. The oscillations are sound waves selected to "fit" onto the solar surface, as for a bell, and also to fit in depth, as in an organ pipe or pulsating stars. (National Optical Astronomy Observatories)*

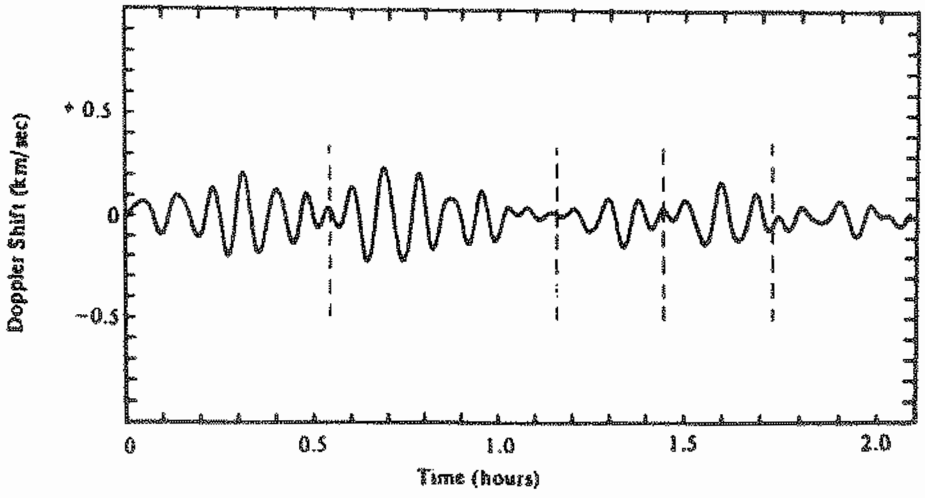

***Figure 5.*** *Five-minute oscillations. Wavelength shifts and velocities, recorded for about two hours at a single point of the Sun, show intervals lasting about an hour, during which the velocities oscillate regularly with a period of close to 5 minutes. (Courtesy Oran R. White)*

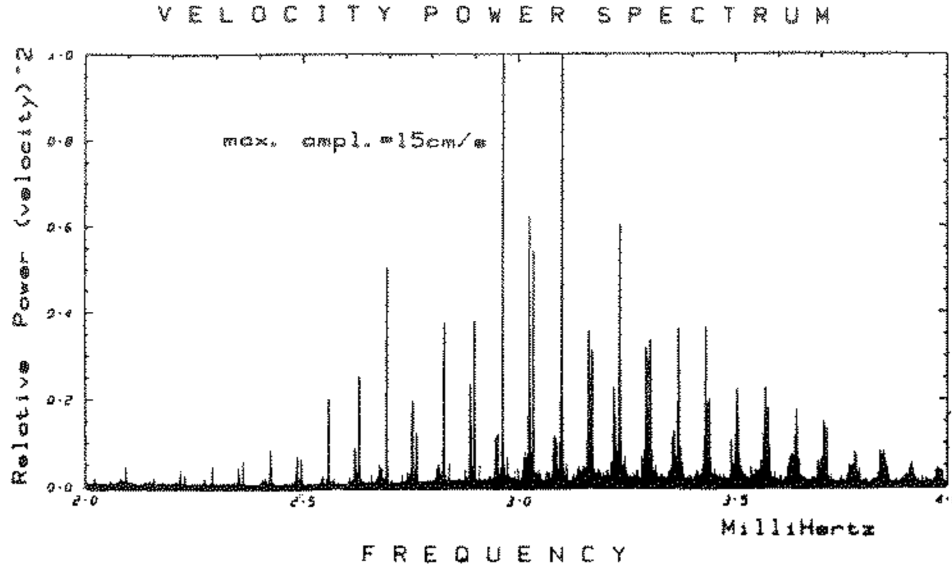

**Figure 6** *Solar oscillation frequencies, measured over a period of 3 months from Hawaii and from Tenerife, Spain. The Sun oscillates at hundreds of highly tuned frequencies between 2.5 and 3.8 millihertz, corresponding to periods between 6.7 and 4.5 minutes, respectively. The strongest mode has a velocity amplitude of merely 0.15 meter per second (0.5 kilometer per hour). Radial velocities were averaged over the entire solar disk. Within each group of modes, the frequency separation between modes informs us of the deep solar interior. (Courtesy G. Isaak, University of Birmingham)*

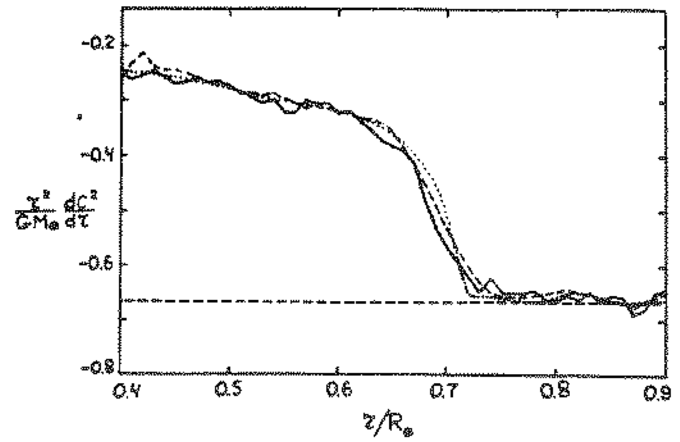

**Figure 7** The region around the base of the convection zone. The dotted line corresponds to the actual values of $W = r^3/(GM_\odot)\cdot dc^3/dr$ in the standard model. The dashed curve corresponds to the squared velocity of sound obtained by inverting the eigenfrequencies of this model. The solid line represents the result obtained from the inversion of the experimental frequencies. The horizontal dashed line is drawn at $-2/3$.

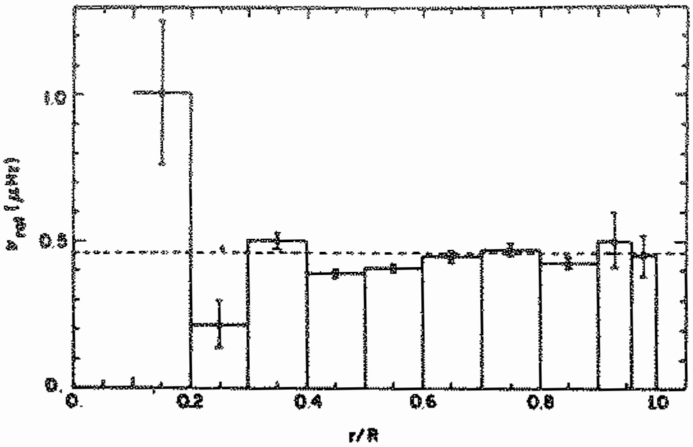

Figure 8 **Results of a determination of the radial dependence of the rotational frequency in the solar interior from the splitting of the oscillation frequencies shown in Fig. 23. The horizontal dashed line is the surface equatorial rotation frequency (Duvall *et al.* 1984).**

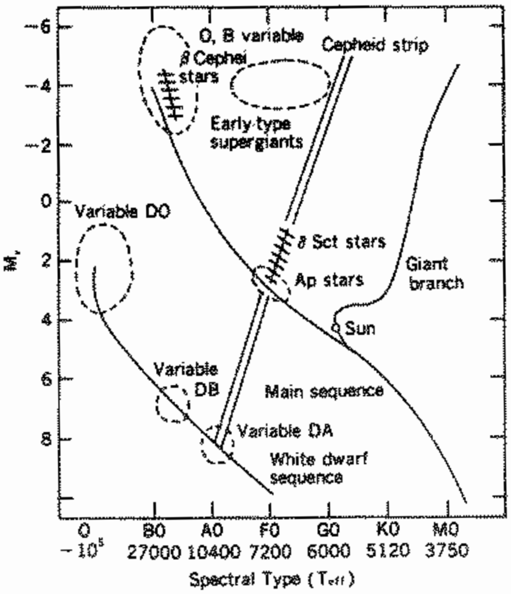

Figure 9 Location of the stars given in Table 5.1 for which nonradial oscillations are suspected to be involved and other related stars.

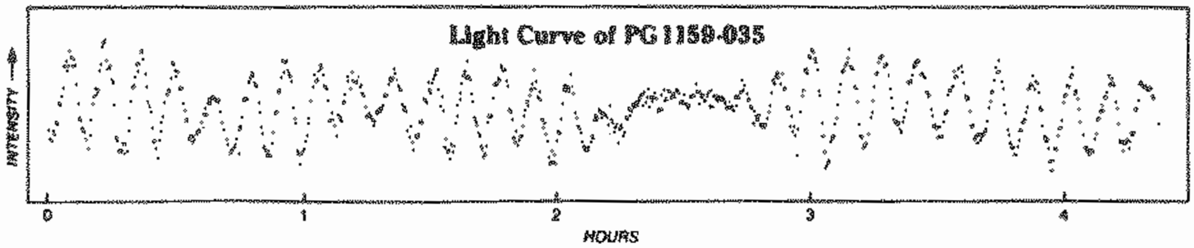

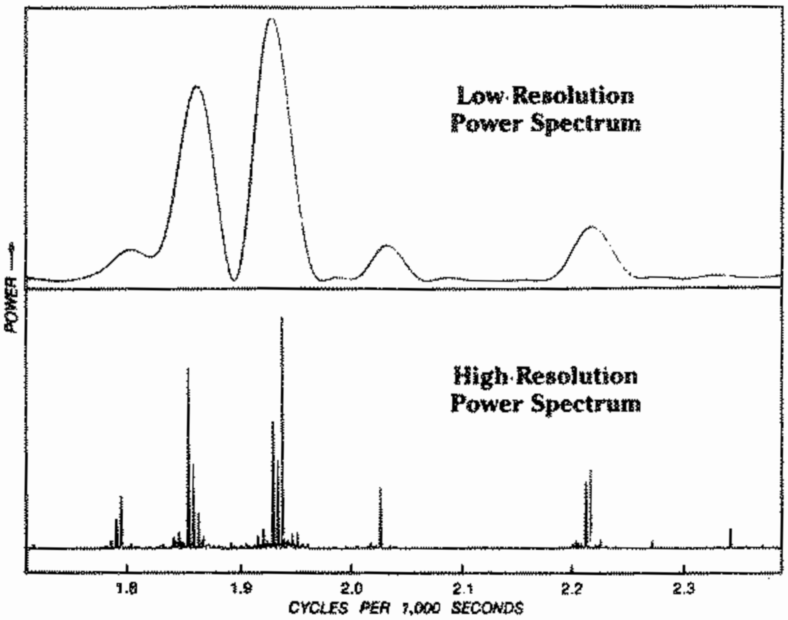

*Top:* Many complex oscillations are present in the white dwarf star PG 1159 − 035. They are all impressed upon the star's light curve, such as this segment obtained from a 4½-hour observing run.

*Left:* To untangle the oscillations, a computer analyzes the light curve into a "power spectrum" showing the periods and strengths of all the oscillations. The low-resolution power spectrum at left is from a light curve only a few hours long, obtained at a single site. It fails to resolve the star's many closely spaced periods. But they stand revealed (lower left) when a much longer, continuous light curve is obtained by the Whole Earth Telescope. This is only a small segment of the full power spectrum, which abounds with data about the star's many modes of vibration; 101 separate frequencies have been identified so far.

All illustrations with this article were provided by the authors except as noted.

Figure 10

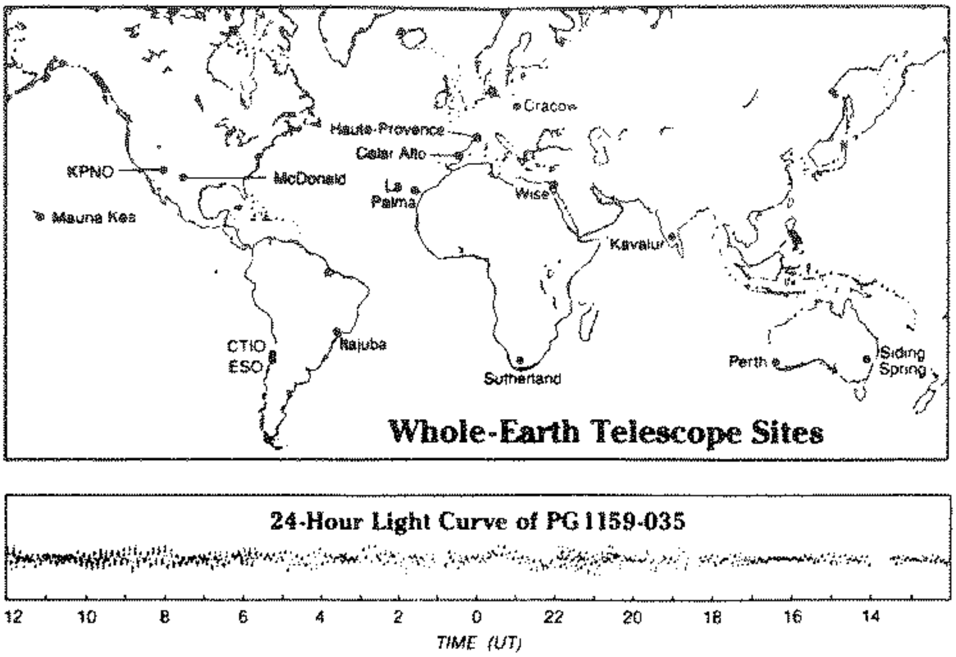
Cracow
Haute-Provence
Calar Alto
KPNO
McDonald
La Palma
Wise
Mauna Kea
Kavalur
CTIO
ESO
Itajuba
Sutherland
Perth
Siding Spring
Whole-Earth Telescope Sites
24-Hour Light Curve of PG1159-035
12
10
8
6
4
2
0
22
20
18
16
14
TIME (UT)

**The observatories that have joined the Whole Earth Telescope. At least one is almost always in darkness under clear skies, allowing nearly unbroken, round-the-clock monitoring of a star's brightness. Below the map is a 24-hour section of a light curve for the white dwarf PG 1159 −035. Individual pieces of the light curve are aligned with the observatories that obtained them. Notice that time runs from right to left, as the world turns.**

Figure 11

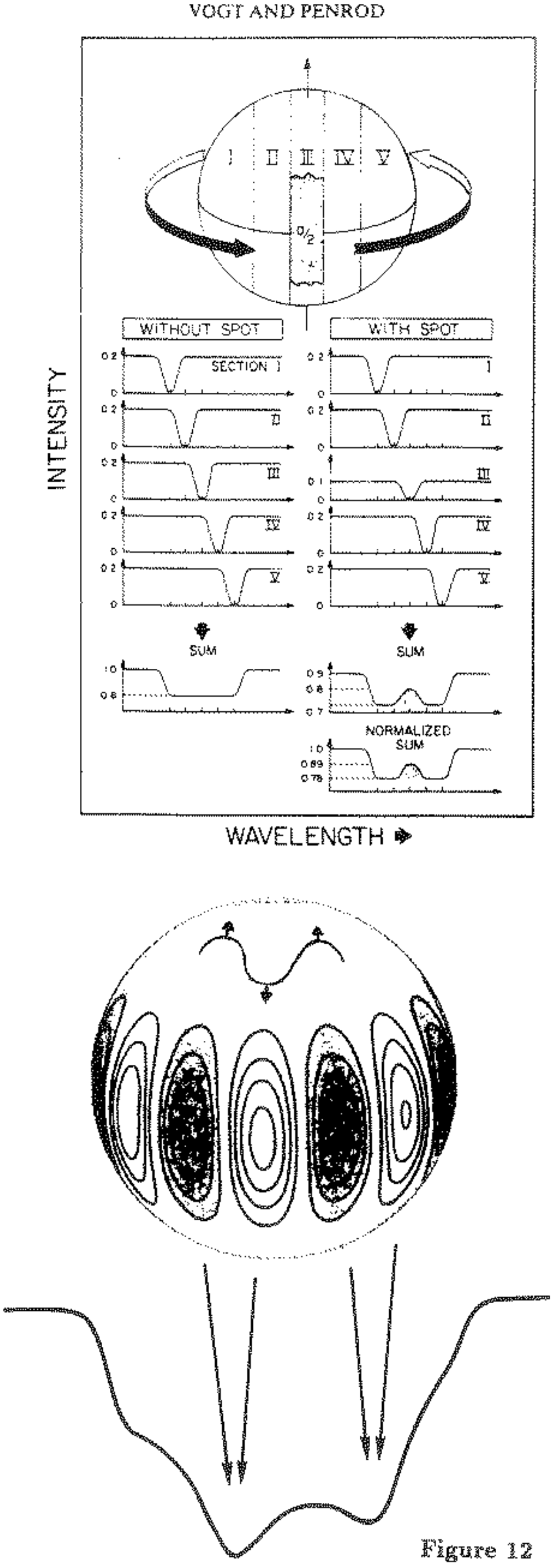
VOGT AND PENROD
I
II
III
IV
V
$v/2$
WITHOUT SPOT
WITH SPOT
SECTION I
0.2
0.1
0
SUM
1.0
0.9
0.8
0.7
NORMALIZED SUM
0.89
0.78
INTENSITY
WAVELENGTH

Figure 12

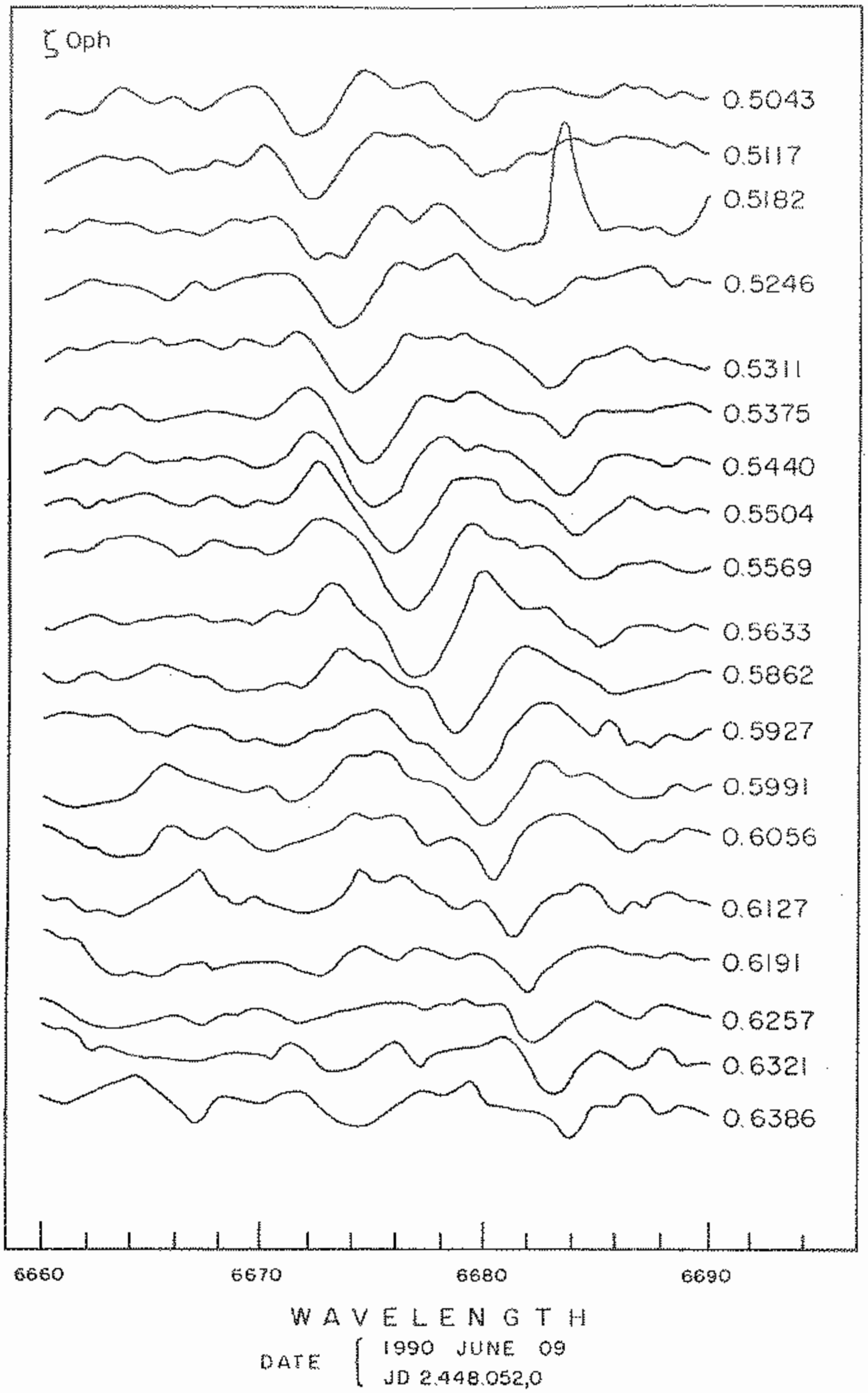
ζ Oph
0.5043
0.5117
0.5182
0.5246
0.5311
0.5375
0.5440
0.5504
0.5569
0.5633
0.5862
0.5927
0.5991
0.6056
0.6127
0.6191
0.6257
0.6321
0.6386
6660
6670
6680
6690
WAVELENGTH
DATE
1990 JUNE 09
JD 2.448.052,0

Figure 13

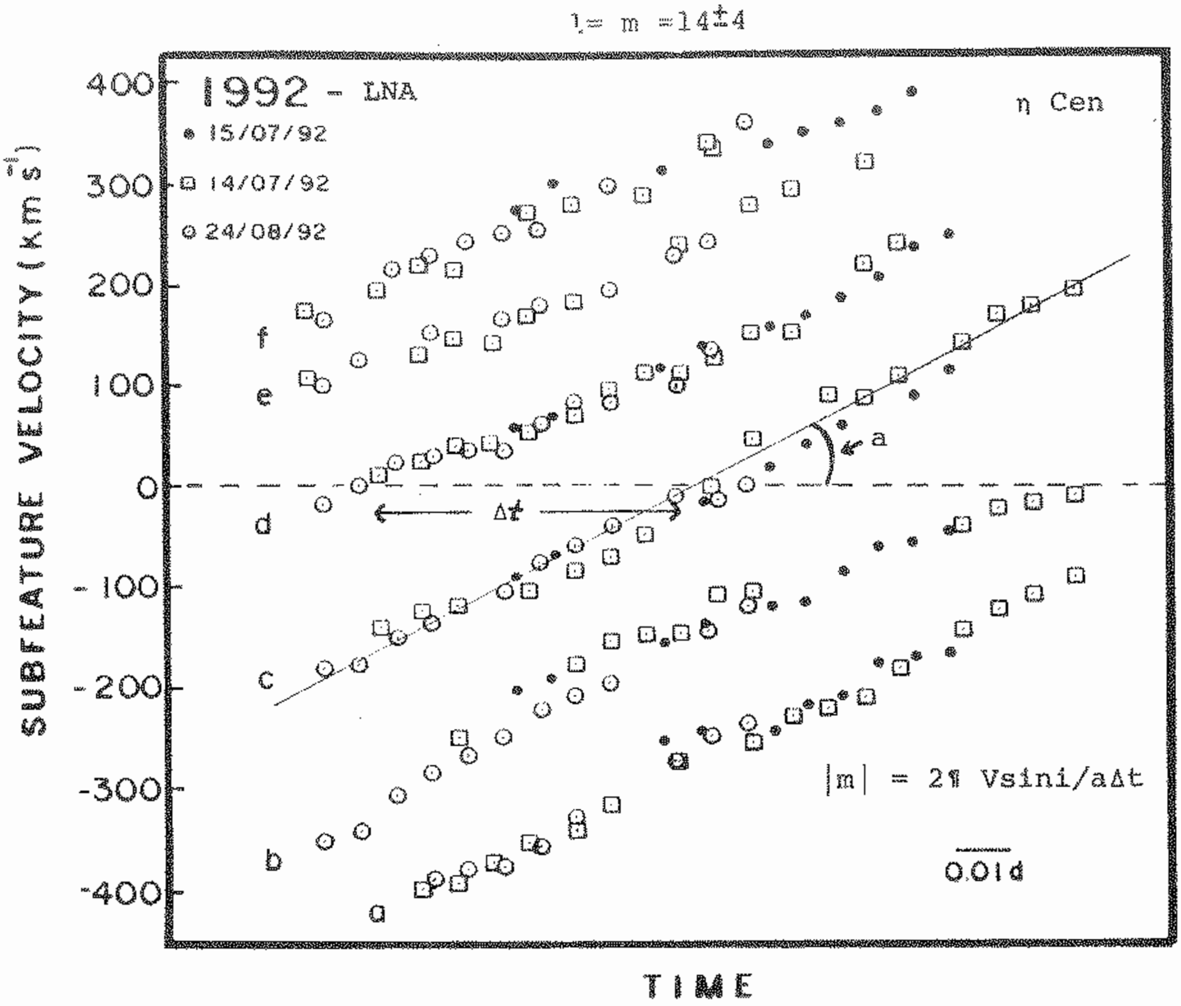

l= m =14±4

Figure 14

# Doppler Tomography of Polars: indirect imaging of VV Pup[1]

M. P. Diaz[2] and J. E. Steiner

Instituto Astronômico e Geofísico, Universidade de São Paulo, Brazil

## ABSTRACT

Recent time-resolved spectrophotometric observations of VV Pup are presented. On the basis of the line profile behavior the dynamical solution of the system is revised and improved system parameters are obtained. The H$\alpha$ line profile is analyzed with the Doppler Tomography technique aiming to identify the region of emission line formation and to investigate the main characteristics of the Doppler images of classical polars. The detection of the stream and the absence of an accretion disk is conspicuous in the derived image. From the flux distribution in the map and the theoretical location of the stream, column, and the stellar components we conclude that most (75%) of the H$\alpha$ flux is produced in the upper stream and in the secondary star surface. A small contribution for the Balmer lines should come from the magnetic funneled matter. An upper limit for the magnetospheric radius of $\sim 3\times 10^{10}$ cm is suggested.

## 1. INTRODUCTION

The line emission region in polars has been commonly associated with the low density plasma present in the accretion column. In the classical study of EF Eri by Schneider and Young (1980a) the radial velocity behavior of broad and narrow line components are explained by the emission of gas trapped in the primary's magnetic funnel. It was shown that the high radial velocity amplitudes observed in the emission lines are not correlated with the white dwarf orbital motion and represent the intrinsic velocity field of the gas undergoing accretion. On the other hand, the time resolved observations of the emission profile in AM Her (Young and Schneider 1979) and VV Pup (Schneider and

---

[1] Partially based on observations made at Laboratório Nacional de Astrofisica LNA/CNPq, Brazil

[2] Visiting Astronomer, Cerro Tololo Inter-American Observatory, which is operated by the Association of Universities for Research in Astronomy, Inc., under cooperative agreement with the National Science Foundation

Young 1980b SY hereafter, and Cowley, Crampton and Hutchings 1982 CCH hereafter) suggest that the sharp component of the lines in both systems arises on the exposed face of the secondary star. This behavior is straightforward to understand since the secondary photosphere should be very sensitive to the illumination by the soft X-ray emission. Among others, these early investigations on the line profile behavior in polars pointed to a complex line formation scenario where multiple components with different intrinsic widths are formed in distinct locations in the binary system. These components are summed with different projected velocities to form the observed profile. Such effects usually lead to puzzling phased spectrograms (Hutchings *et al.* 1982). The relative contribution of the secondary, the stream and the column in the line emission of polars is still an open question. Different stream densities and different companion and stream illumination by X-rays will directly affect the emissivity of these regions. For the system investigated in this paper, the sharp component was previously assumed to be more likely formed in the stream (Patterson *et. al.* 1984). However, the problem of the missing secondary sharp emission was previously discussed by these authors and remains unexplained since the dipole orientation in VV Pup avoids the complete shielding of the inner secondary hemisphere.

Aiming to improve our knowledge on these topics, we propose the investigation of the orbital behavior of the line profiles in polars by using an indirect imaging technique. On the other hand, the establishment of the tomographic characteristics of polars is fundamental as the results from this method may be used in the discrimination between systems with and without disks. Therefore, the results of Doppler imaging studies may be specially important in the identification of new AM Her binaries with low polarized fractions.

## 2. OBSERVATIONS AND DATA REDUCTION

The spectrophotometric measurements analyzed in this investigation were obtained at the Cassegrain spectrographs of the 1.5m telescope of the CTIO and of the 1.6m telescope of the LNA. In both sites GEC CCD's were employed to observe at H$\alpha$. The spectral dispersion employed yield a final resolution of 1.95 Å and 2.1 Å for our observations at 1.5m and 1.6m telescopes, respectively. The spectrograph slit was rotated o allow simultaneous observations of a comparison star 74 arcsec away from VV Pup. The

the uncertainty in our timing, it will be assumed that the secondary inferior conjunction takes place at Walker's phase 0.01 ± 0.04.

The dynamical solutions for VV Pup are partially based on the spectroscopic observations of SY and CCH. In these previous works, sinusoidal semi-amplitudes of K = 437±15 km/s and K = 346±13 km/s were obtained. Both values correspond to the average of Balmer lines and HeII $\lambda$4686 narrow component measurements covering only 1.5 orbital cycles. The sharp component in our observations of the H$\alpha$ line was measured by weighting the wavelength with a high power of the flux. The semi-amplitude found from the sinusoidal fit to the peak radial velocities is K = 321± 21 km/s with systemic velocity $\gamma$ = 5±17 km/s. At the moment we are not able to explain the difference between our value and the measurements of SY. Taking into account the relative uncertainties, the mean of the three available determinations yield the final value of K = 373 ± 40 km/s. However, this value should not characterize the orbital motion of the companion since such a line emission is produced in the unevenly illuminated hemisphere and in the accretion stream. It will be shown in the next section that most of the H$\alpha$ narrow component is formed in a region that is very close to the companion star. The displacement between the effective line emission region and the geometric center of the secondary resulting from the illumination motivates the employment of the inverse K-correction (Wade and Horne 1988) to the observed radial velocity semi-amplitudes. As a first order approximation we will assume that the hemisphere that faces the white dwarf is uniformly illuminated while the back hemisphere has no emission. For instance let us assume the mass ratio $q = M_2/M_1 \cong 0.18$ suggested by Szkody, Bailey and Hough (1983), high orbital inclination ($i$=78°±5°, c.f. Cropper and Warner 1986), and the radius and mass of a M4-5 secondary (Szkody, Bailey and Hough 1983) from Allen (1973). With these parameters we find $K_2$(corr) = 467±40 km/s. According to the $K_2$ value given above, we found the following secondary's mass function: $f(M_1) = (0.74 \pm 0.19)$, from which we derive a white dwarf mass $M_1 = 1.10 \pm 0.25\ M_\odot$ and predict a primary radial velocity semi-amplitude $K_1 = 85 \pm 36$ km/s.

### 3.2. *Doppler Tomography*

Doppler Tomography is a very robust technique applied in the analysis of the orbital behavior of emission lines. On the basis of the observed line profiles only, the Doppler Tomography method produces a model for the line emission distribution in a two-dimensional velocity-space. This map is applied in the investigation of the location and data were reduced using the spectroscopy reduction procedures in IRAF[3]. The object frames were corrected for bias, flatfield, and slit illumination. Small scattered light residuals were found and removed from the flatfield frames. After that, the variable and comparison star sky-subtracted spectra were extracted using an optimal algorithm (Horne, 1988). Low order dispersion solutions were interpolated in time to each object measurement. Finally, the spectra were flux calibrated using standard stars (Hamuy *et al.* 1992) measurements and a scaled average extinction curve for each site. The slit losses for every exposure were corrected by using the measurements of the comparison star. This observational procedure allows us to flux calibrate the time-series with the narrow slit required to preserve wavelength resolution and stability. The differential measurements are also robust to small seeing and sky transparency variations along the night. VV Pup was observed in two runs with a coverage of 9 orbital cycles. Considering the short orbital period of 101 minutes, an integration time of 420 seconds was chosen to preserve phase resolution. Phase binning 104 spectra yielded an average continuum S/N = 15 in 0.08 phase bins. The reduction of the differential spectrophotometry as well as all the calculations presented in this contribution were performed by a spectroscopy analysis package added to IRAF.

## 3. RESULTS

### 3.1 *Orbital Phasing and Radial Velocities Revisited*

The orbital phasing of VV Pup has been usually derived from the ephemeris for photometric maximum of Walker (1965). The secondary inferior conjunction has been assumed to occur at Walker's photometric phase $\phi_0 = 0.05(\pm 3)$; a figure derived from the observations of the secondary's ellipsoidal modulations in 1980 by Allen and Cherepashchuck (1982). To check the accuracy of the Walker's ephemeris we performed synthetic continuum photometry using a line-free (6255Å to 6505Å) passband. By fitting the hump in the phase-folded light curve we found that the maximum occurs at photometric phase 0.96±0.03. Considering the error in the ellipsoidal variation phasing and emissivity of the line producing regions in the binary system. The application of this technique to the study of accretion disks in CVs was first described by Marsh and Horne (1988). Since then, Doppler maps have been employed in the study of several CVs with disks, e.g., IP Peg (Marsh and Horne 1990), U Gem (Marsh *et al.* 1990), V1315 Aql (Dhillon, Marsh, and Jones 1991), and KT Per (Ratering, Bruch, and Diaz 1993). Recently, this method was applied to the investigation of the accretion kinematics in the magnetic nova GQ Mus (Diaz and Steiner 1993). The image reconstruction is made by sampling the Doppler-broadened line profile at many different orbital phases and combining all the available signal at the corresponding velocity ($V_x$,$V_y$) in the map. The coordinate system definition follows the usual form; the X-axis points from the primary to the secondary while the Y-axis points in the direction of motion of the secondary. The origin lies at the center of mass.

---

[3] IRAF is distributed by National Optical Astronomy Observatories, which is operated by the Association of Universities for Research in Astronomy, Inc. (AURA) under cooperative agreement with the National Science Foundation.

The Doppler map of VV Pup is shown in Figure 1. This tomogram was calculated using the systemic velocity and the orbital phasing derived in the previous section and has a FWHM resolution of 200 km/s at the image center. This resolution suffers a rapid degradation close to the edges of the map (for velocities higher than 800 km/s) up to 430 km/s (FWHM). The linear structures in the high velocity region of the map are sampling artifacts (aliasing streaks) and should not be taken into account. The main characteristics of the Doppler image of VV Pup are substantially different from those seen in the maps of systems with disks. In lines produced in accretion disks the Keplerian rotation kinematics defines an intense and broad axisymmetric component in the tomograms (Marsh and Horne 1990 and Dhillon *et al.* 1992). This component is centered at the white dwarf position and is easily seen in the high velocity region of the maps (V>~800 km/s). Its radial emissivity profile in the velocity space behaves close to $f_v(V) \propto V^{-c}$, where V is the velocity modulus and c~3 (Horne & Saar 1991). This characteristic is not observed in the mapping of this polar; a direct consequence of the remarkable difference between the gas velocity field in polars and in systems with disks.

Considering the system parameters discussed above, the position of the stellar components are plotted over the observed emissivity. The free-particle trajectories of the plasma in the stream (Lubow and Shu 1975) are also shown in the map. The stream tracking was truncated at the Alfvén radius which was calculated using the magnetic field B=31.5 MG at dominant pole (Barret and Chanmunghan, 1985) and assuming the mass transfer rate $\dot{M} = 3\times10^{-11}\ M_{\odot}$/yr given by the empirical relation of Patterson (1984). A dipole colatitude $\beta = 146°\pm2°$ (Piirola, Reiz and Coyne 1987) and an azimuth $\psi = 49°\pm13°$

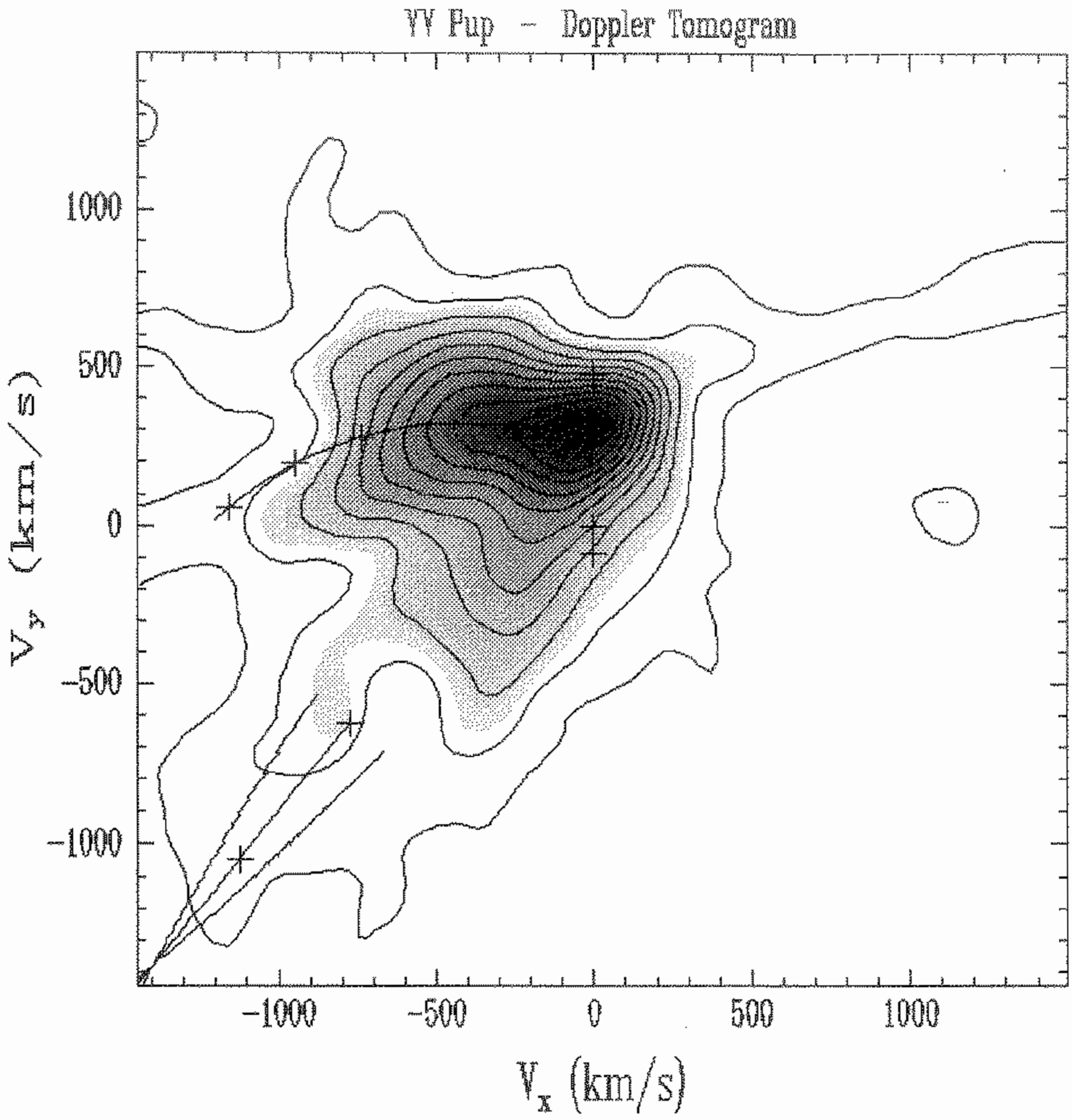

Figure 1. Doppler tomogram of VV Pup in Hα. The resolution (FWHM) of the map at origin is 200 km/s. This value increases to 440 km/s close to the border of the image due to the limited phase resolution of individual exposures. The pluses along the Vx = 0 axis correspond, from bottom to top, to the position of the white dwarf, the center of mass, the first Lagrangian point, and the companion center. The curved line from L1 represents the free-particle stream trajectory. From right to left the plusses on the stream curve represent the magnetic coupling radius crossing for a fractional column area $f = 0.004$, $f = 0.002$ and $f = 0.001$. The first plus sign in this sequence indicates the magnetosphere radius from Meggit and Wickramasinghe (1989). The line with pluses in lower left corner represent the expected position for the emission from the accretion funnel for $f = 0.001$. The lines beside the funnel path indicate the lower limit to the resolution of the column emission caused by "gamma smearing" (see text). For larger values of $f$ the funnel path moves leftward due to the change in the magnetic field geometry. The pluses marked on this line correspond, from top to bottom, to heights of 25 $R_{wd}$ and 17 $R_{wd}$ over the white dwarf surface.

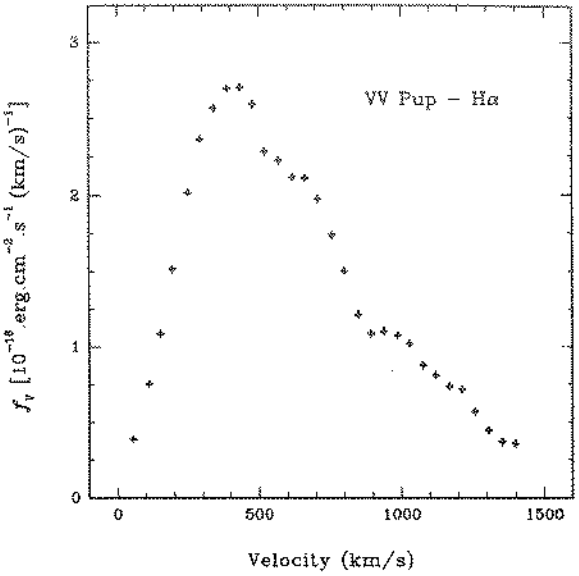

Figure 2. Hα line emissivity average distribution obtained from the Doppler imaging. The velocity scale is relative to the center of mass of the binary system while the FWHM resolution is 170 km/s.

(Cropper 1988 and references therein) for the main accreting funnel together with the Roche potential and the magnetic field geometry were used to derive theoretical "S-wave" components along the column, by using the method described by Ferrario, Wickramasinghe and Tuohy (1989). The semi-amplitudes and orbital phases of such sinusoidal components define the expected trajectory of magnetically trapped gas in the tomogram. Considering the tomogram resolution achieved (FWHM(res.) ≅ 200 km/s), the differences between the S-wave gamma velocities and the binary systemic velocity (<300 km/s) suggests that a significant "gamma smearing" occurs for the structures in the accretion column. The "gamma smearing" tends to increase when the binary inclination is low and the dipole is far from the orbital plane. Our calculations of "synthetic S-waves" indicate that this effect must be taken into account in the interpretation of structures in Doppler maps of polars and its evaluation depends on the model adopted for the accretion funnel.

## 4. DISCUSSION

In good agreement with the observed kinematics, the theoretical stream trajectory indicates that the Hα line is produced in the stream and close to the inner Lagrangian point. The magnetically driven gas gives a small contribution to the total emission in this line. The accretion column is not seen in the reconstruction indicating that it should be faint in Hα. From the flux distribution in the Doppler tomogram we derive that 30% of the average line emission or $5\times10^{-14}$ erg/cm²/s is produced close to the secondary star while about 40% or $7\times10^{-14}$ erg/cm²/s is radiated in the stream. On the basis of the limits chosen for these measurements on the reconstruction, we estimate the uncertainty of about ±30% in these values.

From the Doppler map we derived the emissivity distribution as a function of the velocity modulus with respect to binary center of mass (Figure 2). This distribution is free from projection effects and may be more easily compared with theoretical models for line emission in polars than the phase averaged profiles. It is clear from this graph that the line emissivity at high velocities (higher than the velocity at coupling radius) is strongly suppressed. This behavior agrees with the claim that the column has a small line emissivity. Considering the magnetic field strength and the dipole orientation given in section 3, a lower limit for the extension of the stream was defined by its crossing of the half intensity isophote. This is a conservative limit since the shape of this structure is well defined even at much lower intensities. Such a limit for the free-particle path indicates a magnetospheric radius $R_m < 3\times10^{10}$ cm and a column fractional cross section at white dwarf surface $f < 6\times10^{-3}$. The magnetosphere radius $R_m \cong 52\times R_w \approx 2.5\times10^{10}$ cm suggested by Meggit and Wickramasinghe (1989) implies in a column cross section $f \approx 4\times10^{-3}$. These previous findings are consistent with our measurements using the tomogram. Stream velocities corresponding to smaller coupling radius are plotted on the map for comparison. Future high-resolution spectrophotometry of this system is encouraged. Doppler reconstructions using the HeII λ4686Å profile should be appropriate to attempt the imaging of the lower part of the accretion column.

We would like to acknowledge Keith Horne for useful discussions and Stephen Lubow for his help in the free-particle calculations. We also thank Ivo Busko for his comments on the manuscript. M.P.D. thanks R. E. Williams for the hospitality at CTIO during part of this investigation.

## References:

Allen, C. W. 1973, "Astrophysical Quantities", The Athlone Press"

Allen, D. A., and Cherepashchuck, A. M. 1982, MNRAS, 201, 521

Barret, P. E. and Chanmugan, G. 1985, ApJ, 298, 743

Cropper,M. 1988, MNRAS, 231, 597

Cropper, M, and Warner, B. 1986, MNRAS, 220, 633

Cowley, A. P., Crampton, D., and Hutchings, J. B. 1982, ApJ, 259, 730

Diaz, M. P., and Steiner, J. E. 1993, ApJ, in press

Dhillon, V.S., Marsh, T.R, and Jones, D.H.P.: 1991, MNRAS 252, 342

Ferrario, L., Wickramasinghe, D.T, and Tuohy, I. R. 1989, ApJ, 341, 327

Hamuy, .M., Walker, A. R., Suntzeff, N. B., Gigoux, P., Heathcote, S. R., and Phillips, M. M. 1992, PASP, 104, 533

Horne, K. 1988, in Proceedings of the Workshop New Directions in Spectrophotometry (Davis, Schenectady)

Horne, K., and Saar, S. H. 1991, ApJ, 374, L55

Huchings, J. B., Cowley, A. P., Crampton, D., Fisher, W. A., and Liller, W. A. 1982, ApJ, 252, 696

Lubow S. H., and Shu, F. H. 1975, ApJ, 198, 383

Marsh, T.R., Horne, K.: 1988, MNRAS 235, 269

Marsh, T.R., Horne, K.: 1990, ApJ 349, 593

Marsh, T.R., Horne, K., Schlegel, E.M., Honeycutt, K., and Kaitchuck, R.H. 1990, ApJ 364, 637

Meggit, S.M.A. and Wickramasinghe, D.T. 1989, MNRAS, 236, 31

Patterson, J. 1984, ApJS, 54, 443

Patterson J., Beuermann, K., Lamb, D. Q., Fabbiano, Raymond, J. C., Swank, J., and White, N. E. 1984, ApJ, 279, 785.

Piirola, V., Reiz, A., and Coyne, G. V. 1987, ApSS, 130, 203

Ratering, C., Bruch, A., and Diaz, M. P. 1993, A&A, 268, 694

Schneider, D. P., and Young, P. 1980a, ApJ, 238, 946

Schneider, D. P., and Young, P. 1980b, ApJ, 240, 871

Szkody, P. and Capps, R. W. 1980, AJ, 85, 882

Szkody, P., Bailey, J. A., and Hough, J. H. 1983, MNRAS, 203, 749

Wade, R. A., and Horne, K. 1988, ApJ, 324, 411

Walker, M. F. 1965, Mitt. Sternwarte Budapest, 57, 1

Young, P., and Schneider, D. P. 1979, ApJ, 230, 502

# ON THE ROTATION OF EVOLVED STARS

J. Renan De Medeiros
Departamento de Física — CCE / UFRN
Campus Universitário, 59072-970, Natal, RN, Brasil
e-mail address: renan@brufrn.bitnet

## 1 INTRODUCTION

The study of the rotation of the evolved stars has as its main challenging goal to understand the stellar angular momentum history once stars evolve through the H-R diagram. Besides, rotation can provide important contraints for models of angular momentum evolution during stellar life as well as important informations on the connection between surface rotation and atmospheric phenomena. It has long established that rotation velocities of single evolved stars tend to decrease with decreasing effective temperature. The most usual explanation for this trend has been evolutionary expansion which changes the moment of inertia, coupled with the conservation of angular momentum, for stars which have developed a convective envelope lately and the loss of angular momentum by magnetic braking for stars which have a magnetic solar-type wind. There have been numerous attempts to try to answer this problem but they have been only partially successful. Essentially, detailed tests based on the comparisons of rotational velocities predicted by theoretical models with observed stellar rotation rates are still very poor due to the scarcity of the observations. Of course, only surface rotational velocity can be directly determined from the observations but there are strong evidences that these rotational velocities are governed largely by the efficiency of angular momentum transport inside the stars.

Evolutionary models taking into account rotation have shown that substantial differences exist between these models and their nonrotating counterparts, in particular in the late stages of evolution (Endal and Sofia, 1976,1979; Gray and Endal, 1982; Rutten and Pylyser, 1988; Pinsonneault et al., 1989). In rotating models there are several additional problems that must be solved in order to explain the stellar evolution. The most important of these are the effects of rotation on the structure of the star, the effects of angular momentum loss due to the magnetic wind on the upper atmosphere, the effects of the transport of angular momentum due to induced instabilities on the internal mixing and the uncertainties in the initial conditions. Endal and Sofia (1976, 1979) have computed rotation velocities for population I stars at 10, 7, 5, 3 and 1.5 $M_\odot$ for three different cases of angular momentum redistribution: No radial exchange of angular momentum which means that each shell retains its original angular momentum; complete radial exchange of angular momentum, leading to rigid-boby rotation; and partial redistribution of angular momentum as predicted by detailed consideration of circulation currents in rotating stars. Endal and Sofia (1979) have shown, for example that on the red giant branch, angular momentum distribution reduces surface rotation by a factor 2 or more, relative to the rotation expected for no radial distribution.

Gray and Endal (1982) have claimed that their model with an uniform specific angular momentum in convective regions can explain the observed surface rotational velocity of the Hyades giant stars. In the models treated by these authors, either loss of angular momentum or violation of the rigid-body rotation hypothesis is required to explain the low rotation rates in the giant phase.

Rutten and Pylyser (1988) have suggested that rigid-body rotation and conservation of angular momentum can describe the observed decrease of rotational velocities with colors for giant stars of luminosity class III, whereas for subgiants with masses of about $1.5\mathrm{M}_{\odot}$ angular momentum losses sbould be take into account to explain their rotation rate distribution.

More recently, Pinsonneault et al. (1989) and Sofia et al. (1990) have developed more complete evolutionary models of rotating solar-like stars, taking into account for angular momentum redistribution by rotationally induced instabilities as well as angular momentum loss through a magnetic wind. The rotation velocities predicted by tbese models seem to be consistent with rotation rate measurements for low-mass subgiant stars.

Concerning the angular momentum loss effects, it is now well accepted that a stellar wind forced by a magnetic field to co-rotate up to the Alfven radius, transports angular momentum from tbe stellar surface to tbe interstellar medium, thus decreasing tbe rotation velocity of tbe stellar surface layers (Ex.: Schatzman, 1962). In a serie of works Gray (1981, 1982, 1983, 1988) has claimed a sudden declaine in rotation rate to occur for giant stars, near tbe spectral type G5III and that tbese stars slow down from about 25 km $\mathrm{s}^{-1}$ to about 5 km $\mathrm{s}^{-1}$ in only a few spectral subclasses. Gray interprets this decline as the result of an abrupt magnetic braking due to the increase of deptb of the convective envelope. This generates a very strong dynamo-generated magnetic field, which coupled to tbe stellar wind reduces the surface rotational velocity very rapidly.

This sudden rotational discontinuity at G5III was ratber surprising for us. First of all, it is very hard to understand this extremely rapid braking into the Hertzsprung gap, because evolutionary calculations show that the first crossing evolution of giant stars through this region is very rapid (Iben, 1965). For exemple, most recent evolutionary models of Meynet and Maeder (1990) and Schaller et al. (1992) show that the evolution of a $2.0\,\mathrm{M}_{\odot}$ giant, with a solar metallicity, from about G3III to about G5III occurs in a time of 2 to 3 millions of years. This means that the time scale for a rotational braking as that one proposed by Gray at G5III should therefore be of this order.

The second questioning about the nature of the braking at G5III was based essentially on some early *Vsini* measurements that we have made with the CORAVEL spectrometer (Baranne et al., 1977). In fact these preliminary measurements shown solely low rotators between stars of this spectral type.

These questioning have inspired us to develop a systematic survey of stars of luminosity classes IV through Ib, by using the CORAVEL spectrometer, to study the rotational behaviour of evolved stars of low to intermediate masses. As shown by Benz and Mayor (1981, 1984) the cross-correlation spectroscopy with the CORAVEL scanner allows the determination of rotational velocities as low as 2.0 km s$^{-1}$ with an excellent precision of 1.0 km s$^{-1}$.

From this survey De Medeiros and Mayor (1989,1990) have shown in a preliminary study that the rotational discontinuity at G5III does not exist. In fact, We have found a discontinuity at G0III, consequently at the same spectral region where Herbig and Spalding (1953, 1955) have suggested a cutoff in the distribution of rotational velocities. Gray (1989) have obtained this same result independently, by combining his data with $Vsini$ values given by Hoffleit and Jaschek (1982). The modification at the location of the discontinuity is not insignificant: in fact, there is a displacement from the centre to the blue side of the Herztsprung-gap.

We have looked carefully for the origin of the previous discontinuity claimed by Gray at G5III. As we have shown in a previous work (De medeiros and Mayor, 1989), clearly, the rotational discontinuity at G5III was just an artifact.

For the subgiants, Gray and Nagar (1985) conclude that also occurs a rotational cutoff near G0IV. These authors suggest that the origin of this discontinuity parallels that one seen for giant stars in all its characteristics. Concerning the higher luminosity classes, Gray and Toner (1986, 1987) have determined rotational rates for several dozen of F to K bright giant and Ib supergiant stars, but no evidence for some rotational decline was found.

These recent studies indicate, in the broadest sense, that many of the observational and theoretical aspects of the rotation of evolved stars are not in agreement. What is not clear, particularly, is whether angular momentum is conserved as stars evolve through the Hertzsprung-gap and during the subsequent phases of the evolution, or whether a magnetic braking is needed. Of course, one might also inquire about the nature of rotational discontinuities discussed above

In this work we attempt to address some of these questions, by taking into account in the evolution of the stellar rotation, not only the variation of momentum of inertia, the transfer of the angular momentum inside the star and magnetic braking effects but, particularly, the mixing of masses of the giant stars as a function of the color index $(B-V)$. Indeed, the $Vsini-$ $(B-V)$ diagram for the field giant stars does not represent an evolutionary sequence for a given mass. This fact indicates that mixing of masses for field giant is of major importance for the discussion of the origin of the rotational discontinuity. In this talk, we present the main points of the observational survey that we have began in march 1986 at the Geneva Observatory, as well as some of the most interesting results that we have found up to date.

## 2 THE OBSERVATIONAL SURVEY

The main characteristics of the sample of stars selected for our survey, as well as the observational procedure have already been described by De Medeiros and Mayor (1992). Let us therefore just recall some important points. We have selected about 1925 evolved stars covering the spectral range from middle F to middle K in the luminosity classes IV, III, II and Ib. Such a large spectral interval represents the possibility for a study of the stellar rotation into the Hertzsprung-gap, as well as on the blue side of the gap and on the red giant clump. The sample is composed by 200 subgiants, 1020 giants III, 425 bright giants of class II and 233 supergiants class Ib, all stars selected essentially from "The Bright Star Catalog" (Hoffleit and Jaschek, 1982; Hoffleit et al., 1983) and the list of supergiants compiled by Egret (1980). A few dozen of G and K objects were selected from Fekel et al. (1986) and Alschuler (1975), for comparative purpose. The observations were carried out with the CORAVEL Spectrometer (Baranne et al., 1979) at the Haute Provence Observatory in France, and at the European Southern Observatory in Chile. The data discussed in this paper were acquired between March 1986 and January 1991. In principle, we have tried to make 2 measurements for each star, looking for spectroscopic variability. This point is very important because as already well established, rotation may be altered by tidally induced synchronization in close spectroscopic binaries. Thus, the presence of binary stars must be take into account for a judicious statistical analysis of the stellar rotation. The comparison of our measurements, obtained by the cross-correlation technique, with those acquired by D. Gray and co-workers, with the Fourier transform technique, shows an excellent agreement. From a sample of about 150 stars with $V sini$ values measured respectively by CORAVEL and Gray we found that the r.m.s. of the rotational velocity differences is of about 1.1 to 1.2 km $s^{-1}$.

This external comparison with Fourier transform measurements indicate a precision of about 1.0 km $s^{-1}$ for the CORAVEL $V sini$ of subgiant and giant stars. However, for the bright giant and the Ib supergiant stars we have adopted conservatively an incertainty of 2.0 and 3.0 km $s^{-1}$ , respectively, to take into account the increase of the macroturbulence with luminosity.

## 3 MAIN RESULTS AND DISCUSSION

We turn now to the presentation and discussion of some results from the CORAVEL survey.

First of all, there is a sudden decline in rotational velocities for all luminosity classes discussed here, which corresponds to a "rotational dividing line". The location of this well established "rotational dividing line" in each luminosity classes is:

| | | | | | |
|---|---|---|---|---|---|
| Subgiants: | $(B-V)$ | = | 0.55 | or | F8IV |
| Giants: | $(B-V)$ | = | 0.60 | or | G0III |
| Bright Giants: | $(B-V)$ | = | 0.60 | or | F9II |
| Supergiants Ib: | $(B-V)$ | = | 0.70: | or | F9Ib |

For the Giants III and the most luminous classes the location of this rotational discontinuity is relatively close of the blue side of the Hertzsprung gap, but a somewhat slightly reddder. explanations for the origin of these rotational discontinuities are given in a forthcoming work.

On the blue side of the discontinuity we found, for all luminosity classes, a wide range of V*sini* values with a significant number of low rotators. A such picture is very important because, for the luminosity classes IV and III it does indicate that most of these stars have already lost a large fraction of their angular momentum during the main-sequence phase and, consequently, they must arrive on the spectral region of the discontinuity with low rotation rates. In fact, this large spread in the distribution of the V*sini* values is consistent with the broad distribution of rotation rates for stars on the main-sequence (Kraft, 1965; Wolff et al., 1982; Stauffer and Hartmann, 1986;). For the Ib supergiants we believe that most of the low rotators in the blue side of the discontinuity are stars in the blue loop part of their evolution path.

The observed range of rotation rates on the blue side of the discontinuity is not similar for all luminosity class. Within the uncertainties concerning the high V*sini* values we can consider that for subgiant and giant stars the rotation rates scatter over a range of about 2.0 km $s^{-1}$ to about 150.0 km $s^{-1}$ . However from the bright giants towards the supergiants the spread decreases with increasing luminosity: for the luminosity class II the rotational velocities range from a few km $s^{-1}$ to about 100.0 km $s^{-1}$, whereas the observed spread for the class Ib is from 2.0 km $s^{-1}$ to 70.0 km $s^{-1}$. We can understand this feature, as a result of the changes in the moment of inertia during evolution. As stars evolve from the main sequence to the giant branch, the moment of inertia increases as the result of the increasing in stellar radius and the changes in the internal radial distribution of mass. Theoretical evolutionary models (e.g., Endal and Sofia, 1979) predict that rotational velocity follows changes in the moment of inertia and stellar radius in a such way that at a given spectral type the decreasing in rotation is most important for the higher luminosity classes.

It is important to emphasize here that despite the presence of binary systems all along the spectral region that we have studied in all luminosity classes, for the subgiants, giants and bright giants there is a strong concentration of binaries showing high rotation rates relative to the mean, which seem to be synchronized, located in a spectral interval characteristic for each luminosity class. Beyond a critical value of $(B-V)$ in each luminosity class, respectively 1.10, 1.40 and 1.20 for subgiants, giants and bright giants, there are no binary stars with high rotation rates. In fact, there is a sort of cutoff in the distribution of binary systems with significant rotation. f) If one put aside the synchronized binary systems, all subgiant and supergiant stars located at the red side of the discontinuity rotate very slowly. The great majority of giants and bright giants present also a similar behaviour. Nevertheless, there is a small group of G and K stars in these latter luminosity classes, all apparently single, that appear to violate the general rule. The survey of De Medeiros and Mayor (1989, 1993) has revealed about 20 of such stars, which are presented in table I. A few of them have already been identified by Fekel et al. (1986). Their individual rotational velocities range from 10 to 50 km s$^{-1}$, which are substantially higher than the mean $Vsini$ value for the corresponding $(B-V)$ color. UP to date, the nature of these moderate or rapidly rotating single or pseudo-single giants can be considered essentially unknown. Currently such stars have been hypothesized as the descendants of WUma binary systems whose components have merged, following the scenario envisioned by Bopp and Stencel (1981), or a coalescing Algol binary systems on the basis of the model suggested by Walter and Basri (1982), to explain the high rotation of the FK COMAE star.

At this point we would like to discuss the nature of the discontinuity at G5III claimed by Gray (1981, 1982, 1988). In fact, as discussed preliminarly by De Medeiros and Mayor (1989), the discontinuity at G5III was just the result of the combination made by Gray between his own $Vsini$ values and some low resolution $Vsini$ measurements, associated with a selection effect. In the first instance, Gray has combined his $Vsini$ measurements, obtained with a precision of about 1.0 km s$^{-1}$, with those measured by Alschuler (1975) for which the uncertainty is of about 20.0 km s$^{-1}$. Secondly, Gray in his early work, selectively, did not observe stars bluer than G5III, which have introduced a strong bias in the behaviour of rotation as a function of colors.

Let us finally recall that the origin of the rotational discontinuity is not the same for the subgiant and the giant stars, as has for exemple proposed Gray (1990) and Gray and Nagar (1986). By considering that rotation of evolved stars with masses between 0.80M$_\odot$ and 1.5M$_\odot$ will depend on the initial $Vsini$ distribution ($Vsini$) and the evolution of stellar structure associated with a magnetic braking which follows the relation (age) one can account for the rotational discontinuity for the subgiant stars, as well as for their rotational behaviour after such discontinuity. The kinematical analysis indicates that giant stars on both side of the the discontinuity have significantly different ages. Stars on the blue side are significantly younger than those on the red side and in addition the high rotators are younger than those stars showing low rotation rates. Thus, in our view, for the giant stars, this cutoff is essentially the result of the age mixing associated with the extremely rapid evolution of stars of masses greater than 1.5 M$_\odot$ into the Hertzsprung gap. From the simulation of the plan $Vsini-$ $(B-V)$ and in accordance with Mermilliod's diagrams for open clusters one see quite clearly that the location of the cutoff corresponds to the blue edge of the Hertzsprung gap. A complete study on the observational and theorethical aspects of the rotation of evolved stars will be presented in a forthcoming paper. The results of the CORAVEL observational survey will be published in a forthcoming CATALOG OF RADIAL AND ROTATIONAL VELOCITIES FOR EVOLVED

STARS. Because the extensive list of references, we do not present this one here. Those interested readers can receive the complete list on request.

## References

Alschuler, W. R. 1975, ApJ, 195, 649

Baranne et al. 1979, Vistas in Astron., 23, 279

Benz, W. and Mayor, M. 1981, Astron. Astrophys., 93, 235

Benz, W. and Mayor, M. 1984, Astron. Astrophys., 138, 183

Bopp, B. W. and Stencel, R. E. 1981, Ap. J. Lett. 247, L131.

De Medeiros, J. R. and Mayor, M. 1990, in Astron. Soc. Pac. Conf. series, vol. 9, pp 404

De Medeiros, J. R. and Mayor, M. 1993, in preparation

Egret, D. 1980, Bull. Inf. CDS, 18, 82

Endal, A. S. and Sofia, S. 1976, ApJ, 210, 184

Endal, A. S. and Sofia, S. 1979, ApJ, 232, 531

Fekel et al. 1986, ApJ Supp., 60, 551

Gray, D. and Nagar, P. 1985, Ap. J. 298, 756

Gray, D. and Toner, C. G. 1986, P.A.S.P. 97, 543

Gray, D. and Toner, C. G. 1987, ApJ, 322, 360

Gray, D. and Endal, A. S. 1982, ApJ, 254, 162

Gray, D. 1988, Lectures on Spectral-Line Analysis: F, G and K Stars (Arva, Ontario)

Gray, D. 1981, 1982, 1983, see Gray (1988)

Gray, D. 1989, ApJ, 347, 1021

Herbig, G. H. and Spalding, J. F. 1953, P.A.S.P., 65, 192

Herbig, G. H. and Spalding, J. F. 1955, ApJ, 121, 118

Hoffleit, D. and Jaschek, C. 1982, The Bright Star Catalogue (4th ed., Yale University).

Hoffleit et al. 1983, A supplement to The Bright Star Catalogue (Yale University).

Kraft, R. 1965, ApJ, 142, 681

Meynet, G. and Maeder, A. 1990, private communication

Pinsonneaut et al. 1988, ApJ, 338, 424

Rutten, R. G. M. and Pylyser, E. 1988, Astr. Astrophys., 191,227

Schaller et al. 1992, private communication

Sofia et al. 1990, in Angular Momentum Evolution, NATO ASI vol. 340, series C

Schatzman, E. 1962, Annales d'Astrophys., 3, 331

Stauffer, J. R. and Hartmann, L. W. 1986, P.A.S.P., 98, 1233

Walter, F. M. and Basri, G. 1982, ApJ, 260, 735

Wolff et al. 1982, ApJ, 252, 322

# TOWARDS A NEW SOURCE OF $^7$Li IN THE GALAXY

Ramiro de la Reza and Licio da Silva

Departamento de Astronomia
Observatorio Nacional - CNPq
Rio de Janeiro

**ABSTRACT** Is the Lithium abundance increasing or decreasing from the beginning of the Universe ?. Even if the most popular scenario is the one in which the Li abundance increases, the answer to this question will depend on cosmological models and on the existence of different sources of Li in the Galaxy. In this paper we discuss the possibility of a new source of $^7$Li in the Galaxy: the very strong Li K giant stars.

## INTRODUCTION

The light elements Li, Be and B are important tools of knowledge. In fact, the study of these elements connect physical process at the beginning of the universe with those of today. A great step in research will be made when we will obtain a good set of data of all them. Nevertheless, at present time, only the element Li is easy to be observed. Concerning this element, the main question consists in knowing whether its abundance is increasing or decreasing from the beginning of the universe. The most popular scenario is that of the first option, however Mathew, Alcock and Fuller (1990) examined both possibilities concluding that the two scenarios fit the observed data reasonably. In those circumstances these authors conclude that only Li observations in other less processed galaxies, as the Magellanic Clouds, can decide between these two possibilities. Anyhow, observations of Li in the line of sight to SN 1987A were not conclusive. The decreasing scenario begins with a high Li primordial Li abundance, produced by an inhomogeneous cosmology ($Li/H \sim 7\ 10^{-9}$). The following decreasing is produced only by astration process with no sources of fresh Li. The increasing scenario begins with a low Li abundance produced by an homogeneous cosmology ($Li/H \sim 10^{-10}$) compatible with the observed abundance in population II objects. The following increasing is produced by galactic sources of Li surpassing the astration destructive process. The end product of both scenarios consists in obtaining the present population I abundance ( $Li/H \sim 10^{-9}$). A new view independant on evolutionary models, using the interstellar ratio of $^6$Li/$^7$Li was suggested very recently by Steigman (1993).

In this paper we will limit to discuss the sources of Li and we will propose a new probable Li galactic source of this element.

## SOURCES OF LITHIUM

Several sources of $^7$Li have been taken into consideration in the galactic evolutionary models (Mathews ,Alcock and Fuller,1990 ; D'Antona and Matteucci,1991); 1) **Cosmic Rays**: spallation reactions with cosmic rays impinging target atoms of C,N and O are the only way to produce $^6$Li atoms, but can also produce small quantities of $^7$Li. However past $^7$Li production is related to uncertain initial abundances of CNO.In any case $^7$Li production by cosmic rays must be studied in connection with $^9$Be production, which is another spallative product.2) **Supernovae**: $^7$Li can be formed in shocked heated regions in supernovae ( Dearborn et al.,1989; Woosley and Haxton,1988). This mechanism depends essentially in the original quantity of the seed material $^3$He contained in the envelope.This instrument of Li production remains nevertheless only theoretical. In fact, up to now, no presence of Li has been detected in the filaments of young supernova remanants. 3) **Novae**: Nova outbursts have been proposed as sites of $^7$Li production ( Starrfield et al. 1978). As all the other stellar sources, this mechanism depends on the quantity of $^3$He present in the envelope together with the enhancement of CNO elements to obtain a fast nova event necessary to produce $^7$Li. 4) **Asymptotic Giant Branch (AGB) stars**: Smith and Lambert (1989,1990 ) discovered that AGB stars at $M_{bol} = -6$ in the Magellanic Clouds present strong Li I resonant lines at 6708 Å . If this represents, a Li abundance larger than that of the interstellar medium, then these stars could be sources of Li in the MC. Due to the larger masses of these giants," The Cameron-Fowler $^7$Be mechanism " can work effectively and produce super rich giants with Li abundances up to $\log \varepsilon = 5.5$ ( in the scale $\log \varepsilon_H = 12.0$ ) during a short time (Boothroyd and Sackmann 1992). For eventual Li rich AGB stars in the Galaxy, we have to know first, how many stars may survive above $M_{bol}=-6$ before mass loss removes the outer stars envelope, in order to consider these stars as effective sources of Li ( Smith 1993). 5) **Carbon Stars**: Few carbon giant stars with very strong Li resonant lines are known. These stars can partially contribute, via mass loss, to the Li enrichment (Abia, Isern and Canal,1993). We believe, however, that the potentiallity of these sources will be better estimated when a detailed calculation of their abundances is made. This can be done by correcting the blending of the Li line with the typical strong CN lines of these stars.

## A NEW STELLAR SOURCE

The Li strong K giant stars were not taken into account in a recent past as stellar sources of Li in galactic evolutionary models (Mathews , Alcock and Fuller 1990 ; D'Antona and Matteuci,1991), because their LTE abundances were less or at maximun equal to that of the interstellar medium, producing then no galactic enrichment. The first survey to detect strong Li K giant stars were made on bright stars (Brown et al. 1989) obtaining an efficiency of less than 3%. Apart from this survey, some few stars were detected by others authors. The "Pico dos Dias Survey" (Gregorio Hetem et al,1992, Torres et al.1993) made at the LNA (Brasil) originally intended to search for new pre main sequence stars, obtained a very important secondary result: the discovery of several very strong Li K giants. This survey was based on the use of selected IRAS sources having far infrared colors typical of T Tauri stars. In a certain way, the success of the PDS survey is explained by the fact that the search was based on faint and distant stars that had not been explored before. These results had incited other surveys based on a fine tunning analysis of the distribution of IRAS colors : Gregorio Hetem, Castilho and Barbuy 1993, Castilho, Barbuy and Gregorio Hetem (presented at this SAB meeting ), with promising results giving efficiencies larger than 10%.

As a first step to examining the potentiallity of K Li giants as sources of Li in the Galaxy, we made a detailed analysis of the Li lines formation in view to obtain a realistic determination of the Li abundances. The detailed results of this analysis can be found in de la Reza and da Silva (1993). We will summarize here some results which concern only the Li enrichment problem.

LTE and non LTE (NLTE) line profiles analyses have been performed, based on observations of the resonance Li I at 6708 Å and the secondary Li I line at 6104 Å. To our knowledge, this was the first time that an observed 6104 line was considered in a NLTE analysis. The observations were made at ESO (Chile), LNA ( Brasil) and with the IUE satellite. Low resolution IUE spectra were obtained with different purposes, as we will see later. One of them was to obtain the measurement of the continuous radiation shortward than 3500 Å. This radiation, which is very important in NLTE analysis, controls the ionization from the two first levels of the Li I atom. The selected stars were the following: 1) HD787, a K 5 Li strong star with solar metallicity having a medium strong 6104 line with a equivalent width of 60 mÅ. This star was selected from the survey of Brown et al.(1989). 2)HD39853, a K 5 giant belonging to the old disk with a very large velocity and a middly metallicity. This star, studied by Gratton and D'Antona (1989), was the only known, very strong Li giant as represented by the 6104 line, with an equivalent width of 165 mÅ. HD19754, a K0-1 giant with solar metallicity and lower chromospheric activity. This star is the only one among the three to be an optical counterpart of an IRAS source. Their 6104 line is even stronger than in HD 39853 and is equal to 172 mÅ. This star is a new object recently discovered in the PDS survey.

LTE abundances fit well the observed profiles of the secondary line 6104, giving only for this line the following abundances (log $\varepsilon_{Li}$): HD787 (2.20), HD39853(2.92) and HD19745 (4.08). Nevertheless the use of the same abundances do not permit to fit the observed profiles of the stronger resonance lines ( with equivalent widths in mÅ respectively equal to; HD787 ( 427 ), HD39853 ( 479 ) and HD 19745 ( 487 ). It is interesting however, to see that even in LTE, the Li abundance of the hotter K giant HD 19745 is much larger than that of the interstellar medium ( log $\varepsilon$ = 3.0). The other abundances are smaller or almost equal to this interstellar abundance.

In NLTE, even with somewhat larger microturbulences, the resulting abundances necessary to fit the profiles of both lines simultaneously give the following results : HD787 ( 3.10 ∓ 0.1), HD39853 ( 3.90 $\mp$ 0.1 ) and HD19745 ( 4.75 $\mp$ 0.1 ). The super strong Li giants HD39853 and HD19745 ( clearly distinguished especially by the non saturated 6104 line) have NLTE abundances larger than those from LTE and than that of the interstellar medium. Accepting these results we are in condition to propose these stars as possible sources of Li in the Galaxy.

The next step will consist in examining the statistical distribution of these stars and calculate the chemical evolution equations in order to measure the real contribution of these stars ( de la Reza and da Silva,1993a). One difficult and interesting problem, however must be solved: What is the origin of the Li in these stars? In fact, these K giant stars are objects of very low mass for which the "Be mechanism" that works in AGB and probably on carbon stars, will not operate . Also any high Li abundance induced by strong rotation will also not work. The three stars mentionned here have low normal rotation values of vsini of the order of 4 Km/s or less. The explanations then, must appeal to other types of mechanisms. Gratton ad D'Antona(1989) ;Gratton (1991); de la Reza and da Silva (1993) have discussed the various tentatives to explain this stellar enrichment. These are: 1) **Maintainance of an original Li** - this very improbable mechanism, requires that these stars conserve an original and very high pre main sequence abundance of Li. The observed values of $^{12}C/^{13}C$ indicates nevertheless, the existence of mixture processes (Gratton,1991). 2) **Engulfing planets or Brown Dwarfs**- if these K stars had planetary material, some of the planets could be engulfed in the process of giant formation contributing to their original Li. Brown Dwarfs can also do the job, however, this can be done on extreme conditions. **Enrichment by a Nova**- if a nova is the hot companion of a K giant star located near the Roche lobe, the fresh Li produced by the nova can contaminate the giant star. Our IUE observations of the giants HD 39853 and HD 19745 do not show the presence of hot companion. Nevertheless, a larger number of IUE observations must be done in order to discart or not this process.

## REFERENCES

Abia, C., Isern,J. and Canal,R. 1993, A&A,275,96

Boothroyd, A. I. and Sackmann, I. J. 1992, ApJ, 393, L21

Brown,J.A.,Sneden,C.,Lambert,D.L. and Dutchover,E.Jr 1989,ApJS 71,293

D'Antona,F and Matteuci,F. 1991, A&A, 248, 62

Dearborn,D.S.P.,Schramm,D.N.,Steigman,G. and Truran,J.W. 1989,ApJ,347,455

de la Reza, R. and da Silva, L. 1993, to be published by the ApJ.

de la Reza R. and da Silva, L. 1993a, in preparation

Gratton,R.G. and D'Antona,F. 1989,A&A 215,66

Gratton, R. 1991, Memorie della Soc Italiana 62,53

Gregorio-Hetem,J.,Lepine, J.R.D.,Quast,G.R.Torres,C.A.O. and de la Reza,R.1992,AJ, 103,549

Gregorio-Hetem,J.,Castilho,B.V. and Barbuy,1993,A&A 268,L25

Mathews,G.J.,Alcock,C.R. and Fuller,G.M.,1990,ApJ,349,449

Smith, V.V. and Lambert, D.L. 1989,ApJ.345,175
Smith,V.V. and Lambert, D.L. 1990, ApJ. 361,L69
Smith,V.V. 1992, Newsletter of Chem. Pec Red Giant Stars ed. S.Yorka 12,3
Steigman,G. 1993,ApJ, 413,L73
Torres,C.A.O., Quast,G. de la Reza, R. Gregorio-Hetem,J. and Lepine,J.R.D.1993, preprint to be submitted to the AJ
Woosley,S.E. and Haxton, W.C. 1988, Nature,334,45

# Section 3:

# The Galaxy and the Magellanic Clouds

# THE DELAYED FORMATION OF THE GALACTIC BULGE

Michael Rich

Columbia University, Dept. of Astronomy, Box 46, Pupin Hall
538 West 120th Street, New York, NY 10027, USA

**Abstract:** A confluence of evidence supports the idea that central bulges and possibly most spheroids are not the oldest stars, being younger than extreme halo/globular clusters by at least a few Gyr. Extended giant branches are found in the spheroids of M31, M32, and M33. Discovery by HST of a bright turnoff in the bulge is reinforced by the presence of long period Miras that cannot be the progeny of the oldest stars.

While contradicting the standard scenario that the densest parts of galaxies should form first, late bulges are in harmony with new ideas in galaxy evolution. Of the *luminous* stellar population in galaxies like the Milky Way, only $\approx 5\%$ is "extreme population II", so that if one could view the evolution of a typical galaxy it would appear very faint for the first few Gyr.

## 1.0 Introduction

The discovery of stellar populations still recent in their minds, the participants of the 1958 Vatican meeting appreciated the fine distinctions between various galactic populations. Over time, the presence of RR Lyrae stars in both the Galactic bulge fields and globular clusters makes it easy to conclude, at first glance, that the bulge is old, like the globular clusters.

Straightforward physics makes this view attractive as well; as Renzini (1993) points out, the free fall time is shortest in this dense region of the Galaxy.

I am going to try to convince you that despite its simplicitly and logic, this idea is not correct. I believe that evidence is accumulating that the metal rich, rapidly rotating bulge (the portion imaged by *COBE* for example) is in fact younger than the halo and globular clusters. Further, evidence is accumulating that this is the case in M31 as well—formation of these central components may be a significant step in galaxy formation.

This shift in viewpoint is the direct result of new technology being applied to the observations. Infrared and crowded field techniques are revealing that bulges contain evolved stars too luminous to be as old as the globular clusters. These findings are being confirmed with *HST* data. Further, our theoretical vision is expanding to accomodate these new viewpoints. In this article, I address the extended giant branches recently found in local group bulges; returning to the Milky Way bulge (§3), I find support for an intermediate age population coming from the Miras as well as the main sequence turnoff. Concluding, I give a plausible delayed formation scenario, and show how this is consistent with models in which bar/triaxial structures thicken into bulges.

## 2.0 Extended Giant Branches

### 2.1 The Bulge of M31

Imaging the bulge of M31 in the infrared, we can hope to reduce the extreme crowding somewhat because AGB stars are both rare and luminous. Rich &Mould (1991) found a luminosity function extended brighter than $M_{bol} = -5$ in a field 500 pc SW on the minor axis. This would imply a giant branch at least 0.5 mag brighter than that found by Frogel &Whitford (1987) in Baade's Window (500 pc from the Galactic nucleus). The presence of AGB stars $\approx 1$ mag beyond the tip of the first giant branch is normally considered evidence for a population younger than the globular clusters, although luminous stars can also occur in populations of high metallicity.

Davies *et al.* (1991) countered that the the bright stars may actually belong to the disk. In order to test this hypothesis, Rich *et al.* (1993) expanded the survey of the inner portion of M31 to include fields as distant as 11 $'$ , where Kent's (1989) model predicts that the disk stars should outnumber bulge by 5 to 1. Also included is a field within 2 $'$ of tbe nucleus, on the minor axis, where bulge:disk would be 6:1.

Both disk and bulge fields have extended giant branches, but the bulge fields have a sharp dropoff at the bright end not seen the disk. Strangely, more bright stars are found toward the nucleus of M31, with the central most field extending to $M_{bol} = -6$.

Renzini (1993) countered that the crowding in the inner bulge fields of M31 is extreme. Using the Fuel Consumption Theorem, he predicted in the innermost field one might conceivably find $> 1$ AGB star per pixel, even in the infrared. The giant branch extends 1.5 mag beyond the termination points of the metal rich Galactic globular clusters, which reach $M_{bol} = -4.5$. To account for all the brightening by crowding, one would have to measure clumps of 3-4 stars of equal brightness. One can construct a simulated stellar population using a model luminosity function, such as that of Baade's Window. This kind of test shows that one cannot explain the bright luminosity function as a crowding effect. On the other hand, Luppino &Tonry (1993) find no evidence that M31 has a high K band luminosity variance relative to other galaxies. However, note that M31 and M32 differ by $\bar{M}_K$ of 0.18 mag, and that the assertion that intermediate age stars are detected in M32 but not in M31 rests on Worthey's (1993) theoretical trend of AGB luminosity with $Mg_2$, which must be considered uncertain at this time. (Further, note that Pahre &Mould (1993) find little scatter in the K band luminosity variance for a sample with a wide range in $Mg_2$, including Virgo ellipticals.)

Luppino &Tonry (1993) also find no population gradient, in contradiction with the finding (from both space and ground based photometry) that the $I$ brightness of the giant branch tip increases toward the nucleus (cf. Mould, 1986). The K band surface brightness technique clearly promises great power as a distance indicator, but may not actually be a good discriminant of the evolved stars associated with interemediate age populations.

In the end, we conclude that it is necessary to undertake direct observations at high resolution. We have found further support for an extended giant branch in M31 based on observations with the *Hubble Space Telescope*.

### 2.1.1 HST Imaging of the Inner Bulge of M31

In collaboration with Kenneth Mighell, I have undertaken to image the bulge as close to the nucleus as possible. The brightness gradient is so steep that one sees individual stars on the images only with difficulty. However, artificial star experiments confirm that the giants are fully resolved.

There has been a recent confluence of evidence supporting the idea that something unusual is happening in the central region of M31. Bica *et al.* (1991) find that with increasing metallicity (particularly near the Solar abundance) globular cluster giant branches tend to be fainter than there metal poor counterparts by up to 2 mag in the Cousins I band. Instead of reaching $M_I = -4$, TiO blanketing limits these stars to as faint as $M_I = -2$. As cluster metallicity increases, the brightest giants fade monotonically in the Cousins I band.

Mould &Kristian (1986) imaged the halos of M31 and M33, finding stars at $I_C = 20.7$, or at $M_I = -3.7$ for a modulus of 24.4. Working closer to the nucleus, Mould (1986) studies two fields 1.5 and 1 kpc distant from the nucleus; converting his Gunn $i$ to Cousins I, we find the giant branch rises to $I_C = 20$, then $I_C = 19.5$ at these locations. Our *HST* imaging finds that the giant branch terminates no fainter than $I_C = 19.5$ and may be brighter than this, perhaps reaching $I = 19$ or $M_I = -5.5$. Although metallicity increases toward the center, the giant branch termination point brightens by at least 1 mag, ***opposite to the fading observed in Galactic metal rich globular clusters.*** If the inner bulge of M31 is of approximately solar abundance, ***the discrepancy is no less than 2 mag and the space and gound-based data are in agreement.*** As Rich *et al.* (1989) found, these stars are M giants, ranging in spectral type from M2 to M7, like the Galactic bulge giants studied by Blanco *et al.* (1984). There are a large number of relatively bright, early M giants which might be the progeny of a relatively metal poor starburst.

So the work of Bica, Ortolani, and Barbuy in establishing the $V, I$ color-magnitude diagrams for the metal rich globular clusters turns out to be crucial, providing the key part missing from the puzzle. The metal rich giant branches are fainter in the Cousins I band; enhanced metallicity cannot possibly explain the concentration of bright giants to the nucleus of M31. In fact, a solar metallicity cluster like those in our Galaxy, say NGC 6553, would reach to $I_C = 22.5$, and those stars would have been undetectable; rather, we find stars as bright as $I_C = 19$—fully 3.5 mags brighter than this. It is difficult to see how such luminous stars could be metal rich; it is attractive to suggest they may be similar to the LMC population.

The number of AGB stars detected in the M31 *HST* image is 1/4 that expected for the observed luminosity and reasonable AGB lifetimes. The young population might relate to a merger event that may account for the double nucleus structure. More likely, since we require detection of AGB stars at both R and I, we have missed most of the very red stars. Artificial star experiments confirm that this result cannot be explained by crowding alone. Furthermore, a red central population has recently been discovered in M33.

### 2.2 A Central Bulge in M33?

As in M31, Mould & Kristian (1986) find a halo population in M33. Again, this population agrees with what is known about globular cluster giants. Imaging in the infrared 1.6 $\mu$m H band, Minniti *et al.* (1993) find a central population of luminous AGB stars in the central 30 $''$ of M33. This population extends to $M_{bol} = -6$. Here is a case where high metallicity simply cannot explain the extended giant branch. The IR-bright population is centrally concentrated.

We have analyzed images of the M33 core obtained by the WFPC team. We find a blue main sequence of OB stars from the disk, and a red population. The red stars are more centrally concentrated than the blue stars, as one would expect. In M33 we see three major stellar populations. First, a disk population that is still forming stars and continues into the center. Second, a halo population that is consistent with the metal poor Galactic globular clusters—a giant branch extended to $M_I = -3.7$. The bulge population, with its extended giant branch and *no recently formed stars* is a third major population. Here in M33 we have evidence for at least 3 distinct stellar populations. The central component formed later than the halo, but appears to have formed quickly and is no longer forming any stars. Perhaps we are seeing the same phenomenon in M31, but at a more subtle level.

## 3.0 The Galactic Bulge

From our Galactic vantage point, study of the bulge is difficult because of obscuration and copious foreground contamination. For $R_0 = 8$kpc, the giant branch extends to $M_{bol} = -4.8$, with some stars brighter than this. The bulge giant branch extends brighter than the Galactic metal rich globular clusters, but this may be due to the evolution of the most metal rich stars.

The main sequence turnoff is equally confusing. Observed clearly with *HST* (cf. Holtzman *et al.* 1993) the turnoff point appears at $I \approx 20$, or at $M_I = +4$.

Were we dealing with an issue less controversial than the age of the bulge, this bright turnoff luminosity would alone be sufficient evidence to prove that the bulge is younger than the clusters.

Unfortunately, stronger evidence is required to convince the vast majority of astronomers that the bulge is younger than the globular clusters. Such evidence may come from the period distribution of the Galactic Bulge Miras. Following the lead of Michael Feast, the South African Astronomical Observatory group has recently concluded a remarkable campaign on the bulge Miras (Whitelock *et al.* 1991; Glass *et al.* 1993). More than half the Miras exceed the 300 day upper limit characteristic of globular clusters. Until recently, it would have been possible to ascribe such long periods to apparent high abundances in the bulge. Recent studies of the K giants (McWilliam & Rich, 1993) find the mean bulge abundance to be solar; a preliminary study on the M giants by Smith (1993) also finds that late bulge M giants appear to have Solar values of Fe-peak elements. While still somewhat controversial, it is clear that we cannot explain the Mira periods by abundance alone, making age the most attractive explanation for their properties.

### 3.1 The Abundance Picture

Trends of element ratios (such as [O/Fe]) as a function of Fe abundance may be one of the best constraints on the formation timescales of stellar systems (Spite, 1993; Barbuy, 1993). The basis for the technique is that elements formed in massive star SNe should be the first to form (such as O and other $\alpha-$process elements. As most Fe-peak elements are almost certainly produced in Type I (WD) SNe, they will appear on the timescale associated with the appearance of the AGB, or $\approx 10^8 - 10^9$yr. Oxygen is the ideal element to use in this exercise (as has been done for the halo/disk transition) because Type II SNe typically produce $\approx 10$ times the Oxygen of Type I SNe. However, night sky contamination by the 6300Å line, along with natural star-to-star variation, make it impractical to use Oxygen for this purpose in bulge giants. Fortunately, there are many lines available for Si, Ti, Ca, and other alpha-capture elements, and Eu II $\lambda\lambda$6645Å (r-process) is readily measurable. If a stellar system forms too rapidly for Type I SNe to contribute to the enrichment, the alpha-capture and r-process elements should remain high over the whole range of [Fe/H], which is not the case for the Milky Way halo/disk transition. In rapidly forming bulges and spheroids, it might be expected that alpha/r elements would remain high over the full range. Evidence that a system forms rapidly does not imply that it is also ancient (compared, say, to the globular clusters). For example, the blue bulge of NGC 5102 and M82 are both recent starbursts yet are also experiencing substantial current enrichment.

McWilliam & Rich (1994) have performed fine abundance analysis on 11 bulge K giants observed at $R = 17,000$. The results are puzzling, and do not support or refute any particular enrichment scenario. Mg and Ti are both enhanced over the full range of [Fe/H], up to [Fe/H]=+0.5, but Ca and Si (also alpha-capture elements) drop to Solar abundance levels at [Fe/H]=−0.5, behaving precisely as the standard disk/halo enrichment pattern. There is evidence (cf. Worthey *et al.* 1993) that elliptical galaxies may have enhanced Mg; this may occur in the bulge, but it remains a mystery that Ca and Si do not behave in lockstep. I refer to this phenomenon as the "decoupling of the alphas".

Eu may be enhanced over the full abundance range, but that is not certain. And the s-process elements (with origin almost certainly in the envelopes of AGB stars) have Solar abundances across the entire range of [Fe/H]. If it is confirmed that s-process elements always have Solar abundance in bulge giants, this would be compelling evidence that the material out of which these stars formed was enriched by a prior generation of AGB stars. This would strongly suggest that the bulge is at least a Gyr younger than the earliest stars which enriched the proto-bulge material.

To summarize, the enhancement patterns of bulge giants is consistent with a later rapid enrichment. The ubiquitous presence of s-process elements suggests that the bulge formed out of material enriched by at least one generation of AGB stars, quite consistent with the ideas of delayed bulge formation.

In order to determine the abundances, it was necessary to also measure accurate effective temperatures for the bulge giants. It has been known (since Frogel *et al.* 1984) that the bulge giant branch locus has a $(J-K)$ similar to that of 47 Tuc, while having a mean metallicity of at least the Solar value. While this could be a symptom of intermediate age, it was felt (Frogel & Whitford, 1987) that this was likely due to some unknown source of blanketing in the infrared bands. McWilliam & Rich determined effective temperatures both using $(V-I)$ colors and using the IR photometry and the infrared flux method (Blackwell & Shallis, 1977). These two independent methods confirm that the bulge giant branch is intrinsically hotter than would be expected for an old population of Solar metallicity. The new careful abundance analysis and temperature determination add further support to the bulge being younger than the globular clusters.

## 4.0 Globular Clusters Younger Than Spheroids?

Since the work of Strom *et al.* (1981) and Forte *et al.* (1981), we accept as an observational fact that globular clusters are bluer and less spatially concentrated than their underlying populations. In a study of 3 Virgo ellipticals, Forte*et al.* concluded that the clusters must have a dynamical and chemical history distinct from the spheroids, in principle being considerably more ancient. Our Galactic bulge is also more concentrated and more metal rich than most of the globular clusters. In fact, nearly all of the mass can be enclosed in a 1 kpc radius, quite a contrast to the halo which extends to 25 kpc. While less extreme, the spheroids of elliptical galaxies are also more concentrated than the clusters. In the case of the

Milky Way, the bulge's rapid rotation, high metallicity and spatial concentration all support a dissipative history. Correlations between abundances and kinematics of the stars (cf. Rich, 1990; Zhao *et al.* 1993) lend further support to that picture. How can the clusters and spheroid light show such striking differences in composition and spatial distribution without an accompanying gap in age?

### 4.1 New Formation Scenarios

How are the luminous parts of galaxies assembled? Our intuitive picture of galaxy formation is almost contrived, and probably neglects important physical processes. Consider that in the Magellanic Clouds and the Milky Way, the extreme halo population comprises about 5% of the luminous mass. The bulge rotates rapidly, and has a vertical scale height of order 400 pc, not mucb greater than the disk (Kent *et al.* 1991). Metal rich stars in tbe bulge have smaller velocity dispersions (Rich, 1990) and rotate more rapidly than stars of lower metallicity. Every part of the picture is consitent with a dissipative formation scenario, in contrast to the halo where correlations between abundances and kinematics are not found. Indeed, the outer halo shows an age dispersion, while the enrichment pattern of the inner halo suggests a possible extended formation period, leaving bot ($\approx 10^7$K) low density gas that might have cooled and dissipated into a proto bulge/disk (Truran & Burkert, 1993). Wyse &Gilmore (1992) also suggest tbat proto-bulge gas might have originated in tbe halo, based on angular momentum considerations.

Many bulges may be triaxial, even bar shaped (including our own). Several groups have advanced scenarios in which bars (perhaps the result of disk instabilities) can thicken vertically due to various dynamical instabilities, thus resembling bulges in appearance. Bars and triaxiality are more easily understood in tbe context of the delayed formation scenario. Perhaps the formation of a central bulge marks the first stage in the disk formation, rather than the first stage in galaxy formation. The gap in age between tbe oldest disk stars and the age of the classic halo globular clusters is best understood in terms of disk formation beginning a few Gyr after the oldest halo population is formed. If the bulge is $\approx$ 10 Gyr old, the age would agree with that of the oldest disk stars.

It is fitting to note at this important meeting in Latin America that astronomers in both Brazil and Argentina have made key contributions to what may possibly be a very significant revolution in the concept of stellar populations and galaxy formation. Notably, the work of Bica and Barbuy in establishing that old globular clusters of high metallicity have *faint* giant branches has been critical in establishing the nature of the M31 bulge population. Forte's pioneering discovery that globular clusters are bluer and less spatially concentrated than the field populations of spheroids remains to be fully appreciated. The picture of delayed spheroid formation may be counter-intuitive, but we should be prepared to accept some rather surprising turns in the journey toward a realistic picture of galaxy formation.

## References

Bica, E., Barbuy, B., Ortolani, S. 1991, ApJ, 382, L15
Blackwell, D.E., and Shallis, M.J. 1977, MNRAS, 180, 177
Blanco, V.M., M.F. McCarthy, S.J., Blanco, B.M. 1984, AJ, 89, 636
Davies, R.L., Frogel, J.A., Terndrup, D.M. 1991 AJ 102 1729
Forte, J.C., Strom, S.E., Strom, K.M. 1981 ApJ 245, L9
Frogel, J.A., Whitford, A.E., Rich, R.M. 1984, AJ, 89, 1536
Glass, I. *et al.* 1993 Preprint.
Holtzmann, J.H., Light, R.M., Baum, W.A. *et al.* 1993 AJ 106, 1826
Kent, S.M. 1989, AJ, 97, 1614
Kent, S.M., Dame, T.M., Fazio, G. 1991, ApJ 378, 496
Luppino, G.A., Tonry, J.L. 1993, ApJ, 410, 81
McWilliam, A., Rich, R.M. 1994 ApJS in press
Minniti, D., Olszewski, E.W., Rieke, M. 1993, ApJ 410, L79
Mould, J., and Kristian, J. 1986, ApJ, 305, 591
Renzini, A. 1993 in Galactic Bulges, H. Dejonghe and H.J. Habing (eds.) (Dordrecht: Kluwer) p. 169
Rich, R.M. 1990 ApJ 362, 604
Rich, R.M., & Mould, J.R. 1991, AJ, 101, 1286
Rich, R.M., Mould, J.R., Graham, J.R. 1993, AJ, 106, 2252
Rich, R.M., *et al.* 1989 ApJ 341, L51
Smith, V. 1994 in preparation
Strom, S.E., Forte, J.C. *et al.* 1981 ApJ 245, 416
Truran, J.W., and Burkert, A. 1993 Physics Reports 227, 235.
Whitelock, P.A., Feast, M.W., Catchpole, R.M. 1991, MNRAS, 248, 276
Worthey, G., 1993 ApJ 409, 530
Worthey, G., Faber, S.M., Gonzalez, J.J. 1992 ApJ 398, 69
Wyse, R.F.G., and Gilmore, G. 1992, AJ, 104, 144
Zhao, H.S., Rich, R.M., Applegate, J.H., Biello, J. 1994 ApJ in press.

**Figure 1** - Color-magnitude diagram of the central 30" of M33, obtained from archival data using the Hubble Space Telescope Planetary Camera. These data, obtained prior to the repair, illustrate the principle sequences in M33 and prove the existence of an intermediate-age bulge. Blue sequence is the young main sequence disk population. Bright red stars (with blue extension at I=17) are Cepheids on their blue loops. The first giant branch tip is found at I=20.7, precisely where Mould and Kristian (1986) find it in the outer halo. However, an additional population (including some stars too red to have V counterparts) extends to I=19.5. This population is more centrally concentrated than the disk, and is probably an intermediate-age bulge population. Thus in M33, one finds 3 main stellar populations: a current star-forming disk, an old globular cluster-like population, and finally, an intermediate age population that has ceased forming stars for at least a few Gyr. At least in this case, one galaxy has formed a late bulge.

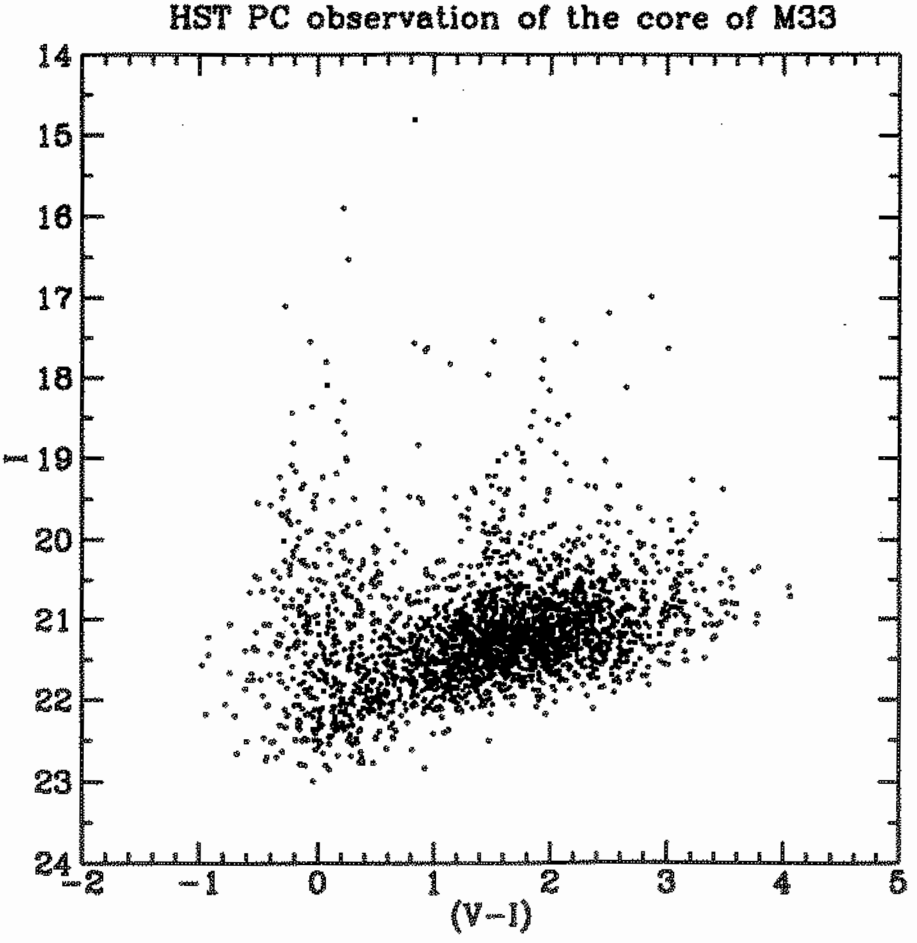

# ELECTRON DENSITIES OF HII REGIONS IN THE MAGELLANIC CLOUDS

Marcus Vinicius Fontana Copetti
MVFC@BRUFSM.BITNET
Departamento de Matemática and NEPAE
Universidade Federal de Santa Maria
97119-900 Santa Maria, RS

ABSTRACT: We present the results of a systematic study on internal variations of electron density $N_e$ in HII regions of the Magellanic Clouds. The density indicator used was the [SII]$\lambda6717/\lambda6731$ ratio. The observations were made on November 1992 with the Cassegrain spectrograph attached to the 1.6 m telescope of the Laboratório Nacional de Astrofísica, Brasópolis, Brazil. We have obtained long-slit spectrophotometry at high signal to noise. All four objects studied show spatial variations of density, the brightest zones being in general associated to higher values of electron density. Three of them, DEM 8b (LMC), DEM 138 and DEM 161 (SMC) present radial gradients, with the density decreasing from the centre. In 30 Doradus the density variation is more irregular, the bright rims being denser than the adjacent zones. We discuss the consequences on the chemical composition studies of electron density values higher than commonly assumed for extragalactic HII regions.

# 1 Introduction

Basically, there are two distinct methods for determining the electron density $N_e$ in HII regions. The first one is based on the relationship between the electron density (and temperature) and the relative intensity of collisionally excited emission lines, which are common for metallic ions (see Aller, 1984, Osterbrock, 1989, and references therein). The best examples are the ratios [OII]$\lambda3729/\lambda3726$ and [SII]$\lambda6717/\lambda6731$ for which the electron temperature plays a secondary role for typical electron densities in HII regions, between $10^2$ and $10^4$ cm$^{-3}$ approximately.

The second class of methods for determining electron density is based on the fact that the electron recombination rate per unit volume is proportional to ${N_e}^2$. Consequently, the emission rate of photons in any recombination line or in the nebular continuum is proportional to ${N_e}^2$. So, the HII region surface brightness S in recombination lines or nebular continuum is a function of the distribution of the electron density (and secondarily, of the temperature) in the nebula. More exactly, S is proportional to the so called **emisson measure** $\int N_e^2 ds$, where ds is an infinitesimal element of distance and the integral is calculated along the line of sight. In order to estimate densities it is necessary to assume some geometry for the nebula, since its dimensions along the line of sight are unknown. Mean electron densities can then be directly obtained from surface brightness of the nebula. These densities are called root mean square (rms) densities and represented by $\langle N_e \rangle_{rms}$. In a more sophisticated analysis, the distribution of electron density in the nebula can be obtained from brightness profiles, solving the corresponding inverse problem.

Osterbrock and Flather (1959) applied both methods for studying the distribution of electron density in M 42, the Orion Nebula, and found a steep radial gradient of density, with $N_e$ decreasing from $1.8 \times 10^4$ cm$^{-3}$ in the centre to $2.6 \times 10^2$ cm$^{-3}$ near the edge. Similar density gradients were found later in many other galactic HII regions (Meaburn, 1969). Osterbrock and Flather (1959) have also found a large difference between the densities obtained from the [OII] or [SII] ratios and those calculated from the surface brightness of the nebula, which are systematically lower than the former ones by orders of magnitude. This discrepancy is removed by assuming an irregular distribution of the matter in the nebula. According to the current model, the ionized gas is concentrated in clouds, filaments or shells, which represent a small portion of the total volume and are embedded in a extremely tenuous medium (vacuum, hypothetically). The electron density measurements based on the ratios of collisionally excited lines correspond to the values of $N_e$ in the clouds or filaments, whereas those obtained from surface brightness are smaller since the amount of ionized gas is overestimated from the geometrical dimensions of the nebula. The fraction of the total volume actually occupied by clumps of ionized gas is named volume **filling factor** $\phi$. Typical values of the filling factor are in the range $0.001 \le \phi \le 0.1$ (Kennicutt, 1984). It is easy to verify that $\langle N_e \rangle_{rms}$ and $N_e$ are related to each other by $\phi = \langle N_e \rangle_{rms}^2 / N_e^2$.

Kennicutt (1984) has derived the radial distribution of $\langle N_e \rangle_{rms}$ for many galactic and extragalactic HII regions from emission measure profiles obtained from H$\alpha$ interference filter photographs or radio continuum maps, assuming spherical symmetry for the nebulae. According to his calculations, most objects present steep gradients of rms electron density. Excepting shell nebulae, the central $\langle N_e \rangle_{rms}$ values are larger than those in the outskirts by two or three orders of magnitude. However, we must take his quantitative results with caution because of the strong symmetry hypothesis.

We have recently conducted a systematic study on the spatial variation of electron density in extragalactic HII regions belonging to M 51, M 101 and NGC 6822 (Castañeda *et al.*, 1992). We have obtained long-slit spectrophotometry of the [SII] doublet with the 2.5 m telescope at the Roque de Los Muchachos, La Palma, Canary Island. We have found evidence of internal variation of density in some of the studied objects. The best example is NGC 5461 in M 101, which shows a clear density gradient. In general, the brightest zones are associated with maximum density values, which indicates the existence of density gradients with $N_e$ decreasing from the centre. Although the relative success of the project, a more quantitative study of the internal density variation in these objects is difficult to execute due to the low spatial resolution.

The HII regions of the Magellanic Clouds are fundamental objects for density structure studies. They have angular diameters from few tenths to tens of arcminutes, so integrated observations are easy to obtain. On the other hand, the proximity of these galaxies allow us to make observations with high spatial resolution ( $1'' \approx 0.3$pc ) and to identify the ionizing stellar clusters, which is not the case for most extragalactic HII regions. The weak interstellar extinction towards the Magellanic Clouds makes possible to study low surface brightness HII regions, which cannot be carried out by optical observations even for galactic nebulae, excepting those in the solar vicinity. These facts have driven us to carry out a systematic study of electron density in HII regions of the Magellanic Clouds.

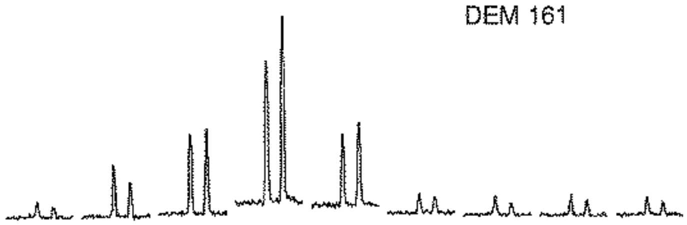

Figure 1. Variation of the doublet [SII]$\lambda\lambda$6717,6731 across the slit.

## 2 Observations

We have obtained long-slit spectrophotometry of the doublet [SII]$\lambda\lambda$6717,6731 at high signal to noise with the Cassegrain spectrograph of the 1.6 m telescope at the Laboratório Nacional de Astrofísica, Brasópolis, MG, Brazil. The observations were made on November 1992. The detector was a 1152×1152 pxl$^2$ CCD. We used a 1200 grooves mm$^{-1}$ grating resulting in a reciprocal dispersion of 0.7525 Å pxl$^{-1}$. The spatial scale was 0.903" pxl$^{-1}$. The data reduction was performed following the standard procedure using the IRAF package. The 2D spectra were corrected for bias, flat-field and had cosmic rays removed iteratively. A series of 80 1D spectra was extracted from each frame binning every four rows together resulting in a spatial scale of 3.6" pxl$^{-1}$. The wavelength calibration was made by comparison with a copper-neon-argon lamp measured before and after each exposition. The final spectra range from 6435 to 6810 Å, including the emission lines H$\alpha$, [NII]$\lambda\lambda$6548,6584 and HeI$\lambda$6671 besides the [SII] doublet.

Four HII regions were observed: DEM 138 e DEM 161 of the Small Magellanic Cloud and 30 Doradus (at two position angles) and DEM 8b of the Large Magellanic Cloud. On average the objects were integrated for 1h in three different expositions. The line fluxes were obtained by direct integration after extracting the continuum. The reddening correction was negligible since the [SII] lines are separated by only 14.4 Å.

# 3 Results

Electron densities were obtained by numerical solution of the five-level [SII] atom (see Castañeda *et al.*, 1992). In figure 1 we illustrate the variation of the [SII] doublet along the slit for DEM 161. Figures 2 to 6 show the relationship between the ratio R = [SII]$\lambda$6717/$\lambda$6731, the electron density N$_e$ and the H$\alpha$ flux (in arbitrary units) with the position along the slit.

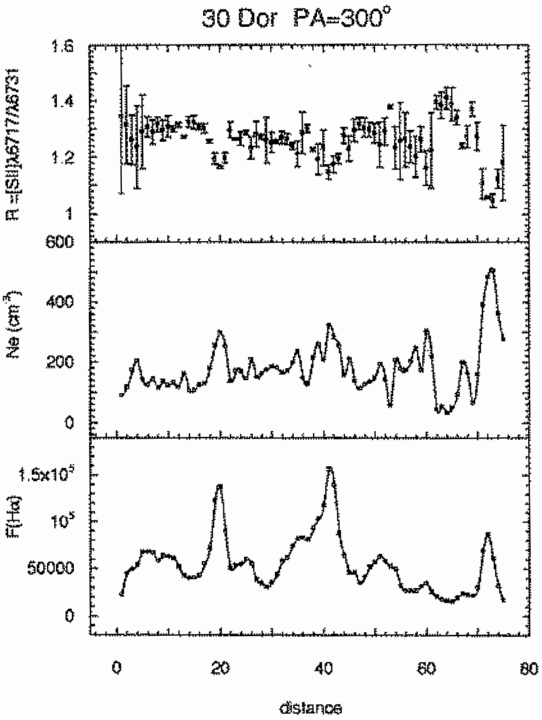

Figure 2

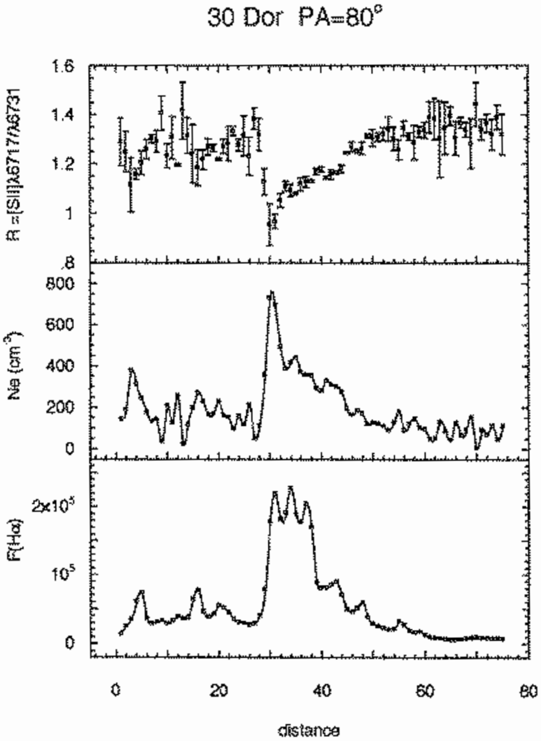

Figure 3

All four objects studied show clear density variations, the brightest zones being in general denser. Three of them, DEM 8b (LMC), DEM 138 and DEM 161 (SMC) present radial gradients, with the density decreasing from the centre. In 30 Doradus the density variation is more irregular, the bright rims being denser than the adjacent zones, in agreement with the results of White (1981) obtained from the [OII]$\lambda\lambda$3726,3729 doublet.

## 4 Discussion

The mesured values of electron density correspond to weighted means along the line of sight. The internal density structure and specially the central density values are difficult to estimate with accuracy due to two facts. First, because we have to solve a mathematical inverse problem, which usually accepts multiple solutions. Besides, we have to assume an arbitrary geometry for the nebula. The second difficulty and probably the most fundamental one is due to the fact that both [SII] and [OII] doublets, the most popular density indicators, correspond to low excitation ions, which according to the stratified structure of the HII regions are more abundant in the external parts of the nebula.

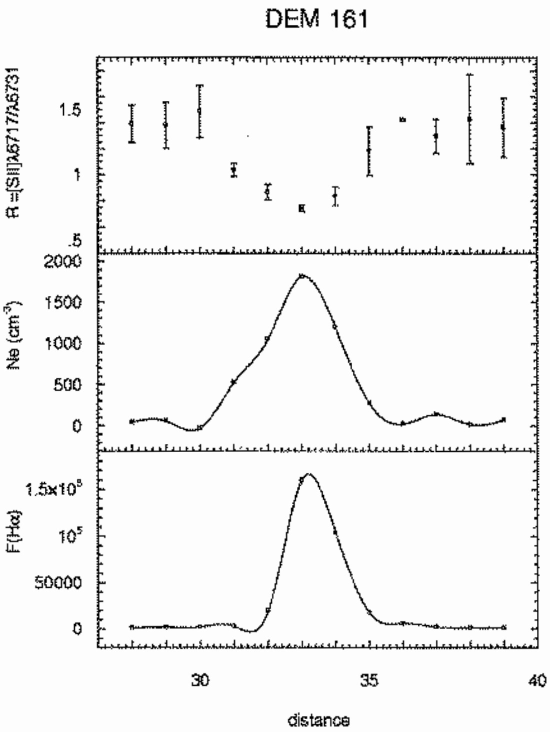

Figure 4

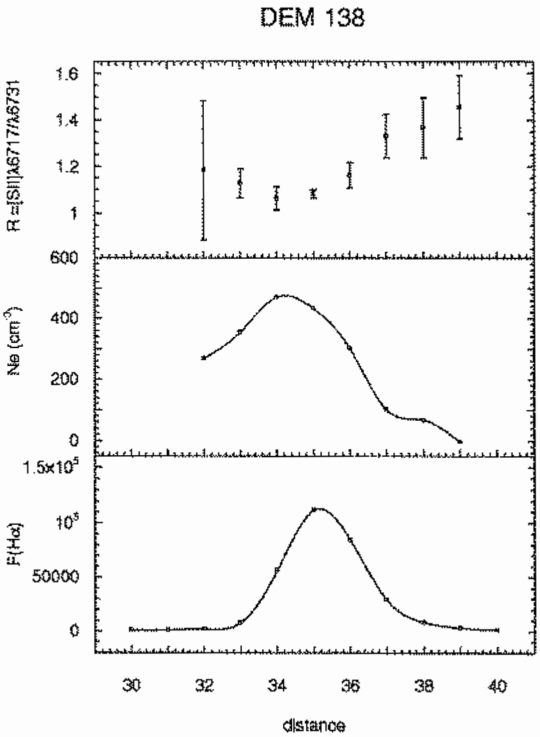

Figure 5

The most reliable way of determining central density values would be by adopting a density indicator associated with a high excitation ion. The problem is that, at least in the optical range, the doublets that could be used are very faint. Some crude estimation of the central density can be obtained from comparison of the Hα and R [SII] profiles with *ad hoc* models of the density distribution (see Castañeda *et al.*, 1992). For example, if the density variation can be described by a Gaussian function with the density falling to 50% of the central value at positions far from the center by half of the radius of the nebula, then the central density would be $\sqrt{2}$ times the measured peak value. However, this kind of modelling must be taken with caution, since we could obtain completely different results assuming other hypothese for the density distribution. In summary, little is known about the central values of density in HII regions with density gradients, besides the obvious fact that they are higher than the measured values.

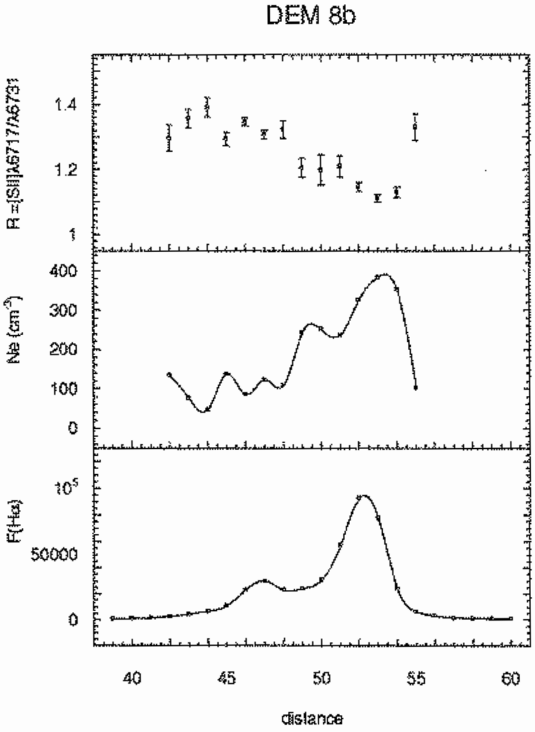

Figure 6

The HII regions have been intensively used for chemical abundance determination of many galactic and extragalactic systems. They are fundamental for the estimation of primordial chemical abundance. Usually, a constant density is assumed. Specially for giant extragalactic HII regions, low values of density ($N_e \leq$ 200-300 $cm^{-3}$), in agreement to the average values obtained for these objects, are adopted. So, many collisional excitation corrections are neglected. The present work indicates that density gradients with higher values of electron density in central parts are likely to occur in many HII regions. Robin (1989) has shown that empirical methods for determining the physical properties of the HII regions based on integrated properties may be subject to significant biases due to internal density variations.

*Acknowledgements.*

This work was partially supported by the Brazilian Institutions CNPq and FAPERGS. Part of the data reduction was done by Márcio J. Rossi and Sérgio S. Kucera. The present observational programme has been carried out in colaboration with Alex A. Schmidt, Héctor O. Castañeda and Bernard E.J. Pagel.

## REFERENCES

Aller, L.H., 1984, Physics of Thermal Gaseous Nebulae, Reidel, Dordrecht.

Castañeda, H.O., Vilchez, J.M., Copetti, M.V.F., 1990b. *Astrophys. J.*, **365**, 164.

Evans, I.N., Dopita, M.A., 1985. *Astrophys. J. Suppl.*, **58**, 125.

Kennicutt, R.C., 1984. *Astrophys. J.*, **287**, 116.

Meaburn, J., 1969. *Astrophys. Space Sci.*, **3**, 600.

Osterbrock, D.E., 1989. Astrophysics of Gaseous Nebulae and Active Galactic Nuclei, University Science Books, Mill Valley, CA.

Rubin, R.H., 1989, *Astrophys. J. Suppl.*, **69**, 897.

Stasińska, G., 1980, *Astron. Astrophys.*, **84**, 320.

White, N.J., 1981, *Astron. Astrophys. Suppl.*, **78**, 443.

# ASTRONOMY WITH THE SPACE SHUTTLE: THE ASTRO-1 OBSERVATORY

Antonio Mário Magalhães
Departamento de Astronomia, Instituto Astronômico e Geofísico,
Universidade de São Paulo, Caixa Postal 9638, São Paulo - SP 01065-970, Brazil
*e-mail: magalhaes@vax.iagusp.usp.br*

**Abstract**

The WUPPE experiment has collected the first spectropolarimetric data ever in the Ultraviolet. Polarimetry is an important tool for several astrophysical situations and a brief overview of these is given. A description of imaging polarimetry techniques with CCD detectors under development is also presented. Some of the WUPPE results are then described, in particular those that deal with circumstellar envelopes, interstellar dust and active galactic nuclei.

## I. Introduction

Astronomical Polarimetry is a technique which has been increasingly and successfully employed throughout the last few years. Basically, it uses the fact that a beam of light is completely described by four quantities, called Stokes parameters, the Intensity (I) being the most commonly measured one in Astrophysics. The other three parameters describe the state of polarization of the beam: two of them, Q and U, for the linear polarization and V for circular polarization. They bring encoded information about physical processes that originated and modified the beam of radiation under study.

### I.1. Description of Polarized Light

Four parameters are required to describe a light beam. The Stokes parameters are the ones more frequently used; they are often called the Stokes vector (please see Clarke and Grainger 1971, for a formal, full definition in terms of the beam electric vector components).

The Stokes parameters are usually represented by [I, Q, U, V] where:

$I$ = Intensity $\geq [Q^2 + U^2 + V^2]^{1/2}$
$Q = P \cos 2\theta$ [P = Degree of Linear Polarization,
$U = P \sin 2\theta$ $\theta$ = Position Angle of the Linear Polarization]
$V$ = Circular Polarization

A few particular situations will help to illustrate these parameters:

- For unpolarized light, Q=U=V=0, and the only non-zero quantity is the intensity I.
- When the beam is completely (elliptically, in this case) polarized, $I=[Q^2+U^2+V^2]^{1/2}$.
- For a totally linearly polarized beam, V=0 and $I = [Q^2 + U^2]^{1/2}$. Note that Q represents the linear polarization component with position angle 0° and U the one at 45°.
- In general, for a partially polarized beam, $I \geq [Q^2 + U^2 + V^2]^{1/2}$, with $P = [Q^2 + U^2]^{1/2}/I$ and V/I the degrees of linear and circular polarization, respectively. They are expressed between 0 and 1 (or, more commonly, 0 and 100%). Circular polarization degree carries a sign, while P is a positive definite quantity. The amount $\{I - [Q^2 + U^2 + V^2]^{1/2}\}$ is the intensity of the unpolarized fraction of the beam.

In this talk, we will discuss **linear** polarization data only.

### I.2. Physical Processes that Polarize Light

Several processes may originate polarization in the light received from astronomical sources. Among them we may cite, together with examples of occurrence (Serkowski 1974):

- reflection by solid surfaces: Moon, planets, asteroids.

- scattering by small solid particles (Mie scattering): zodiacal light, some planetary atmospheres, interstellar polarization, luminous late type variables, reflection nebulae.

- molecular (Rayleigh) scattering: planetary atmospheres, luminous late-type variables.

- electron (Thomson) scattering: early-type star envelopes.

- resonant scattering of bound electrons (Hanle effect): chromospheric and coronal emission lines; possibly, luminous late-type variable atmospheres.

- cyclotron radiation: AM Her binaries.

- synchrotron radiation: Crab nebulae, quasars.

- Zeeman effect: sunspots, magnetic stars.

We should also mention that some of the processes above may produce preferentially one kind of polarization (linear or circular) but often both. For instance, interstellar grains produce mainly linear polarization, the resulting circular polarization being usually two orders of magnitude smaller. Yet Rayleigh scattering, as it does not involve a phase shift of the scattered wave, does not originate circular polarization at all. Cyclotron radiation by non-relativistic electrons, such as observed in AM Herculis binaries, causes linear and circular polarization of comparable magnitude, although the circular component usually prevails.

In addition, more than a single process is often operative in a given astrophysical situation. For instance, interstellar polarization usually affects to a varying degree most of observations in the optical regime. In addition, the combination of distinct causes may show up in data of the same object, as is the case of the envelopes of late-type variables and symbiotic stars.

In summary, by neglecting the observation of possible systematic oscillations in the radiation field of the collected radiation, that is, its polarization, we would be literally throwing away information. Polarimetric observations allow us to better constrain the models built to explain observed phenomena. Moreover, certain types of physical information (magnetic fields, asymmetries, etc.) may often be obtained more clearly only by studying their signatures encoded in the form of Stokes parameters.

## I.3. Analysis of Polarized Light - Imaging Polarimetry

The basic techniques for determining the polarization state of a beam under study are described elsewhere (eg., Serkowski 1974; Magalhães 1989). One of them includes the use of a retarder plate, followed by an analyzer, both placed before the detector (eg., a photomultiplier or CCD). In order to measure linear polarization, we employ a half-wave retarder, while a quarter-wave plate is used to measure circular polarization. The latter plate can actually measure linear and circular simultaneously, albeit with slightly less efficiency for linear than the half-wave plate.

Basically, the intensity of the light beam is measured as a function of the angular position of the retarder. For instance, a fixed half-wave retarder has the property of rotating the incoming polarization plane at an angle $-\psi$, say, to its optical axis to a direction $+\psi$ with respect to the same axis. We then see that, at every $90^o$ of physical rotation of the waveplate, optical equivalent positions are obtained.

Let's suppose now that an analyzer, such as a Polaroid, is placed after the half-wave plate. As the retarder rotates, the intensity exiting the Polaroid will suffer a sinuosoidal modulation, whose amplitude is proportional to the incoming polarization we want to measure.

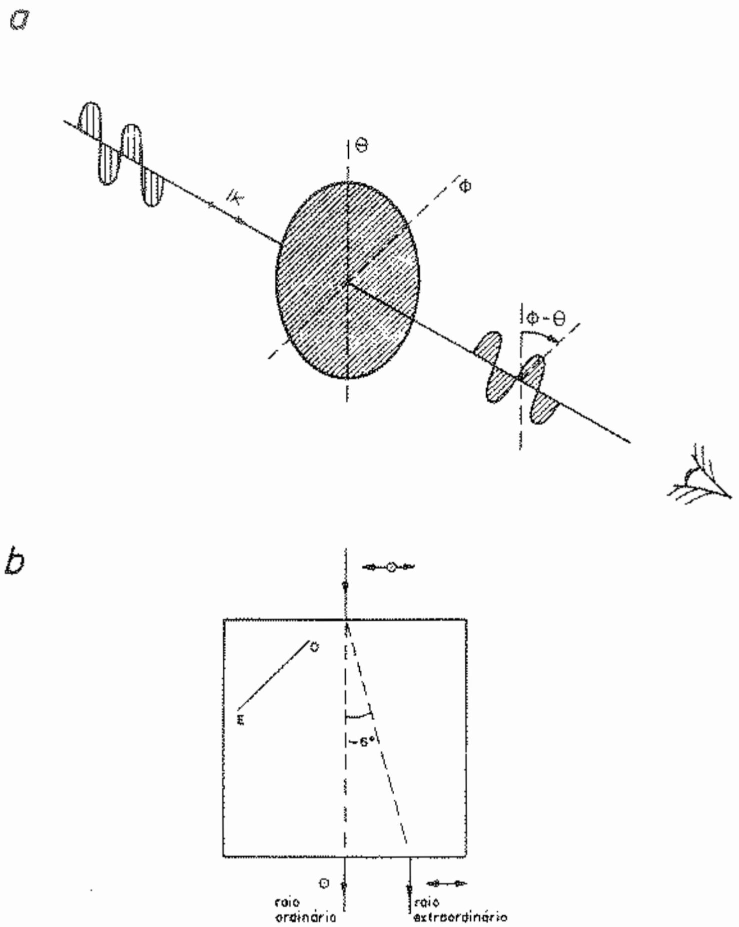
a
Θ
Φ
k
Φ-Θ
b
o
e
~6°
o
raio
ordinário
raio
extraordinário

Figure 1. Two analyzers. a) a Polaroid sheet and the outcoming polarization plane. b) a calcite block. From Magalhães (1989).

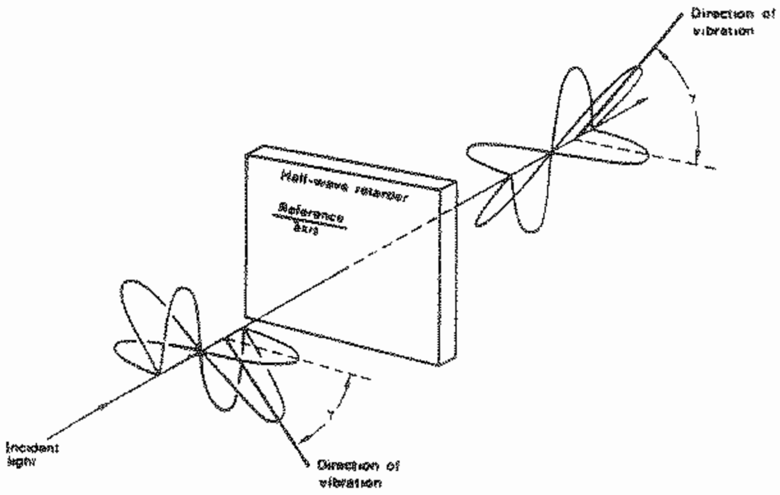
Direction of
vibration
γ
Half-wave retarder
Reference
axis
γ
Incident
light
Direction of
vibration

Figure 2. Action of a half-wave retarder on incoming linearly polarized light. Adapted from Clarke and Grainger (1971).

Another type of analyzer we may want to use is one made of birrefringent material, such as calcite. Instead of extinguishing one of the beams, as the Polaroid does, a calcite prism splits the incoming beam in two, an ordinary (undeflected) beam and an extraordinary beam, orthogonally polarized. Figures 1 and 2 summarize the actions just described of the analyzers and retarders on polarized light. Specifically, the intensity emerging from a half-wave/analizer combination may be described as

$$I'(\psi) = \tfrac{1}{2} \cdot I \cdot [\, 1 \pm Q \cos(4\psi) \pm U \sin(4\psi)], \qquad (1)$$

where I' and I are the emerging and incoming intensities, respectively, and $\psi$ the angle of the waveplate axis in the equatorial system (North as zero reference, increasing through East). It was also assumed that the analyzer position angle was 0° in the same frame. If Q and U are the Stokes parameters of the incoming beam, they are related to the familiar degree of polarization P and position angle $\theta$ by:

$$Q = P \cdot \cos(2\theta) \qquad \text{e} \qquad U = P \cdot \sin(2\theta). \qquad (2)$$

There is an important variation of the simple calcite prism called Savart plate. It is made of two identical prisms, cemented with their optical axis at 90° from each other. When we use a simple prism, the extraordinary, off-axis ray suffers from astigmatism, in addition to color dispersion. In the Savart plate, the ordinary and extraordinary beams have their roles switched going from the first to the second individual plate. In this manner, most of these effects cancel. More importantly, the resulting images form in the same plane, which is important for a panoramic detector such as the CCD.

Very recently, we have started to use a Savart plate in our projects in imaging polarimetry. The particular prism we use gives a 1mm separation between the ordinary and extraordinary images. For the retarder, we use a 50mm circular achromatic half-wave plate. A polarimetric measurement consists then of at least 4 frames, with the retarder at positions 0°, 22.5°, 45° and 67.5°. Other retarder positions offer optically equivalent positions and can also be used. For a given object of interest in the frames, its magnitudes in each frame are obtained using routines in IRAF. The Stokes parameters are then obtained from such magnitudes by a least squares solution using equation (1) above.

We have been employing such an arrangement successfully with the CCD cameras at the Cerro Tololo Interamerican Observatory, Chile. At the Brazilian LNA observatory site, a specially built module will be used in place of the traditional filter drawer, while the IAG-USP CCD camera will also have built-in imaging polarimetry capabilities. With the 1.60m, four images of 15min integration each should provide a polarimetric precision of about 0.1% for a 17 mag stellar object.

Figure 3 shows an image obtained with the [retarder+calcite] arrangement. Note the double images of every object in the field caused by the calcite block; the picture gray scale was chosen so as to show only the brighter objects. The star of interest is a hot supergiant located in a small cluster in the LMC. In the picture detail, the object is below

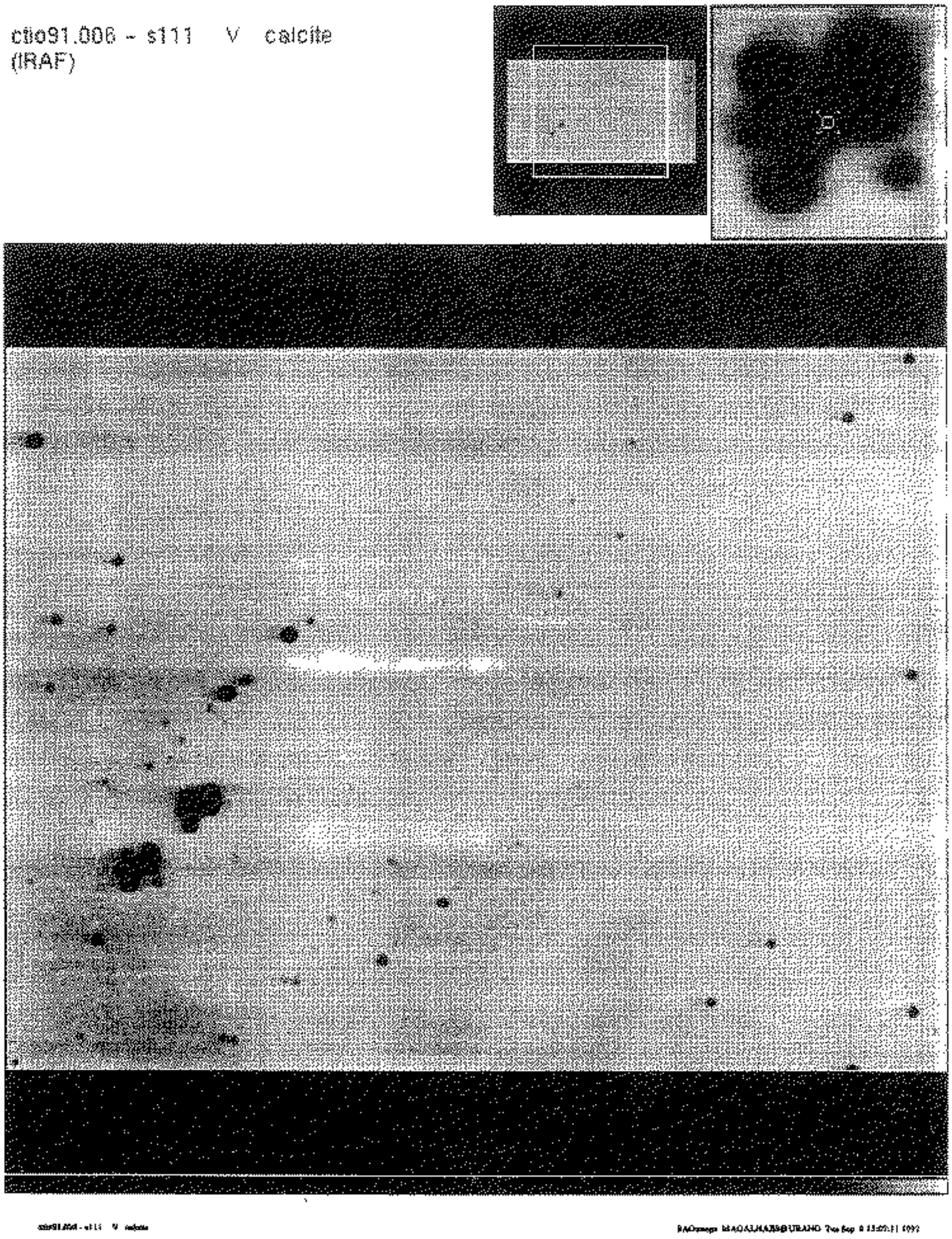

Figure 3. Image taken with the CTIO CCD camera equipped with a Tektronix 1024x1024 chip. The camera was modified for imaging polarimetry as described in the text: the picture was taken through a half-wave retarder and a calcite block. The calcite produces two images separated by 1mm on the chip, which equals 18" at the 1.5m telescope at f/7.5. Data taken by the author.

and left of center. The cluster is contained in just ≈10"; thus, a more traditional observation using a photoelectric photometer with a diaphragm to isolate the star of interest would clearly have been extremely difficult.

This observing technique has revealed itself as extremely accurate for imaging polarimetry. As two images of each object in the field are obtained, the technique is less affected by the seeing, atmospheric transparency and sky fluctuactions. Actually, the precision rivals or surpasses those with the traditional photoelectric techniques (for an example of the latter, see Magalhães et al. 1984).

## II. The Astro-1 Observatory

The Astro-1 observatory consisted of 4 telescopes that flew on board the Space Shuttle Columbia. The mission lasted from December 2 through 9, 1990. After lift-off, the Shuttle orbit was at an altitude of about 300km, with an inclination of 28° with the terrestrial equator. Mission control was performed from Johnson Space Flight Center, Houston, TX, while the experiments and data themselves were received and monitored at Marshall Space Flight Center, Huntsville, AL, where the science teams remained throughout the flight.

The three, co-pointing UV telescopes were mounted on a single, movable platform. They were:

- **Hopkins Ultraviolet Telescope (HUT)**: Spectroscopy from 850Å to 1850Å
- **Ultraviolet Imaging Telescope (UIT)**, NASA/Goddard: Imaging from 1200Å to 3200Å
- **Wisconsin Ultraviolet Photo Polarimeter Experiment (WUPPE)**: Spectropolarimetry from 1400Å to 3200Å .

An X-ray telescope was also on board and mounted on a separate, two-axis platform:

- **Broad Band X-Ray Telescope (BBXRT)**, NASA/Goddard: Spectroscopy from 0.3keV to 12keV.

Astro will fly again as Astro-2 at the end of 1994, this time with the UV experiments only.

# III. The WUPPE Experiment

WUPPE was the first telescope ever to perform UV spectropolarimetry. Until then, this technique had been restricted to the optical region.

WUPPE was conceived and built at the Space Astronomy Laboratory, University of Wisconsin-Madison. The several members of the team were:

**Principal Investigator:** Art Code

**Co-Principal Investigator:** Ken Nordsieck

**Co-Investigator:** Chris Anderson

**Project Scientists:** Karen Bjorkman, Geoff Clayton, Antonio Mário Magalhães, Marilyn Meade, Regina Schulte-Ladbeck, MaryJane Taylor and Barbara Whitney.

**Project Team:** Don Michalski (Project Manager), Cathleen Accettura, Allisane Apple, Andrew Cheng, Samuel Gabelt, Thomas Jones, John Lemke, Mark Nook, Richard Pfeiffer, Laurie Salzman, Helena Renz, Kathy Stittleburg, Neal Wolfe, Michael Wolff.

WUPPE has the following characteristics:

- Telescope: Cassegrain, 50cm dia., f/10
- Field of View: 3.3 x 4.4 arc-minute$^2$
- Grating spectrograph, Monk-Gilleson mount, with polarimetric module: three waveplate pairs, followed by a Wollaston prism.
- Intensified, two-channel Reticon detector: an array for the ordinary spectrum and the other for the extraordinary spectrum.
- Spectral resolution: about 10Å
- Spectral coverage: 1400Å to 3200Å

# IV. Some of WUPPE Results

## IV.1. Disks around hot stars

Several Be stars were among WUPPE targets. Be stars are objects near the Main Sequence in rapid rotation and with optical emission lines. They are highly

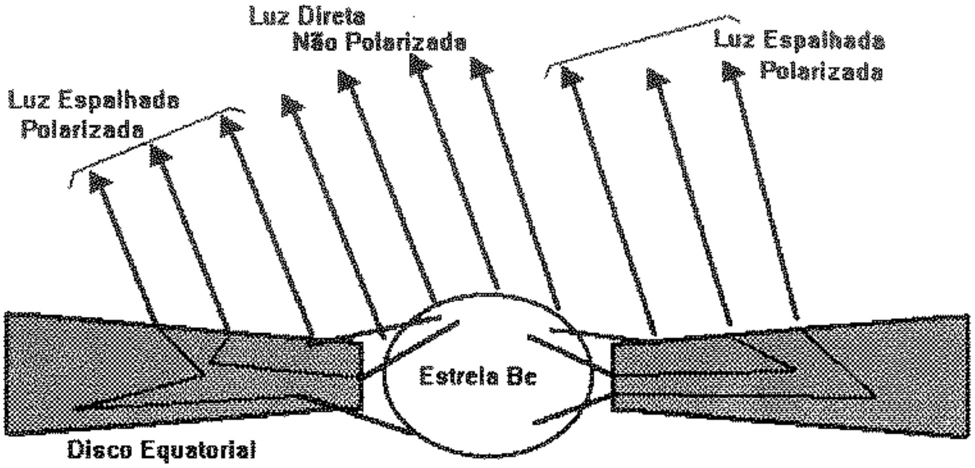

Figure 4. Illustration of a disk around a Be star, giving rise to an observed polarization. The Observer is located towards the arrows. Adapted from Nordsieck (1991).

variable and show distinct properties in distinct spectral regimes: UV lines from a stellar wind, optical shell lines from a dense envelope and an IR excess due to an ionized circumstellar envelope.

Optical polarization data show that Be stars are significatively polarized, at the 1%-2% level. In combination with the IR excess, shell lines and rapid rotation, this fact suggests a disk-shaped circumstellar envelope around them. Figure 4 illustrates the concept: to the direct, unpolarized stellar light, scattered (and hence polarized) light from the disk is added. Since the envelope is asymmetric, there is a net polarization observed at the telescope, where the stellar disk is of course unresolved. The degree of linear polarization is of the order of the fraction of observed light which is scattered off the disk.

Typical models for the wavelength dependence of the polarization of Be stars assume that the polarizations results from such electron scattering, independent of frequency $\upsilon$ but modified (i.e., decreased in this case) by the Hydrogen opacity (proportional to $\upsilon^{-3}$ between series discontinuities) and dilution by unpolarized thermal emission from the disk itself. In this way, the models necessarily predicted a rise in the polarization towards the UV, after the Balmer discontinuity.

Figure 5 shows the WUPPE data for the Be star $\zeta$ Tau (Bjorkman et al. 1991), a star for which the interstellar polarization component is negligible. The figure combines UV and optical data taken with Pine Bluff observatory spectropolarimeter, an equipment

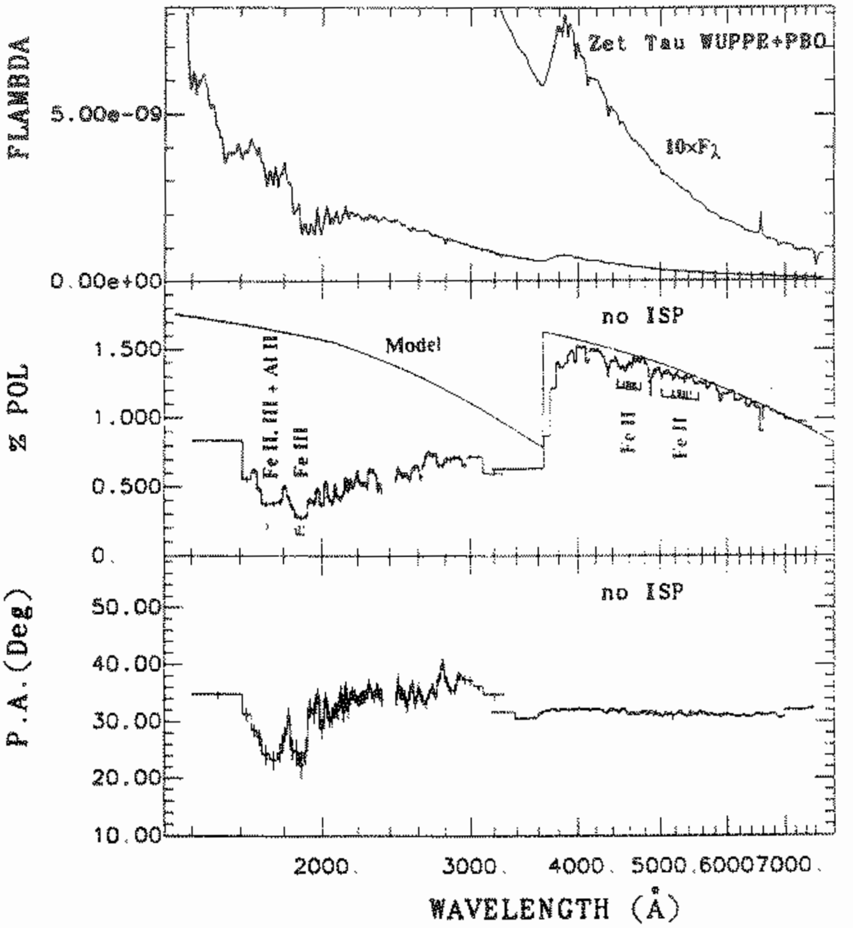

Figure 5. Combined WUPPE and ground based Pine Bluff Observatory (PBO) data for $\zeta$ Tau, showing Flux ($F_\lambda$, erg cm$^{-2}$ s$^{-1}$ Å$^{-1}$), % polarization (%P) and position angle (P.A.) vs. wavelength (Å). The %P and P.A. data are binned to a constant error of 0.02% for WUPPE data and 0.01% for PBO data (shown by error bars). The interstellar polarization (ISP) is negligible, so these data represent the intrinsic polarization of the star. The gap near 2400Å is due to a flaw in one of the detector arrays. Positions of Fe II and Fe III lines are marked with vertical ticks in the second panel (%P). The solid line overplotted on the %P data is a model from Cassinelli et al. (1987) and illustrates predicted wavelength dependence from typical polarization models. From Bjorkman et al. (1991).

similar to WUPPE but for wavelengths longer than 3500Å. Looking at the middle panel of figure 5, we see that the model chosen to approximate conditions in the envelope of ζ Tau contrasts greatly with the UV observations, that show a polarization lower than predicted. The data show that the metal line opacity, eg. around 1700Å and 1900Å (Fe III, Fe II and Al III) has to be taken into account for disk models to explain the UV polarization. Looking closely at the optical data, we note that some of these elements' lines also play a role in the visual. Further observational and theoretical details, such as the possibility of obtaining information about the locations of H and Fe absorption in the disk, are discussed by Bjorkman et al. (1991, 1993).

### IV.2. Interstellar Polarization in the UV: Nature of the Interstellar Grains

The extinction by interstellar dust in the optical and IR domains is relatively well behaved and characterized mainly by one parameter, $R_V$, the ratio of total ($A_V$) to selective ($E_{B-V}$) extinctions; $R_V$ is typically 3.1 for the diffuse interstellar medium in the Galaxy. In the UV, the extinction curve shows large variations from sightline to sightline, and several parameters are needed to characterize its spectral dependence between 1200Å and 3200Å.

The interstellar polarization in the optical and IR is similarly basically described by a single parameter, $\lambda_{max}$, the wavelength of maximum polarization. Until WUPPE, however, the wavelength dependence of the interstellar polarization in the UV was unknown. In particular, whether the semi-empirical Serkowski relation (Serkowski et al. 1975; Codina-Landaberry and Magalhães 1976) would also hold in the UV and how the polarization would vary across the famous 2175Å bump were questions that needed an answer. Interstellar polarization is normally credited to non-spherical grains aligned hy the Galactic magnetic field through a mechanism called paramagnetic relaxation, modified by suprathermal rotation and/or superparamagnetic damping. As the nature of the interstellar grains is uncertain, details of the alignment mechanism are obscure as well.

WUPPE performed the first observations of interstellar polarization in the UV. Figure 6 (Clayton et al. 1992) shows the spectra in the line of sight to six stars reddened by interstellar dust. Distinct forms and strengths of the increased extinction at ≈2175Å may be noted. Figure 7 (Clayton et al. 1992) shows the polarization spectra towards the same stars. The objects HD37903, HD62542 e HD99264 show a wavelength dependence that follows an extrapolation of the Serkowski law reasonably. HD25443 and α Cam show an 'excess' of polarization as compared to the Serkowski law, while HD197770 shows a polarization excess that follows the 2175Å bump closely. This polarization 'peak' may be fitted by small aligned graphite disks, with sizes around 100Å (Clayton et al. 1992); prolate grains, on the other hand, would also cause a change in polarization across the bump but with an orthogonal position angle, resulting in a decrease in polarization across the feature, which is not observed.

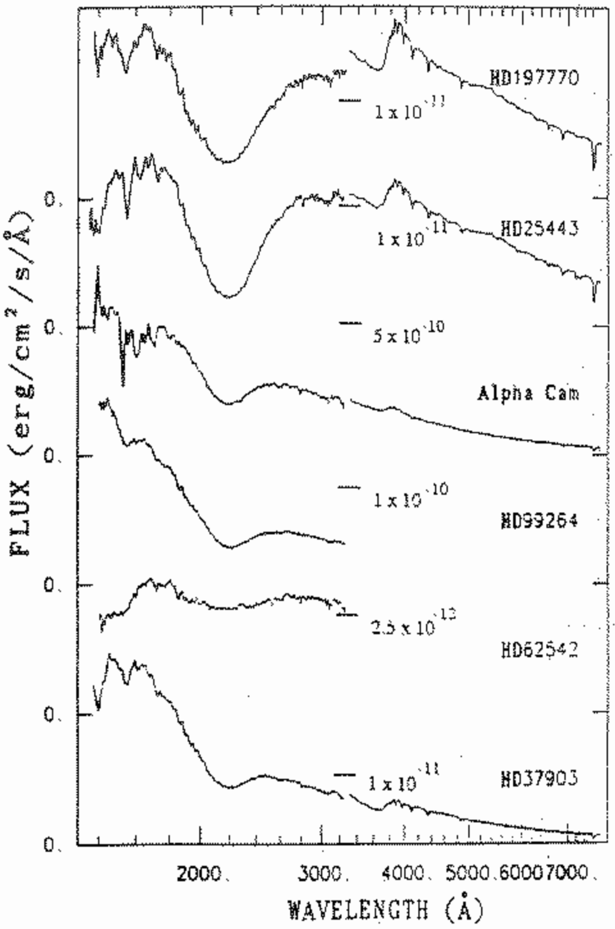

Figure 6. The flux spectra of the six stars discussed in the text. WUPPE UV data are combined with PBO ground based data. WUPPE data are normalized to the ANS fluxes and those from PBO to the V flux. The zero points on the flux scale have been displaced vertically and are indicated on the left. At the center of the wavelength scale, a tick mark and a numerical value indicate a flux value (erg cm$^{-2}$ s$^{-1}$ Å$^{-1}$) for each spectrum. From Clayton et al. (1992).

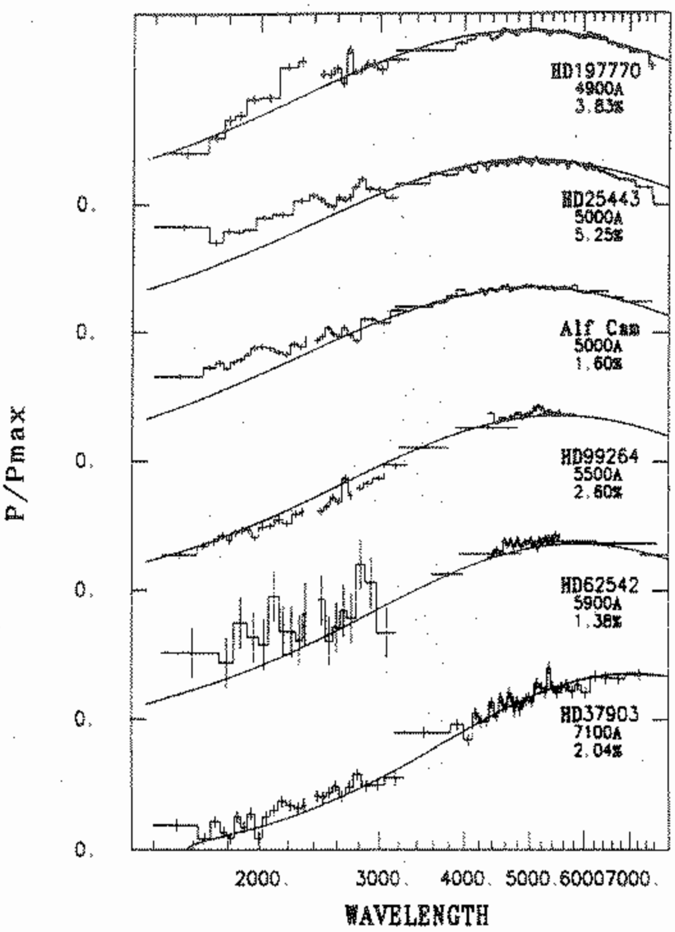

Figure 7. The polarization spectra, normalized to Pmax - maximum of polarization, of the stars discussed in the text. The stars are arranged in order of increasing λmax - wavelength of maximum polarization. The solid line in each spectra is the Serkowski fit. The gap in the data at around 2400Å is due to a defect in the image intensifier affecting one array. From Clayton et al. (1992).

How to align grains such as graphite platelets is not clear however. On the other hand, the observed differences along the several lines of sight are probably the result of differences in the environment in each direction and which affect the size and alignment of the grains (Clayton et al. 1992).

## IV. 3. Structure of Circumstellar Envelopes

Stars in several stages of evolution may have a circumstellar envelope, such as the Be stars we discussed. Another example, this time of evolved objects, are the B[e] stars, hot supergiants that show simultaneously low excitation absorption lines, such as Fe II and [Fe II] in the optical, and high excitation ones, such as Si IV and C IV in the UV. Observations of the optical polarization of B[e] stars in the Magellanic Clouds (Magalhães 1992) effectively show that they present non-spherically symmetric envelopes. Such data are consistent with the picture of a dense, slow equatorial disk and a fast, hot polar wind put forward by Zickgraf (1990) and collaborators.

Interestingly, the evolutionary stage of some *Galactic* B[e] stars is still a topic of debate. In fact, distances and luminosities for the Galactic objects are well known only for some of them. Suggestions from pre-Main Sequence objects to evolved, post-AGB stars have been put forward. HD45677 is one such B[e] star that, in contrast to the well defined class in the Clouds, is highly variable. Like the ones in the Clouds however, it has an IR excess ascribed to circumstellar dust.

The observations of HD45677 obtained by WUPPE are in Figure 8 (Schulte-Ladbeck et al. 1993). The rotation of the position angle with wavelength is clear, indicative of at least two distinct components producing the observed polarization. In order to correctly interpret the observations, they need to be corrected by the interstellar polarization between us and the star. When that is done (Figure 9, Schulte-Ladbeck et al. 1993), the position angle of the intrinsic polarization flips by 90° at around 3000Å. This result may be interpreted as HD45677 possessing a bipolar nebula: the optical polarization comes mainly from the denser parts of the circumstellar disk, while in the UV, the polarization comes mainly from the less dense polar regions, which are optically thinner at those wavelengths. This model is illustrated in Figure 10 (Schulte-Ladbeck et al. 1993). Recent observations (Grady et al. 1993) with the IUE satellite show that material is being accreted by the star; all these data concur to suggest that HD45677 is probably a Herbig Ae/Be star that may be forming a proto-planetary system (Grady et al. 1993).

## IV.4. UV Polarization of Seyfert Galaxy Nuclei: NGC1068 and AGN models

The basic observational distinction between Seyfert galaxies of Types 1 and 2 is that the former have very broad components (≈3000km/s) in their permitted lines besides the narrow components both in forbidden and permitted lines common to both types. The

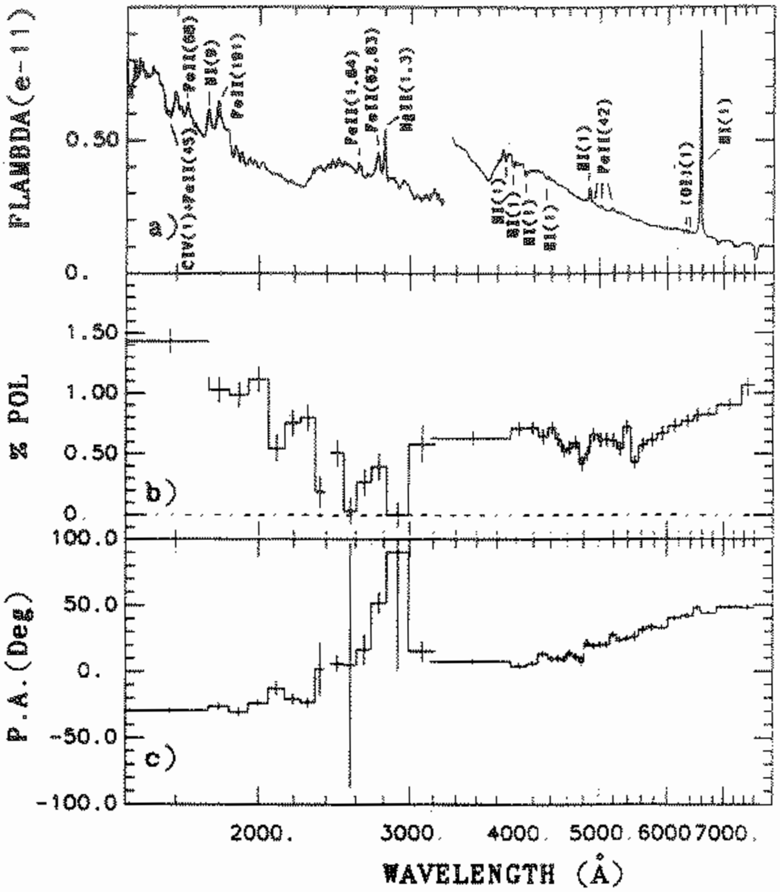

Figure 8. Combined WUPPE and PBO data for HD45677. The flux units are erg cm$^{-2}$ s$^{-1}$ Å$^{-1}$(a). The other panels are % Polarization (b) and Position Angle (c). The offset between optical and UV fluxes is due to pointing problems. The polarization was binned to constant errors, 0.1% for the UV and 0.06% for the optical. The gap around 2400Å is due to a detector problem. From Schulte-Ladbeck et al. (1993).

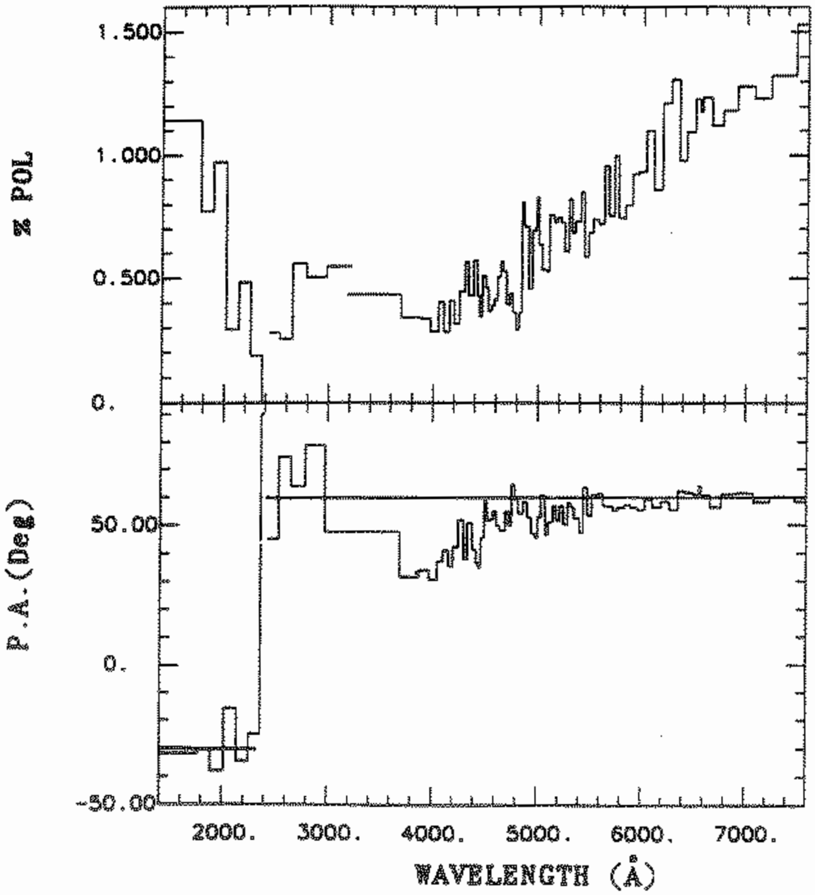

Figure 9. Polarization data from Fig. 8 but corrected for interstellar polarization. The binning is the same as Fig. 8. The horizontal lines show the 90° difference in position angle on each side of the polarization reversal. From Schulte-Ladbeck et al. (1993).

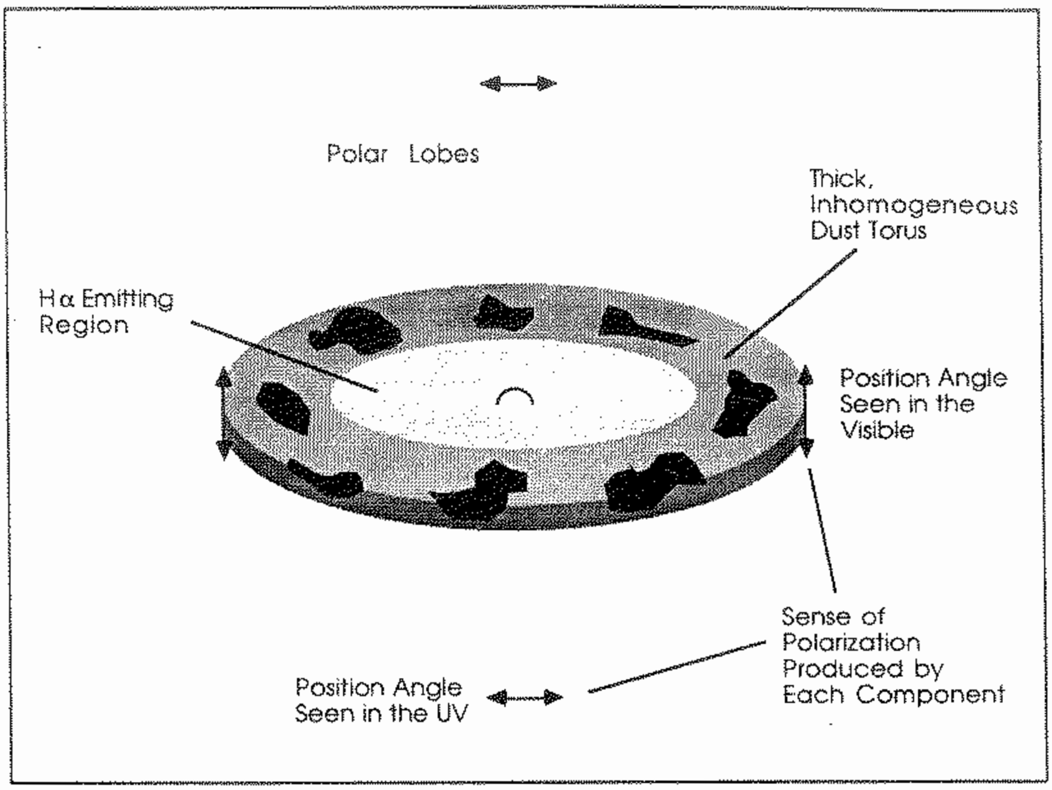
Polar Lobes
Thick, Inhomogeneous Dust Torus
H α Emitting Region
Position Angle Seen in the Visible
Sense of Polarization Produced by Each Component
Position Angle Seen in the UV

Figure 10. A schematic picture of the circumstellar environment around HD45577. More recent data of Grady et al. (1993) suggest in addition that there is an accreting gas disk around the star. From Schulte-Ladbeck et al. (1993).

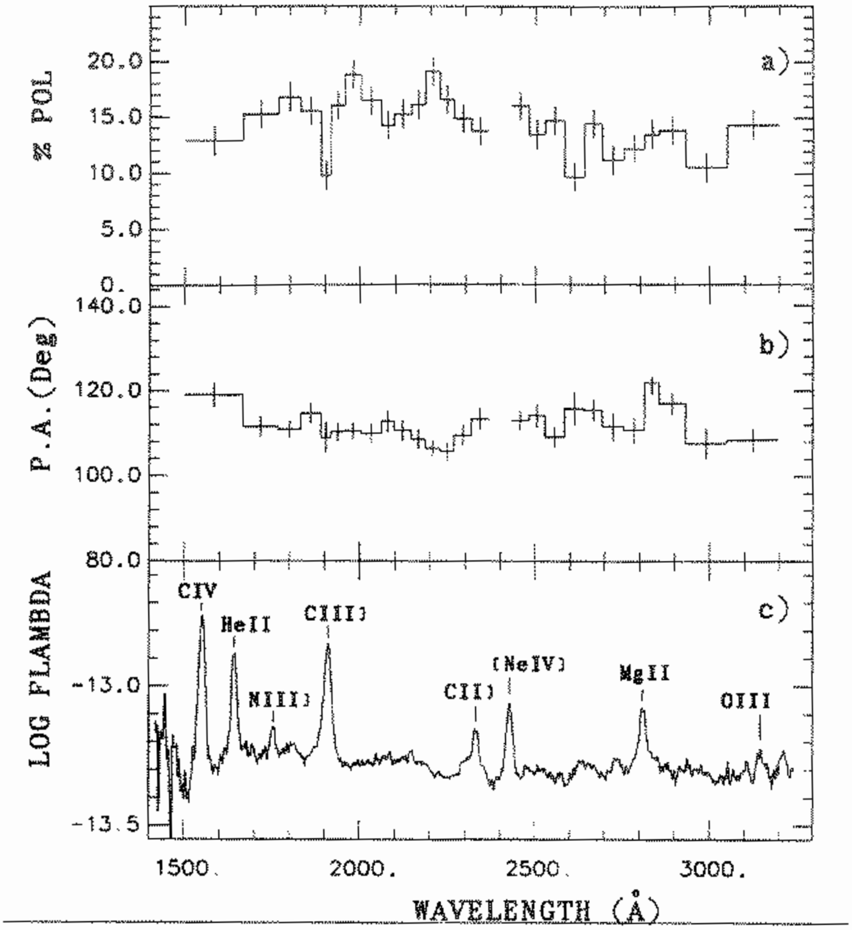

Figure 11. WUPPE data for NGC1068, a Type 2 Seyfert galaxy. The panels are % Polarization (a), Position Angle (b) and Flux (log Fλ) spectra. The percent polarization and position angle are binned to achieve an internal error of 1.3%. In the flux spectrum, the resolution element is 6 pixels. The gap around 2400Å is due to a flaw in one of the detector arrays. From Code et al. (1993).

prototypical examples of Types 1 and 2 are NGC4151 and NGC1068, respectively. From optical polarization data of NGC1068 and allowing for the contribution of unpolarized light by the underlying galaxy, Miller and Antonucci (1983) have obtained a flat intrinsic polarization of around 16% in the visible range, which suggested electron scattering as the main polarigenic agent in the nucleus of NGC1068. Antonucci and Miller (1985), based on optical spectropolarimetry, verified that the polarized flux (= $P(\lambda) \times F(\lambda)$) of NGC1068 does have broad emission lines of H I, He I and He II, similarly to the intensity spectrum of a Type 1 Seyfert. They then suggested that a Seyfert 1 nucleus is present in NGC1068 but is hidden of direct view by a thick disk; material out of the nucleus and close to the disk axis reflects and polarizes part of the nuclear light. The main distinction between Seyfert 1 and 2 would basically be that due to an inclination effect, that would or not allow a direct vision of the broad line nucleus.

Some of these hypothesis could be tested by WUPPE. In the UV, the contamination of the (mainly) red giant light by the underlying galaxy is much less important. Besides, any interstellar component in the UV will be smaller. Finally, it is expected that the active galactic nucleus is more intense in this spectral region. Figure 11 (Code et al. 1993) shows the WUPPE observations of NGC1068. We first note that the observed polarization is essentially independent of wavelength. It would be very difficult to find a mechanism other than electron scattering that would result in a white polarization throughout the UV and the optical regimes. In addition, the level of the observed UV polarization of 16% is in excellent agreement with the picture put forward by Antonucci and Miller (1985) for NGC1068. The middle panel in figure 11 shows a position angle (≈ 112°) that differs from that of Antonucci and Miller's (95°). It so happens that the WUPPE aperture includes a NE polarized elongation (Code et al. 1993). This elongation was measured in the optical by Scarrot et al. (1991) and has a distinct polarization and position angle; the WUPPE observation is consistent with the observed polarization being the vector sum of the two sources, the nucleus and the elongation.

## V. Conclusions

We have seen that optical and UV polarimetry may help elucidate the nature of several classes of astrophysical phenomena. In particular, data collected by the WUPPE experiment were used to illustrate the physics of disks around hot stars, the nature of interstellar grains, the structure around massive stars and finally the nature of Seyfert galaxies.

## Acknowledgments

I would like to acknowledge the meeting organizers for inviting me to give this talk. I am thankful to WUPPE PI Art Code and WUPPE Co-PI Ken Nordsieck, for inviting me to take part of the WUPPE team. I am also thankful for everyone else in the team. They all made my working at University of Wisconsin a very rich experience; they should really be co-authors of this article. I would like to thank Art Code for the support with modifying the CTIO CCD camera and FAPESP, São Paulo state funding agency, which supports Astronomical Polarimetry projects at Instituto Astronômico e Geofísico, Universidade de São Paulo.

## References

Antonucci, R.R.J. e Miller, J.S. 1985, ApJ **297**, 621.

Bjorkman, K. et al. 1991, ApJ **383**, 367.

Bjorkman, K. et al. 1993, ApJ **412**, 810

Clarke, D. e Grainger, J.F. 1971, *Polarized Light and Optical Measurement* (Oxford: Pergamon).

Cassinelli, J.P., Nordsieck, K.H. and Murison, M. 1987, ApJ **317**, 290.

Clayton, G. et al. 1992, ApJ **385**, L53.

Code, A. et al. 1993, ApJ **403**, L63.

Codina-Landaberry, S.J. and Magalhães, A.M. 1976, A&A **49**, 407.

Magalhães, A.M. 1989, Tese de Livre-Docência, IAG-USP.

Magalhães, A.M. 1992, Ap. J. **398**, 286.

Magalhães, A.M., Benedetti, E. e Roland, E. 1984, PASP **96**, p. 383.

Miller, J.S. and Antonucci, R.R.J. 1983, ApJ **271**, L7.

Nordsieck, K. 1991, IAU 21st General Assembly, Commission 25 meeting.

Schulte-Ladbeck, R.E. et al. 1993, ApJ **401**, L105

Serkowski, K. 1974, in *Methods of Experimental Physics*, vol.12, pt. A Astrophysics, ed. N. Carleton (New York: Academic Press), p. 361.

Zickgraf, F.J. 1990, in *Angular Momentum and Mass Loss for Hot Stars*, ed. L.A. Willson and R. Stalio (Dordrecht: Kluwer), 245

# A spectroscopic study of galactic planetary nebulae

**R.D.D. Costa , J.A. de Freitas Pacheco**

Instituto Astronômico e Geofisico da USP, Av. Miguel Stefano 4200,
04301-904, São Paulo, SP, Brazil

**Abstract.** We report the spectroscopic diagnostic of a 46 planetary nebulae sample, classified among the types I, IIa, IIb, and III. For each of them, chemical abundances of He, N, O, S, Ar were derived from new spectroscopic data. From these results we discuss the chemical enrichment processes occurring during the evolution of intermediate mass stars, as well as the radial gradient of abundances of the galactic disk. In particular, the time evolution of the oxygen abundance, which is reflected in its abundances for each type of planetary, is discussed in view of our results.

## 1. Introduction

Planetary nebulae (PNe) are the final evolution stage for intermediate mass stars. Due to dredge-up episodes occurring in the evolution of these objects, surface abundance of elements like helium, nitrogen and carbon are altered in the progenitors, and these altered abundances will appear in the ejected nebulae. On the other hand, elements whose abundances are not affected in the evolution, like sulphur and argon, probably have abundances which reflect the conditions of the interstellar medium at the epoch of formation of the progenitors. The oxygen abundance is still an open question. If only products of the CN cycle are dredged-up, its abundance should remain unaltered, however, if the ON cycle is operating, some alteration in the oxygen abundance should be expected. Model calculations for massive progenitors (Renzini & Voli 1981) predict a maximum reduction of only 0.11 dex in the surface oxygen abundance.

According to scheme originally proposed by Peimbert (1978) and modified by Peimbert & Torres-Peimbert (1983), type I planetary nebulae are those originated from the upper part of the intermediate mass range. These objects have probably undergone the third dredge-up episode, and show expressive He and N enrichments: He/H>0.125 and/or log(N/O)>-0.30 (Iben & Renzini 1983; Renzini & Voli 1981). Type II are those originated from other disk population I stars; type III are originated from disk population II and type IV are those originated from the halo population. Later, Faundez-Abans & Maciel (1987) proposed the division of type II in IIa and IIb based on different chemical abundances found for each subtype.

In this work we report the current status of a long-term program of chemical abundances determination of southern planetary nebulae. New spectroscopic data were collected for each nebula and chemical abundances are then derived. The objects were classified and the results are discussed in view of the chemical enrichment processes. Their relation with the radial gradient of abundances is also briefly discussed. More complete versions of this work, for different sub samples, appear in Freitas Pacheco et al. 1989; 1991, 1992. A full analysis for the complete sample is in Costa (1993).

## 2. Observations and data reduction

All the observations were performed at the National Laboratory of Astrophysics (LNA), in Brasópolis, MG, Brazil. The spectra were obtained using a Boller & Chivens Cassegrain spectrograph attached to the 1.6 m telescope. Two detectors were used during our observational runs. Up to 1989, an intensified reticon was used, and since 1990 a GEC CCD. Both detectors were used with a grating allowing a reciprocal dispersion of 4.4 Å/pixel. A long slit aligned east-west was used in all cases. The logbook of the observations is in Costa (1993).

CCD data reduction was performed using the IRAF package, and followed the standard procedures, including flat-field correction, wavelength calibration, correction for the atmospheric extinction, and flux calibration. Reticon data were reduced with our own programs, following the same scheme. Observation of flux standard stars in each night secured the flux calibration in all cases.

Emission line fluxes were calculated by adopting gaussian profiles for each line and by fitting the continuum using a spline algorithm. The code allows de-blending procedures by fitting more than one gaussian to a profile and imposing constrains like wavelength separation, expected relative intensities or FWHM. Typical errors in the intensities are of about 15% for the lines stronger than 10 (in the scale I(Hβ)=100) and of about 30 for the weaker lines. It has to be noted that only relative fluxes are available, since the slit area in general covers only a fraction of the nebula. Observed and extinction-corrected fluxes for the emission lines of all nebulae are in Costa (1993).

Color excesses were calculated based on the expected and measured values of the Balmer ratio Hα/Hβ, assuming case B.

## 3. Physical parameters and chemical abundances

To compute ionic concentrations, electron density and temperature have to be derived. This was done using the following line intensity ratios:

$$R(OIII)=\frac{\lambda4363}{\lambda5007} \quad ; \quad R(NII)=\frac{\lambda5755}{\lambda6584} \quad ; \quad R(SII)=\frac{\lambda6716}{\lambda6730}$$

The derived values for E(B-V), $N_e$ and $T_e$ are in Costa (1993). The determination of ionic abundances was performed using a three levels atom model, including radiative transitions and collisional excitation and de-excitation in the statistical equilibrium equations. The atomic data were those of the Mendoza (1983) compilation. Elemental abundance of helium was obtained by summing the derived abundances of HeI and HeII. For the other elements, abundances were estimated by adopting the following ionization correction factors: for oxygen and nitrogen we used the factors derived by Peimbert & Torres-Peimbert (1977); for sulphur, that derived by Köppen et al. (1991), and for argon that from Freitas Pacheco et al. (1989). Table 1, in the next page, shows the mean elemental abundance and dispersion for each type, using the notation $\varepsilon(X)=\log(X/H)+12$.

**Table 1** Elemental abundances and classification

| Type | He/H | ε(N) | ε(O) | ε(S) | ε(Ar) |
|---|---|---|---|---|---|
| I | 0.139±<br>0.012 | 8.55±0.46 | 8.80±0.20 | 7.07±0.32 | 6.66±0.28 |
| IIa | 0.104±<br>0.015 | 8.34±0.16 | 8.92±0.17 | 6.95±0.23 | 6.59±0.21 |
| IIb | 0.097±<br>0.012 | 7.75±0.15 | 8.60±0.17 | 6.67±0.26 | 6.22±0.31 |
| III | 0.094±<br>0.015 | 7.51±0.21 | 8.35±0.37 | 6.55±0.35 | 6.14±0.24 |
| Sun | 0.098 | 8.00 | 8.92 | 7.23 | 6.57 |

## 4. Discussion

Each nebula of our sample was classified in the Peimbert classification scheme using its derived elemental abundances. The results show 15 objects classified as type I, 14 as type IIa, 10 as type IIb and 7 as type III.

Figure 1 shows the correlation between He/H and log(N/O) for the objects of our sample; with type I objects placed in the upper part of the figure, and other types distributed as expected from the theory, indicating that types I, IIa, IIb, and III configure a scale of decreasing progenitor masses, with the presence of more nucleosynthetic products in type I PNe.

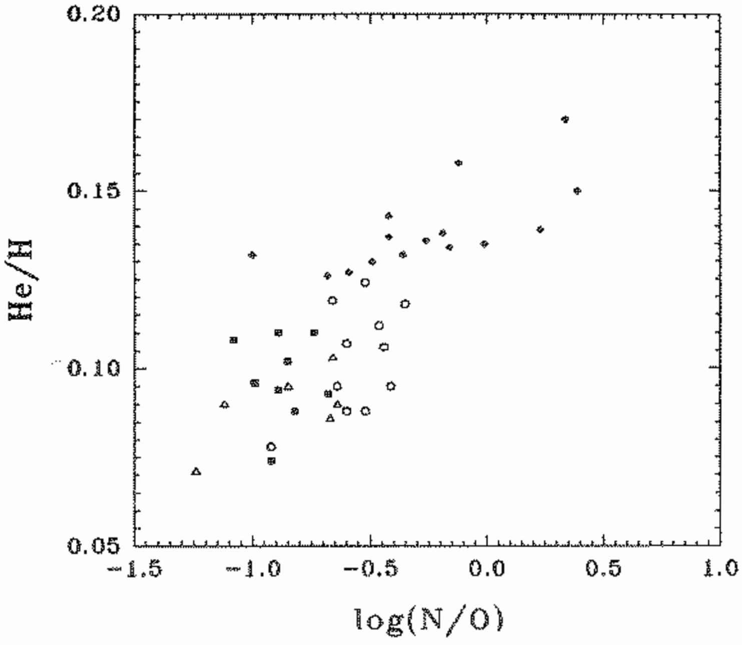

**Figure 1.** He/H vs. log(N/O) for the objects of our sample. Their distribution in the figure show the presence of more nucleosynthesis products for type I objects, as expected from theory. Diamonds represent type I PNe, open circles represent type IIa, squares represent type IIb and open triangles represent type III.

Figure 2 show the correlation between the elements not affected by nucleosynthesis in the progenitors. For these elements, abundances should reflect the status of the interstellar medium at the epoch of the progenitor formation. As can be seen, a clear correlation appears, indicating the time enrichment of the interstellar medium for both elements. Two objects are placed apart from the others in both sides of this figure. With high Ar, O, and S abundances appears He2-111,an extreme type I PN whose intense nitrogen lines were already reported by Dopita et al. (1985). With a strong deficiency in the oxygen abundance, appears He2-90, whose abundances were discussed in detail by Costa et al. (1993).

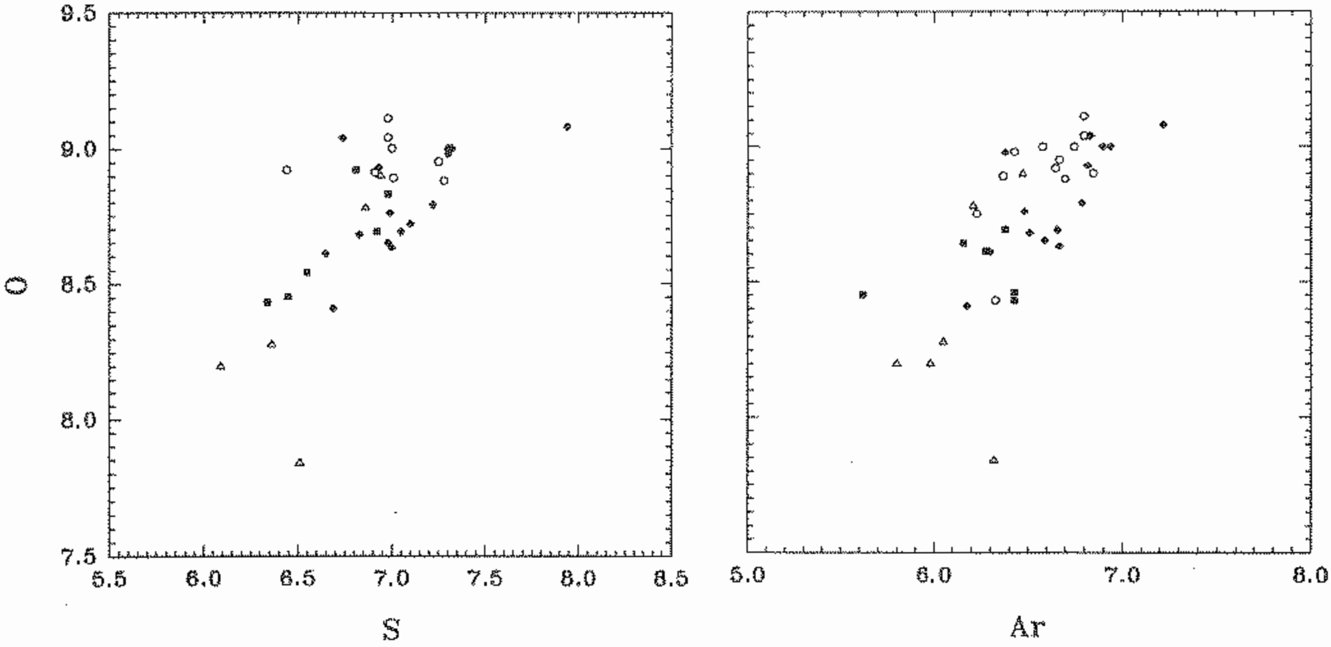

**Figure 2.** Oxygen abundance in function of sulphur and argon abundances. Both correlations show the gradual enrichment of the interstellar medium, with type III PNe progenitors forming from a poor medium and types IIb, IIa and I forming from gradually richer media. Symbols are the same of figure 1.

As can be seen from table 1, mean abundances for each type behave as expected from dredge-up theories. Type I PNe, which are originated from more massive progenitors, have an expressive enhancement in helium and nitrogen abundances when compared with the solar values shown in the same table. This effect indicates that the progenitor have probably undergone the third dredge-up episode, which occurs after the thermal pulses, in the Asymptotic Giant Branch. On the other hand, elements not affected by progenitor nucleosynthesis as sulphur, argon and oxygen should follow the abundances of the interstellar medium. although a small amount of oxygen can be converted into nitrogen if the ON-cycle is operating. Inspecting table 1, one can see that this trend is followed by sulphur and argon, but, in spite of the dispersion, a small decrease in the oxygen abundance can be seen for type I objects.

The trend of a smaller oxygen abundance in young objects, which appears marginally in our data, was also noticed by Freitas Pacheco (1993) in his analysis of the oxygen, sulphur and argon abundances of the galactic disk, based on a larger sample of PNe. This paucity of oxygen can be explained by the infall of metal-poor material from the galactic halo, or by an alteration in the relative frequency of type Ia supernovae in the last 5-6 Gyr. Is interesting to notice that a similar trend of a decreasing oxygen abundance for younger objects can be found also in the Edvardsson et al. (1993) abundance data from their study of disk dwarfs.

For all the object of our sample, galactocentric distances were calculated and, then, we checked the locus of each object in an abundance vs. galactocentric distance plane. This was done for oxygen, sulphur and argon abundances and the figures are in Costa (1993). In spite of the small range of distances available (4<R(kpc)<12), a clear trend can be seen in all figures, with richer objects placed in inner parts of the galactic disk, as we expected.

## 5. Conclusions.

Using optical spectroscopy, we derived chemical abundances for a 46 southern PNe sample. Based on these results, we discussed the chemical enrichment processes occurring during the evolution of the progenitors. In particular, the time evolution of the oxygen abundance was analyzed. The relation between chemical abundances of each object and the radial gradient of abundances of the galactic disk was also analyzed, and, in spite of the small range of abundances available, our results follow the expected trend for the abundances, with richer objects placed in the inner parts of the disk.

## 6. References.

- Costa, R.D.D. 1993, Thesis, IAG-USP
- Costa, R.D.D., Freitas Pacheco, J.A. de, Maciel, W.J. 1993, A&A, in press
- Dopita, M.A., Ford, H.C., Webster, B.L. 1985, ApJ **297**, 593
- Edvardsson, B., Andersen, J., Gustafsson, B., Lambert, D.L., Nissen,, P.E. Tomkin, J. 1993 A&A, in press
- Faundez-Abans, M., Maciel W.J. 1987, A&A **183**, 324
- Freitas Pacheco, J.A. 1993, ApJ **403**, 673
- Freitas Pacheco, J.A., Codina, S.J., Lopes, D.F. 1989 ApJ **337**, 520
- Freitas Pacheco, J.A., Maciel, W.J., Costa, R.D.D., Barbuy, B. 1991, A&A **250**, 159
- Freitas Pacheco, J.A., Maciel, W.J., Costa, R.D.D. 1992, A&A **261**, 579
- Iben Jr.,I., Renzini, A. 1983, Ann. Rev. A&A **21**, 271
- Köppen, J., Acker, A., Stenholm, B. 1991, A&A **248**, 197
- Peimbert, M. 1978, in: Y. Terzian (ed.) IAU Symp. 76, Reidel, Dordrecht, p. 215
- Peimbert, M., Torres-Peimbert, S. 1977, MNRAS **179**, 217
- Peimbert. M., Torres-Peimbert, S. 1983 in: Flower, D.R.(ed.) IAU Symp 103, Reidel, Dordrecht, p. 233
- Renzini, A., Voli, M. 1981, A&A **94**, 175

# Section 4:

# Extragalactic Astrophysics

# CHEMICAL ABUNDANCES AND MORPHOLOGY OF THE NARROW LINE REGION IN LOW-ACTIVITY GALACTIC NUCLEI

Thaisa Storchi-Bergmann
Departamento de Astronomia, IF-UFRGS
CP 15051, CEP 91501-970, Porto Alegre, RS, Brasil

**Abstract**

In this work, I review recent results on the chemical abundances of the gas in the Narrow Line Region (NLR) of low-activity galactic nuclei (Seyfert 2 and LINER's). The determination of the abundances is made through the comparison of observed emission-line ratios for a sample of 177 Seyfert 2 and LINER's with photoionization and shock model calculations. It is verified that the emission-line ratios depend on the dimensions of the regions subentended at the galaxy by the aperture, implying possible contribution of gas not only from the NLR, but also from the HII regions in the disk of the galaxies. When this effect is statistically taken into account, it is found that the majority of Seyfert 2 and LINERs present an overabundance of nitrogen relative to the solar value in their NLR. The dependence of the emission line ratios on the aperture used in the observations also evidence the necessity of separating the NLR from the HII regions in order to study its properties, as the ionization source in the latter are blue young stars and not the active nucleus which ionizes the NLR. This can be done through the use of narrow-band images which isolate the gas emission and through the construction of "excitation maps", which show the loci of the high excitation gas (NLR). I discuss the results of such studies for four galaxies in which conical morphologies have been found for the high excitation gas which seems to support the ideas of the "Unified Models" for active galactic nuclei (AGN). For two of these galaxies I also show results obtained from long-slit spectroscopy using the Cerro Tololo 4m telescope, which permit a detailed mapping of the excitation and reddening of the cone region. Photoionization modeling of these data also indicates an overabundance of nitrogen for the high excitation gas, which is also confirmed by abundances determined for neighboring HII regions in one case, thus confirming the results from the statistical study.

## 1 Introduction

The goal of the study of the chemical abundances in AGN is to verify if the circumnuclear regions (namely the narrow-line region –NLR) have experienced unusual chemical processing. Recent ideas point towards a relation between star formation and nuclear activity in galaxies: for example, Terlevich and colaborators (Terlevich and Melnick 1986; Terlevich, 1990; Terlevich et al. 1992) argue that the Seyfert activity is due to the evolution of a massive starburst in a metal rich environment. If Seyfert galaxies have indeed suffered unusually large amounts of massive star formation over their lifetimes in their central regions, enhancement of heavy element abundances in comparison with "normal" spirals would be expected. Nevertheless, determining chemical abundances of the NLR is not an easy task. Unlike the abundances calculations for HII regions, which involve standard procedures (McCall et al. 1985; Dopita and Evans 1986), in AGN there are too many uncertain physical processes which can make the abundances determinations unreliable. Efforts have been made by researchers working with photoionization models to consider the effects of such processes like shocks, heating by relativistic electrons, as well as the possibility of density stratification and the presence of matter-bounded clouds (e. g., Cesar, Aldrovandi and Gruenwald, 1985; Viegas-Aldrovandi and Gruenwald, 1988, 1990; Filippenko and Halpern 1984). In this work, I discuss some results on the study of the gas abundance using a sample of 177 Seyfert 2's and LINER's, for which emission line ratios have been measured from integrated spectroscopy. The approach for the determination of the abundances was to use photoionization and shock models to compare the emission-line ratios predicted by the models with the observed ones.

A related topic that I also address in this paper is the detailed mapping of the morphology, excitation and reddening conditions of the NLR. As discussed hellow, when using data from integrated (within a fixed aperture) spectroscopy, one is frequently including in the slit not only the NLR but also emission from HII regions in the disk. In order to properly isolate the NLR and study the physical conditions and chemical abundances inside it, it is necessary to map the high excitation gas through narrow-band imaging (e.g. Pogge 1988, Wilson 1992 and references therein) and/or use long-slit spectroscopy, in which one has spatial resolution and thus can isolate regions with different emission characteristics. I discuss the results for a few galaxies in which this kind of study has been made.

## 2 Abundance Determinations

Using a sample of 90 Seyfert 2 and 77 LINER's, Storchi-Bergmann and Pastoriza (1989, 1990) have measured and collected from the literature emission-line ratios which have then been compared with values obtained from photoionization and shock models. Fig. 1 shows a typical Seyfert 2 spectrum, where the main emission-lines used in the comparison with the model calculations are identified. The models used were the photoionization code CLOUDY (Ferland 1990) and the integrated shock models of Viegas-Aldrovandi (1988).

In the calculation of the photoionization models, a constant density nebula photoionized by a power-law continuum of the form $F_\nu \alpha \nu^\alpha$ was considered. In order to reproduce the observations, several parameters of the model were varied: the slope "$\alpha$" of the ionizing continuum, the gas density and the abundance of the elements. In the shock models, it was considered the contribution of clouds of different velocities in the range $100 < v < 600 km\ s^{-1}$ according to the distribution law $f(v)\ \alpha\ v^{-b}$.

It was concluded that the shock models do not reproduce most of the data. The best agreement with the observations was obtained for photoionization models with $\alpha = -1.5$, and the observed range of emission-line ratios was only covered when a selective variation of the nitrogen and sulphur abundances in the gas relative to the solar value was considered, from 0.5 to 5 times solar, the other elements being kept at the solar abundance value. Fig. 2 shows the comparison between the observed emission line ratios and models in diagrams involving the stronger emission lines. It was not possible to reproduce the observations varying only the gas density or the abundances of the elements altogether.

# 3 Effect of the slit dimensions at the galaxy

While working with the integrated spectra of the 177 Seyfert 2 and LINER's mentioned above, Storchi-Bergmann (1991) verified that the observed emission-line ratios, and in particular [NII]$\lambda\lambda$6548,84/H$\alpha$ was dependent on the dimensions at the galaxy subtended by the slit used in the observations: the larger the region observed at the galaxy, the smaller was the [NII]/H$\alpha$ ratio. This is due to the fact that, while for the closer galaxies one is probably observing only the nuclear NLR gas, for the more distant nuclei one is probably observing also HII regions in the disk. The effect was quantified: using an effective length $l$ defined as the square root of the area at the galaxy subtended by the slit, it was concluded that, for $l < 0.5$ *kpc*, 72% of the galaxies presented [NII]/H$\alpha > 1.5$, while for the whole sample the percentage of galaxies with [NII]/H$\alpha > 1.5$was only 44%. ([NII]/H$\alpha$=1.5 corresponds to $\approx$ solar abundance for nitrogen). This result has direct influence on the conclusions about the nitrogen abundance obtained by Storchi-Bergmann and Pastoriza (1990): while in the previous work it was concluded that there was an even distribution of nitrogen abundances, it is now verified that, when the effect of different apertures is considered, the majority of Seyfert 2 and LINER's actually present an overabundance of nitrogen in the nucleus.

# 4 The origin of the nitrogen overabundance

Overabundance of nitrogen is not rare in astronomical objects. It is observed, for example, in several advanced stages of stellar evolution, like planetary nebulae of type I (Perinoto, 1991), supernovae, like SN1987A (Fransson et al. 1989), and supernova remnants, like Cas A and Pup A (Fesen et al. 1987). These results can be understood considering that the circunstellar gas in these stars, which was lost in the supergiant phase, was enriched by convection of stellar material processed in the CNO cicle ocurring in intermediate mass stars ($\approx$ 6–9 $M_{\odot}$). In other words, in these stars the bulk of nitrogen production has secondary origin (Serrano and Peimbert 1983; Mateucci 1986; Garnett 1990), in which a selective enhancement of the nitrogen abundance is expected, as the ratio between the nitrogen and oxygen abundance is proportional to the oxygen abundance in secondary nucleosynthesis.

Overabundance of nitrogen is also found in Wolf-Rayet stars. It is interesting to point out that the presence of these stars in AGN nuclei is predicted in the WARMERS scenario (Terlevich and Melnick 1985). Cid Fernandes et al. (1992) have calculated the chemical enrichment by winds of Wolf-Rayet stars and concluded that nitrogen is indeed the first element to be enriched, the highest enrichment relative to oxygen being coincident with the most luminous phase of the ionizing cluster.

Another related result is the finding by Hamman and Ferland (1992) that the nitrogen enrichment in luminous QSO's should be up to 10 times solar, on the basis of observations of the [NV]$\lambda$1240 line. They interpret this result as an evidence that luminous quasars are associated with early stages in the formation of massive galaxies, the high metallicity being due to the rapid evolution expected in the cores of these galaxies.

## 5 Isolating the NLR

The verification that the observed spectra of the AGN is significatively affected by the slit dimensions used in the ohservations evidence the necessity of making observations with spatial resolution, in which it is possible to separate the NLR from surrounding HII regions or even HII regions in the disk. The ideal approach for such observations is to make both imaging using narrow-band filters in order to separate the gas from the continuum light emission and long-slit spectroscopy, in which one can map the variation of the gas emission-line ratios.

### 5.1 Imaging the NLR

Recent imaging studies have shown that the NLR region can be isolated from the continuum light using narrow-band filters, usually centered in the strongest NLR emission lines, namely [OIII]$\lambda$5007 and H$\alpha$. The high excitation can be separated from the lower excitation gas by the construction of "excitation maps", consisting of the ratio between the [OIII] and H$\alpha$ images, as the NLR gas presents a (usually much) higher [OIII]/H$\alpha$ ratio than the HII regions. These studies have shown that the high excitation gas (or NLR) has elongated morphologies, usually aligned with the radio axis, when radio emission is present (Haniff, Wilson & Ward, 1988), and in several Seyfert 2 galaxies clear conical morphologies have been observed (e.g. Pogge 1988; Corbin, Baldwin & Wilson 1988; Tadhunter & Tsvetanov 1989).

We show in Fig. 3 the conical morphologies found in the Seyfert 2 galaxies NGC1365 and NGC7582 by Storchi-Bergmann and Bonatto (1991). The cones were readily apparent in the [OIII] images after the subtraction of the continuum contribution, have a projected extent of about 1.5 kpc, and seem to be oriented approximately perpendicular to the plane of the galaxies. Kinematic studies by Phillips et al. (1983) and Morris et al. (1985) show that, in both cases, the gas in the cone presents an outflow relative to the nucleus. The analysis of the available data on these two galaxies favor the so-called "Unified AGN Models", in which the active nucleus and broad-line region in the Seyfert 2 galaxies are hidden by a dusty torus which is responsible for the collimation of the ionizing radiation in two opposite cones. In the model of Krolik and Begelman (1986), a wind driven by the nuclear continuum is also predicted.

Another Seyfert 2 galaxy which seems also to present all the characteristics predicted in the Unified Models is NGC3281, studied by Storchi-Bergmann, Wilson & Baldwin (1992). Fig. 4 shows the conical morphology found in the continuum-subtracted [OIII] image of this galaxy. As in the cases of NGC1365 and NGC7582, the cone bas a high angle relative to the plane and extends to a projected distance of about 1.5 kpc. A (mild) gas outflow was also observed in the cone.

Higb excitation gas with elongated morphology was also found by Schmitt, Storchi-Bergmann & Baldwin (1994) in the Seyfert 2 galaxy NGC5643 (Fig. 5). As opposite to the other cases discussed above, in this object the high excitation gas seems to be oriented along tbe direction of the bar, with only a small tilt relative to the plane of the galaxy and extends to about 1 kpc from the nucleus.

## 5.2 Long-slit spectroscopy

Long-slit spectroscopy is a powerful technique to study the variation of physical conditions over the emitting-gas region, as well as to study the gradient of stellar population over the central regions. I discuss here the results of this kind of study for two Seyfert 2 galaxies: NGC3281 (Storchi-Bergmann, Wilson & Baldwin 1992, hereafter SBWB) and NGC5643 (Schmitt, Storchi-Bergmann & Baldwin 1994, hereafter SSBB).

### 5.2.1 Equivalent width of absorption lines

The equivalent width of absorption lines can be used to study the characteristics of the stellar population over the central region (Bica, 1988), as well as to verify and quantify the contribution of the ionizing continuum in the nucleus.

For both NGC3281 (Sab) and NGC5643 (Sc), it was found that the stellar population in the central region (within $\approx$ 1.5 kpc) is old, typical of the bulges of early type galaxies.

For NGC5643, SSBB verified that the equivalent widths of absorption lines (W's) were diluted at the nucleus and in the extracted spectra within 10″ from the nucleus, as shown in Fig. 6; this was interpreted as being due to scattered light from the ionizing blue continuum. For NGC3281 no dilution was found, indicating that the active nucleus is hidden from direct view and that we also do not see scattered light. But it was verified that the equivalent width of the Na I D line ($\lambda$5890) varied from 3 to about 6.5Å over the central region, not due to the stellar population but to interstellar absorption in NGC3281. It was indeed found that the larger W(Na I) corresponded to the largest E(B-V) obtained from both the continuum and the Balmer H$\alpha$/H$\beta$ emission line ratio, as can be observed in Fig. 7.

### 5.2.2 Gas reddening, density and excitation

From the emission line fluxes, several line ratios were calculated in order to study their variation over the central region. From the H$\alpha$/H$\beta$ line ratio, the corresponding reddening, as measured by E(B-V), was calculated on the assumption that the intrinsic value is H$\alpha$/H$\beta$=2.9. For NGC3281 it was found that the reddening reaches the highest value at the apex of the cone, in agreement with the results presented in Fig. 7 and suggesting that the active nucleus is hidden there. For NGC5643, the highest reddening value was found at 3$''$ W from the peak of the continuum light, again presumably the locus corresponding to the active nucleus, as suggested by the kinematic data of Morris et al. (1985). Another interesting result is that the highest density values, as determined from the line ratio [SII]$\lambda$6717/$\lambda$6731 is also found at approximately the same loci where the highest reddening is found.

### 5.2.3 Gas Excitation and Chemical Abundance

The gas excitation can be studied through the emission line ratios [OII]$\lambda$3727/[OIII] $\lambda\lambda$4959,5007 or [OIII]/H$\beta$, as well as [NII]$\lambda\lambda$6548,84/H$\alpha$ and [SII]$\lambda\lambda$6717,6731/H$\alpha$. High excitation gas was found in the conical structures in NGC3281 and throughout the elongated NLR of NGC5643.

SBWB and SSBB have used the photoionization code CLOUDY (Ferland 1990) in order to model the emission line ratios of the NLR of, respectively, NGC3281 and NGC5643. Fig. 8 shows diagrams involving the strongest emission lines for models of a nebula with density $n=10^3 cm^{-3}$ photoionized by a typical AGN continuum as well as for shock models, which are compared to the observed emission line ratios of NGC3281. The data is best reproduced by models in which the abundances of nitrogen and sulphur are selectively enhanced to 3 times the solar value. A similar selective enhancement of nitrogen and sulphur was also obtained for NGC5643. Nevertheless, when the effects of dust are incorporated in the calculations, an overabundance of 2 times solar is found instead of 3 times solar. ¿From Fig. 8 it can be seen that the long-slit data are reproduced by sequences of models of varying ionization parameter (the [OII]/[OIII] emission line ratio is mostly sensitive to variations of the ionization parameter), which is highest in the middle of the cone in NGC3281 and of the extended emission in NGC5643 and decreases outwards. One additional check on the abundances values obtained for the NLR was possible for NGC5643: long-slit data along the bar of the galaxy included 5 HII regions at a range of distances from the nucleus. Calculations of the gas abundances of these HII regions showed a gradient in both oxygen and nitrogen abundances, which increase towards the center., shown in Fig. 9. Extrapolation to the nucleus give an oxygen abundance about the solar value and a nitrogen abundance about 2 times solar, in agreement with the results obtained from the models for the NLR.

# 6 Infrared Emission and Torus Model

The presence of ionization cones is consistent with the "Unified Scheme" for Seyfert galaxies (Antonucci & Miller 1985; Krolik & Begelman 1986), in which the conical morphology results from shadowing by a dusty obscuring torus, which hides the nuclear source and broad line region from direct view. Storchi-Bergmann, Mulchaey & Wilson (1992) have used imaging and long-slit spectroscopic measurements of 9 Seyfert 2 galaxies with ionization cones to test if the data are consistent with the torus model. From the emission-line ratios measured from gas within the cones, the number of ionizing photons emitted by the compact nucleus was obtained. Then, on the assumption that the nuclear source radiates isotropically, the optical-uv power incident on the torus was calculated. If the torus is indeed present, the incident energy on the torus is expected to be reradiated in the IR and should be observable in the IRAS fluxes. It was found that, for 8 of the 9 objects for which it was possible to perform the calculation, the observed IRAS luminosities are consistent with the torus model. The data on NGC3281 (SBWB) and NGC5643 (SSBB) are also consistent with the torus model.

# 7 Summary and Conclusions

I have discussed some recent results on the chemical abundances, morphology, reddening and excitation of the narrow-line region in Seyfert 2 and LINER galaxies. The main results are:

1. From integrated (not long-slit) spectroscopy of a sample of 177 Seyfert 2 and LINER's, it is found that their NLR's span a range in nitrogen and sulphur abundances from half solar to about 5 times solar;

2. The measured emission-line ratios for the NLR depend on the aperture used in the observations, due to contamination by HII regions (from the disk) in the more distant galaxies, in which even small apertures correspond to large regions at the galaxy. When this effect is taken into account, it is found that 73% of the objects of the sample present line ratios which indicate an overabundance of nitrogen and probably sulfur in the NLR;

3. In order to isolate the NLR from neighboring HII regions and study the run of physical conditions along the NLR, narrow-band images should be obtained to

map the gas and then long-slit spectroscopy in order to measure emission-line ratios with spatial resolution. In a number of nearby Seyfert 2's it is found that the high excitation gas of the NLR has a conical morphology. Long-slit spectroscopy for two of such galaxies reveal an increasing obscuration towards the apex of the cone, suggesting that the nucleus is hidden there;

4. The long-slit data for the NLR's define sequences in emission-line ratio diagrams which can be reproduced by a sequence of models with varying ionization parameter, and nitrogen and sulphur abundances three or two times solar (this last case if dust is included in the models). For NGC5643, extrapolated nuclear abundance values from the abundance gradient obtained from HII regions along the bar of the galaxy agree with the values obtained from the models for the NLR. These detailed results obtained from long-slit data are in agreement with the previous finding (using integrated spectroscopy) of an overabundance of nitrogen and sulphur in the NLR of Seyfert 2's and LINER's.

5. Long-slit spectroscopy is a powerful tool for studying the gradient of stellar population characteristics over the central regions. If the stellar population can be assumed to be uniform within a few arcseconds from the nucleus, the dilution of the absorption lines from the stellar population can be used to verify and quantify the presence of a ionizing continuum from a compact nucleus or of scattered light from the nuclear source.

6. The narrow-band images, together with long-slit data and infrared luminosities were used to test if the cones arise from collimation by a dusty torus, as predicted in the "Unified Scheme" for Seyfert galaxies. In 9 out of 10 galaxies with enough data to perform the necessary calculations, the data is consistent with the torus model.

## Acknowledgments

I acknowledge the help and valuable discussions with a number of people during the development of the papers from which I extracted the results discussed in this work: M. G. Pastoriza, A. S. Wilson, J. A. Baldwin, J. S. Mulchaey, H. R. Schmitt, E. Bica, Z. Tsvetanov, S. M. Viegas, R. B. Gruenwald, S. O. Kepler. I also acknowledge the institutions CNPq, FAPERGS and FAPESP for support.

## References

Antonucci, R. R. J. & Miller, J. S. 1985, ApJ, 297, 621.
Bica, E. 1988, A& A, 195, 76.
Cesar, M. L., Aldrovandi, S. M V. and Gruenwald, R. B. 1985, PASP, 97, 850.

Cid Fernandes Jr., R., Dottori, H. A., Gruenwald, R. B. & Viegas, S. M. 1992, MNRAS, 255, 165.

Corbin, M., Baldwin, J. A. & Wilson, A. S. 1988, ApJ, 334, 584.

Ferland, G. J. 1990, *OSU Internal Report No. 90-001.*

Fesen, R. A., Becker, R. H. & Blair, W. P. 1987, ApJ, 313, 378.

Filippenko, A. V. and Halpern, J. P. 1984, ApJ, 285, 458.

Fransson, C. , Cassatella, A., Gilmozzi, R., Kirshner, R. P., Panagia, N., Sonneborn, G. & Wamsteker, W. 1989, ApJ, 336, 429.

Hamman, F. & Ferland, G. J. 1992, ApJ(Letters), 391, L53.

Haniff, C. A., Wilson, A. S. & Ward, M. J. 1988, ApJ, 334, 104.

Krolik, J. H. & Begelman, M. C. 1986, ApJ(Letters), 308, L55.

McCall, M. L. 1984, MNRAS 208, 253.

McCall, M. L., Rybski, P. M. & Shields, G. A. 1985, ApJS, 57, 1.

Morris, S., Ward, M. J., Whittle, M., Wilson, A. S. & Taylor, K. 1985, MNRAS, 216,193.

Pagel, B.E.J., Edmunds, M. G., Blackwell, D. E., Chen, M. S. & Smith, G. 1979, MNRAS 189, 95.

Perinotto, M. 1991, ApJS, 76, 687.

Phillips, M. M., Turtle, A. J., Edmunds, M. G. & Pagel, B. E. J. 1983, MNRAS, 203, 759.

Pogge, R. W. 1988, ApJ, 328, 519.

Schmitt, H. R., Storchi-Bergmann, T. & Baldwin, J. A. 1994, ApJ, in press.

Storchi-Bergmann, T. & Bonatto, C. J. 1991, MNRAS, 250, 138.

Storchi-Bergmann, T. & Pastoriza, M. G. 1989, ApJ, 347, 195.

Storchi-Bergmann, T. & Pastoriza, M. G. 1990, PASP, 102, 1359.

Storchi-Bergmann, T., Mulchaey, J. S. & Wilson, A. S. 1992, ApJ, 395, L73.

Storchi-Bergmann, T., Wilson, A. S. & Baldwin, J. A. 1992, ApJ, 396, 45.

Tadhunter, C. & Tsvetanov, Z., 1989, *Nature*, 341, 422.

Terlevich, R. J. 1990, in *Windows on Galaxies*, eds. G. Fabbiano, J. Gallagher & A. Renzini (Kluwer:Dordrecht).

Terlevich, R. J., Tenorio–Tagle, G., Franco, J. & Melnick, J. 1992, MNRAS 255, 713.

Viegas-Aldrovandi, S. M. 1988, private communication.

Viegas-Aldrovandi, S. M. and Gruenwald, R. B. 1988, ApJ, 324, 683.

Viegas-Adrovandi, S. M. and Gruenwald, R. B. 1990, ApJ, 360, 474.

Wilson, A. S. 1992 *in Physics of Active Galactic Nuclei*, eds. S. J. Wagner and W. J. Duschl (Springer-Verlag).

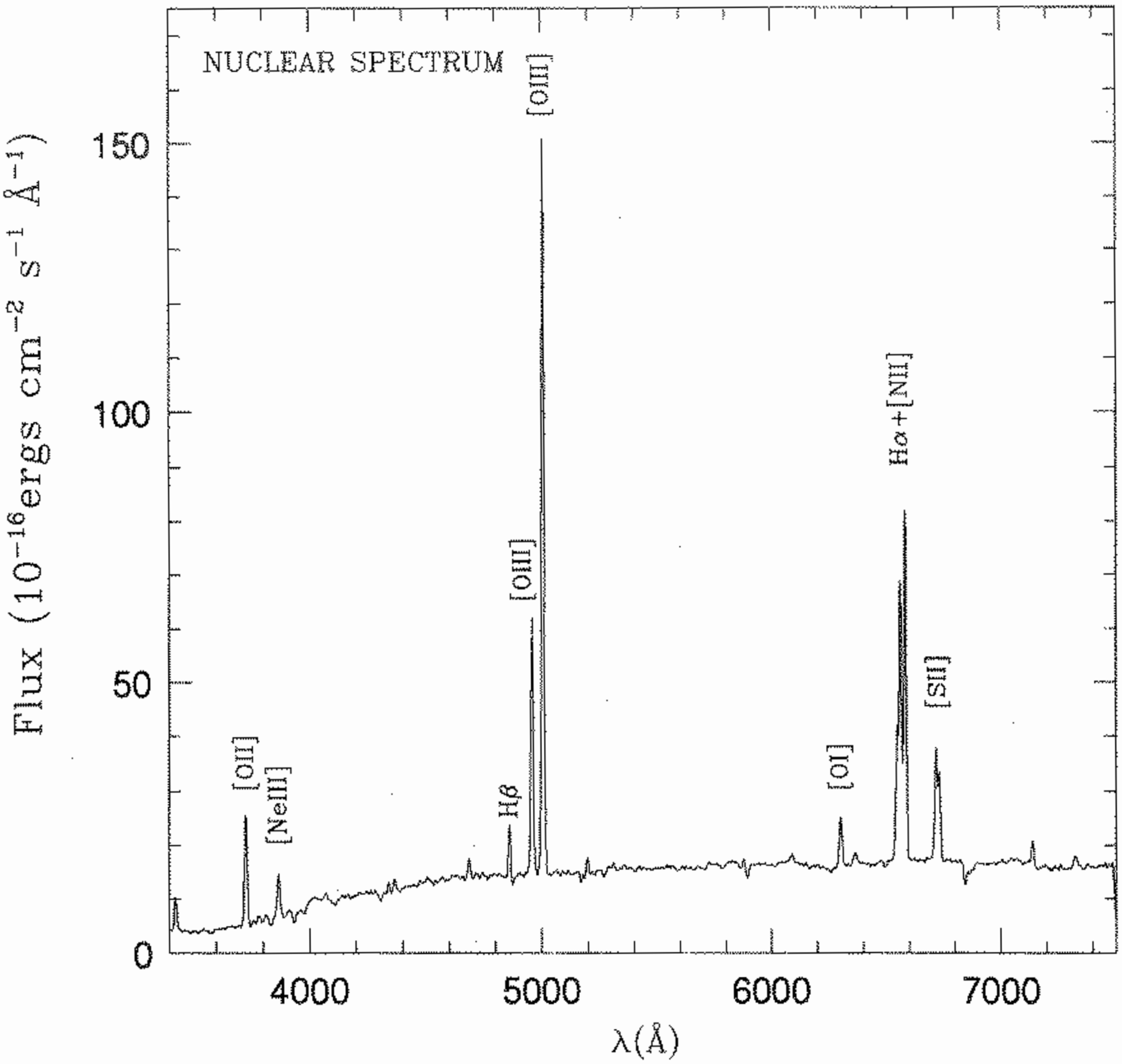

Figure 1: The nuclear spectrum of the Seyfert 2 galaxy NGC5643, where the main emission lines are identified; from Schmitt et al. 1994

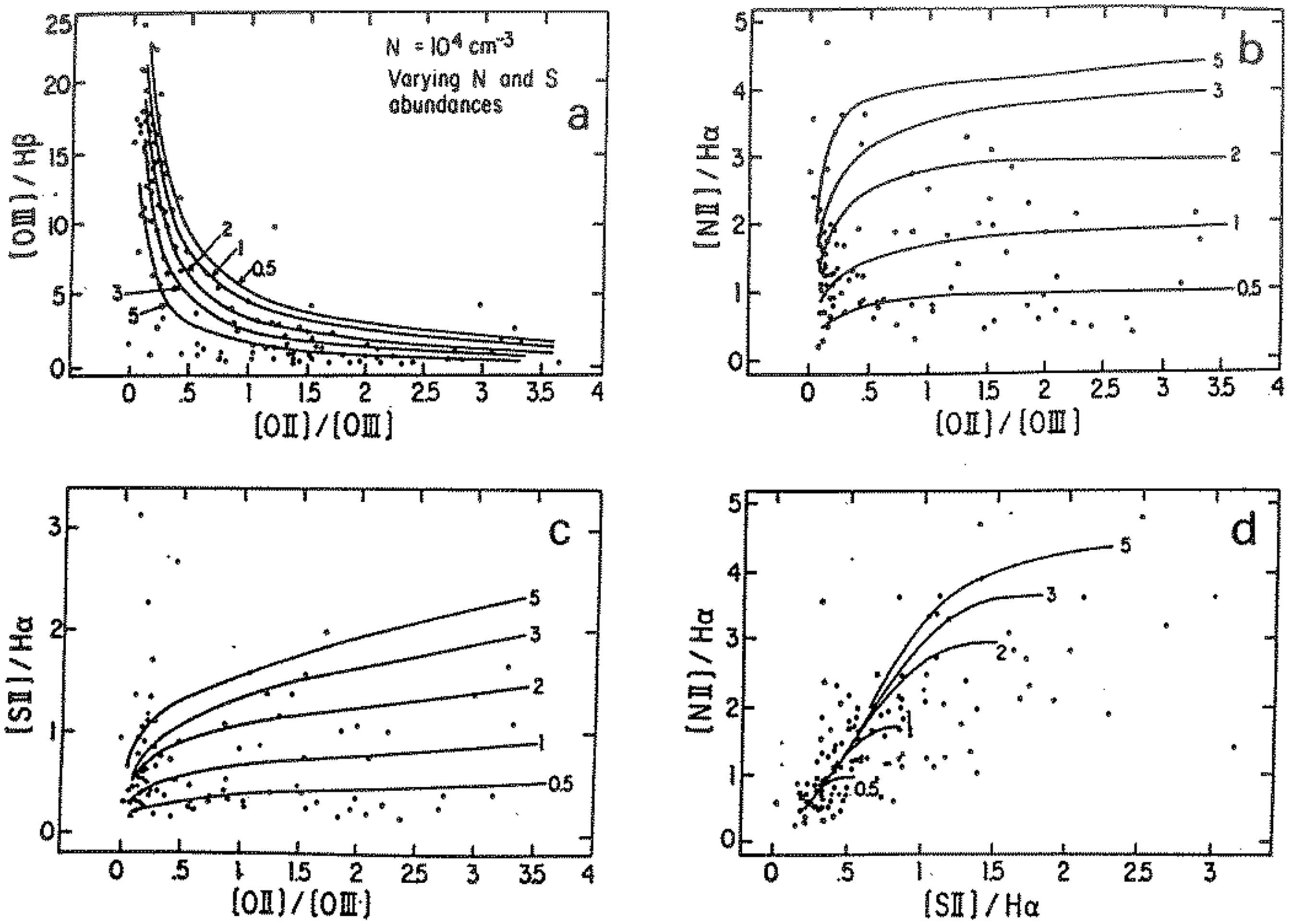

**Figure 2**: Sample galaxies (dots) and photoionization models (continuous lines) for sulphur and nitrogen abundances varying from 0.5 to 5 times solar; from Storchi-Bergmann & Pastoriza 1990

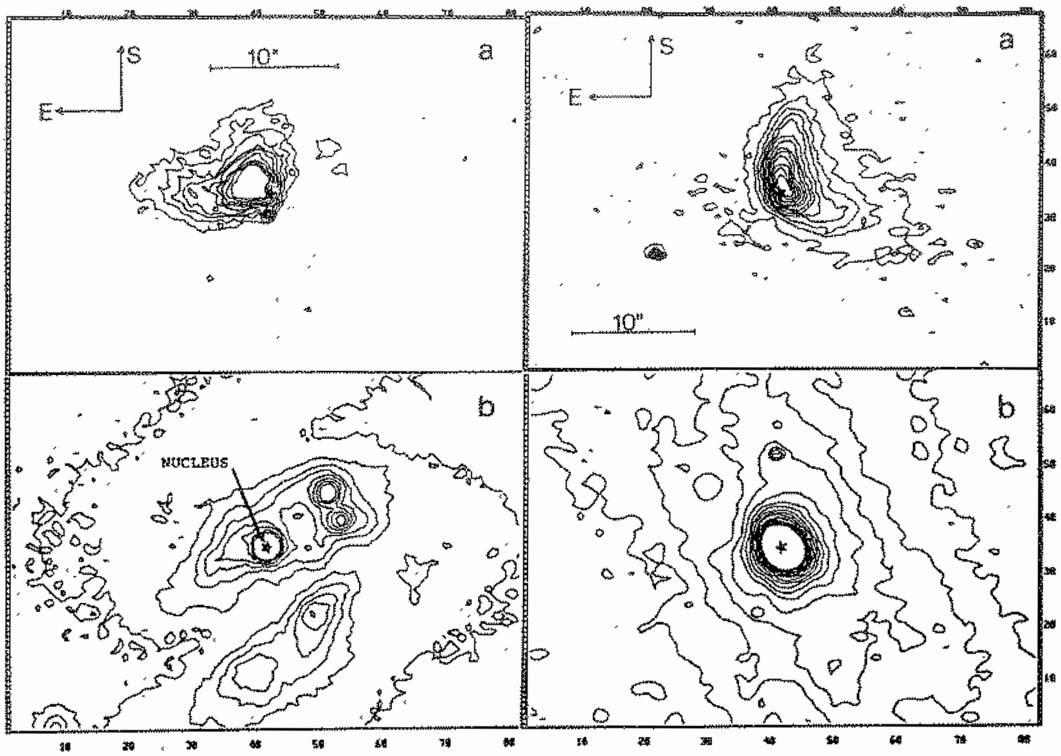

Figure 3: (a) Contour map of the continuum-subtracted NGC1365 (left) and NGC7582 (right) [OIII]$\lambda$5007 image; (b) contour maps of the continuum adjacent to the [OIII] emission line; from Storchi-Bergmann & Bonatto 1991

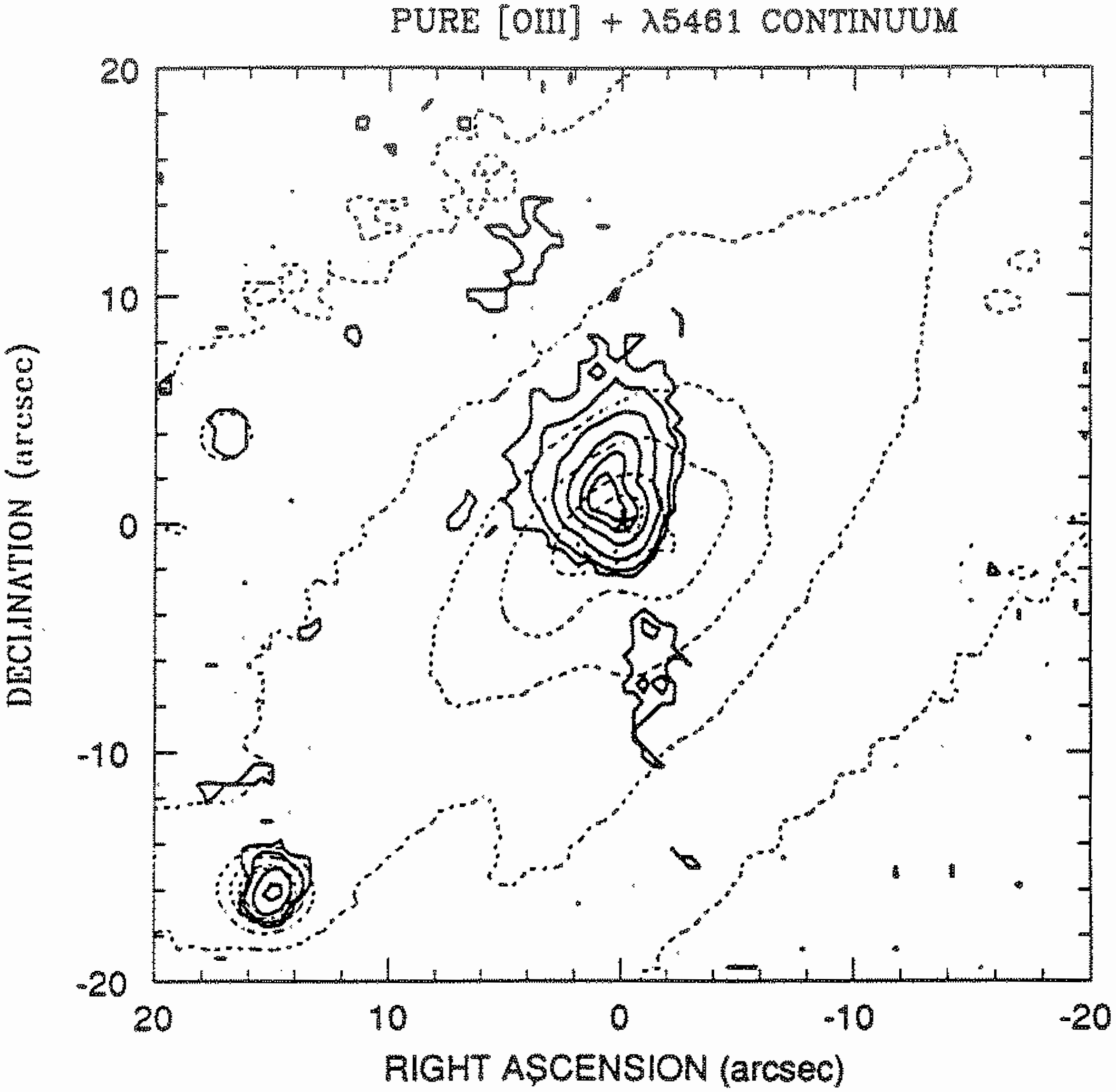

Figure 4: Contours of the continuum subtracted [OIII] emission (continuous lines) superimposed on contours of the adjacent continuum (dashed lines) for NGC3281; from Storchi-Bergmann et al. 1992

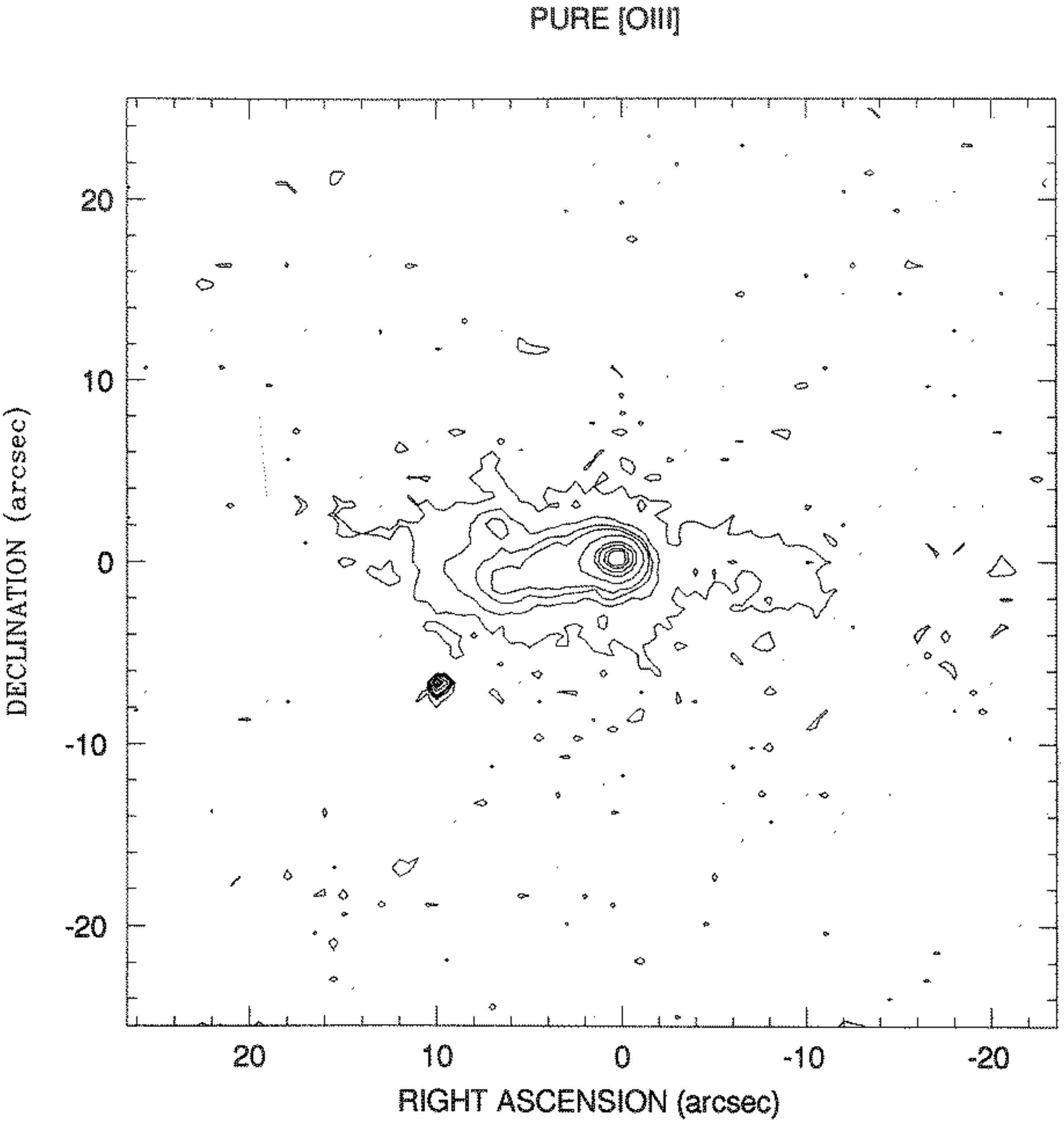

Figure 5: Contour map of the continuum-subtracted [OIII] image of the central region of NGC5643; from Schmitt et al. 1994

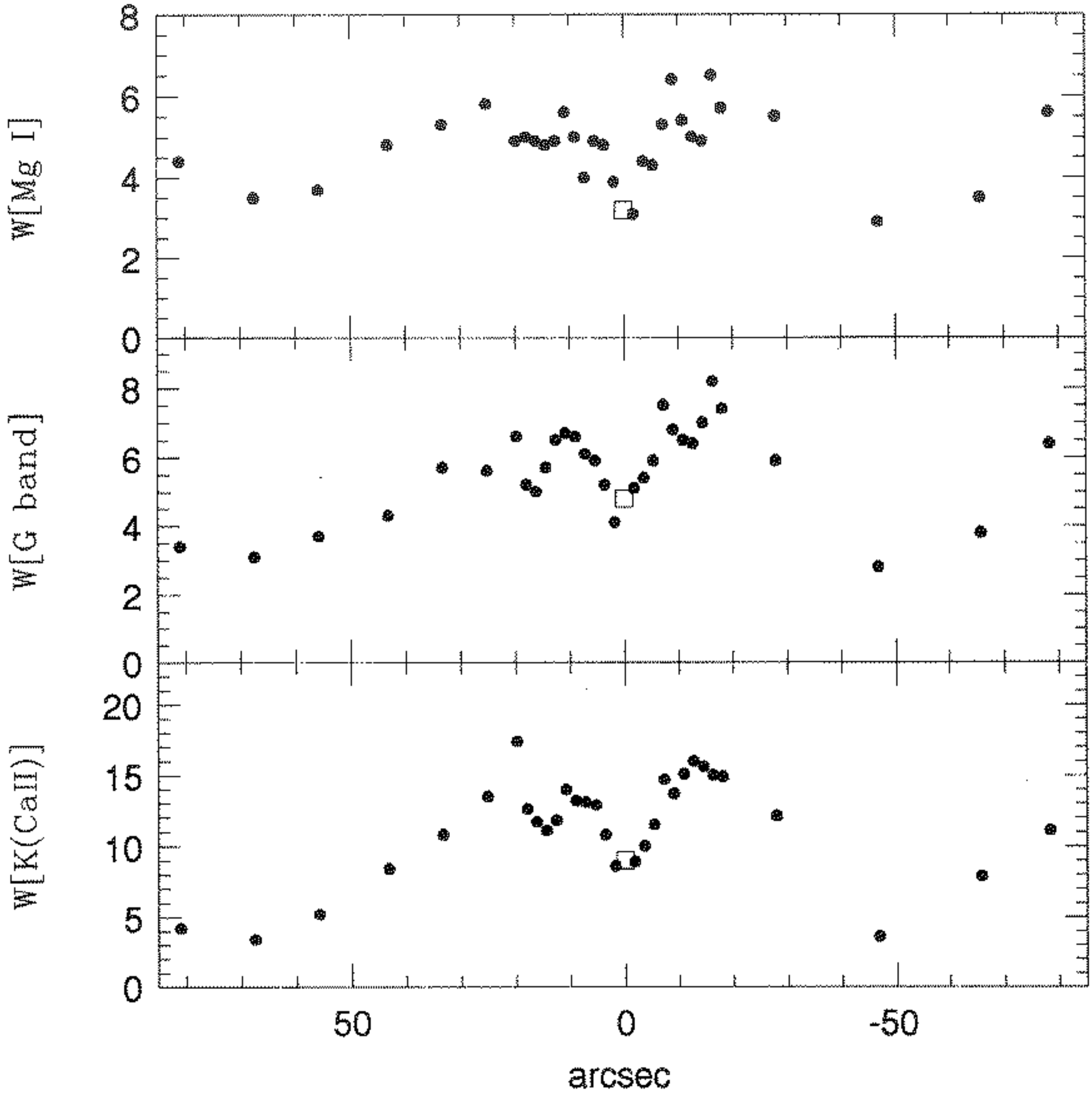

Figure 6: Equivalent widths of the strongest absorption lines in the spectra of NGC5643; lower values at and near the nucleus are probably due to dilution by scattered light from the nuclear source, while the lower values farther than 20 arcseconds from the nucleus are due to younger stellar populations; from Schmitt et al. 1994

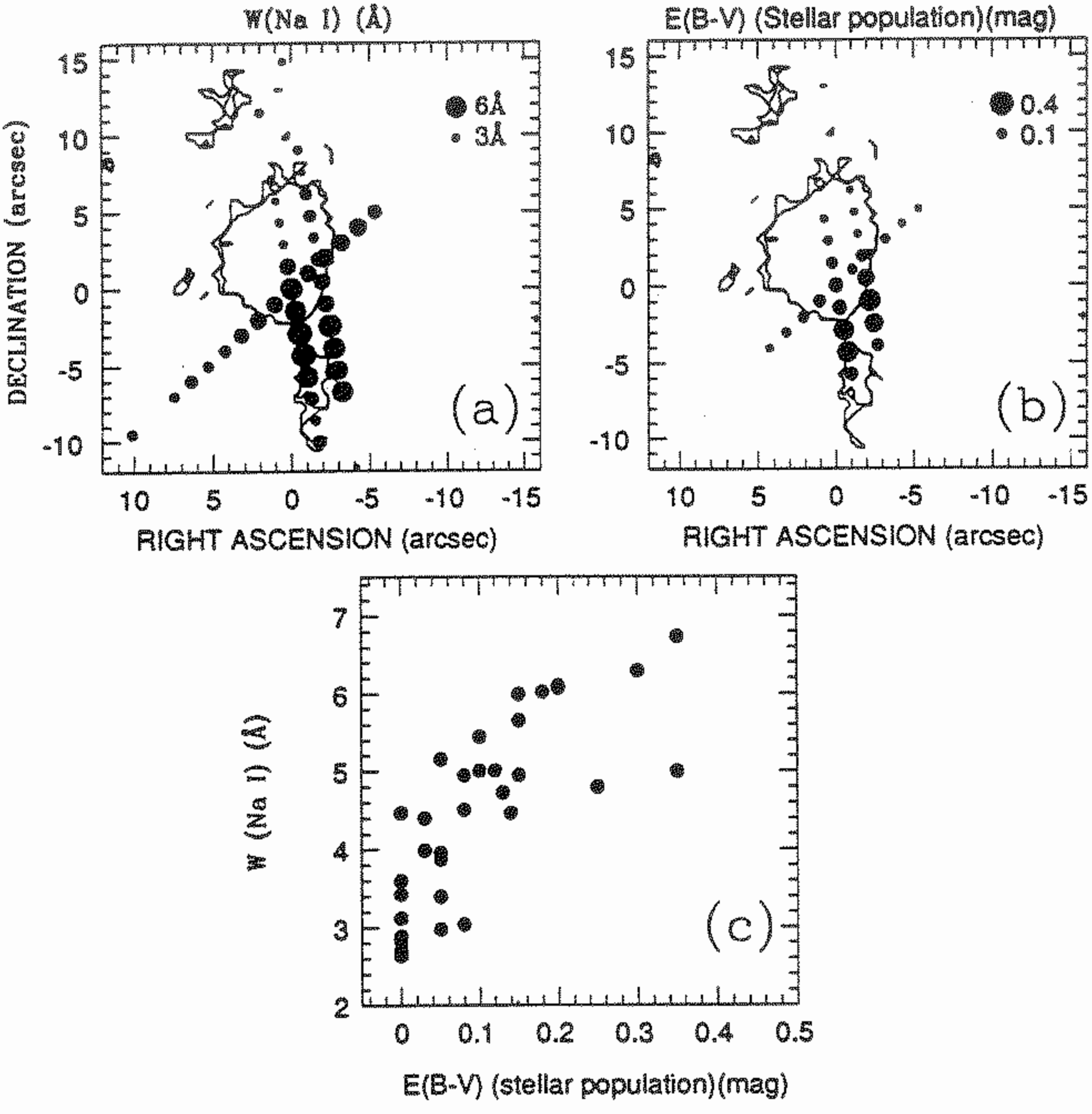

Figure 7: (a)Spatial distribution of the equivalent width of the Na I($\lambda$5893Å) absorption line superimposed on the two outermost isophotes of the continuum-subtracted [OIII] emission-line image of NGC3281; (b) spatial distribution of the reddening E(B-V) derived from the stellar population; (c) relation between W(Na I) and E(B-V)

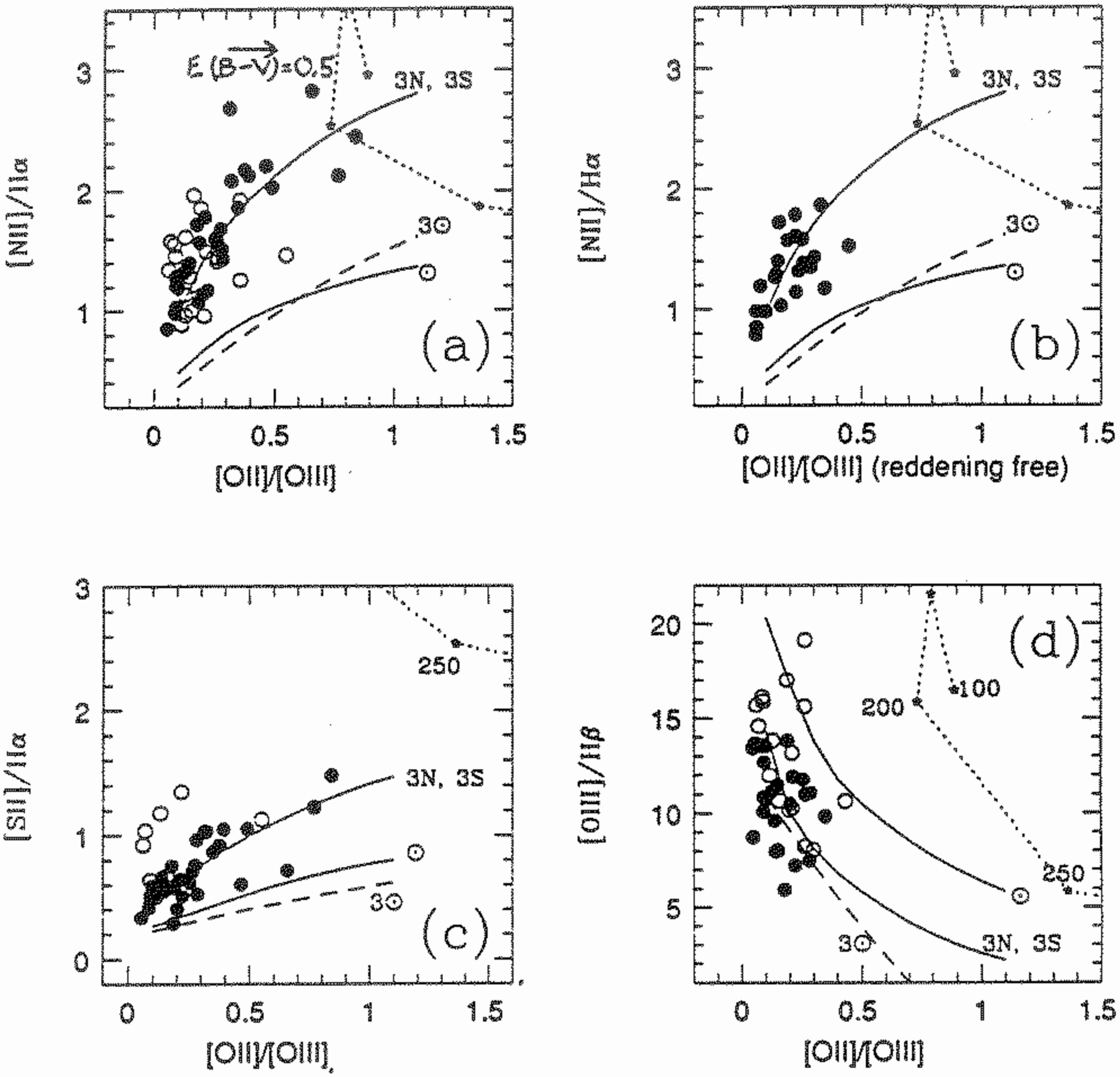

Figure 8: The measured emission line ratios for NGC3281 are compared with a number of models. The dotted line represents shock models for the velocities indicated in (d), while the other lines represent photoionization models for a gas density of $10^3 cm^{-3}$ and ionization parameter in the range $-2.5 \leq logU \leq -3.5$. Models with solar abundance are represented by a continuous line identified by the symbol ⊙; models with nitrogen and sulphur 3 times solar are represented by a continuous line identified by '3N,3S'; the dashed line labeled 3⊙ shows models with the abundance of all the heavy elements enhanced to three times solar; from Storchi-Bergmann et al. 1992

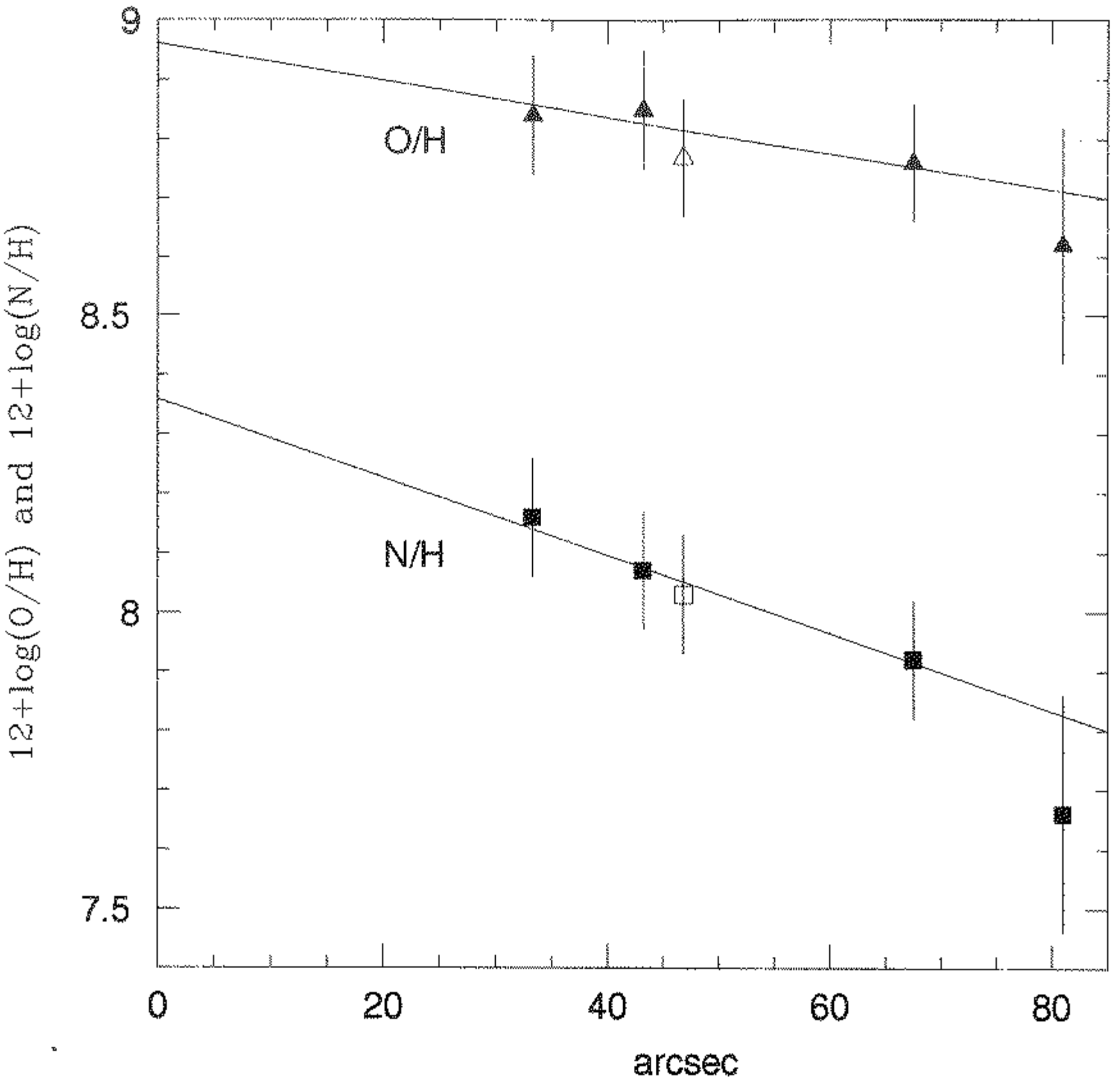

Figure 9: Nitrogen and oxygen abundances as a function of distance from the nucleus for HII regions along the bar of NGC5643; from Schmitt et al. 1994

# Automatic Classification of Galaxies by Artificial Neural Networks

**Laerte Sodré Jr.**
Instituto Astronômico e Geofísico da USP, CP9638, 01065 São Paulo, Brazil

## Abstract

We explore the use of Artificial Neural Networks trained by *backpropagation* in automatic morphological classification of galaxies. We select a sample from the ESO-LV catalogue and train a network to recognize 5 morphological groups using 13 galaxy parameters extracted from the catalogue. The network is trained with 1/3 of the sample and tested on the remaining 2/3. The network classification agrees with the catalogue for 64 % of the galaxies. Considering also neighbour groups, the success rate is 90 %. We also investigate which parameters are well correlated with the morphological type by using a neural network version of Principal Component Analysis. We conclude that central surface brightness and surface brightness at half light are good galaxy descriptors for the data set used.

## 1 Introduction

The morphological type of a galaxy mirrors both its dynamical history and that of its stellar populations. Despite of the great effort put in the study of the properties of the large-scale structure in the last decade, it is surprisingly small the number of galaxies with known morphological types.

Figure 1 shows that Hubble types have been assigned mainly for galaxies with apparent diameters larger than 2 arcmin. The reason is twofold. First, most of these classifications were based on photographic material, mainly Schmidt plates, with plate scales which precluded the classification of small apparent size galaxies. Second, reliable morphological classification has always remained a process dependent on the eyes of a handful of dedicated individuals. Note also that the classification by eye is somewhat subjective and different individuals often produce different classifications for the same set of objects.

It is worth investigating, then, automatic techniques, like Artificial Neural Networks, for morphological classification of galaxies. This kind of procedure has been increasingly used in pattern recognition and shows several advantages. It can be trained according to a subset classified by a human expert, and then it can classify arbitrarily large data sets; it allows a more uniform classification; it may help determining the primary physical parameters defining the Hubble sequence (cf. Brosche 1973).

In this paper we summarize recent results of a project aiming the automatic classification of a large number of galaxies using artificial neural networks. Part of these results were published elsewhere (Storrie-Lombardi *et al* 1992, SLSS92).

## 2 Supervised Classification with Artificial Neural Networks

Artificial Neural Networks (ANN) are computational tools derived from simplified models of the brain (McCullogh & Pitts 1943, Rumelhart & McClelland 1986). They have been used in pattern recognition due to their ability to learn, to generalize, and to cluster or organize data.

There are several paradigms or types of ANN, characterized by a) how the artificial neurons are interconnected (the network topology); b) the characteristics of each artificial neuron (the firing function); c) the strategy for training the network.

We are presently using the so called *backpropagation algorithm*. It consists of nodes (analogous to biological neurons) arranged in a series of layers. The nodes in a given layer are fully connected to the nodes in the next layer. The input layer consists of the input parameters (13 in our case), and the output layer consists of the classes (5 in our case). Any layer between the input and the output layer is called a 'hidden layer'. The input vector for each galaxy, containing the galaxy parameters, is presented to the network and the output is computed. The galaxy is then classified according to the class associated with the largest output component.

The network operates as follows. Each node (except the input nodes) receives the output of all nodes in the previous layer and produces its own output, which then feeds the nodes in the next layer. A node at layer $s$ calculates a linear combination over the input $x_i^{(s-1)}$ from the previous layer $s-1$ according to $I_j^{(s)} = \sum_i w_{ij}^{(s)}\, x_i^{(s-1)}$, where the $w_{ij}$'s are the weights associated with that node. The node then fires a signal $x_j^{(s)} = f(z)$ according to a non-linear threshold function usually of the sigmoid form $f(z) = 1/(1+\exp(-z))$ (producing values in the interval [0,1]), where $z = I_j^{(s)}$.

For a given network architecture the first step is the 'training' of the ANN. In this step the weights $w_{ij}$'s (the 'free parameters') are determined. Note that the 'knowledge' achieved by a network is stored in the $w_{ij}$'s. The network is trained using galaxies with known morphological types. Each one of these galaxies is represented by two vectors. The input vector $\mathbf{p}$ contains parameters measured on the galaxy, often obtained by machine, and which are useful for its morphological description. The target vector $\mathbf{t}$ represents its morphological type, as determined by a human expert. We define $\mathbf{t} = (1,0,0,0,0)$ for Ellipticals, $\mathbf{t} = (0,1,0,0,0)$ for Lenticulars, etc. For each galaxy in the training set the input pattern $\mathbf{p}$ is presented to the network. It produces an output $\mathbf{o}$ which is then compared with the target vector by computing the value of a cost function, usually of the form

$$E = \frac{1}{2}\sum_k (o_k - t_k)^2$$

After a galaxy is presented to the network, the weights $w_{ij}$ are modified in such a way that $E$ decreases. The weights are updated *backwards* from the output layer to one or more hidden layers, by a small change in each time step,

$$\Delta w_{ij}(t+1) = -\eta \frac{\partial E}{\partial w_{ij}} + \alpha \Delta w_{ij}(t)$$

where the 'learning coefficient' $\eta$ and the 'momentum' $\alpha$ control the rate of learning of the network (see e.g. Hertz *et al.* 1991). Note that this kind of ANN does not produce an 'objective' unique classification but replicates the choices of their trainer.

After completion of the 'learning' process the ANN is ready to handle new unclassified data for which only the machine parameters are available. It then produces an output vector for each galaxy. An important aspect of ANN trained by backpropagation is that the $k-th$ component of the output vector can be viewed as the probability for class $k$ given the input parameters, $P(C_k|\mathbf{x})$. In fact, it can be proved (e.g. Gish 1990; Richard & Lippmann 1991) that the output of an ideal ANN is indeed a Bayesian *a posteriori* probability.

## 3 Results of Simulations

We have used in our experiments 5217 galaxies from the ESO-LV catalogue (Lauberts & Valentijn 1989, LV89). We use 13 parameters extracted from the catalogue describing each galaxy and normalized between 0 and 1 (input vectors) . These 13 parameters were chosen because they are distance-independent, and they are very similar to those used by LV89 to perform the automated classification presented in the ESO-LV catalogue (hereafter ESO AUTO). The galaxies were grouped into 5 major classes, E, S0, Sa+Sb, Sc+Sd, Irr, each class corresponding to an output node. See SLSS92 for details on the choice of the sample and on the parameters.

The results presented here were obtained with a topology with 13 input nodes (one for each galaxy parameter), one hidden layer with 13 nodes, and 5 output nodes for classification. The network was then trained with 1/3 of the sample and, after training, it was used to predict the morphological type of the remaining galaxies. Comparing this classification with the visual classification of ESO-LV we found that 64% were correctly classified (for the highest probability choice). If we consider classification to within the nearest neighbour the success rate is much higher, 96 % . For comparison, the percentage of galaxies correctly classified by ESO AUTO is 56 %.

Two interesting quantities which measure the classifier performance are the *hit rate* and the *false alarm rate* (Prusti, Adorf & Meurs 1992). The hit rate of class $C_k$ measures the completeness level of that class, i.e. it gives the fraction of $C_k$ galaxies actually selected of all the galaxies that could have been selected. The hit rates for each class in our test sample are 0.65, 0.39, 0.80, 0.55, and 0.51 for E, S0, Sa+Sb, Sc+Sd, and Irr, respectively. Note that the network, like humans, has difficulties in classifying S0 galaxies! The false alarm rate of class $C_k$ is an estimate of the probability that a galaxy is erroneously classified as a member of class $C_k$. For our five morphological groups we have 0.04, 0.06, 0.33, 0.11, and 0.02. The high false alarm rate of the Sa+Sb group is consistent with the fact that most of the galaxies in our sample are of this class. The *success level* of class $C_k$ estimates the probability to get a true member of class $C_k$ when randomly choosing one object from the set of candidates to class $C_k$. The success level of our classes are 0.63, 0.58, 0.67, 0.59, and 0.69.

It is worth pointing out that the 13 parameters used in this study were parameters already available in ESO-LV. Clearly, by using a more optimal set of galaxy parameters one can improve the performance of the network further.

As discussed earlier, it can be shown that the ANN behaves like a Bayesian classifier. In order to estimate probabilities, the network outputs should sum to one for each galaxy presented. Indeed we find for the test sample that on the average $\sum_k t_k = 1.01 \pm 0.15$. Also, the output $t_k$ averaged over all inputs should be the *a priori* class probability $P(C_k)$ for a class $C_k$. These expected values can be estimated by averaging the network outputs over all input data. Our simulations indicate that our network correctly estimates these probabilities.

## 4 Principal Component Analysis and Artificial Neural Networks

Principal Component Analysis (PCA) is a widely used statistical tool for extracting information from a data set (e.g. Murtagh & Heck 1987, Hertz *et al.* 1991) A pattern can be thought of as being characterized by a point **X** in a N-dimensional parameter space. One may wish a more compact data description, where each pattern is described by M quantities, with M << N. By identifying the combination of input parameters with maximum variance, PCA finds M variables ("principal components") that can be most effectively used to characterize the inputs.

One interesting aspect of ANN theory is that a very simple artificial neuron can be trained to extract the first principal component of the input parameters (Oja 1982). Consider an artificial neuron which receives a set of $n$ scalar-valued inputs $X_1, ..., X_n$ through $n$ connections with coupling strengths $w_1, ..., w_n$ and produces an output $Y$:

$$Y = \sum_{i=1}^{n} w_i X_i$$

During the training of this neuron, the connections $w_i$ are changed after the presentation of a pattern according to the so called Hebbian rule, with the additional constraint that the connections $w_i$ are normalized, i.e.

$$w_i(t+1) = \frac{w_i(t) + \gamma Y X_i}{\{\sum_{j=1}^{n} [w_j(t) + \gamma Y X_j]^2\}^{\frac{1}{2}}}$$

where $\gamma$ is the learning coefficient. Expanding this expression as a power series in $\gamma$ and retaining only the first order term yields the learning equation known as Oja's rule:

$$w_i(t+1) = w_i(t) + \gamma Y(t)(X_i - Y(t) w_i(t))$$

Oja (1982) shows that, after training, this model neuron tends to extract the first principal component of the data set. Also, although no explicit normalization appears in the learning equation, $\sum_{i=1}^{n} w_i^2$ tends to be bounded and close to one.

Sanger (1989) has extended the above treatment. He proposed a new algorithm able of extracting all principal components of a given data set. Consider an input-output net with $n$ inputs and $n$ outputs. The net receives a set of inputs $X_1, ..., X_n$ and the $i$th output produced is given by

$$Y_i = \sum_{j=1}^{n} w_{ij} X_j$$

The learning equation, known as Generalized Hebbian Algorithm (GHA), is

$$w_{ij}(t+1) = w_{ij}(t) + \gamma Y_i(t)(X_j - \sum_{k \leq i} w_{kj}(t) Y_k(t))$$

Sanger (1989) has shown that if random weights $w_{ij}$ are assigned at time zero, then the weight matrix will approach the matrix whose rows are the eigenvectors of the correlation matrix of the input data, ordered by decreasing eigenvalues. Since the training of the $i$th output needs only knowledge of the previous $i-1$ outputs and eigenvectors, the procedure is sequential, each principal component being extracted each time, ordered by decreasing eigenvalues.

Although this algorithm has poor numerical accuracy, this is not a problem if only the first few eigenvectors are needed. Also, if the data has high dimensionality, it may be hard to find the eigenvalues of the correlation matrix by traditional methods and GHA may provide an attractive computational alternative.

We have applied the GHA to a sub-set of the ESO-LV data, with 754 galaxies. The input data was first standardized, i.e. it was transformed to zero mean and unit variance because we know that PCA suffers from scaling problems. A sequential implementation of Sanger's algorithm was used, with $\gamma = 0.1$. It can be shown that 90% of the input variance is explained by the first 6 principal components (PCs).

The PCs don't allow an obvious physical interpretation since they are linear combinations of all parameters. In order to obtain some insight on which parameters contribute most to a given PC we computed Pearson's $r$ between each parameter and each PC. Another procedure which gives the same result is to look for the parameter with the largest coefficient in the linear combination defining a given PC. The result is that the first component is well correlated with $\mu_{oct}^{B}$ ($r$=-0.915) and the second with $\mu_e^B$ ($r$=0.781). Hence, central surface brightness and surface brightness at half light radius are apparently good galaxy descriptors. It would be interesting to verify if this result holds for other data sets, since it can provide interesting clues on the physical nature of the Hubble sequence (e.g. a sequence of stellar concentration, as measured by surface brightness). It is worth noting that the first PC correlates well with morphological type: $r = -0.807$. For the other components, $r$ is always lower than 0.18 in absolute value.

## Acknowledgements

I am pleased to thank O. Lahav, M. C. Storrie-Lombardi, L. J. Storrie-Lombardi, and A. Naim, from the Institute of Astronomy, Cambridge, UK, with whom this project has been conducted in collaboration.

## References

Brosche P., 1973. *Astr. Astrophys.* , **23**, 234.

Gish H., 1990. *in Proc. IEEE Conf. on Acoustics Speech and Signal Processing, p. 161.*

Hertz J., Krogh A., Palmer R.G., 1991. *Introduction to the Theory of Neural Computation, Addison-Wesley, Redwood City, California.*

Lauberts A., Valentijn E.A., 1989. *The Surface Photometry Catalogue of the ESO-Uppsala Galaxies, ESO (LV89).*

McCullogh W.S., Pitts W.H, 1943. *Bull. Math. Biophys.*, **5**, 115.

Murtagh F., Heck A., 1987. *Multivariate Data Analysis, Dordrecht, D. Reidel.*

Oja E., 1982. *J. Math. Biol.*, **15**, 267.

Prusti T., Adorf H.-M., Meurs E.J.A., 1992. *Astr. Astrophys.* , **261**, 685.

Richard M.D., Lippmann R.P., 1991. *Neural Comput.*, **3**, 461.

Rumelhart D.E., McClelland J.L., 1986. *Parallel Distributed Processing: Explorations in the Microstructure of Cognition, Vol. 1: Foundations, MIT Press, Cambridge.*

Sanger T.D., 1989. *Neural Networks*, **2**, 459.

Storrie-Lombardi M.C., Lahav, O., Sodré L., Storrie-Lombardi L.J., 1992. *Mon. Not. R. Astr. Soc.* , **259**, 8p (SLSS92).

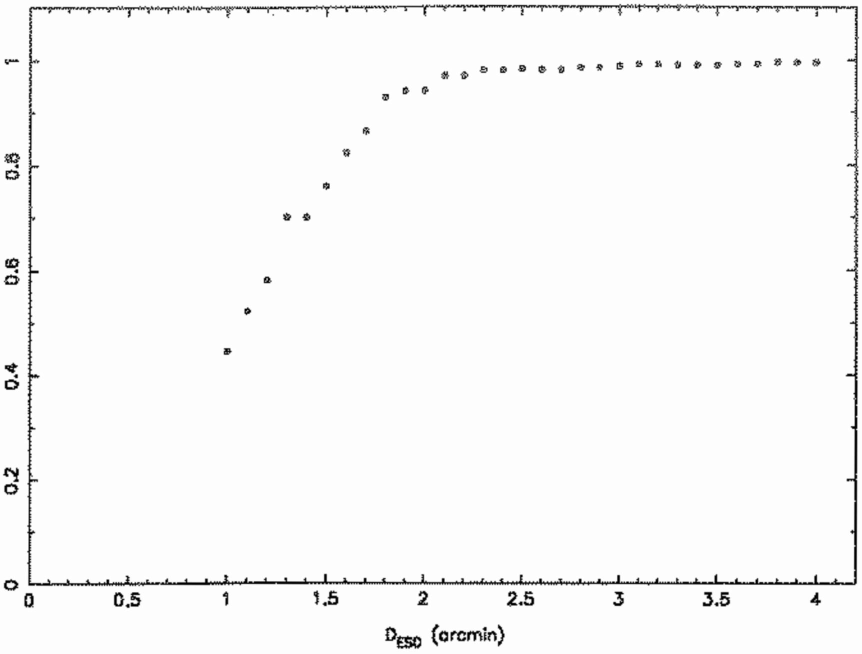

**Figure 1:** fraction of galaxies in the ESO LV catalogue with "good" morphological types, i.e. Corwin or Visual Revised classifications.

# Progress Report of the Redshift Survey on the Declination Strip +9° to +15°

MARCIO A. G. MAIA

Departamento de Astronomia, Observatório Nacional, Rua Gal. José Cristino 77, Rio de Janeiro - 20921 - RJ, Brazil. E-mail: maia@on.br

## ABSTRACT

This paper contains the first results of the 21 cm redshift survey in the declination strip +9° to +15°. Most of the data was obtained using the 305 m Arecibo radiotelescope and is used to map the nearby galaxy distribution, as well as to identify groups of galaxies and examine effects of the environment on the H I content of galaxies.

## I. Introduction

Since the first major effort to map the nearby universe galaxies (Humanson, Mayall and Sandage 1956), astronomers have been trying to improve the capacity to get new redshifts. In particular, the last 15 years have been fruitful with the construction of new generations of optical detectors and radio receivers allowing the acquisition of great amount of data with reasonable low integration times. The redshift surveys samples and instruments are selected as a function of the goals to be achieved, but a major concern when designing a survey proposal, is the amount of observing time that will be necessary to carry out the project.

The H I content can be an important tool in the determination of the total mass of a galaxy and can also reflect the influences of the environment over the galaxy such as tidal interactions, evaporation, collisions between galaxies, ram pressure sweeping. Those mechanisms could trigger a depletion in the interstellar H I gas content in a galaxy (*e.g.*, Haynes, Giovanelli and Chincarini 1984, Giovanelli and Haynes 1985, Haynes *et al.* 1990). With the aim to understand better the importance of each mechanism we are carrying out a H I survey of spiral galaxies in order to associate the 21 cm line information to parameters such as local density of galaxies or distance to the closest companion as well as to infrared and radio continuum flux measurements. The use of information in other range of the spectrum will help also to differentiate the external effects quoted above, from possible internal ones like galactic winds or low mass star formation, that could cause H I depletion. The redshifts obtained in this effort can also be used to map the galaxy distribution in our neighborhood as well as in the study of peculiar motions throughout the use of the Tully-Fisher relation.

In this paper we present the first results from a H I survey currently undergoing in the declination strip +9° to +15°. The sample selection is described in section II and, in section III the observations carried out at the Arecibo Observatory[1], and in section IV we present the first analysis of our data. This work is being carried out in collaboration with L.A.N. da Costa (ON/CNPq), R. Giovanelli, and M.P. Haynes (NAIC/Cornell University).

## II. The Sample

The galaxies belonging to this sample currently being surveyed were extracted from the *Catalog of Galaxies and Clusters of Galaxies* (Zwicky *et al.* 1961–68, hereafter CGCG). They are in a strip 6° wide in the declination range of +9° to +15° spread over the entire range of right ascension, and with apparent Zwicky magnitudes $m_Z \leq 15.7$. No constraints were applied in the selection procedure concerning to the galactic plane, resulting in a preliminary list of 3300 galaxies. All the galaxies in this list had their offset positions measured from the overlays of the Palomar Observatory Sky Survey plates and new corrected positions were determined. The major and minor diameters as well as the morphological types were also obtained. Whenever possible, multiple systems had the above parameters measured and magnitudes estimated for individual members. The accuracy in the coordinates measurements is estimated to be $\approx$ 0.1 arcmin. For those CGCG galaxies also listed in the *Uppsala General Catalog of Galaxies* (Nilson 1973, UGC) the morphological classification and diameter measurements were maintained as quoted in the UGC, unless we had a case of a split multiple system. All the galaxies classified as S0a or later types, were chosen as targets for this H I survey. This amount corresponds to 70% of the galaxies in this region with $m_Z \leq 15.7$.

---

[1] The Arecibo Observatory is part of the National Astronomy and Ionosphere Center, which is operated by Cornell University under a cooperative agreement with the National Science Foundation.

In Fig. 1 we show the projected distribution for all the galaxies selected in this slice. Two major regions can be identified. The first one, in the right ascension range of $20^h$ to $6^h$, is part of the region called "Pisces-Perseus" (see Giovanelli and Haynes 1985, Giovanelli, Haynes, and Chincarini 1982, Haynes *et al.* 1988, Giovanelli 1990). The second region is delimited by $8^h$ to $18^h$ in right ascension and contains part of the Virgo (between $12^h$ and $13^h$ of R. A.) cluster and Hercules ($14^h$ and $17^h$ of R. A.) supercluster as major features. This paper reports results from 21 cm observations carried out mainly on this second region.

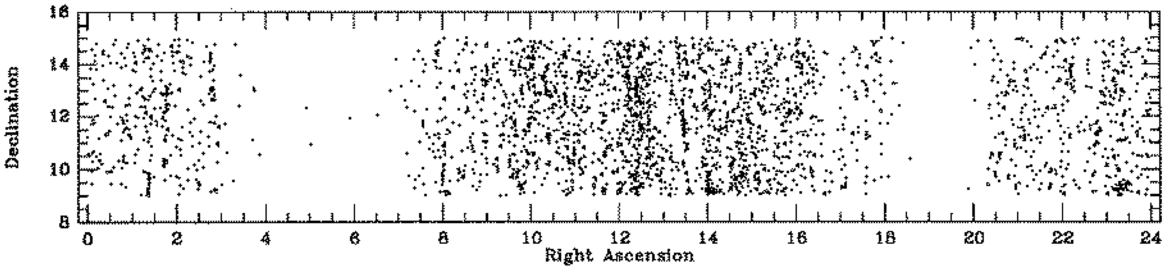

Fig.1 - Projected distribution (not in scale) of galaxies in the slice survey.

## III. Observations

The observations were done using the Arecibo Observatory 305 m radiotelescope in the last 3 years. The dual circular tunable 22 cm feed (L-band) used, are characterized by a half-power beam width of 3$'$.3. The autocorrelator with 2048 channels is subdivided in four quadrants, each one covering 10 MHz, resulting in a resolution of 8 km s$^{-1}$ per channel. After the smoothing procedure during the reduction, the resolution drops to 15 km s$^{-1}$. In the mode called 'search' the two polarization channels were centered at different frequencies allowing the observations to be done over a range of velocities twice as large as if all the quadrants were centered at the same frequency, procedure adopted when the velocity of a galaxy was known or a recent detection had to have its s/n improved.

The observations were made in a total power mode, in which 5 minutes of integration ON source, were followed by 5 minutes OFF source. Both ON and OFF scans were made at the same zenith angle and azimuth in order to minimize the degradation of the system temperature and gain of Arecibo radiotelescope that are very dependent on the position. Absolute fluxes were obtained by measuring the observed antenna temperatures relative to those of noise diodes, that were fed into the waveguide between the feed and receiver. The noise diodes calibration was performed by observing standard calibration continuum point sources listed in Bridle *et al.* (1972). The spectra were reduced using the ANALYZ and GALPAC Arecibo packages. For a more detailed description about the observational procedures see Freudling, Haynes and Giovanelli (1988).

## IV. Discussion

Up to date, the completeness of redshift information achieved in this region is now better than 85% (including optical redshift measurements). The information for late-type galaxies is more complete than the one for the early counterparts. The current spatial distribution can be examined in the wedge diagram of Fig. 2. In this figure are displayed $\approx$ 1800 galaxies with measured redshifts smaller than 15000 km s$^{-1}$ in the range of right ascension $8^h$ to $18^h$ and declination interval $+9°$ to $+15°$.

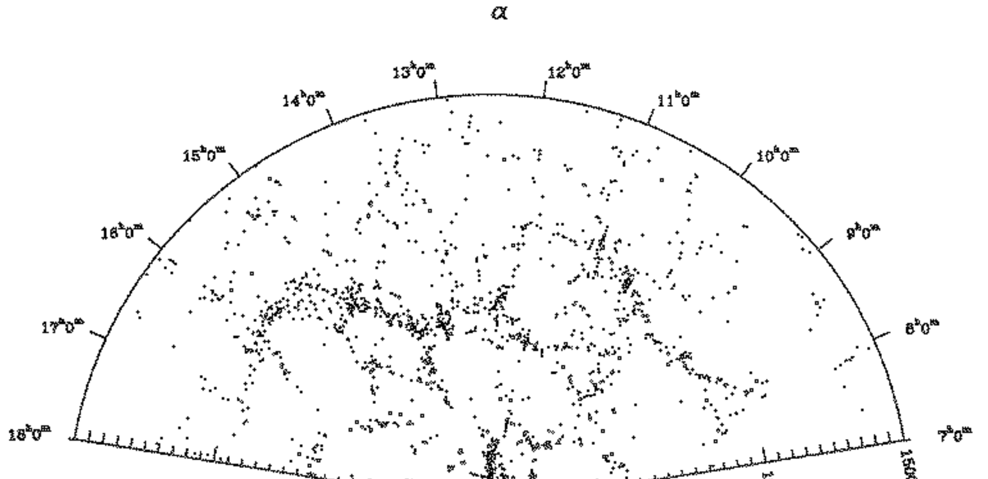

Fig. 2 - Wedge diagram for galaxies in the range of right ascension $8^h$ to $18^h$.

Some prominent features like part of Virgo cluster ($12^h$ $30^m$) and part of Hercules supercluster ($14^h$ to $16^h$) can be easily recognized. The chain of galaxies from $7^h$ $30^m$ to $11^h$ at v $\approx$ 10000 km s$^{-1}$ is a new interesting feature emerging as a result from this work. This "paredon" (using latin-american taxonomy), seems to be similar to the "Great Wall" in extension, but not so spread in velocity. Further observations will help to delineate better this other remarkable structure. Also interesting to note, are the voids suggesting a distribution of matter around them like a honeycomb.

The application of a group finding algorithm (Huchra and Geller 1982, Ramella *et al.* 1989) to the present catalog resulted in the finding of new members for previously known groups and also new groups are identified. The groups were selected with a density contrast, $\delta\rho/\rho$=80 relative to the mean density of galaxies, and the groups with 4 or more members are displayed in Fig. 3. They more or less delineate the large scale structures.

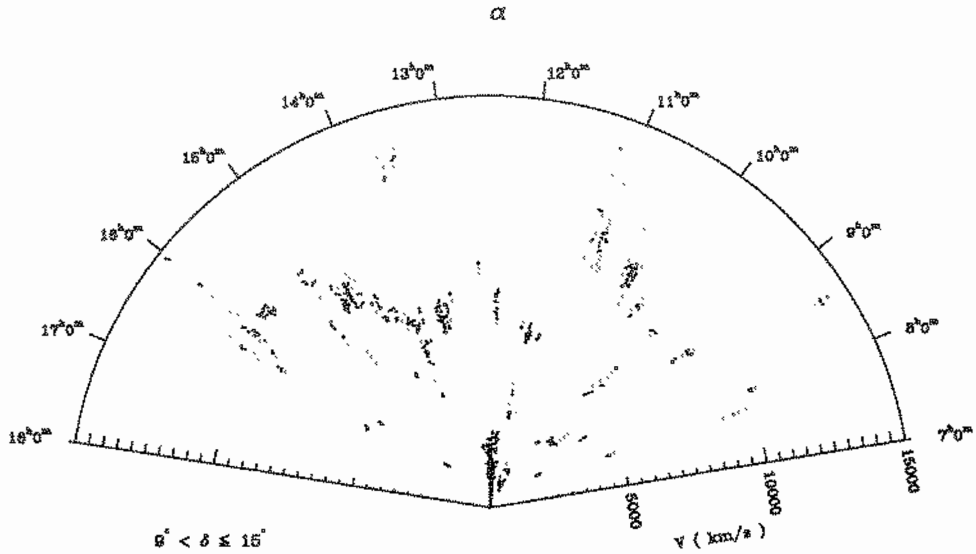

Fig. 3 - Wedge diagram for groups of galaxies in the range of right ascension $8^h$ to $18^h$.

The amount of neutral hydrogen of a galaxy was found to be dependent of the environment for a same class of morphological type (*e.g.*, Haynes and Giovanelli 1986, Scodeggio and Gavazzi 1992). Galaxies in more dense regions, such as core of clusters of galaxies are H I deficient, and ram pressure sweeping is normally the physical mechanism attributed to the gas removal. We examine the H I content for the spirals in the slice region, using as estimator of the neutral hydrogen content the H I mass-to-light ratio $M_{HI}/L_B$, since the H I is also dependent of galaxy luminosity. The $M_{HI}$, in solar units ($M_\odot$), is given by

$$M_{HI} = 2.356 \times 10^5 \ d^2 F_c \ ,$$

where $d$ is the distance in Mpc ($H_o$ = 100 km s$^{-1}$ Mpc$^{-1}$), and F$_c$ is the 21 cm line flux corrected for galaxy self-absorption, in Jy/km s$^{-1}$ as described by Haynes and Giovanelli (1984). The density, ($\rho$) in gal/Mpc$^3$, in the surroundings of a considered galaxy is obtained by the expression

$$\rho = 3N/4\pi[R(v)]^3,$$

where $N$ is the number of galaxies found inside the distance $R(v)$, which is given by

$$R(v) = R_o/[\phi(v)]^{1/3},$$

where $R_o$ is a fixed length (in our case 2 Mpc) and $\phi(v)$, is the appropriate selection function for the catalog. We expect this way, to minimize the effects of incompleteness with distance present in magnitude limited samples. For this analysis we used only galaxies in the interval of absolute magnitudes $-18 > M_Z > -20$, and velocities smaller than 10,000 km $s^{-1}$. The results can be seen in the plot of Fig. 4, where is displayed the $M_{HI}/L_B$ ratio *versus* $\rho$ for a sample of Sb-c, Sc and S... galaxies. It is clear the presence of anemic objects in regions of higher density of galaxies. There is also the suggestion that this effect spans over a large regime of densities in a similar way to the morphology-density phenomena.

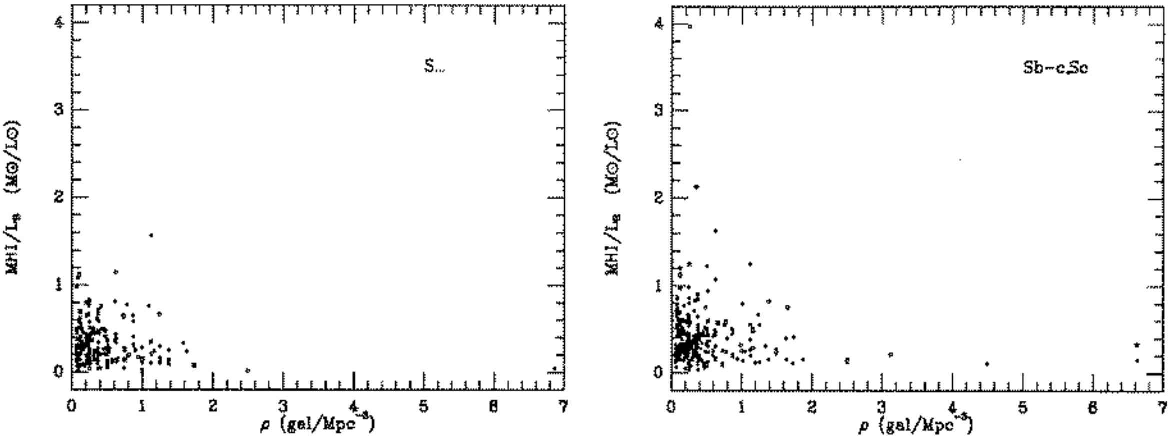

Fig. 4 - HI content estimator against local density of galaxies for two samples of galaxies.

The analysis is being refined in order to consider the distance of the companions as well as their masses on the characterization of the environment conditions, in an attempt to evaluate better the mechanisms involved in the gas removal.

Other environmental effects are to be investigated such as the appearance of barred, infrared luminous and radio galaxies in denser regions. The study of the peculiar velocity field in this region is another subject of our interest. To fulfill this goal we are already reducing and analyzing I-band CCD frames for a subsample of Sb-c, Sc galaxies, and with the 21 cm line widths available, apply the Tully-Fisher relation to measure peculiar motions. This work was partially supported by CNPq grants 204357/88-6, 453471/91-9 and 451076/93-1.

## REFERENCES

Bridle, A.H., Davis, M.M., Fomalont, E.R., and Lequeux, J. 1972, AJ, 77, 405

Freudling W., Haynes, M.P., and Giovanelli, R. 1988, AJ, 96, 1791

Giovanelli, R. 1990, in Large-Scale Structures and Peculiar Motions in the Universe, ed. by L.N. da Costa and D.W. Latham (PASP), p. 303

Giovanelli, R., and Haynes, M.P. 1985, AJ, 90, 2445

Giovanelli, R., Haynes, M.P., and Chincarini, G.L. 1982, ApJ, 262, 442

Haynes, M.P., and Giovanelli, R. 1984, AJ, 89, 758

Haynes, M.P., and Giovanelli, R. 1986, ApJ, 306, 466

Haynes, M.P., Giovanelli, R., and Chincarini, G.L. 1984, ARA&A, 22, 445

Haynes, M.P., Giovanelli, R., Starosta, B.M., and Magri, C. 1988, AJ, 95, 607

Haynes, M.P., Herter, T., Barton, A.S., and Benensohn, J.S. 1990, AJ, 99, 1740

Huchra, J.P., and Geller, M.G. 1982, ApJ, 257, 423

Humanson, M.L., Mayall, N.U. and Sandage, A. 1956, AJ, 61, 97

Scodeggio, M. and Gavazzi, G. 1992, preprint

Nilson, P. 1973 Uppsala General Catalog of Galaxies, (Uppsala Astron. Obs.) (UGC)

Ramella, M., Huchra, J.P., and Geller, M.G. 1989 ApJ, 344, 57

Zwicky, F., Herzog, E., Karpowicz, M., and Kowal, C. 1961-1968 Catalog of Galaxies and Clusters of Galaxies, 6 vols. (Pasadena: California Institute of Technology) (CGCG)

# PRIMORDIAL PERTURBATIONS AND THE GLOBAL PROPERTIES OF ELLIPTICAL GALAXIES

Ronaldo E. de Souza
Instituto Astronômico e Geofísico da USP, Brasil

August 31, 1993

## 1 Introduction

The collapse of an initial perturbation of density $\rho_i$, in a cosmic background density ($\rho_{bi}$), can be exactly calculated in the spherical approximation. The density perturbation follows the same Friedmann equation of general cosmological model (Börner, 1988) with a density parameter given by,

$$\Omega_i = \frac{8\pi G \rho_i}{3H_i^2} > 1 \tag{1}$$

while for the background, in the closed model, the corresponding density parameter is $\Omega = 1$. The general evolution of a perturbation in this framework consist of an initial expansion, with a different rate from the one valid for the background, followed by a collapse and formation of the final object. The initial value of the density parameter of the perturbation can be expressed in terms of the contrast relative to the mean cosmic background by the relation,

$$\Omega_i - 1 = \delta\rho/\rho = \frac{\rho_i - \rho_{bi}}{\rho_i} \tag{2}$$

As time goes on the perturbation evolves and the overdensity region reaches its maximum expansion radius in a time scale $t = t_c/2$, where the collapse time is ,

$$t_c = \frac{\pi}{H_o} \frac{\Omega_i}{(\Omega_i - 1)^{3/2}} \simeq \frac{3\pi}{4} t_o \left(\frac{\delta\rho}{\rho}\right)^{-3/2} \tag{3}$$

where $t_o$ is the present Hubble time (Kolb & Turner, 1990). At turnover the density contrast relative to the background is $\delta\rho/\rho_b \simeq 9\pi^2/16 - 1 \simeq 4.55$.

After the maximum expansion phase the use of the Friedmann equation would predict a collapse to infinite density at $t = t_c$. In a more realistic scenario we expect that before the final colapse, fragmentation of the cloud followed by violent relaxation processes would bring the perturbation near virial equilibrium in a time scale $1/(G\pi\rho)^{1/2} \simeq t_c$. Therefore, the final virialized structure is simply related to the initial perturbation spectrum by the relation,

$$\rho \propto \left(\frac{\delta\rho}{\rho}\right)^3 \tag{4}$$

This relation enables us to estimate the final properties of the virialized structures relative to the initial perturbation power spectra (Gott & Rees, 1975). In fact this relation can be used to explain the scaling relations of elliptical galaxies as observed at the present epoch. In particular if one assumes an initial scale free perturbation spectrum $|\delta_k|^2 \propto k^n$ the corresponding mass density spectrum is $\delta\rho/\rho \propto M^{-(n+3)/6}$, where $M$ is the total mass of the perturbation. After some algebraic manipulation it is possible to show that the Faber-Jackson relation can be reproduced with an spectral index n=-2 (Faber, 1982). More recently Djorgovsky (1991), have used this method to study the Fundamental Plane of elliptical galaxies and found a solution which is degenerate in respect to the spectral index of the initial perturbation. He concludes that these systems lost their memory of the primordial density spetrum because of the violent relaxation and dissipative formation processes.

The use of the standard power spectrum to predict global properties of galaxies in the **cold dark matter** scenario seems however inadequate. This is because the mass spectrum preserves its initial form only on scales of clusters. For galactic scales the relevant perturbation masses have entered in the horizon and the spectrum have the form $\delta\rho/\rho \propto M^{-(n-1)/6}$ (Longair, 1988). For masses bellow $10^{12}M_\odot$ the final spectrum is relatively flat, with larger amplitudes (Kolb & Turner, 1990) and these masses will collapse first, giving rise to an hierarchical clustering picture. The first collapsing systems have a mass of baryons at decoupling era $\simeq 10^5 M_\odot$ with larger ones clustering by association of the smaller ones. Thus we expect that the forming objects obey the relation,

$$\delta\rho/\rho \propto M^{-\frac{n-1}{6}} \tag{5}$$

and therefore the appropriate scaling relations for the protogalaxies in this scenario have the form,

$$\begin{aligned} \rho_i &= \rho_o \left(\frac{M}{M_o}\right)^{-\frac{n-1}{2}} && (6)\\ R_i &= R_o \left(\frac{M}{M_o}\right)^{\frac{n+1}{6}} && (7)\\ \sigma_i &= \sigma_o \left(\frac{M}{M_o}\right)^{\frac{5-n}{12}} && (8) \end{aligned}$$

## 2 The dissipation phase

After virialization we have the dark and baryonic matter homogeneously distributed inside the protogalactic cloud. After the recombination epoch the baryonic component $(10^8 - 10^{12} M\odot)$ is cooled by thermal emission (Börner, 1988) and collapse to a new stable configuration in the potential well of the dark halo. Assuming that the final dark halo have an isothermal truncated profile, follows:

$$\rho(r) = 1/3\rho_i \left(\frac{R_i}{r}\right)^2 \tag{9}$$

Let us also assume that the dissipation mechanisms proceeds up to a point where the internal density in the baryonic region reaches some critical value $\rho_{crit}$ when star forming processes begins to play an important role and the colapse is halted. For an elliptical galaxy this process is quite fast, forming an homogeneous single aged population. At the onset of this copious star formation phase the radius of the region containing the baryonic matter have contracted by a factor $F < 1$, so that a final radius $R_F = FR_i$ is reached.

At this point all the baryonic mass in the protogalactic cloud ($M_B = fM$) is contained inside the final $R_F$ region. In the absence of biasing mechanisms the protogalactic cloud have the same baryonic fraction as the Universe so that $f = \Omega_B/\Omega \simeq 0.2$ for a closed model. On the other hand, the non baryonic mass inside this same final radius is simply given by the scale relation of the dark halo profile ($M_D = (1-f)M$). Therefore, the total mass of the final object can be evaluated and the final density, close to the critical density value, is,

$$\rho_F = \frac{f + (1-f)F}{F^3}\rho_i \simeq \rho_{CRIT} \tag{10}$$

The use of this relation is restricted because of the uncertainties in the estimation of $\rho_{CRIT}$ from first principles. We decided to normalize our results for a "typical" galaxy with total final mass $M_{F_o}$ and a final collapse fraction $F_o$. In that case we obtain,

$$\left(\frac{M_F}{M_{F_o}}\right)^{\frac{n-1}{2}} = \left(\frac{f + (1-f)F}{f + (1-f)F_o}\right)^{\frac{n+1}{2}} \left(\frac{F_o}{F}\right)^3 \tag{11}$$

and for objects not too different from our "typical" galaxy we have $F \simeq F_o$ and the collapse ratio should behave as,

$$F \simeq F_o \left(\frac{M_F}{M_{F_o}}\right)^{-\frac{n-1}{6}} \tag{12}$$

so that the collapsing fraction is weakly dependent on the initial conditions of the primeval spectral index.

# 3 Mass-luminosity relation

Let the final luminosity $L_F$ and the baryonic mass to luminosity $\gamma_B = M_B/L_F = Cte$. In this case the total observable mass to luminosity $\gamma = M_F/L_F$, assuming the approximation given by eq. 12 is,

$$\gamma = \left(1 + F_o \frac{1-f}{f} \left(\frac{M_F}{M_{FO}}\right)^{-\frac{n-2}{6}}\right) \gamma_B \qquad (13)$$

This relation can be compared with the observed correlations of the Fundamental Plane showing a power law dependence of the mass-luminosity ratio with the measured total mass,

$$\gamma_{OBS} \propto M_F^{1/(6\pm2)} \qquad (14)$$

(Faber et al., 1987; Djorgovski, 1988). With such observational constraint we have,

$$n = 1; F_o > \frac{f}{1-f} \simeq 0.3 \qquad (15)$$

And if we consider the error in the observed correlation it results that $0.5 < n < 1.25$.

# 4 Conclusions

A consequence of these results is that the mass-luminosity dependence on the total mass can be combined with the virial theorem to give an approximate solution of the Fundamental Plane. If we consider ellipticals to be self-similar structures (Djorgovski,1990) the the virial equation,

$$\sigma^2 = \frac{GM}{R} \qquad (16)$$

can be combined with the solution coming from the above analysis to yield the solution,

$$R = \sigma^{2\frac{n+4}{8-n}} I^{-\frac{6}{8-n}} \tag{17}$$

and for n=1 we have for the velocity dispersion term an exponent of 1.43, consistent with the reported value of $1.35 \pm 0.15$. For the surface brightness term the predicted value is -0.86 very close to the observed value of $-0.9 \pm 0.1$ ( Djorgovski, 1988).

It is interesting that the expression given in equation 13 for the mass-luminosity ratio is not exactly consistent with a pure power law. In fact it predicts a deviation for small mass objects that may be tested using the appropriate data set. Moreover, this relation may also introduce a bend in the fundamental plane solution that depends on the adopted value for the collapse fraction $F_o$. So that this parameter can be in principle estimated by a careful inspection of the fundamental plane.

## 5 References

-Börner, G., 1988, Chapter 11, *The Early Universe, Facts and Fiction"*, Springer-Verlag.

-Djorgovski, S. G., 1988, in *Starburst and Galaxy Evolution*, Moriond Astrophysics Workshop, TX et al., eds. Frontières, p549.

-Djorgovski,S. G., 1991, in *Cosmology and Large-Scale structure of the Universe*, ed. R. R. de Carvalho, p19.

-Faber, S., et al, 1987, in *Nearly Normal Galaxies*, ed. S. M. Faber, p175, Springer Verlag

-Faber, S., 1982, in *Astrophysical Cosmology*, Pontif. Acad. Scripta Varia # 48, p219.

-Gott, J. R. and Rees, M. R., 1975, *Astron. Astrophys.*, 45, 365

-Kolb, E. W., Turner, M., S., 1990, Chapter 9, *The Early Universe*, Addison-Wesley Pub.

-Longair, M. S., 1988, in *Lecture Notes in Physics*, eds. Appenzeller, I., Habing, H. J. and Léna, P.

# Section 5:

# Software, Modeling and Instrumentation

# Deterministic restoration of Hubble Space Telescope images

Ivo C. Busko
Astrophysics Division – INPE

August 1993

## 1 Introduction

Image restoration techniques are beign used now routinely for Hubble Space Telescope (HST) imagery [1]. However, few image restoration methods were properly tested and characterized for the specific, unique problems associated with that imagery [6, 14, 10, 9, 37, 31]. The question remains: what kind of science is possible to perform on restored images ? Also, very few methods are available in a public domain, easy–to–use format. These are good reasons by themselves for driving a systematic effort in understanding image restoration methods and providing then in a widely usable format. However, we may ask: why should one spend any resources in such an effort, provided HST is going to be "fixed" in the near future ?

The answer is easy:

- There exhists already a large amount of data ($\sim$ 1 Tbyte) collected with HST, suffering from the spherical aberration problem; such data was gathered at a very large cost, and no effort should be minimized in getting *all* scientific useful information from them. In particular, it would be difficult to get time on HST to re–observe a given target present in the data bank, before showing that all information that can be possibily obtained from the available observation was already extracted.
- It is easy to show that, even after the servicing mission (scheduled for December 1993), a gain of $\sim$ 2 in angular resolution can be easily achieved by image restoration techniques.

These arguments led to the development of an Image Restoration Project (IRP), carried out by the Space Telescope Science Institute (STScI), with NASA funding. The project aims specifically at getting the most detailed and exhaustive characterization of image restoration techniques when applyied to HST imagery, as well as providing the most suitable algorithms in public–domain format (as tasks in the IRAF/STSDAS environment).

## 2 The nature of the image restoration problem

The general linear imaging problem can be described, under suitable assumptions [1], by the *superposition* equation in matrix form (assuming lexicographic, or raster–stacked, notation)

$$\mathbf{g} = \mathbf{D}\mathbf{f} + \mathbf{n} \tag{1}$$

---

[1] Linear detection, noise independent from signal, adequate sampling.

where $\mathbf{f}$ is the undegraded *object* or *signal* vector, $\mathbf{g}$ is the observation vector, $\mathbf{D}$ is de degradation (*blur*) matrix, and $\mathbf{n}$ is the noise vector. Notice that, for an $M \times N$ observation frame, $\mathbf{f}$, $\mathbf{g}$ and $\mathbf{n}$ are of size $MN \times 1$, and $\mathbf{D}$ is of size $MN \times MN$. $\mathbf{D}$ has certain "block" properties, which result from the raster–stacking operation.

Given the observation, the blur matrix, and a model for the noise, the image restoration problem poses itself as getting the best estimate $\hat{\mathbf{f}}$ of the signal, given an optimality criterion.

The simplest criterion is the *least squares*, which minimizes the Euclidean norm of the noise vector $\mathbf{n}$. This criterion leads to the so–called *inverse filter* [3]

$$\hat{\mathbf{f}} = \mathbf{D}^{-1}\mathbf{g} \tag{2}$$

Substituting (1), we see that the estimate is equal to the sought signal, plus inverse–filtered noise:

$$\hat{\mathbf{f}} = \mathbf{f} + \mathbf{D}^{-1}\mathbf{n} \tag{3}$$

These results point out to the main problem in image restoration: the *ill–posed* nature of the inversion problem. First, the degradation matrix may be *ill–conditioned*, that is, some of its eingenvalues may be very small or even zero. They will lead to strong fluctuations in the estimate $\hat{\mathbf{f}}$, driven by infinitesimal fluctuations in the data $\mathbf{g}$.

Second, noise amplification may be significant. The degradation matrix usually expresses a sort of *low–pass* filtering operation, that is, degradation is usually associated with the loss of high spatial frequency information (smoothing). Thus, the inverse $\mathbf{D}^{-1}$ represents a high–pass filtering operation. The signal is usually frequency–bound (when properly sampled), but the noise has a more "white" nature, that is, there is usually significant noise power up to the highest spatial frequencies available in the sampled image. So, the inverse filter solution will be dominated by this high–frequency part of the noise spectrum, which will be strongly boosted up by $\mathbf{D}^{-1}$.

The approach to tackle such ill–posed problems is to resort to *regularization* techniques, which attempt to replace the ill–posed problem by an equivalent, but well–posed one. Usually, *external* information on the problem is used to constrain $\hat{\mathbf{f}}$ whitin an acceptable range. Regularization techniques are based on many approaches, as for example:

- Operator modification (Tikhonov–Miller), convergent series truncation [16, 26].
- Projection into convex sets [17, 26].
- Change of variables/topology (set–theoretic methods [18, 20]).
- Replacement of the deterministic ill–posed problem by a stochastic equivalent problem (Wiener filter, Bayesian techniques).

For HST image restoration, the most often used techniques were up to now all stochastic: Richardson–Lucy [28, 30, 34, 32], some versions of the Maximum Entropy technique [10, 14, 38], and Wiener filtering [8, 9]. They may either give reasonably good–looking image estimates, but suffering from lack of linearity, or may be strictly linear but producing estimates with unsatisfactory visual aspect. In this work, we show how deterministic linear techniques may be used in HST image restoration.

## 3 Deterministic image restoration

The word *deterministic* is used in the present context to distinguish the class of methods discussed here from methods that equate one or more of Eq. 1 terms to a realization of an underlying stochastic process [17, 26, 33, 36]. For instance, in the Wiener filter rationale [3, 8], both the signal f and the noise n are seen as particular realizations of stochastic processes, and an esenble average is used to derive the optimal estimator. Deterministic methods, also named *algebraic*, look to Eq. 1 simply as an algebraic equation to be inverted, making no assumptioms at all about the nature of its terms.

The simplest regularization technique in this context consists in adopting the same linear minimum noise norm criterion that leads to the inverse filter, but simultaneously constraining the estimate's high-frequency content by imposing an upper bound $E$ to the Euclidean norm of this high-frequency component [16]:

$$||\mathbf{n}||_R^2 \leq \epsilon^2 \qquad ||\mathbf{C}\hat{\mathbf{f}}||_S^2 \leq E^2 \tag{4}$$

where $\mathbf{C}$ is a $MN \times MN$ matrix denoting a high-pass-type operator (a 2-D Laplacian is often used), and the norms are computed in weighted spaces R and S of general nature (see below).

Combining both criteria, results in the Tikhonov-Miller regularization; that is, minimize

$$\phi = ||\mathbf{g} - \mathbf{D}\mathbf{f}||_R^2 + \alpha||\mathbf{C}\hat{\mathbf{f}}||_S^2 \leq \epsilon^2 \qquad \alpha = \left(\frac{\epsilon}{E}\right)^2 \tag{5}$$

where $\alpha$ sets the amount of regularization [13]. Minimization leads to the solution $\hat{\mathbf{f}}$

$$\hat{\mathbf{f}} = (\mathbf{D}^T\mathbf{R}\mathbf{D} + \alpha\mathbf{C}^T\mathbf{S}\mathbf{C})^{-1}\mathbf{D}^T\mathbf{R}\mathbf{g} \tag{6}$$

where T denotes the transpose, and $\mathbf{R}$ and $\mathbf{S}$ are $MN \times MN$ diagonal matrices which contain the (arbitrary) weights associated to each image pixel.

This arbitrary pixel weighting does not affect the solution's linearity, but enables one to perform ***spatially adaptive*** restoration. The need for spatial adaptivity comes from the existence of the so-called *ringing* phenomenon[25, 26] A space-invariant regularized restoration operator generates estimates which show periodic errors associated whith sharp image structures. These errors have their origin in the well known phenomenon of Gibbs oscillations associated with high-pass filters, and can be strongly enhanced by the zeros of $\mathbf{D}$[27]. These errors are a function of the difference between the regularized operator and the ("perfect") inverse restoration operator $\mathbf{D}^{-1}$. Spatially adaptive restoration uses the fact that the human visual system has a spatial frequency response that strongly depends on image smoothness. Noise amplification is effectively hidden out from vision when it is associated with sharp gradients in the image. In these regions, the restoration operator may approach the inverse operator, thus minimizing ringing and amplifying the (now invisible) noise, while in smooth image regions (where ringing is negligible), the restoration operator may include the regularization term in full and effectivelly prevent noise boost. Usually, the weight matrices $\mathbf{R}$ and $\mathbf{S}$ are computed as a function of the local image variance, taking into account the visual system's frequency response derived from psychophysics experiments [11].

Eq. 6 again includes a matrix inversion operation, but now a well-conditioned one. Several approaches may be used to solve it, but iterative methods are favored[19, 21]. Among them, we may quote

1. Steepest descent:

$$\hat{\mathbf{f}}_0 = \mathbf{0}$$

$$\hat{\mathbf{f}}_{k+1} = \mathcal{P}_k\left[(\mathbf{I} - \alpha\,\beta\;\mathbf{C}^T\mathbf{S}\mathbf{C})\hat{\mathbf{f}}_k + \beta\;\mathbf{D}^T\mathbf{R}(\mathbf{g} - \mathbf{D}\hat{\mathbf{f}}_k)\right]$$

2. Conjugate gradients:

$$\hat{\mathbf{f}}_0 = \mathbf{0}$$

$$\mathbf{r_k} = -(\mathbf{D}^T\mathbf{R}\mathbf{D} + \alpha\ \mathbf{C}^T\mathbf{S}\mathbf{C})\hat{\mathbf{f}}_k + \mathbf{D}^T\mathbf{R}\mathbf{g}$$

$$\mathbf{p_k} = \mathbf{r_k} + \gamma_k\ \mathbf{p_{k-1}}$$

$$\hat{\mathbf{f}}_{k+1} = \mathcal{P}_k\left[\hat{\mathbf{f}}_k + \beta_k\ \mathbf{p_k}\right]$$

3. Convergency order $\mathcal{R} > 1$:

$$\hat{\mathbf{f}}_0 = \beta\ \mathbf{D}^T\mathbf{g}$$

$$\mathbf{B}_0 = \mathbf{I} - \beta\ (\mathbf{D}^T\mathbf{D} + \alpha\ \mathbf{C}^T\mathbf{C})$$

$$\hat{\mathbf{f}}_{k+1} = \sum_{j=0}^{\mathcal{R}_k - 1} \mathbf{B}_k^j \hat{\mathbf{f}}_k$$

$$\mathbf{B}_{k+1} = \mathbf{B}_k\mathbf{B}_k\mathbf{B}_k \ldots = \mathbf{B}_k^{\mathcal{R}_k}$$

4. Combinations of 1 and 3 or 2 and 3.

In the above equations, $k$ is the iteration step, and $\mathcal{P}_k$ is an optional projection into a convex set, applyed at iteration $k$. This projection may be used further to constrain the solution, for instance using the (external) information that all signals $\mathbf{f}$ must be positive. In this case, it takes the form of a simple positivity constraint [26]. Apart from this projection, all solutions are fully linear. Notice that methods 1 and 2 include explicitly the weighting matrices $\mathbf{R}$ and $\mathbf{S}$, that is, they are able to perform adaptive restoration. On the other hand, they have a linear convergency order. Method 3 has a higher convergency order $\mathcal{R}_k$, but does not include space adaptivity. This is the motivation for methods of type 4, in which iterations of 1 (or 2) are intermixed with iterations 3, thus achieving both space adaptivity and accelerated convergency [11]

Iterative solutions have several advantages over alternative aproaches:

- They easily allow implementation of the simplest (and speediest) regularization technique: series truncation. For instance, in the steepest descent solution with $\alpha = 0$ and no space adaptivity ($\mathbf{R}$ is the unitary diagonal matrix), called *modified VanCittert iteration*

$$\hat{\mathbf{f}}_{k+1} = \beta\ \mathbf{D}^T(\mathbf{g} - \mathbf{D}\hat{\mathbf{f}}_k) \qquad (7)$$

  the only way to prevent noise boost is to truncate the series at some suitable $k$.

- In the circulant approximation[2], operations may be performed either in Fourier space or data space, achieving thus maximum computation efficiency:

---

[2] The general space–variant degradation $\mathbf{D}$ may be approximated, in many cases, by a Linear Space Invariant circular convolution, in which case $\mathbf{D}$ becomes a block–circulant matrix. Thus, the matrix operations may be rewritten as scalar operations among their eigenvalues, which in the circulant case are the 2-D Fourier transform coefficients [15]

  - convolutions are more efficient in Fourier space;
  - spatially–variant operations with S and R (non–circulant), as well as the projections $\mathcal{P}_k$, can only be performed in data space.

- S and R can be re–computed at each iteration, using the local variance computed from the current estimate $\hat{\mathbf{f}}$, thus optimizing the method's space adaptation properties.
- If multiple versions $\mathbf{g}_i$ of the same signal f are available (as is often the case with HST observations), they can be used simultaneously to improve restoration quality, with minimal penalty in execution speed [18]. Multichannel–type restoration can be also easily implemented [12].
- R can be used as a "mask" to eliminate bad pixels (cosmic rays, bad pixels/columns, data dropouts) from the restoration process [26].
- There are ways of objectively stopping the iterations at the closest point in which the optimality criteria (4) are fullfiled [35].

## 4 Results

The above described methods are currently beign implemented as an IRAF task, and results are beign evaluated using both "terrestrial" and "astronomical" scenes.

Characterization of image restoration methods is based essentially on objective comparisons between the estimate $\hat{\mathbf{f}}$ and the original signal f; this means that it can only be done with *simulated* data. As terrestrial scene, the "Lenna"" image is beign used in this work, since it became a *de facto* standard in the image restoration literature and numerical data are readily available for it. Astronomical simulated images are beign generated by IRP people and stored as public–domain data in STScI's STEIS data bank. They are all based on HST's TIM (Telescope Imaging Model [7]) and TinyTIM [24] Point Spread Function (PSF) modelling software.

We use both "generic" and "astronomical" criteria to evaluate image restoration performance. The generic criteria do not take into account specific image content; astronomical criteria, on the other hand, are sensitive to the typical science content of an astronomical image. They include linearity in stellar and extended object photometry, photometric error degradation, sky background intensity distribution, etc. [29, 10, 31].

The basic generic criterion for algorithm performance evaluation is defined as a figure–of–merit

$$\eta_2 = 10 \log \frac{\sum_{i,j} (g(i,j) - f(i,j))^2}{\sum_{i,j} (\hat{f}(i,j) - f(i,j))^2} \tag{8}$$

which expresses, in a dB scale, the gain in "quadratic distance" between estimate and object (normalized by the distance between observation and object), achieved by the restoration technique. As an alternative, we are also using

$$\eta_1 = 10 \log \frac{\sum_{i,j} |g(i,j) - f(i,j)|}{\sum_{i,j} |\hat{f}(i,j) - f(i,j)|} \tag{9}$$

in which the quadratic distance is replaced by linear distance. Thus, $\eta_1$ should be less sensitive than $\eta_2$ to a few pixels with large discrepancies, when most image pixels were appropriately restored.

Table 1: "Lenna" image

| Algorithm | | $\eta_2$ | |
|---|---|---|---|
| | | 20 dB$^1$ | 15 dB$^2$ |
| Wiener | | 6.44 | 5.00 |
| iterative | modified VanCittert | 8.35 | 2.28 |
| iterative | $\alpha = 5 \times 10^{-4}$ | 7.31 | 4.70 |
| adaptive | $\alpha = 10^{-3}$ | 8.57 | 5.24 |

(1) Peak signal-to-noise ratio, equivalent to a BSNR = 13.8 dB

(2) Peak signal-to-noise ratio, equivalent to a BSNR = 10.6 dB

Table 2: "Star cluster" image

| Algorithm | | Full image | | Center | | CPU time |
|---|---|---|---|---|---|---|
| | | $\eta_1$ | $\eta_2$ | $\eta_1$ | $\eta_2$ | min., Sparc 2 |
| Lucy | 300 iter., conv. *de facto* | 5.25 | 6.82 | 5.19 | 10.17 | 21 |
| $\sigma$–CLEAN | gain = 0.03, 40,000 iter. | 5.24 | 9.37 | 5.75 | 10.25 | 27 |
| Wiener | | -0.42 | 1.30 | 0.77 | 1.39 | 0.7 |
| VanCittert | $10^3$ iter., $\mathcal{P}$ on all iterations | 5.80 | 8.68 | 4.54 | 10.80 | 23 |
| VanCittert | $10^3$ iter., $\mathcal{P}$ on last 30, every 50th | 5.72 | 8.95 | 5.90 | 11.02 | 7 |
| VanCittert | $10^3$ iter., $\mathcal{P}$ as above, $\beta = 2.$ | 6.30 | 9.92 | 6.25 | 12.10 | 7 |

Tables 1 and 2 depict typical results. For Table 1 data, a Wide Field Camera (WFC) PSF at $\lambda = 0.5\mu m$ was used for the degradation D [6, 2], and white Gaussian, signal–independent noise was added at the levels shown. Results are similar to the ones quoted in the literature for the same test image with similar degradation [11, 18, 20, 21]. In particular, we can see that space adaptivity plays a major role in increasing restoration quality.

Table 2 depicts results for a simulated star cluster imaged by WFC. The same PSF as above was used, but the noise model included both Poisson and CCD readout noise contributions. The full frame, as well as the sub–frame containing the cluster center only, were measured separatelly. The full frame includes a large contribution from the sky background, while the cluster center is strongly dominated by stellar images. The first three lines in Table 2 depict results for the three methods already available as IRAF tasks. The remaining lines depict results for the modified VanCittert iteration (Eq. 7) coupled with a projection into the positive axis (positivity constraint). The projection slows down the computations, so a scheme was devised to turn it on and off along the iteration sequence, following a pre–defined rule, to test its effects on the photometric linearity and sky background pixel distribution, as well as on execution speed. The main result from Table 2 is that the simple VanCittert plus positivity constraint can achieve *global* results comparable, or even better, than other methods currently available for HST image restoration, at a smaller computational cost.

As an example of typical astronomical criteria used in algorithm evaluation, Figure 1 depicts results from stellar photometry performed on the same star cluster simulated image discussed above. Each row in the figure depicts measurements on the image resulting from each method analysed. The last row depicts measurements on the original, degraded observation. First column depicts the pixel intensity distribution in a 50 pixel square area of sky background, devoid of any star light contamination. The second and third columns depict photometric residuals, in the sense restored minus true, as a function of true magnitude. Second column results were obtained using only each star image's *central* pixel, while third column results were obtained using standard aperture photometry techniques (in IRAF's apphot package).

The main conclusion that can be drawn from Fig.1 results is that there seems to be a connection between a given algorithm's linearity, and its ability to control sky background noise boost. The linear (by design) methods, VanCittert and Wiener, produce effectively linear solutions, but at the expense of an increase in background noise. Richardson–Lucy and $\sigma$–CLEAN [23, 22], on the contrary, effectively avoid noise boost, but show a non–linear trend in stellar photometry. This non–linearity results from the fact that fainter stars get buried in noise and are not restored in full. Also, even the linear methods must be seen as that only for *relative* intensities, since zero–point shifts seem to be a common occurrence. The VanCittert iteration shows promising results, since it has full linearity, negligible zero–point shift in a small aperture, and a good potential for reducing confusion among neighbor sources.

## 5 The future

In our continuing effort to fully understand deterministic image restoration methods applied to HST images, we may point out some avenues of research that are beign pursued right now, or will be in the near future:

- The role of the positivity constraint on the VanCittert iteration has yet to be fully understood, since it is in principle a non–linear operation. Other types of projection, using for instance strict local flux conservation by information reshufling among pixels [5], has to be researched also.
- Work has still to be systematically performed on the usefulness of Thikonov–Miller regularization plus space adaptivity, when used on HST images. In particular, since the choice for **R** and **S** matrix diagonal elements is rather arbitrary, other weighting criteria must be tried out. The human visual system's response may not be the best criterion for designing the weighting scheme; something related to the actual content of typical astronomical images (stars, diffuse obbjects, planets, sky background) beign more appropriate.
- Implementation of higher convergency order iterations may result in a large gain in computational speed.
- Other evaluation methods, designed for other astronomical object classes (as e.g. planets, nebulae, galaxies, etc.) have to be developed yet.
- Full testing and evaluation has to be performed also for post–servicing HST data.

As a last comment, we may point out that image restoration techniques can be applied also to ground–based astronomical data. This is a relatively unexplored field (at least in optical wavelenghts [4]) and may be justified by cost arguments (with a similar reasoning as the one presented in the Introduction) for the new generation optical-IR giant ground based telescopes (Keck, VLT, Gemini, Subaru, Magellan, etc.)

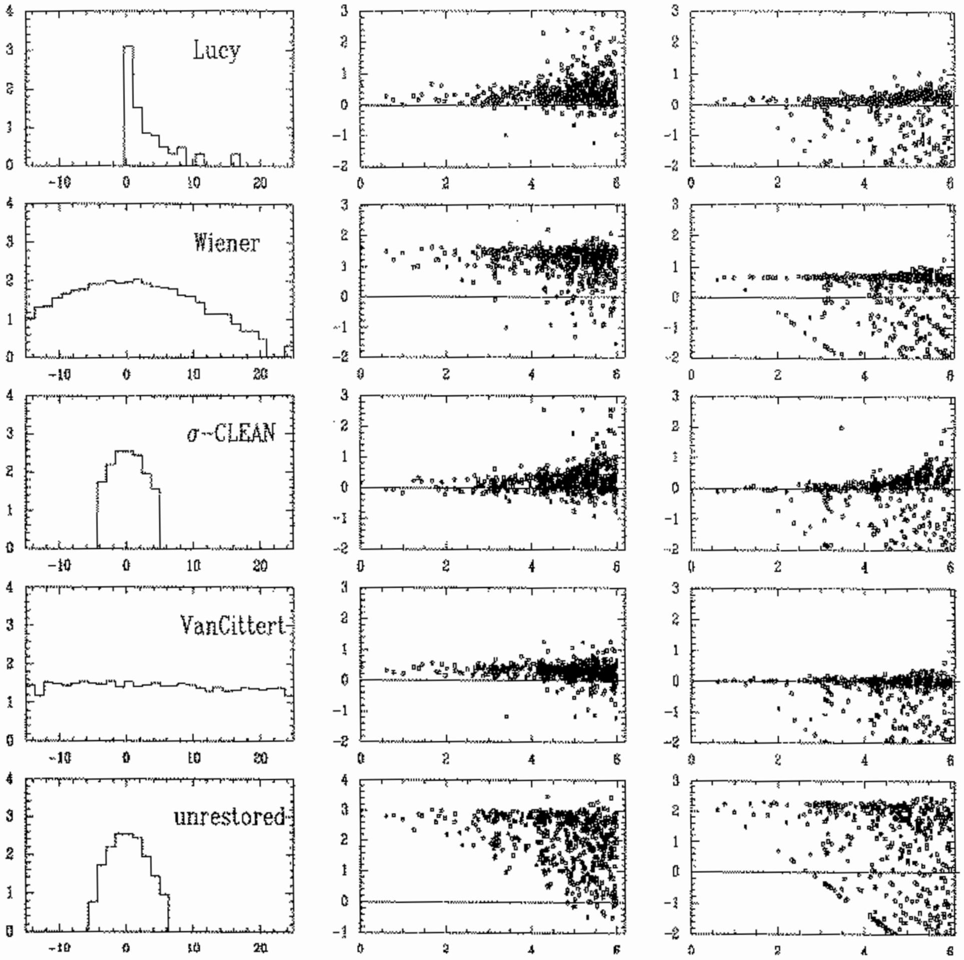

Figure 1: Photometry on star cluster restored images. Left column: background intensity distribution (log scale). Center column: Residuals (restored minus true, in magnitudes) of star central pixel. Right column: Residuals in 2 pixel diameter circular aperture. A positive residual means that the star was restored *fainter* than it should be, and points to a possible non–linearity. Negative residuals are due to crowding/superposition of star images, mostly affecting stars near the star cluster center.

# References

[1] *The Restoration of HST Images and Spectra*, 1990, ed. White, R.L. and Allen, R.J., Space Telescope Science Institute, Baltimore.

[2] Alighieri, S.S., Walsh, J., "The HST Point Spread Function", *ST–ECF Newsletter*, **14**, 4, 1990

[3] Andrews, H.C., Hunt, B.R., "*Digital Image Restoration*", Prentice-Hall, New Jersey, 1977

[4] Arp, H., Lorre, J., "Image processing of galaxy photograps", *Astrophys. J.*, **210**, 58, 1976

[5] Baade, D., Lucy, L.B., "Suppression of High Spatial Frequencies of Background Signals in Direct Images", *in: 1st ESO/ST-ECF Data Analysis Workshop*, ed: Grosbol, P., Murtagh, F., Warmels, R., ESO–Garching, pp 169–172, 1989

[6] Burrows, C.J., Holtzman, J.A., Faber, S.M., Bely, P.Y., Hasan, H., Lynds, C.R., Schroeder, D., "The imaging performance of the Hubble Space Telescope", *Astrophys. J. Letters*, **369**, L21, 1991

[7] Burrows, C., Hasan, H., "*TIM User's Manual*", Space Telescope Science Institute Technical Report, 1991

[8] Busko, I.C., "*Fourier non–iterative image restoration*", Space Telescope Science Institute Technical Report, 1991

[9] Busko, I.C., "Wiener restoration of HST images: signal models and photometric behavior", *in: First Annual Conference on Astronomical Data Analysis Software and Systems*, ed: Worrall. D.M., Biemesderfer, C., Barnes, J., Ast. Soc. Pacific Conference Series, **25**, 220, 1991

[10] Cohen, J.G., "Tests of the photometric accuracy of image restoration using the maximum entropy algorithm", *Astron. J.*, **101**, 734, 1991

[11] Efstratiadis, S.N., Katsaggelos, A.K., "Adaptive iterative image restoration with reduced computational load", *Optical Engineering*, **29**, 1458, 1990

[12] Galatsanos, N.P., Katsaggelos, A.K., Chin, R.T., Hillery, A.D., "Least Squares Restoration of Multichannel Images", *IEEE Transactions on Signal Processing*, **39**, 2222, 1991

[13] Galatsanos, N.P., Katsaggelos, A.K., "Methods for Choosing the Regularization Parameter and Estimating the Noise Variance in Image Restoration and their Relation", *IEEE Transactions on Image Processing*, **1**, 322, 1992

[14] Holtzman, J.A., Groth, E.J., Light, R.M., Faber, S.M., Hunter, D., O'Neil, E.J., Shaya, E.J., Baum, W.A., Campbell, B., Code, A., Currie, D.G., Ewald, S.P., Hester, J.J., Kelsall, T., Lauer, T.R., Lynds, R., Schneider, D.P., Seidelmann, P.K., Westphal, J.A., "Stellar photometry whith the Hubble Space Telescope Wide Field / Planetary Camera: a progress report", *Astrophys. J. Letters*, **369**, L35, 1991

[15] Hunt, B.R., "A Matrix Theory Proof of the Discrete Convolution Theorem", *IEEE Transactions on Audio and Eletroacoustics*, **AU-19**, 285, 1971

[16] Hunt, B.R., "The Application of Constrained Least Squares Estimation to Image Restoration by Digital Computer", *IEEE Transactions on Computers*, **C-22**, 805, 1973

[17] Katsaggelos, A.K., "*Digital Image Restoration*", Springer–Verlag, 1989

[18] Katsaggelos, A.K., "A Multiple Input Image Restoration Approach", *Journal of Visual Communication and Image Representation*, **1**, 93, 1990

[19] Katsaggelos, A.K., Efstratiadis, S., "A Class of Iterative Signal Restoration Algorithms", *IEEE Transactions on Acoustics, Speech, and Signal Processing*, **38**, 778, 1990

[20] Katsaggelos, A.K., Biemond, J., Schafer, R.W., Mersereau, R.M., "A Regularized Iterative Image Restoration Algorithm", *IEEE Transactions on Signal Processing*, **39**, 914, 1991

[21] Katsaggelos, A.K., Kang, M.G., "Iterative Evaluation of the Regularization Parameter in Regularised Image Restoration", *Journal of Visual Communication and Image Representation*, **3**, 446, 1992

[22] Keel, W.C., "Applications of CLEAN to deconvolutions of direct images", *in: First Annual Conference on Astronomical Data Analysis Software and Systems*, ed: Worrall. D.M., Biemesderfer, C., Barnes, J., Ast. Soc. Pacific Conference Series, **25**, 173, 1991

[23] Keel, W.C., "A Simple, Photometrically Accurate Algorithm for Deconvolution of Optical Images", *Pub. Ast. Soc. Pacific* , **103**, 723, 1991

[24] Krist, J., "*The Tiny TIM User's Manual*", Space Telescope Science Institute Technical Report, 1991

[25] Lagendijk, R.L., Biemond, J., Boekee, D.E., "Iterative image restoration with ringing reduction", *in: Signal Processing III: Theories and Applications*, ed: Young, I.T. *et.al.*, Elsevier Science Publishers B.V. (North-Holland) (EURASIP 86), 1986

[26] Lagendijk, R.L., Biemond, J., "*Iterative Identification and Restoration of Images*", Kluwer Academic Publishers, Boston/Dodrecht/London, 1991

[27] Lim, H., Tan, K., Tan, B.T.G., "Edge errors in inverse and Wiener filter restorations of motion-blurred images and their windowing treatment", *Graphical Models and Image Processing*, **53**, 186, 1991

[28] Lucy, L.B., "An iterative technique for the rectification of observed distributions", *Astron. J.*, **79**, 745, 1974

[29] Malumuth, E.M., Neill, J.D., Lindler, D.J., Heap, S.R., "Coping with the Hubble Space Telescope's PSF: crowded field stellar photometry", *in: The First Year of HST Observations*, ed: Kinney, A.L. and Blades, J.C., proceedings of a Workshop held at the Space Telescope Science Institute, Baltimore, 1991

[30] Richardson, W.H., "Bayesian–based iterative method of image restoration", *Journal of the Optical Society of America*, **62**, 55, 1972

[31] Schade, D.J., Elson, R.A.W., "What do you gain from deconvolution ? Observing faint galaxies with the Hubble Space Telescope Wide Field Camera", *Astron. J.*, **105**, 1581, 1993

[32] Stobie, E., "*Lucy deconvolution algorithm*", STSDAS documentation, Space Telescope Science Institute., 1991

[33] Sezan, M.I., Tekalp, A.M., "Survey of recent developments in digital image restoration", *Optical Engineering*, **29**, 393, 1990

[34] Snyder, D.L., "Modifications of the Lucy–Richardson Iteration for Restoring Hubble Space Telescope Imagery", *in: The Restoration of HST Images and Spectra*, ed: White, R.L. and Allen, R.J., Space Telescope Science Institute, Baltimore, 1990

[35] Sullivan, B.J., Katsaggelos, A.K., "New termination rule for linear iterative image restoration algorithms", *Optical Engineering*, **29**, 471, 1990

[36] Tekalp, A.M., Trussell, H.J., "Comparative Study of Some Statistical and Set–Theoretic Methods for Image Restoration", *Graphical Models and Image Processing*, **53**, 108, 1991

[37] Thomson, R.C., Schade, D.J., Elson, R.A.W., Mackay, C.D., Wilkins, T.N., "Deconvolution and photometry of Faint Object Camera images with point sources", *Mon.Not.R.Ast.Soc.*, **259**, 104, 1992

[38] Wu, N., 1993, "Image Restoration by the Maximum Entropy Method", Space Telescope Science Institute Technical Report.

# GAUSSFIT: A Simple Way for Robust Estimate

João Luiz Kohl Moreira
Observatório Nacional, CNPq.

**Abstract:** I present the basic commands for the usage of the package GAUSSFIT. This package is designed to fit a selection of curves allowing a variety of astronomical applications. Very powerful statistical tools, such as: robust estimators, non-linear regressions and fast algorithms are also discussed.

## 1. Introduction.

Statistical sciences have witnessed a huge development on the last decades. Very powerful statistical tools were incorporated to the experimental sciences such as robust estimators, non linear regressions and fast algorithms. The observational astronomer is constrained to learn more about how these tools work to improve its data with more reliable reductions. This manuscript discusses these topics and introduces the package GAUSSFIT that was designed to fit curves allowing a great variety of options.

## 2. Discussion.

Let "f" be a function to be fitted to a set of experimental data $(x_i, y_i)$. The classical Least Square Method minimizes the sum of vertical residuals (Figure 1a):

$$\sum_i W_i(y_i - f(x_i))^2 \tag{1}$$

where $f(x_i)$ is the guessed function and $W_i$ is the weight for each residual in the sum. The term $(y_i - f(x_i))^2$ represents the vertical square distance from the point to the curve. The weight $W_i$ can be written as the inverse of the variance:

$$W_i = \frac{1}{\sigma^2_{y_i}} \tag{2}$$

Astronomers are often confronted with the problem of matching theoretical curves to data that have experimental errors in both axes. Adcock in 1878 proposed orthogonal distances, instead of vertical distances for least square estimate to ensure symmetric regard with respect to $X$ and $Y$ (Figure 1b). The sum (1) becomes:

$$\sum_i \frac{(x_i - \xi_i)^2}{\sigma^2_{x_i}} + \sum_i \frac{(y_i - \eta_i)^2}{\sigma^2_{y_i}} \tag{3}$$

where $\xi$ and $\eta$ are the roots of the equations:

$$\begin{aligned} \eta_i &= f(\xi_i) \\ y_i - \eta_i &= -\left(\frac{\partial f}{\partial \xi_i}\right)^{-1}(x_i - \xi_i) \end{aligned} \tag{4}$$

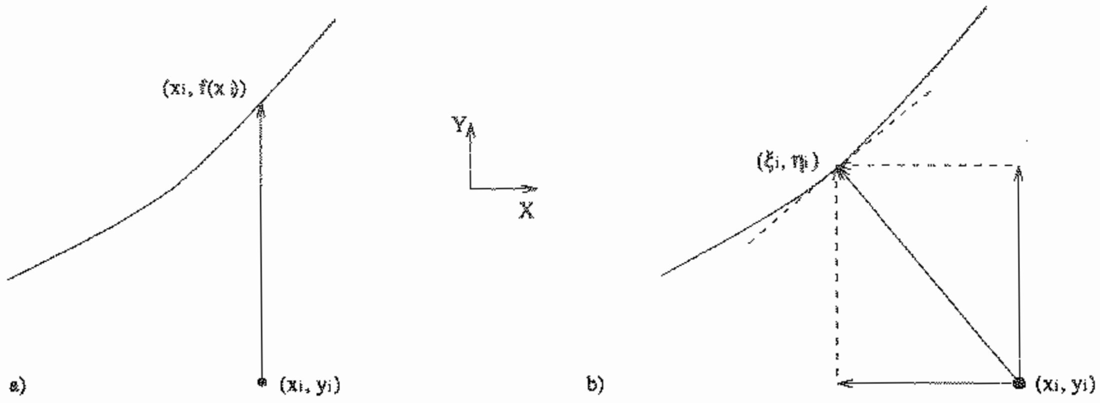

**Figure 1.** **a)** The classical method is to define the residual as the vertical distance between the point and the curve. **b)** The actual procedure is to take the orthogonal distance from the point to the curve.

$\partial f/\partial \xi_i$ is the derivative of the function at $\xi_i$.

These equations represent the distance between the point and the curve. For example, if the $f(\xi)$ is linear with the form: $\eta = a\xi + b$, then

$$\xi_i = \frac{a\,b + ay_i + x_i}{a^2+1}$$

$$\eta_i = \frac{a^2 y_i + ax_i - b}{a^2+1}$$

As we can see from (3) the experimental errors in $X$ and $Y$ are taken into account in this alternative method, but this approach brings out expensive calculations if the analytical function relative to $\eta$ and $\xi$ is not linear. To avoid it, a more simple way is used to estimate the residuals:

$$W_i\,(y_i - f(x_i))^2 \tag{5}$$

where

$$W_i = \frac{1}{(\beta_i^2\sigma_{x_i}^2 + \sigma_{y_i}^2)} \tag{6}$$

and

$$\beta = \frac{\partial f}{\partial x_i}.$$

The residuals remain the vertical distance between the observed points and the theoretical function. However, the weight is a combination of the vertical and the horizontal variances.

In many astronomical problems we need to fit nonlinear functions. Some algorithms are familiar, such as the "steepest-descendent" method and the "linearize-correction" also called Newton's method. The latter is a combination of linear least square and Newton's successive approximations' methods (Bevington[1] 1969, and Press *et al.*[2], 1987). The "steepest-descendent" method is secure but its convergence is *desperately* slow after few iterations. Convergence speed in Newton's method is safer but it can lead to undesirable divergences through the iterations. What we really need is an adequate combination of both previous procedures. A way out for this is to use the steepest-descendent method to provide a first guess, and then apply Newton's method to refine the minimization. This is a good approach because Newton's method diverges specially if the initial guess is far from the solution.

Constraints among the parameters can exist. This problem is solved by the Lagrange multipliers and by adding new equations to the final set of linear equations.

Finally, we often need some robust estimate to discard "outliers" and inaccurate points. Some "metrics" carry out a penalty for such points. Below we list the most popular ones:

fair:

$$\rho(x) = c^2 \left( \frac{|x|}{c} - \ln\Big(1 + \frac{|x|}{c}\Big)\right)$$

huber:

$$\rho(x) = \begin{cases} x^2, & |x| \le c \\ c(2|x| - c), & |x| > c \end{cases}$$

tukey:

$$\rho(x) = \begin{cases} c^{2/3}\left(1 - \left(1 - \frac{|x|}{c}\right)^2\right)^3, & |x| \le c \\ c^{2/3}, & |x| > c \end{cases}$$

The greater $\rho$ is, the lesser is the role that the residuals play in the statistics. The parameter $c$ is arbitrary and ranges between 0.9 and 0.95. A very usual procedure (especially for beginners) is to use the "fair" metric because it does not depend strongly on $c$.

---

[1] Bevington, P.R. (1969), *Data Reduction and Error Analysis for the Physical Sciences*, McGraw-Hill, N.Y.

[2] Press, W.H. *et al.* (1987), *Numerical Recipes*, Cambrigde University Press, Cambridge.

## 3. Developing the Calculus.

For an arbitrary function the iteration process can be written as:

$$\Delta = -[\mathbf{A}^T(\mathbf{X}\sigma\mathbf{X}^T)^{-1}\mathbf{A}]^{-1}\mathbf{A}^T(\mathbf{X}\sigma\mathbf{X}^T)^{-1}\mathbf{F}_0 \qquad (8)$$

where

$\Delta$ - is the correcting parameter vector for each iteration;
$\mathbf{A}$ - first partial derivative matrix $(\partial y_i/\partial a_j)$;
$\sigma$ - weighting factor matrix;
$\mathbf{F}_0$ - Condition equations for the guessed parameters.

After each iteration a correction is applied to the initial set of guessed parameters, so that:

$$\mathbf{v} = \mathbf{v}_0 + \Delta$$

and these new values are used to estimate the function $\mathbf{F}_0$. Then a new solution of (8) is found and this process is repeated until a predefined tolerance to the variation of the merit function is reached.

There are many packages to help the programmer to design its own applications, like "Numerical Recipes" NAG, IMSL and so on. Each has its own style, but all of them yield similar results. Nevertheless, we need to write programs and routines, generally in FORTRAN, that call the package modules specific to each method available in the package. Furthermore, we need to write subroutines with all the theoretical function's derivatives. Once we change the function to be fitted, we must to change the derivative's subroutine. The hardest task: we always need debug our program to be sure we did not make any mistake. Last, we should understand the meaning of all the variables in the program in order to be sure about the interpretation of the results.

Brief, for an astronomer just interested to fit a single straight line to some data points this task becomes a true nightmare! Of course he might plot the points in a graded paper, make a linear regression in a desk calculator, and use the robustness' criteria manually. On other hand, if we have to make the statistics of 150 observations or fit the "King's" or "one-fourth's" law in a dozen galaxy profiles this strategy will bring us back to those romantic ages when astronomers spent their lives filling papers with numbers.

## 4. The GAUSSFIT.

The system GAUSSFIT has come to allow us to do the least square estimate in an easy way. It takes care of all the procedures in weighting correctly the data and in robust criteria. First, it was developed to reduce astrometric data from the Hubble's Telescope by William Jefferys, Michael Fitzpatrick, Barbara McArthur and James McCartney at the "University of Texas at Austin" in 1988. Soon the authors realized that this system could be used to solve any problem on least square fit.

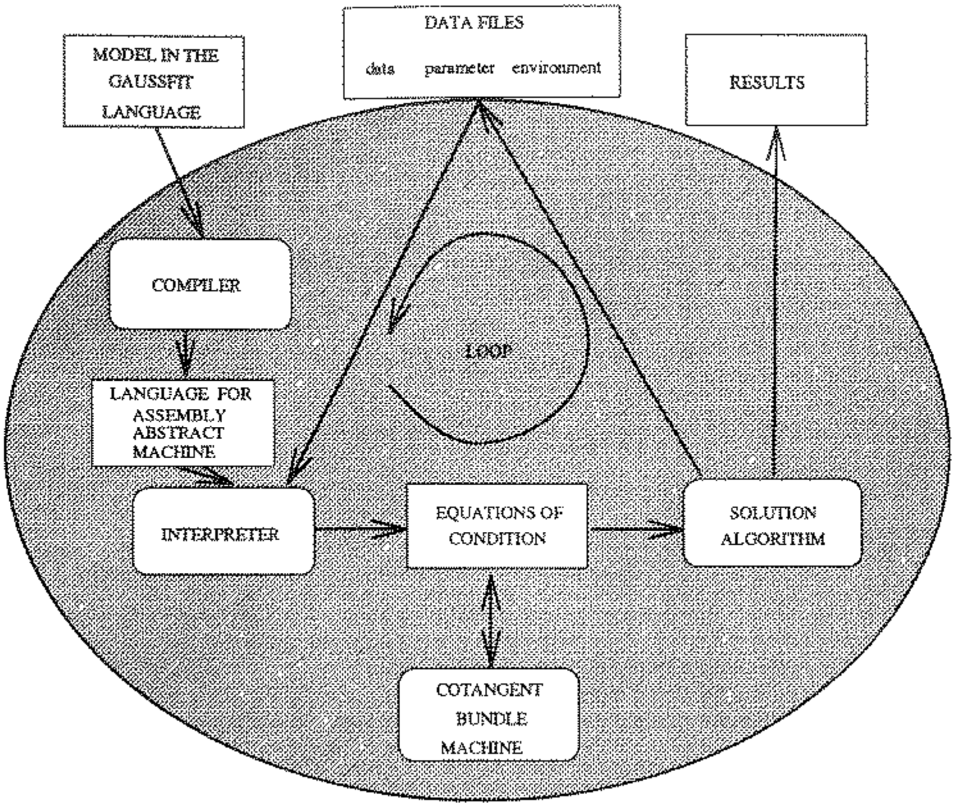
DATA FILES
data parameter environment
MODEL IN THE GAUSSFIT LANGUAGE
RESULTS
COMPILER
LOOP
LANGUAGE FOR ASSEMBLY ABSTRACT MACHINE
INTERPRETER
EQUATIONS OF CONDITION
SOLUTION ALGORITHM
COTANGENT BUNDLE MACHINE

**Figure 2.** The GAUSSFIT's core scheme.

In the Figure (2) we can see how GAUSSFIT works. The shaded area represents the core of the program. The outside boxes represent the files we need to supply.

GAUSSFIT has a compiler similar to"C". It has not the whole features found in this language but it is very simple to use. Everyone who already programmed IRAF scripts, C-modules or even FORTRAN 77 routines could learn quickly the GAUSSFIT language basis.

It compiles the model program, interprets the assembly language, sets the condition equations, decides the best solution's algorithm and runs the loop for the minimization process. Finally it decides when it is time to stop.

We observe a module called "Cotangent Bundle Machine" This is a kind of algebraic manipulator that is in charged of performing all the partial derivatives. These derivatives are those we can find in the equation (8). They are necessary to build the condition equations. However, these calculations are invisible to the user.

### *4.1) The Model Program.*

Let's suppose we want to fit the function

$$y = a\,e^{-bx} \tag{10}$$

to our observations. Although GAUSSFIT can fit arbitrary functions the process will be much faster if we make our functions as linear as possible. Thus the function (10) becomes:

$$\log y = \log a - bx$$

or

$$\log y - \log a + bx = 0 \tag{11}$$

This form is used to build the model program, as follows:

```
parameter a,b;
data x;
observation y;
    main() {
      while ( import()
        export(log(y) - log(a) + b x));
    }
```

The keywords issued in this program have the following meaning:

**parameter** - declares the unknown variables to be found in the estimate;
**data** - declares the error-free data;
**observation** - declares the data subject to errors;
**main()** - shows the program's begin;
**while** - makes the loop reading the data file;
**import** - takes data and observation variables from the data file;
**export** - exports to GAUSSFIT the residuals found for the function to be fitted.

If there is only error-free data we must declare at least a single variable as "observation" Otherwise we could have an error message from GAUSSFIT.

We can define more than a single equation of condition. For example:

```
parameter a,b,c,d;
observation x,y,xi,eta;
    main() {
      while( import()) {
        export(xi-(a*x + b*y + c));
        export(eta-(-b*x + a*y + d));
        }
    }
```

We can also construct intricate programs with nested user-defined functions. Let's see how one can write a program to derive the orbit of double stars:

```
main() {
    setup();
    while(import())
    model();
}

#include kepler
```

Each include-file contains a function defined by the user. We can either include these functions into the program file itself or write it in an independent file as in the example.

An include-file contains:
kepler:

```
kepler(e,M) {   /* Solve Keplers Equation */
    variable E0,E,n;        /* Local variables */

    E0 = 0; /* Initialize old eccentric anomaly */
    E = M;  /* Initialize eccentric to mean anomaly */
    while(abs(E-E0)>1.0e-5) {
    E0 = E; /* Update old eccentric anomaly */
    E = M + e*sin(E);       /* Keplers equation */
    }
    return E;
}
```

Note that the "kepler" routine is an iteration process for solving the Kepler equation. GAUSSFIT takes care of the derivatives of the functions, even if they are calculated by numerical methods.

A constraint is exported to GAUSSFIT by the assignment:

**exportconstraint**( *equation of constraint* );

For example, if we want to constraint the parameter "a" to 1, we write:

**exportconstraint**(a - 1);

For advanced features in the programming language, see the "Gaussfit User's Manual"

### *4.2) The Data Files.*

It may exist more than one data file. All the variables declared as data or observation in the program must appear in one of these files. To build a data file we need to observe the following rules:

1) The first line must contain the name of the data separated by a regular delimiter (space or TAB). If an observation is "eta" its covariance will be named "eta_eta" If two variables are correlated (e. g. "eta" and "x" then the name of the correlation column should be "eta_x" GAUSSFIT will add new columns labeled with the variable name preceded by

an underscore. The entries in these columns contain the residuals calculated by the most recent iteration;

2) The second line must be filled with the word "double" For each keyword in the first line there must be a word "double" in the second line separated by the same regular delimiters (spaces or TABs). This directive suggests that we shall choose words like "single" or "complex" in the future. For while only the word "double" should appear.

3) In the sequence of the second line, we write the entries of experimental data with the same delimitation rules. No blank lines are allowed.

Here, a sample of a data-file:

```
x       eta     x_x
double  double  double
221.5   -138.2  0.1
338.8   322.5   0.1
-720.0  -462.1  0.2
```

We can go further and build more complicate combinations like indexed parameters, linked data between data files and program files, and so on. See "User's Manual" to learn more about it.

### *4.3) The Parameter Files.*

GAUSSFIT looks for the files that contain the initial guess of the parameters. We can build as many files as the parameters being fitted. The rules for the parameter files are the same as the data files: the first line is for the parameters' name and their correlations, the second line is for the word "double", and so on.

### *4.4) The Results File.*

GAUSSFIT writes the final results into a previously declared file (see the environment file description) Furthermore, GAUSSFIT will create two results-files with suffixes ".cov" and ".corr" The former contains the covariance matrix and the latter, the correlation matrix. The "Results" file contains the whole report of the GAUSSFIT execution. At the end of this file, we can see the fitted parameters and their variance.

## 5. Extended Needs.

Beyond the files listed above, GAUSSFIT requires yet another a file. It is also classified as Data File. One is the file described above containing the initial values for the parameters. Because GAUSSFIT is always iterative, it needs a set of initial guessed values. These values are stored in the "Parameter File" The program update these values after each iteration and uses them to the next one. When the process ends, the "Parameter File" contains the final parameter values so we can see the fitted parameters either in the Results File or the Parameter File.

In the environment file we insert all the variables that reflect our choices of the statistics and the name of the Data File, Results File, Parameter File and so on. The way we form the environment file is as follows.

Each keyword has up to eight characters. At the ninth column we write the "=" sign. Then we write the value for the keyword until the twentieth column. Let's see a sample of this file:

```
results = 'MyResults'       # Results filename
data3   = 'MyData'          # One of the data files
param1  = 'MyParamFile'     # Parameter filename
data1   = 'MoreData'        # Other data file
iters   = 5                 # limit for the n. of iterations
tol     = 0.0001            # tolarance for stopping iterations
triang  = 1                 # Use triangular matrix method
fair    = 0.9               # choose ``fair'' metric with c=0.925
END                         # end of environment variables
```

## 6. How to Execute GAUSSFIT.

We call GAUSSFIT from the package "stsdas.contrib" in IRAF V2.10. The help facilities are available. We type:

```
cl> gaussfit
```

A query for the model program is prompted. We type the name of the model file. Then we give the environment file name under its prompt. The report scrolls on the screen while the program runs, until the process stops. Then we can make the needed modifications or collect the results.

*"You can't win GAUSSFIT. Enjoy it."*

# 3-D SIMULATIONS OF CONTINUOUS AND PULSED ASTROPHYSICAL JETS

Elisabete M. de Gouveia Dal Pino[1]

[1]University of São Paulo, Instituto Astronômico e Geofísico, Av. Miguel Stéfano 4200, São Paulo, SP 04301, Brazil

## ABSTRACT

Astrophysical jets play an important role in the evolution of both young stars and active nuclei of galaxies. These highly collimated flows may be the primary way that the sources lose the angular momentum that they gain when they accrete material from a dense surrounding disk.

In this work, we present fully three-dimensional simulations of supersonic jets performed with the Cartesian Smoothed Particle Hydrodynamics technique (Refs. 1, 2, 3, 4 & 8). The structure and evolution of radiative cooling jets ejected from the source with both constant and variable velocities are examined.

## 1. INTRODUCTION

The astrophysicaal jets are generally observed to have a chain of well-aligned, nearly equally spaced emission knots along the flow. The knots often become fainter and disappear at large distances but, in some cases, the jet eventually reappears as a bow shock-shaped region of emission which corresponds to the head of the jet (e.g., Ref. 5).

Recently, we have performed fully three-dimensional (3-D) hydrodynamic simulations of supersonic flows ejected with a constant velocity $v_j$ from the source (Refs. 1, 2 & 4). In these studies, the dynamics of the jet interaction with the ambient medium and the structure of the jet head were examined in detail. In this work, we present simulations of supersonic flows ejected with both constant and also non-constant velocities from the driving source and explore the possibility that the emitting knots are internal shocks produced in the jet flow as a result of time variations in the ejection velocity. (Ref. 3). This possibility has also been investigated by a number of authors (e.g., Refs. 6 & 7 ). We have recently proposed a similar mechanism to explain the multiple bow shock structures that appear in some souces (Ref. 8). Such time variations could be associated to eruptive phenomena in the accretion disk at the central source (e.g., Ref. 9).

We assume here that the jets are *overdense* (i.e., denser than the ambient medium in which they propagate), and *radiative cooling*. Such characteristics are particularly relevant in jets which emanate from young stars but our results are also applicable to extragalactic jets.

## 2. THE NUMERICAL SIMULATIONS

The hydrodynamics conservation equations that describe the evolution of the flow are solved numerically using the 3D Cartesian, gridless, Lagrangian Smoothed Particle Hydrodynamics (SPH) technique (cf., Refs. 1, 3 & 4). The jet and the ambient gas are treated as a single ionized fluid with a ratio of specific heats $\gamma = 5/3$.

The radiative cooling (due to collision excitation and recombination) is implicitly calculated using the cooling function for a gas of cosmic abundance, cooling from $T=10^6$ K.

A uniform background gas is represented by a 3D rectangular box. A collimated, supersonic jet of radius $R_j$ is injected in the bottom of the box which has dimensions up to $30R_j$ in the z-axis and $12R_j$ in the transverse directions x and y, where $R_j$ is the jet radius. The boundary conditions on the xy peripheries of the box are assumed to be periodic and on the z peripheries are continuitive ($\partial \mathbf{v}=0$).

A supersonic jet propagating into a stationary ambient gas will develop a double shock structure at its head. The impacted ambient material is accelerated by a forward bow shock and the jet material is constantly decelerated at a shock wave at the end of the jet, i.e., the jet shock. Models of non adiabatic jets are characterized by three dimensionless parameters: $M_a=v_j/c_a$ the ambient Mach number , where $c_a$ is the ambient sound speed; $\eta \approx n_j/n_a$ the ratio of the density of the jet to the ambient medium; and $q_{bs} = d_{cool}/R_j$ the ratio of the cooling length in the postshock gas behind the bow-shock to the jet radius (which, for shock velocities ≥90 km/s, is related to the ratio measured in the postshock behind the jet shock $q_{js}$ *via* $q_{js} \approx q_{bs}\eta^{-3}$ (cf., Ref. 1)). Based on the observations, we adopt here standard initial conditions to compute the propagation of the stellar jets.

As an examlple, Fig. 1. depicts the evolution of a cooling jet ejected with a constant velocity $v_j$=250 km/s, $\eta$=1, $n_j$=20 cm$^{-3}$, $R_j$=2x10$^{16}$ cm, $M_a$=20, $M_j=v_j/c_j$=20, and $q_{js}=q_{bs}\approx 0.63$. The entire evolution corresponds to an age $t=z/v_{bs}\approx 1115$ yrs (where $v_{bs}\approx v_j/(1+\eta^{-1/2})$ is the bow shock speed). A dense shell develops in the head of the jet. It is formed by the cooling of the shock-heated gas in the working surface. The head becomes dynamically unstable and disrupts into clumps which eventually spill out to the cocoon that surrounds the beam, forming an elongated plug

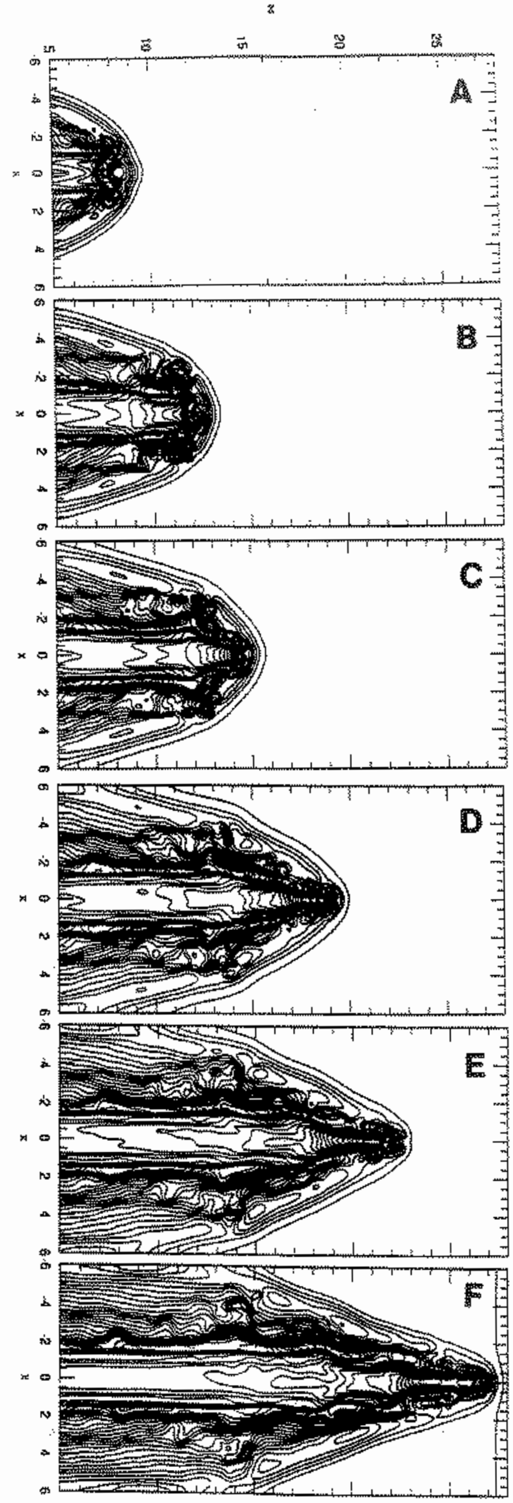

Figure 1. Density contours of a continuous jet with $\eta=1$, $n_a=20\ cm$-$3$, $v_j=250$ *km/s*, and $M_j=M_a=20$. The contour lines are separated by a factor of 1.2 and the density scale covers the range from ≈0 up to ≈ $170/n_a$.

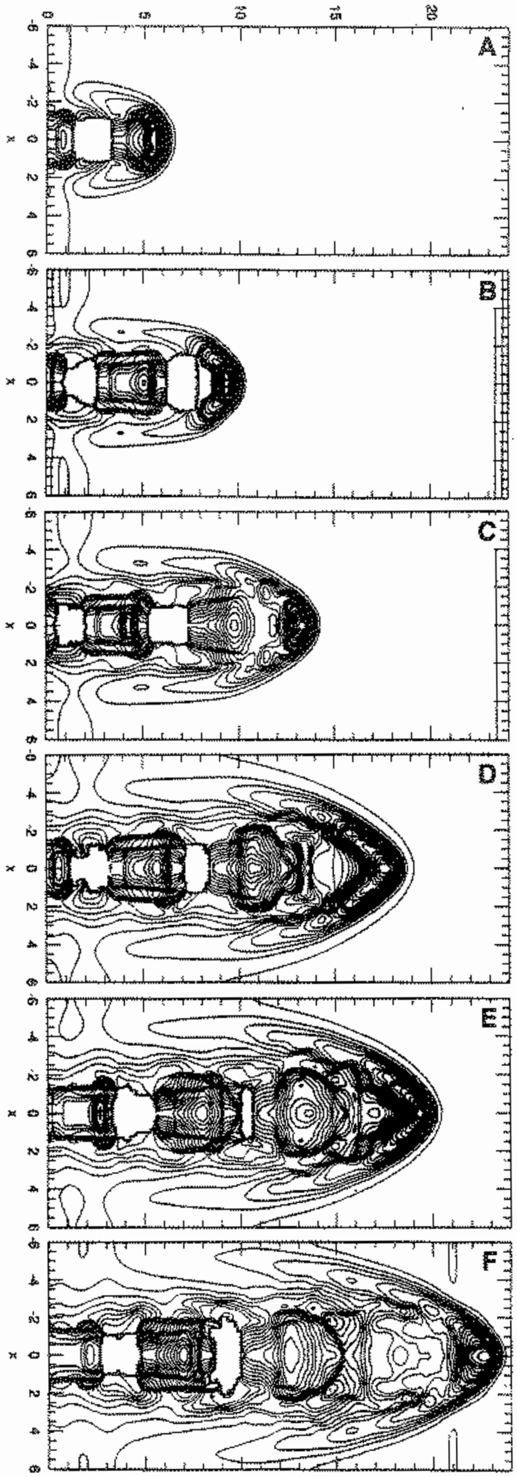

Figure 2. Density contours of a pulsed jet with $\eta=10$, $n_a=1000\ cm^{-3}$, $v_j=150$ *km/s*, and $M_j=9.48$, $M_a=3$. The contour lines are separated by a factor of 1.2 and the density scale covers the range from ≈0.01 up to ≈ $65/n_a$.

(Figs. 1b-d) . The disruption is caused by the combined effect of non uniform cooling and the Rayleigh-Taylor instability (Ref. 1).

As the dense shell disrupts, its density may also undergo time oscillations which are due to the development of global oscillatory thermal instabilities (cf., Ref.1).

Both, the formation of clumps and the density oscillations on the shell are consistent with the knotty and variable emission pattern observed at the head of the cosmic jets.

We note that in Fig. 1, no internal knots are formed along the jet. The radiative cooling reduces the thermal pressure which is deposited in the cocoon that envelopes the beam. As a consequence, fewer (or none) internal shocks are excited by the pinch mode of the Kelvin-Helmholtz instability. In fact, in our simulations of jets with constant ejection velocity, only very heavy jets ($\eta \approx 10$) have developed few internal shocks (through this mechanism of beam pinching) with periodic spacing, as required by the observations of the knots in the cosmic jets.

Fig. 2 depicts the evolution of a pulsed jet which is periodically "turned on" with a supersonic velocity $v_j$=150 km/s and periodically "turned off" to a subsonic regime with velocity 15 km/s. The turning on and turning off periods are both equal to ≈127 yrs. The other initial parameters are $\eta = n_j/n_a = 10$, $n_a = 1000$ cm$^{-3}$, $R_j = 2 \times 10^{16}$ cm, $M_j = 9.48$, *and* $M_a = 3$. The entire evolution in these plots corresponds to a jet age $t \approx 1335$ yrs. The cooling distance parameters are given by $q_{bs} = 6.8 \times 10^{-3}$ and $q_{js} \approx 8.8 \times 10^{-2}$, implying that both shocks in the jet head cool very fast ($q_{bs}$, $q_{js} << 1$) and are nearly isothermal. The cold shell is, therefore, very thin as shown in Fig. 2.

We see that the high amplitude velocity variations at the jet inlet causes the formation of pulses which quickly evolve to a chain of shocks. For each pulse, a shock (propagating downstream approximately at the jet speed $v_j$) is formed as the pulse sweeps up the low velocity, rarefied material ahead of it. As the shocks travel downstream they widen and fade. This is due to the pressure in the postshock material which eventually causes the jet material to be ejected laterally to the cocoon. The maximum density behind these internal shocks is $n_{is}/n_a \approx 30$, while the maximum density in the leading working surface at the jet head is $n_{ws}/n_a \approx 65$. This implies that the emission from these shocks is of smaller intensity and excitation than the emission from the head, as required by the observations.

## 3. CONCLUSIONS

Our simulations show the presence of a dense cold shell at the jet head which is formed by the cooling of the shock-heated gas when $q_s = d_{cool}/R_j \leq 1$. The shell is, in general, dynamically and thermally unstable and fragments into clumps. The clumpy shell and its variable density resemble the knotty and variable emission pattern often observed at the head of the cosmic jets.

The radiative cooling reduces the thermal pressure which is deposited in the cocoon/shroud that envelopes the beam. As a consequence, fewer internal shocks are produced via beam pinching in cooling, continuous jets. Jets ejected with time-dependent velocities, on the other hand, develop a chain of radiative internal shocks which fade as they move away from the source with approximately the jet velocity, in agreement with the observed internal knots of cosmic jets.

## REFERENCES

1. Gouveia Dal Pino, E.M., & Benz, W. 1993, *Astrophysical J., 410.*

2. Gouveia Dal Pino, E.M., & Benz, W. 1993, in *Proc. of the International Toki Conference, on Plasma Physics and Astrophysics, Japan , Nov. 1992* (in press).

3. Gouveia Dal Pino, E.M., & Benz, W. 1993, *Astrophysical J.*, (submitted).

4. Chernin, L., Colin, M., Gouveia Dal Pino, E.M., & Benz, W. 1993, *Astrophysical J.*, (in press).

5. Reipurth, B. 1989, Nature, 340, 42.

6. Raga, A.C. & Kofman, L. 1992, *Astrophysical J.*, 386, 222.

7. Stone, J. & Norman, M. 1993, *Astrophysical J.*, (in press).

8. Gouveia Dal Pino, E.M., & Benz, W. 1993, in *Proc. of the Sub-Arcsecond Radio Astronomy Conferecne, University of Manchester, England, July 20-24 1992* (in press).

9. Hartmann, L., Kenyon, S., & Hartigan, P. 1993, in Protostars and Planets III (Tucson: Univ. of Arizona Press), (in press).

# THE IMMINENT AURORA OF GRAVITATIONAL WAVE ASTRONOMY

Odylio Denys de Aguiar
Instituto Nacional de Pesquisas Espaciais - INPE
C.P. 515, São José dos Campos, SP 12201-970
and
Nadja Simão Magalhães
Postdoctoral Fellow / CNPq

> "...Gravitational waves pass through surrounding matter with impunity,
> by contrast with electromagnetic waves which are easily absorbed and scattered,
> and even by contrast with neutrinos which, although they easily penetrate normal matter,
> should scatter thousands of times while leaving the core of a supernova.
> These differences make it likely that,
> if cosmic gravitational waves can be detected and studied,
> they will create a revolution in our view of the universe comparable to
> or greater than which resulted from the discovery of the radio waves."
> Kip S. Thorne
> (in "300 years of Gravitation", Cambridge Univ. Press, 1987).

## 1. Introduction

Gravitational Waves are ripples in the curvature of the spacetime, which propagate with the speed of light. They are radiated whenever matter has a nonnull third time derivative of its quadrupole moment. However, due to the weakness of the gravitational force, one believes that present technology can only detect these waves if they were produced in our galaxy from highly anisotropic material sources having relativistic velocities and dimensions equal to their masses times $G/c^2$. The astrophysical probability that at least one of these events occur in the next seven years is, optimistically, expected to be about 50%. Therefore, the strategy of the various groups, which are trying to observe these waves for the first time, has been to keep on air, with no time interruption, detectors sensitive to events in our own galaxy and/or trying to make more sensitive detectors. Improving the sensitivity of these detectors would capable them to observe events occurring in our neighbor galaxies (like the ones in the Virgo cluster) increasing the chances of detection in one year of operation.

Solving Einstein field equations for vacuum in a weak field approximation, we find wave solutions which present two transverse and independent modes of polarization (+ and ×) shown in Fig. 1. The observation of these polarizations in a measured wave would be an important test of General Relativity. However, the astrophysical outcome will be, perhaps, the most profitable one. The astrophysical observation of gravitational waves would give important data about:
- the distribution of neutron stars and black holes in space;
- the mechanism of explosion, rotation, mass and angular momentum of supernovas;
- the masses and viscosities of neutron stars;
- the distribution of coalescing (or inspiraling) binaries in space;
- the amount of dark matter;

and would determine the Hubble constant with much more precision.

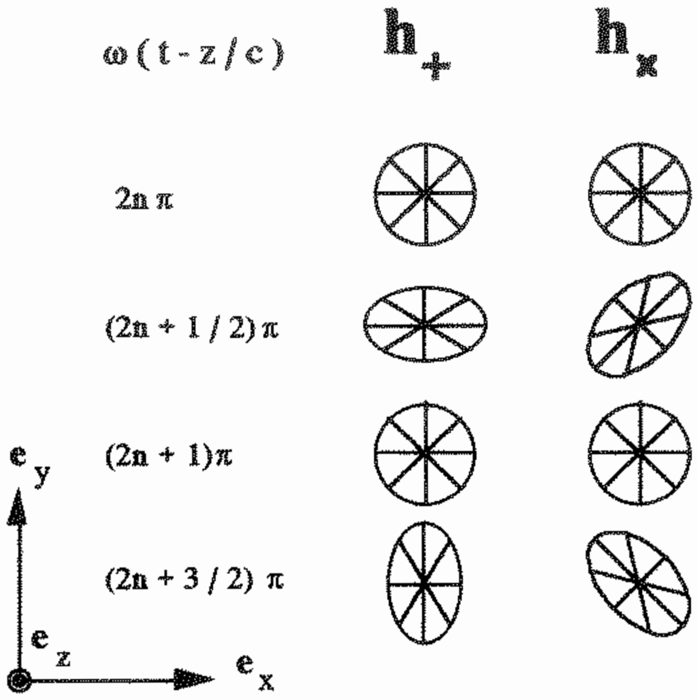

Fig. 1 - Deformation of a circle of test particles due to forces induced by pure $h_+$ or $h_\times$ waves.

## 2. Current ground-based detectors

Bar detectors and laser interferometers are the two principal types of current ground-based detectors under development. The most sensitivity ones in operation are those which are cooled to liquid helium temperatures (2 - 4.2 K). They belong to the second generation of resonant-mass detectors, while the first generation of these detectors was composed of those which operated at room temperature.

*Most sensitive detectors in activity:* [1]

- Louisiana State University (Baton Rouge): ALLEGRO (M=2300kg, L=3 m, T= 4.2 K, f ~ 900 Hz, h ~ 6 x $10^{-19}$, Al 5056);
- University of Rome I (the detector is in Geneva): EXPLORER, (M=2300 kg, L=3 m, T= 4.2 K, f ~ 900 Hz, h ~ 8 x $10^{-19}$, Al 5056);
- Istituto di Fisica dello Spazio Interplanetario / CNR (Frascati): ALTAIR (M=389 kg, L=1.5 m, T= 4.2 K, f = 1763 Hz, h ~ 3 x $10^{-18}$, Al 6061);
- University of Western Australia (Perth): (M=1500 kg, T= 4.2 K, f ~ 900 Hz, Nb);

*for continuous waves:*

- University of Tokyo (Tokyo): Crab IV (M=1200 kg, L=1.5 m, T=4.2 K, f = 60 Hz, h ~ 1 x $10^{-23}$, Al 5056);
- University of Tokyo (Tokyo): disc (D=2m, E=0.2m) (M=1700kg, T=394K, f=1.2 kHz, Al 5056, 200 mW laser, Fabry-Perot (finesse=3 k), h~1 x $10^{-18}$);

*Other resonant-mass detectors:*

- University of Maryland (College Park): (M=1200kg, Al 6061, T= 4.2 K, f ~ 1700 Hz), and (M=3000kg, Al 6061, T= 394 K, f ~ 1660 Hz, h ~ 2 x $10^{-17}$);

- University of Rome II (Frascati): AGATA (M =3100kg, Al 6001, L=3 m, T= 394 K,
  f ~ 860 Hz, h ~ 8 x $10^{-17}$);
- University of Rochester (Rochester): (Al 5056 dumbbell, M=100kg, T= 4.2 K,
  f=950 Hz, Δf~300 Hz, h ~ $10^{-16}$);
- Stanford University (Palo Alto) (not in operation) (M =4800kg, L=3 m, T= 4.2 K,
  f ~ 900 Hz, h ~ $10^{-18}$);
- Zhongshan University (Guangzhou) (M=2000kg, AILY 4, T=394 K, f = 1400 Hz,
  h ~ 3 x $10^{-17}$);
- University of Moscow (Moscow) (M ~ 20-30 kg (sapphire), T =394 K, f= 8 kHz,
  h ~ $10^{-17}$);
- University of Tokyo (Tokyo): Crab III (M =100kg, L=0.5 m, T= 4.2 K, f ~ 60 Hz,
  h ~ 1.9 x $10^{-21}$) (for continuous waves).

*New detectors in final phase of construction*
(3rd generation ⇔ bars at T ≤ 0.1 K) (expected h ~ $10^{-20}$):
- University of Rome II (Frascati): NAUTILUS (M =2300 kg, L=3 m, T ≤ 0.1 K,
  f ~ 900 Hz);
- Laboratori Nazionali di Legnaro / INFN (Padova): AURIGA (M =2300 kg, L=3 m,
  T ≤ 0.1 K, f ~ 900 Hz);
- Stanford University (Palo Alto): (M =1800kg, L=3 m, T ≤ 0.1 K, f ~ 1200 Hz).

*New projects* (4th generation ⇔ spheres or buckyballs at T ≤ 0.1 K)
(M=38 Ton, D=3 m, T ≤ 0.1 K, f ~ 900 Hz) (expected h ≤ $10^{-21}$ , Δf ~ 100-500 Hz):
- Louisiana State University (Baton Rouge): TIGA;
- INPE (a site in the state of São Paulo): EINSTEIN;
- University of Rome II (Frascati): ELSA;
- Kamerlingh Onnes Laboratory (Leiden): GRAAL.

*Laser interferometers:*
- Max-Planck-Isntitut (Garching): (L =30 m, L'=3.3 km), h~3x$10^{-18}$/ Hz$^{-1/2}$ (1-10 kHz);
- California Institute of Technology (Passadena): (L =40 m, L'=4-8 km);
- Massachusetts Institute of Technology (Cambridge): (L =1.5 m, L'=82 m);
- Glasgow University (Glasgow): (L =10 m, L'=1-2 km),
  h ~ $10^{-18}$/Hz$^{-1/2}$ (500 Hz - 3 kHz), 500 mW laser;
- Institute of Space and Astronautical Science (Kanagawa):
  TENKO - 10 (L=10 m), h ~ $10^{-18}$/ Hz$^{-1/2}$ ( 1 - 10 kHz);
- Institute of Space and Astronautical Science (Kanagawa):
  TENKO - 100 (L=100m), 7 W argon laser, US$10 M.

*New projects of laser interferometers*
(expected h ~ $10^{-21}$ or smaller, f ~ 10 Hz -10 kHz):
- LIGO (CALTECH - MIT), L =4 km (1-7 lasers), sites at: Hanford (Washington)
  and Livingston (Louisiana)
  US$105 M each (US$ 210 M total),
  US$20 M already approved in 1992;
- VIRGO (French - Italian collaboration), L =3 km;
- GEO (German-British collaboration), L =3 km;
- AIGO (Australian universities);
- Puna (India).

## 3. The GRAVITON Project

The GRAVITON Project is a project to initiate gravitational wave astronomy in Brazil. The major objective of this project is to built a large spheroidal resonant-mass antenna capable to determine the direction and polarization of detected gravitational waves emmited from supernovas or in the final stages of inspiraling binaries.

Sphere antennas have already been proposed more than twenty years ago.[2,3,4] Recently this idea has been resurrected by colleagues at LSU,[5,6] who are investigating other spheroidal geometries such as truncated icosahedrons.[7]

The feasibility studies for the GRAVITON Project[8,9,10] started in March of 1991, and they are expected to be completed by 1995, when the final form of the proposal should be submitted to the financial sources. A very preliminary view of the planned detector, which has been named EINSTEIN (**E**nergy **IN**novation **S**ensor using a **T**runcat**E**d **I**cosahedro**N**) is shown in Fig. 2. The "heart" of this fourth-generation resonant-mass detector is a three-meter diameter spheroidal antenna suspended in vacuum from its center of mass and cooled to ultralow temperatures (< 0.1 K).

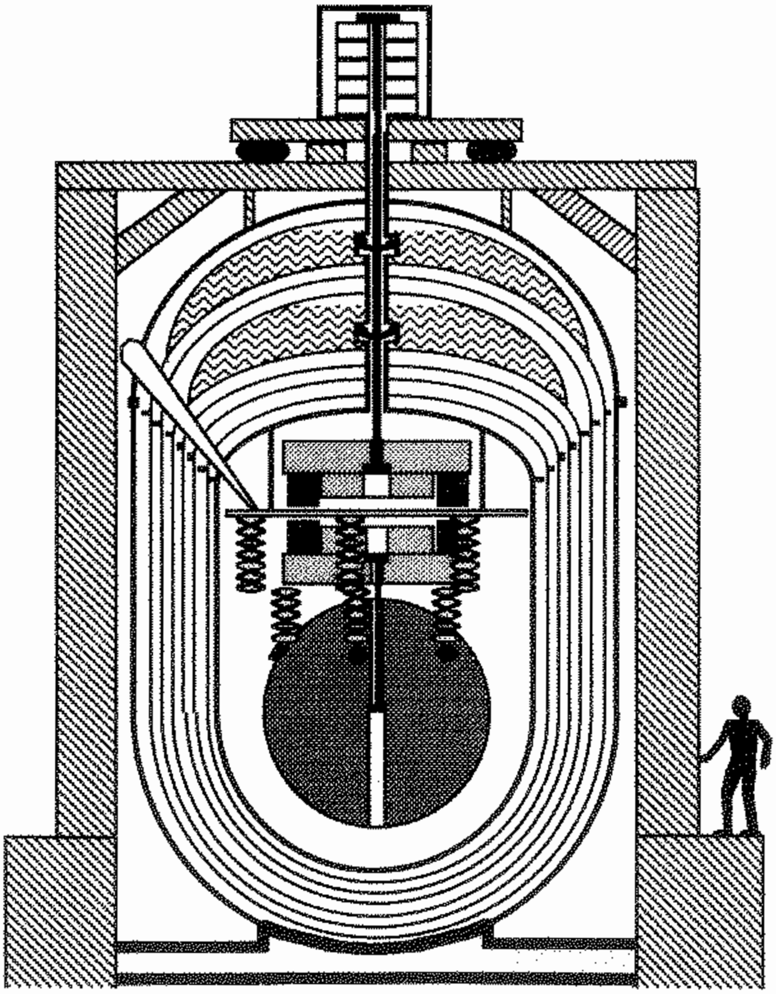

Fig. 2 - The Gravitational Wave Detector "EINSTEIN".

The total cost for the construction of EINSTEIN is about US$ 7M. Compared to the most expensive Brazilian projects in physics this is not very much. Furthermore, the scientific and technological benefits this project is going to bring to the country are priceless.

This project is so appealing that, recently, Giorgio Frossati from the Kamerlingh Onnes Laboratory, in Leiden, and Eugenio Coccia and Guido Pizzella from the University of Rome II ("Tor Vergata") are making plans for the construction of other two large spherical antennas, named GRAAL and ELSA, respectively. Following this enthusiasm, Warren Johnson and William Hamilton from LSU are trying to implement their idea of building a giant truncated icosahedral antenna, named TIGA, in collaboration with all the other US groups (Maryland, Rochester, and Stanford). EINSTEIN, together with these other three detectors, could make a reliable system for reconstructing a gravitational wave burst event completely, from which the astrophysical information could be derived.

## 4. Angular Resolution of a Single Spherical Antenna

Neither a single bar detector nor a two-arm laser interferometer can, alone, find the direction, polarization and amplitude of the detected waves. At least three and preferably more of these detectors are necessary to accomplish these tasks. [11,12] A spherical resonant-mass, on the other hand, is an omnidirectional antenna, therefore, it has the potential to find the direction, polarization and amplitude of the detected waves. In order to achieve these goals one just needs to monitor all its five quadrupole modes of vibration, for example, using five or more transducers uniformly distributed on its surface. Johnson and Merkowitz[13] have shown that six transducers arranged to match half the pentagonal face-centers of a truncated icosahedron would do the job.

Now, the question one can ask is the following: How precise can we determine, for example, the direction of a detected wave?

In order to simplify the solution of this problem, we will consider the case of scalar waves, which produce tidal forces in all directions perpendicular to the direction of the wave propagation. For this case, and using six transducers located on the antenna surface, the following relation holds:

$$\frac{h_{s1}}{\sin^2\varphi_1} = \frac{h_{s2}}{\sin^2\varphi_2} = \ldots = \frac{h_{s6}}{\sin^2\varphi_6} = h_o \qquad (1)$$

where $h_o$ is the dimensionless amplitude of the incident wave (strain), $h_{si}$ is the amplitude portion of the wave signal captured by the transducer $T_i$, and $\varphi_i$ is the angle between the wave direction and the vertical to the antenna surface at the point where the transducer $T_i$ is located.

In the presence of noise, the measured "signal" is $h_i = h_{si} \pm \delta h_i$ and, therefore, we can approximate the expression (1) to:

$$\frac{h_1}{\sin^2\varphi_1} \approx \frac{h_2}{\sin^2\varphi_2} \approx \ldots \approx \frac{h_6}{\sin^2\varphi_6} \cong h_o \qquad (2)$$

On the other hand, for the pentagonal faces of a truncated icosahedron ("buckyball") we have that

$$\sum_{i=1}^{6} \sin^2 \varphi_i = 4 \qquad \text{so, expression (2) implies that} \qquad \sum_{i=1}^{6} h_i \sim 4\, h_o \,.$$

Supposing, now, that all transducers are the same ($\delta h_i = \delta h$), we find that:

$$\delta h_o = \frac{\sqrt{6}}{4}\, \delta h$$

After same calculations we, finally, arrive to the expression

$$\sigma_{\varphi i} = \frac{1}{2}\left[\left(\frac{\delta h}{h_o}\right)\left(\frac{1}{\cos^2 \varphi_i} + \frac{\sqrt{6}}{4}\,\frac{\sin^2 \varphi_i}{\cos^2 \varphi_i}\right)\right]^{1/2} \tag{3}$$

which is the uncertainty in each $\varphi_i$ (in radians). For $\varphi_i = 0$, the expression above is the minimum:

$$\sigma_{\varphi i\ \min} = \frac{1}{2}\left(\frac{\delta h}{h_o}\right)^{1/2} \tag{4}$$

Evidently, for $\varphi_i = 0$ there is no signal in the transducer $T_i$ . So, in practice the minimum uncertainty for each $\varphi_i$ will be bigger than the one given by equation 4. For the purpose of calculating the minimum uncertainty in $\varphi_i$ a good criterion is to consider that $h_i \geq \delta h$. This implies, from equation 2, that

$$\sin^2 \varphi_i \geq \delta h / h_o \,. \tag{5}$$

If (5) is not satisfied the expression (3), for the uncertainty of $\varphi_i$ , is meaningless. However, if (5) holds, then, the minimum of (3) is:

$$\sigma_{\varphi i} = \frac{1}{2}\left[\left(\frac{\delta h}{h_o}\right)\left(\frac{h_o + \delta h_o}{h_o - \delta h}\right)\right]^{1/2} \tag{6}$$

Table 1 presents the average uncertainty $\sigma_\varphi$ (= average ($\sigma_{\varphi i}$ )) in the determination of the gravitational wave direction (bII, ℓII) for the EINSTEIN antenna ($\delta h \sim 10^{-21}$), equipped with six transducers located on half the pentagonal face-centers of the buckyball. Equation 3 was computed in order to find the $\sigma_{\varphi i}$ . For comparison, it is shown the minimum possible uncertainty for each $\varphi_i$ (equation 6).

| $h_o$ | $h_o / \delta h$ | $\sigma_\varphi$ | $\sigma_{\varphi i\ \text{mim}}$ |
|---|---|---|---|
| $10^{-16}$ | $10^5$ | 0.22° | 0.09° |
| $10^{-17}$ | $10^4$ | 0.7° | 0.29° |
| $10^{-18}$ | $10^3$ | 2.2° | 0.91° |
| $10^{-19}$ | $10^2$ | 7° | 2.9° |
| $10^{-20}$ | 10 | 22° | 9.6° |
| $3\times10^{-21}$ | 3 | 40° | 20° |
| $10^{-21}$ | 1 | 70° | 58° |

Table 1 - Uncertainties for a given "signal to noise ratio" ($h_o / \delta h$)

## 5. Conclusion

The dawn of Gravitational Wave Astronomy is imminent. In spite of tremendous technological challenges the various groups had to overcome during the past twenty-five years, today, some of their detectors are ready to observe a strong gravitational wave signal produced somewhere in our galaxy, and some others, in final stages of construction, will be able to observe strong waves from neighboring galaxies in the local group. Also, the construction of even more sensitive detectors have already started. They will extend the limits of observation to a few hundreds of megaparcecs. Because of their capability to determine the direction and polarization of a detected wave, spherical antennas will certainly be of fundamental importance for the next half century in the pioneering work of paving the road of Gravitational Wave Astronomy.

---

[1] Cryogenic Gravitational Wave Antennae: a progress workshop, Legnaro (Padova), Italy, June 19-22, 1993.

[2] R.L. Forward, "Multidirection, Multipolarization Antennas for Scalar and Tensor Gravitational Radiation", *General Relativity and Gravitation* , **2** , 149 (1971).

3 N. Ashby and J. Dreitlein, "Gravitational wave reception by a sphere", *Physical Review* , **12D** , 336 (1975).

[4] R.V. Wagoner and H.J. Paik, "Multi Mode Detection of Gravitational Waves by a Sphere", In. "Proceedings of the Academia Nazionale dei Lincei, International Symposium on Experimental Gravitation, Pavia, Italy, Sept. 1976, pp 257-65 (1977).

[5] W.W. Johnson, Workshop C of the 12th International Conference on General Relativity, Boulder CO, July 1989, In: General Relativity and Gravitation, 1989, ed. by N. Ashby, D.F. Bartlett, and. W. Wyss, Cambridge Univ. Press, Cambridge (1990), p.351.

[6] W.O. Hamilton and W.W. Johnson, "Proposal for a Gravitational Wave Observatory", Proposal to the National Science Foundation, May 1990.

[7] W.W. Johnson and S.M. Merkowitz, "Truncated Icosahedral Gravitational Wave Antenna", *Physical Review Letters* , **70** (6), 2367 (1993).

[8] O.D. Aguiar, letter to the gravitational wave detection gronps at the Sixty Marcel Grossmann Meeting, Kyoto, Japan, June 23-29, 1991.

[9] O.D. Aguiar et al. "The GRAVITON Project". In: 13th International Conference on General Relativity and Gravitation, Huerta Grande, Argentina, June 28-July 4, 1992, Abstracts of Contributed Papers, ed. by P.W. Lamperti and O.E. Ortiz, p. 455.

[10] O.D. Aguiar, "The GRAVITON Project: first feasibility study", In: Cryogenic Gravitational Wave Antennae: a progress workshop, Legnaro (Padova), Italy, June 19-22, 1993, Program and abstracts of contributions.

[11] M. Tinto and S. Dhurandhar, "Astronomical observations with a network of detectors of gravitational waves II. Solution to the four and three detector problem", *Monthly Notices of the Royal Astronomical Society*, **236** , 621 (1989).

[12] B.F. Schutz, "Data processing, analysis,and storage for interferometric antennas", In. The Detection of Gravitational Wave, Edited by D.G. Blair, Cambridge University Press, 1991.

13 W.W. Johnson and S.M. Merkowitz, "Truncated Icosahedral Gravitational Wave Antenna", Physical Review Letters, 70 (16), 2367 (1993).

# AN INTERNATIONAL ANTARCTIC OBSERVATORY

**V.V. Burdyuzha**

It is a pleasure to give talk to the Congress of the Brasilian Astronomical Society on the behalf of the Astronomical Society of the former USSR.

I want to draw your attention to beginning of the collaboration in Antarctic Astronomy. As you know, Antarctic ice plateou is the best site for astronomy (and for some other scientific studies) on the Earth's surface. For example, at Russian station Vostok the average level of precipitate water is only 0.2 mm. At Pamir, for example, this level is 1.2 mm at the altitude of 4500 meters (a similar level to Hawaii).

Recognizing the unique importance of astronomical observations in the Antarctic espessially in submm, IR and mm wavelengths, the latest General Assembley of the International Astronomical Union (Buenos-Aires, August 1991) recomended that National Astronomical Committees and Agencies studied the Antarctic to set up the International Astronomical Observatory in Antarctica and organized a Working Group for coordination in collaboration to choose the best site for the building of an Observatory, fitting out it with equipment and so on. The long term aim is the establishment of a broadly international scientific base at the highest point on the East Antarctic ice plateau, known as Dome A. Everyone understands the importance and usefulness of astronomical measurements for global ecological research. The project of building an Antarctic Observatory is uncluded in the schedule of the Megascience Forum together with the setting up of an Astronomical Observatory on the Moon.

The main scientific problems of astrophysics and cosmology which can be decided with the help of an Antarctic Observatory are:

1) to understand the creation and the evolution of our Universe

2) to understand the creation and the evolution stars (protostars).

3) to understand what is "central machine" in quasars and how they work and so on. I won't touch problems of astrometry and gravimetry part of which may be successfully decided in the Antarctic. The observational limits on the middle-scale anisotropy of relic radiation have already been obtained in the Antarctic.

The national groups of USA and Russia are more active in Antarctic Astromony at the moment. In USA a 1.7 meter submm telescope is preparing for astrophysical and atmospherical research in rotational lines of CO. The Special Center for Astrophysical Research in the Antarctic (CARA), which has the finaucial support of the NSF, has been set up in the USA. Astronomical projects on the Antarctic are having carried out in France, Italy, England, India and experimental estimates of possibilites for future research in Antarctic are being conducted in Japan, Australia and Spain. In Russia the working group was organized 2 years ago under the Astronomical Society. I am the chair of this group.

Our group together with the Antarctic and Arctic Institute in S. Peterburg have worked out the astroclimatic date (aerometeorological information) for the 30 years of the existence of the Vostok station and have also worked up engineering reports on the base moduls of the proposed observatory using the experience of longstays of orbital stations working in extreme conditions. Now we want to make the submm telescope (diameter $\approx$ 1 meter; $\lambda \simeq 200 \div 225\ \mu$, $345\ \mu$; weight $\approx$ 40 kg) together with the State Optical Institute (leader this project is G.B. Sholomitsky).

A French/USA/Australian cooperative program to critically measure atmospheric properties crucial for astronomy, at the South Pole, is under way. We hope that such measurements will be made at the Russian Antarctic site of Vostok (which is more favorably located for astronomy than the Pole), and later, at Dome A.

In future the Antarctic Astronomical Observatory will have the submm telescops up to 10 meters in diameter and also a submm interferometer. If Brazilian scientists are interested in Antarctic Astronomy the we can join our efforts to set up an Antarctic Observatory which will be the first step to the creation of an International Observatory of the Moon.

Chairman of Antarctic Astronomical Working Group of IAU
Dr. Peter Gillingham - Keck Observatory Operations Director (USA)
FAX: (808) 885-4464

Chairman of Russian Antarctic Astronomical Working Group
Prof. Vladimir Burdyuzha - Astro-Space Center Physical Institute (Russia)
FAX: (011) 276-3848 São Paulo
(095) 310-7023 Moscow

# THE TIMAX PROJECT

João Braga
*Astrophysics Division, Instituto Nacional de Pesquisas Espaciais,*
*CP 515, S. J. Campos, SP 12201-970, Brazil*
*e-mail (Internet):* `braga@das.inpe.br`

### Abstract

In this paper we present calibration results and laboratory images produced by the balloon-borne hard X-ray imaging telescope TIMAX. The images were produced with an $^{241}$Am radioactive source placed 45 m from the detector system, in the center of the field of view. It is shown that the mask-antimask imaging reconstruction process is very effective at recovering signal-to-noise lost to systematic differences in the background measured by the 35 NaI(Tl) detectors. The experiment was launched in June 8th, 1993 from Birigüi, SP, Brazil, in a 186 m$^3$ stratospheric balloon, and remained at atmospheric depth of $\sim$2 g cm$^{-2}$ for $\sim$10 hours. Even though no scientific data were gathered in this first flight, we have obtained valuable engineering data and could also calculate the sensitivity of the experiment based on the instrumental background spectrum at balloon altitudes. In the 60–70 keV energy band, the experiment can detect $3\sigma$ sources at a level of $\sim 4.3 \times 10^{-5}$ photons cm$^{-2}$ s$^{-1}$ keV$^{-1}$ for an integration of $10^4$ s at 2.5 g cm$^{-2}$.

## 1 Introduction

The TIMAX experiment (Braga *et al.*, 1991, hereinafter Paper I) is a balloon-borne hard X-ray coded-aperture imaging telescope designed to image $10° \times 10°$ fields with a $\sim 2°$ angular resolution. The experiment incorporates a one-piece mask-antimask system, based on a $7 \times 5$ uniformly redundant array (URA) pattern (Fenimore and Cannon, 1978), which has been shown to be very effective on reducing systematic variations of the background in the detector plane (Paper I and Jayanthi & Braga, 1991). The detector plane consists of 35 1¼" -diameter 2mm-thick NaI(Tl) detectors, with a total area of $\sim$400 cm$^2$.

The main goal of the experiment is to study the Galactic Center (GC) region, where several sources have recently been discovered and identified. The Caltech GRIP experiment (Cook *et al.*, 1984; Althouse *et al.*, 1985) has found that the bulk of the GC hard X-ray/soft gamma-ray emission was coming from the previously unremarkable Einstein source 1E1740.7−2942 (Hertz & Grindlay, 1984) located $0\overset{\circ}{.}8$ away from the dynamical center of the Galaxy in Sgr A* (Cook *et al.*, 1988 and 1991). The SIGMA coded-aperture imager aboard the Soviet satellite GRANAT (Paul *et al.*, 1991) measured a strong and broad feature in the spectrum of this object (Bouchet *et al.*, 1991), readily interpreted as intense 511 keV annihilation radiation. The line was centered at ~480 KeV and was extremely broad (~240 keV FWHM), with a total flux of $\sim 1.3 \times 10^{-2}$ photons $\mathrm{cm}^{-2}\,\mathrm{s}^{-1}$, which is one order of magnitude stronger than the typical mean flux measured during the 1970's. This caused great excitement in the gamma-ray astronomy community, inasmuch as the origin of the 511 keV line had been one of the main puzzles in this field since its discovery and subsequent detections in the 1970's (Riegler *et al.*, 1981 and references therein).

In 1990, the SIGMA experiment discovered another hard X-ray source near the GC: GRS 1758-258 (Mandrou, 1990; Sunyaev *et al.*, 1991). This source is 40 arcmin away from the bright quasiperiodic source GX 5-1; probably much of the hard X-ray emission attributed to this object in the past was in fact coming from GRS 1758-258. Further observations of the GC region showed that most of the sources are variable in nature. Another set of images produced by SIGMA between February 17 and March 12, 1992 (Gilfanov *et al.*, 1992), showed the presence of 5 bright sources in the 40 to 100 keV range: the X-ray burster GX 354-0 (with a flux at a level of about 75 mCrab and increasing gradually); 1E1740.7−2942; the well-known X-ray pulsar GX 1+4 (which was detected in 1982 at energies above ~200 keV by Jayanthi, Jablonski and Braga, 1987), at an average level of 35 mCrab, apparently variable; the globular cluster Terzan 2 (about 20 mCrab average flux); and the Spacelab-2 source SLX 1735-269 (also ~20 mCrab average flux) which had been discovered at softer energies by Skinner *et al.* (1987) with a coded mask X-ray telescope. GX 1+4 has also been recently detected in a very intense outburst state by the BATSE experiment onboard the Compton Gamma Ray Observatory (CGRO) with a pulse period of 120.567 ± 0.005 s, showing that it is currently undergoing a spindown phase (Finger *et al.*, 1993).

All these exciting discoveries and observations show clearly that the nature and spatial distribution of the GC sources are still far from being determined with precision. Imaging telescopes, which can measure both locations and spectra of the sources, subtracting background simultaneously, are very important to the further study of this region. In particular, the coded-aperture imaging technique using URA patterns has several advantages over time-modulation techniques (see Dean, 1984, for a review of imaging techniques in high-energy astrophysics). For a overview of the main experiments that have used the coded-aperture imaging concept, see Caroli *et al.* (1987). In this paper we describe the development of the TIMAX telescope and show the first results of the imaging system obtained in the laboratory. We also present the preliminary results of the first balloon flight of the experiment in the Southern Hemisphere. TIMAX is a prototype for a much larger experiment currently under development in our laboratory (Villela *et al.*, 1993).

## 2 Laboratory images

The calibration of the imaging system of the TIMAX telescope was performed in the laboratory using radioactive sources. A 100 mCu $^{241}$Am source, which emits a hard X-ray line at 60 keV, was placed at a distance of 45 m from the detector plane. In order to align the X-ray axis of the telescope with the position of the source, we used a laser beam that passed through holes opened in the carbon fiber wheel that supports the mask elements. The location of each hole with respect to the mask was chosen in such a way that it matched the position of the origin of the laser beam with respect to the detector. By using this procedure, we placed the source exactly in the center of the field of view of the instrument. The distance of 45 m was sufficient to ensure that no magnification factor would be present in the shadowgram of the mask on the detector plane, so as to simulate an astronomical observation.

Fig. 1 displays an image built with the telescope in the "mask" (as opposed to "antimask") configuration (see Paper I) for an integration time of 2 hours. This image was reconstructed using the raw counts from the detectors integrated over all 32 energy channels, thereby including the 60 keV line. Since there were slight gain variations as well as differences in the energy resolutions of the detectors, we decided to start by producing images of the total energy range and then proceed with gain-correction algorithms and resolution normalization techniques. The signal-to-noise ratio (SNR) of this image is 18.57.

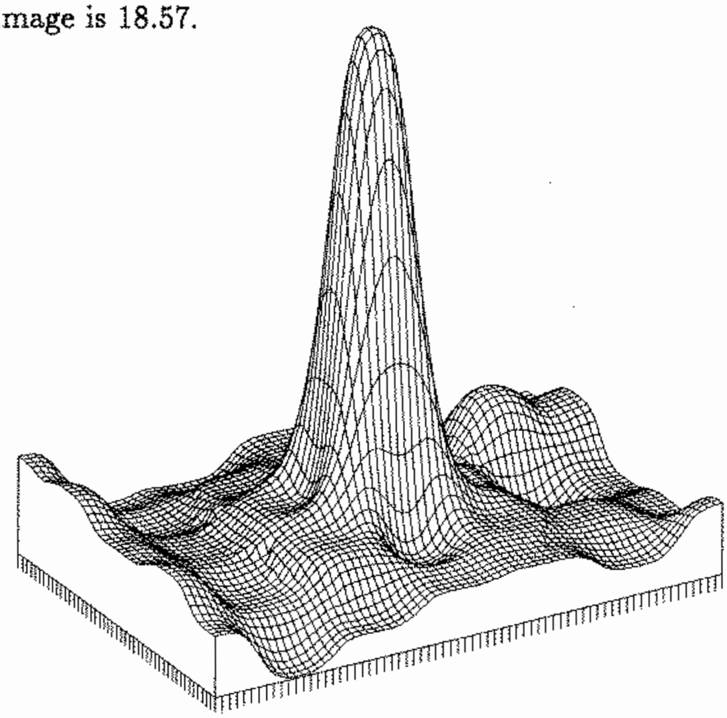

Figure 1: Raw image built with the telescope in the "mask" configuration. $SNR = 18.57$.

Fig. 2 shows the same image after being flat-fielded using the photon distribution on the detectors obtained by an integration of 3 hours without the mask. The SNR is 69.30. With this "flat-fielder" file, we can determine the multiplicative correction factors which are applied to each detector to eliminate differences in sensitivity across the detector plane (Braga, 1990). This method, which was employed successfully on the EXITE experiment (Braga, Covault and Grindlay, 1989), improved the SNR by a factor of ~4.

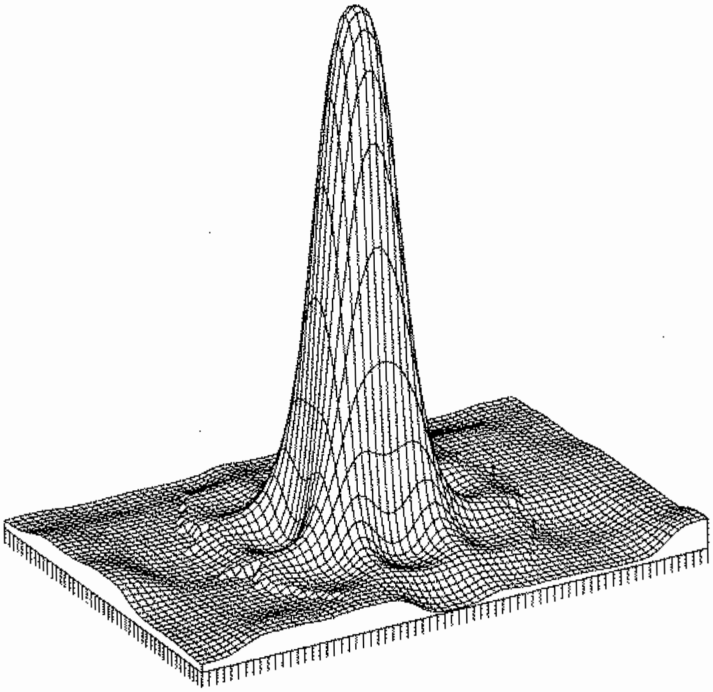

Figure 2: Flat-fielded image built with the telescope in the "mask" configuration. $SNR = 69.30$.

An image built with the telescope in the "antimask" configuration (Fig. 3) reflects the degradation of the SNR (now 15.87) with respect to Fig. 1, due to intrinsic noise caused by the antimask pattern. This is expected, inasmuch as the antimask does not have perfect URA properties due to the fact that the central element is opaque, which in turn is a consequence of the mechanical solution found in order to keep the mask-antimask system in only one piece (Paper I). These raw images are completely dominated by systematic noise due to differences on detector performances, so there is no significant change in SNR for integration times beyond one hour. It should be pointed out that, in order to "flat-field" the antimask count distribution on those highly-exposed images, the counts of the central detector, which is underneath the ever-opaque element, had to be replaced by the average value of its nearest "open" neighbors. As it was shown by the computer simulations of Paper I (in which no differences in detector sensitivity were taken into account), this is not the case in a real astronomical image; in this case the noise in the image will have an important contribution from the Poissonian statistical fluctuations, since the sources are usually very weak. The destructive effect of the opaque element is then overwhelmed by the gain in SNR provided by the mask—antimask method.

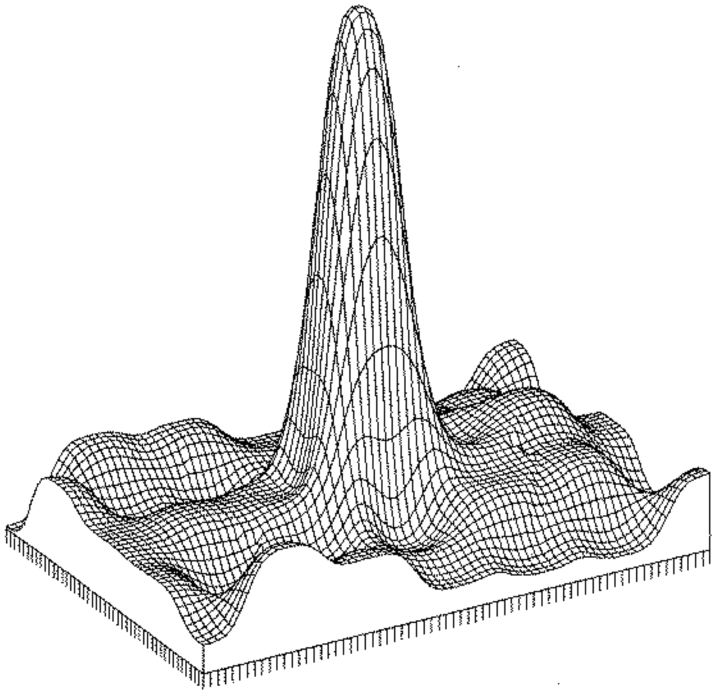

Figure 3: Raw image built with the telescope in the "antimask" configuration. $SNR = 15.87$.

An image reconstructed using the mask—antimask method (described in detail in Paper I) is illustrated in Fig. 4. With this technique the count distribution on the detectors obtained with the telescope in the "antimask" configuration are subtracted out from the count distribution obtained in the "mask" configuration, in order to eliminate systematic spatial non-uniformity in the background measured by the 35 NaI detectors. In this example we integrated over 1 hour for each configuration (mask and antimask). The SNR (25.47) improved 37% with respect to Image 1. This shows that, even though the central element of the mask remains opaque in the antimask configuration, as mentioned above, a significant net gain in SNR is obtained by using the mask—antimask method.

The mask—antimask "subtractive" flat-fielding procedure has to be superimposed on the multiplicative flat-fielding to get the final flat-fielded, mask-antimask image. This is shown in Figure 5. The SNR of this image (140.06) is a factor of ~2 higher than that of Image 2, which demonstrates the efficacy of the method.

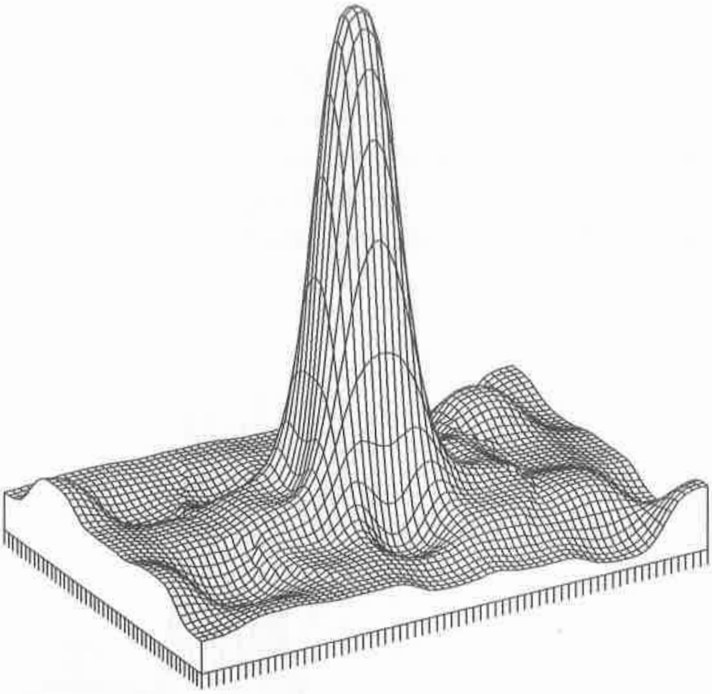

Figure 4: Image reconstructed using the mask−antimask correction method. $SNR = 25.47$.

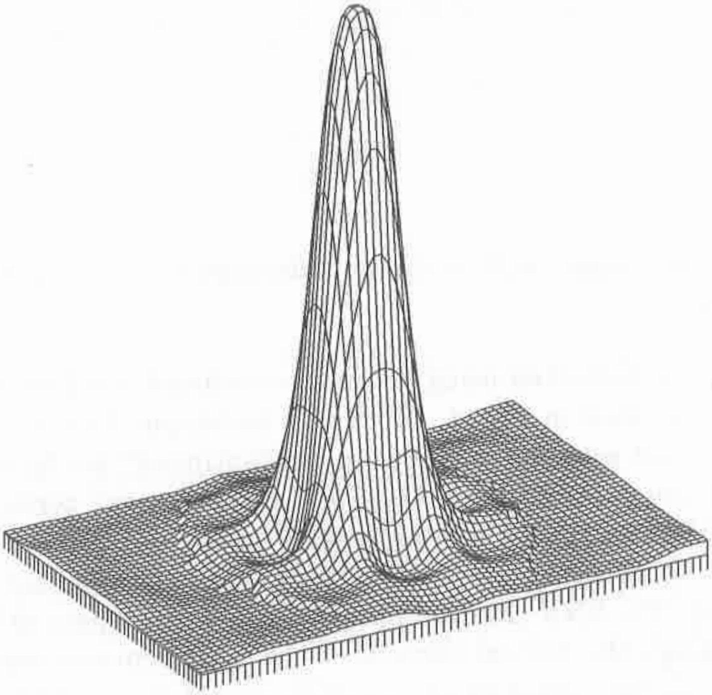

Figure 5: Final flat-fielded, mask−antimask image. $SNR = 140.06$. The "ring" structure seen is an artifact of the interpolation algorithm, and it is not taken into account in the calculation of the SNR.

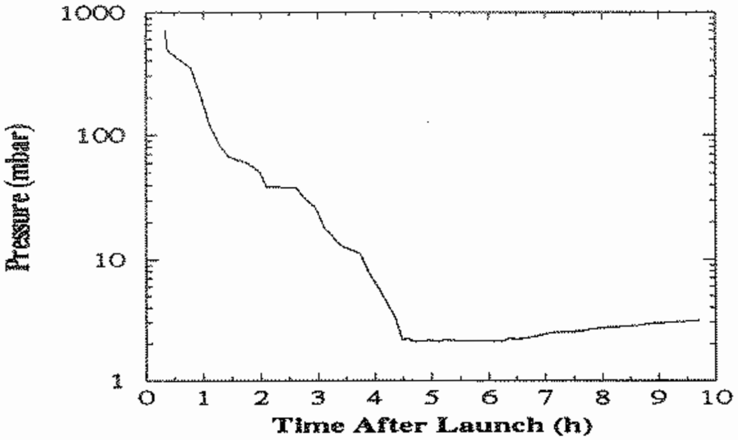

Figure 6: Atmospheric pressure as a function of time for TIMAX first balloon flight

The expected total counts for one hour of integration with this source at a distance 45 m, according to its activity, is ~2.7 million, which would mean a Poissonian SNR of ~1500. Due to severe dead-time losses in the front-end electronics, which was not designed to handle these high counting rates, we measured about 460,000 counts for one hour of integration with the mask. Since the measured hackground counts for the same integration time is 252,000, the Poissonian ideal SNR is ~300. Since the measured SNR of the final image was 140, we see that we are still a factor of ~2 low in SNR. This could be due to systematic effects not accounted for in the two flat-fielding procedures described above, such as gain variations that would change the energy range being considered and so the detectors would be measuring different portions of the spectrum of the $^{241}$Am source. We are currently in the process of developing algorithms to improve the reconstruction of the images.

# 3 The balloon flight

The TIMAX experiment was launched from the town of Birigüi, São Paulo, Brazil (latitude: 21°16'53" S; longitude: 50°19'35" W), on July 8th, 1993, 21:27 UT, in a 186m-diameter Winzen stratospheric balloon. The balloon reached float altitude (42.4 km, 2.1 g $cm^{-2}$) at 23:30 UT, and remained at this altitude for ~10 hours. Figure 6 shows the variation of the pressure with time as measured by the pressure gauge on board. The balloon flight was extremely smooth and the altitude reached was excellent for hard X-ray observations of cosmic sources.

During the ascent, all gondola systems performed nominally. However, due to extremely low temperatures, atypical at these altitudes, the alkaline batteries (D cells) that powered the experiment started to fail just after reaching float altitude and just prior to the automatic observations of the GC. In Figure 7 we can see

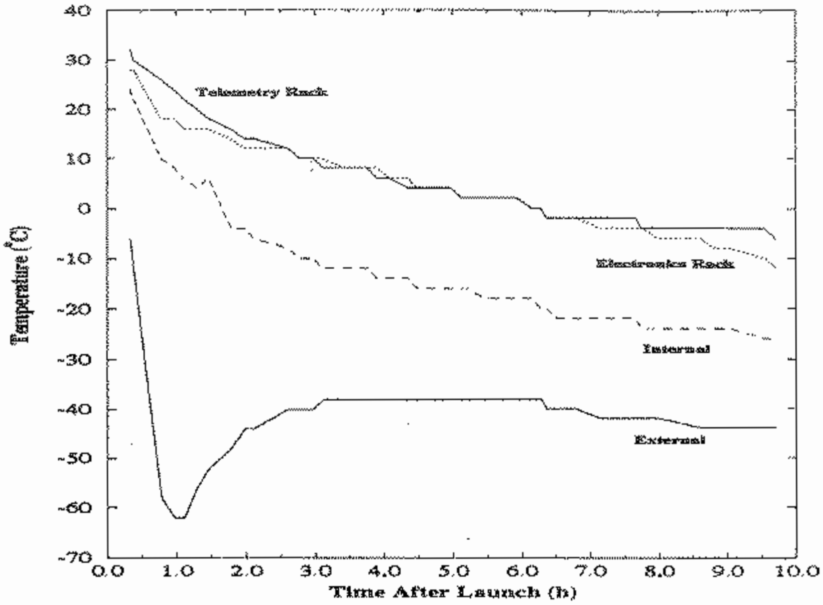

Figure 7: Temperature measured by several onboard sensors as a function of time for the TIMAX first balloon flight

the temperatures measured by several sensors on board. We note that the external temperature was about −40°C throughout the flight. Even though we had used standard high-density styrofoam thermal insulation in the gondola, the temperature in the internal environment varied from ∼−8° to −24°C, whereas typical values range between 0°and 10°C. In the pre- and post-flight tests of the D cells, they began to fail below ∼−12°C, which explains why they did not function properly during the flight.

The instrumental hard X-ray background spectrum measured at ceiling altitudes showed a total counting rate of 44 counts/sec, which is in good agreement with the estimate of 42 counts/sec made in Paper I. This spectrum enabled the calculation of the sensitivity of the experiment as a function of energy, for several energy bands, which is shown in Fig. 8. We can see that the main scientific objectives of the project are feasible inasmuch as most of the GC bright sources can be detected by images generated with integration times of $10^4$ s.

## 4 Conclusions

The TIMAX experiment was calibrated in the laboratory and flown for the first time in a stratospheric balloon in the Southern Hemisphere. The calibration of the imaging system showed that the mask/antimask method of suppressing the systematic background non-uniformity over the detector plane is very effective at recovering the SNRs of the images, when combined with multiplicative flat-fielding techniques. The

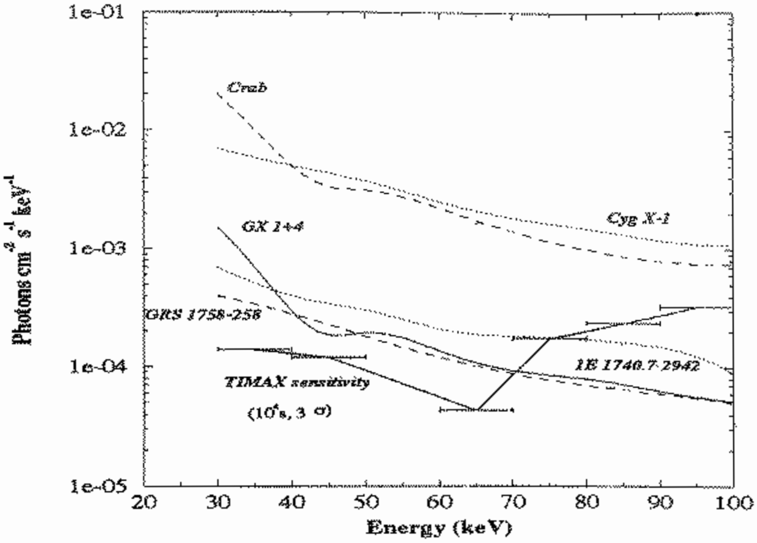

Figure 8: Sensitivity of the TIMAX experiment, for an atmospheric depth of 2.5 g cm$^{-2}$, an integration time of $10^4$ seconds and a confidence level of $3\,\sigma$. Also shown are the spectra of several hard X-ray sources which are potential targets of the experiment.

overall improvement in SNR for highly-exposed images was a factor of ~10. The instrumental background measured in the first flight of the experiment demonstrated its ability for imaging the Galactic Center region, where recent results have shown the presence of a very interesting field of highly-variable hard X-ray sources. We plan to launch the experiment again in the near future.

## Acknowledgements

I thank T. Villela and F. D'Amico for useful discussions, and A. M. R. Alves, J. A. Neri and E. R. da Silva for invaluable technical support. I am very grateful to Ricardo Varela and INPE's balloon group for a perfect balloon flight and all the support and friendship during the balloon campaign. I am also grateful to Geoffrey M. Henebry for a patient review of the manuscript. This research is partially supported by FAPESP (Brazil) under grant 92/0625-2.

# References

Althouse, W. E., Cook, W. R., Cummings, A. C., Finger, M. H., Prince, T. A., Schindler, S. M., Starr, C. H., Stone, E. C. 1985, *Proc. 19th Int. Cosmic Ray Conference (La Jolla)*, **3**, 229.

Bouchet, L., Mandrou, P., Roques, J. P., Vedrenne, G., Cordier, B., Goldwurm, A., Lebrun, F., Paul, J., Sunyaev, R., Churazov, E., Gilfanov, M., Pavlinsky, M., Grebenev, S., Babalyan, G., Dekhanov, I., Khavenson, N. 1991, *Ap. J. Lett.*, **383**, L45.

Braga, J. 1990, *Ph.D. Thesis*, University of São Paulo, Brazil.

Braga, J., Covault, C. E., Grindlay, J. E. 1989, *IEEE Trans. in Nucl. Sci.*, **NS-36**, 871.

Braga, J., Villela, T., Jayanthi, U. B., D'Amico, F., Neri, J. A. 1991, *Experimental Astronomy*, **2**, 101.

Caroli, E., Stephen, J. B., Di Cocco, G., Natalucci, L., Spizzichino, A. 1987, *Space Science Reviews*, **45**, 349.

Cook, W. R., Finger, M., Prince, T. A., and Stone, E. C. 1984, *IEEE Trans. Nucl. Sci.*, **NS-31**, 771.

Cook, W. R., Palmer, D. M., Prince, T. A., Schindler, S. M., Starr, C. H., Stone, E. C. 1988, *B.A.A.S.*, **20**(4), 1070.

Cook, W. R., Grunsfeld, J. M., Heindl, W. A., Palmer, D. M., Prince, T. A., Schindler, S. M., Stone, E. C. 1991, *Ap. J. Lett.*, **372**, L75.

Dean, A. J. 1984, *Nucl. Instr. Meth. Phys. Res.*, **221**, 265.

Fenimore, E. E., Cannon, T. M. 1978, *Appl. Opt.*, **17**, 337.

Finger, M. H., Wilson, R. B., Fishman, G. J., Bildstein, L., Chakrabarty, D., Prince, T. A. 1993, submitted as an *IAU Circular*.

Gilfanov, M., Churazov, E., Claret, A., Dezalay, J. P. 1992, *IAU Circular 5474.1.*

Hertz, P., Grindlay, J. E. 1984, *Ap. J.*, **278**, 137.

Jayanthi, U. B., Braga, J. 1991, *Nucl. Instr. and Meth.*, **A310**, 685.

Jayanthi, U. B., Jablonski, F., and Braga, J. 1987, *Astrophys. Space Sci.*, **138**, 183.

Mandrou, P. 1990, *IAU Circular 5032.1.*

Paul, J. et al. 1991, *Adv. Space Res.*, **11**(8), 289.

Riegler, G. R., Ling, J. C., Mahoney, W. A., Wheaton, W. A., Willett, J. B., Jacobson, A. S. 1981, *Ap. J. Lett.*, **248**, L13.

Skinner, G. K., Willmore, A. P., Eyles, C. J., Bertram, D., Church, M. J., Harper, P. K. S., Herring, J. R. H., Peden, J. C. M., Pollock, A. M. T., Ponman, T. J., Watt, M. P. 1987, *Nature*, **330**, 544.

Sunyaev, R., Churazov, E., Gilfanov, M., Pavlinsky, M., Grebenev, S., Babalyan, G., Dekhanov, I., Yamburenko, N., Bouchet, L., Niel, M., Roques, J.-P., Mandrou, P., Goldrwurm, A., Cirdier, B., Laurent, Ph., Paul, J. 1991, *Astron. Astrophys. (Letters)*, **247**, L29.

Villela, T., Braga, J., Jayanthi, U. B., Wuensche, C. A., Neri, J. A., Souza, M. A. P. 1993, *Astr. Space Sc.*, in press.

not display proper motions and sometimes they are not linked to a fundamental catalogue. Moreover the FK5 and FK5 Supp. stars are excessively bright.

This situation will be completly modified after HIPPARCOS. The density will increase to 26 stars for 3° x 3° with much superior accuracy, except for the proper motions.

b) Trigonometric parallaxes

The trigonometric parallax is the only direct mesure of stellar distance and it forms the base upon which all other methods of astronomical distance determination rely. The precision of various quantities, for example stellar masses and luminosities, are very dependent on the quality in the adopted parallax.

The present situation is very, very bad. Only a bit more than 1000 stars have parallaxes with relative errors below 20%, and all are contained within a radius of 20 to 30 pc.

In this case HIPPARCOS apports a radical change. We multiply the number of well known parallaxes by a factor of 30, approximately, extending the explored radius to 100 pc. Besides, the HIPPARCOS parallaxes are absolute and they are very well distributed among the various star types.

## 4. Limitation of the HIPPARCOS mission and ground based complementation

In spite of the extraordinary importance of the HIPPARCOS mission, certain limitations are still present.

First of all, the HIPPARCOS reference system is not absolute and it must be linked to other systems. The link to an inertial reference frame can be made through the observations of extragalactic or solar system objects. Since the HIPPARCOS list of such objects is very limited, the necessary link will not be established to the desired accuracy.

Second, the magnitude limit is too bright.

Finally, we whould point out the degradation of the HIPPARCOS system in the course of time. After a few years the accumulated errors, due to the relatively poor proper motions, will become large and will severely impair the system quality.

These limitations can be surpassed with a new astrometric space mission in the near future. They can also be attenuated through ground based observations, provided that traditional instrumentation is upgraded to attain the highest quality possible. The modern observation and reduction technics must improve the precision and extend the observable magnitude limit.

Particularly, the Instituto Astronômico and Geofísico of the São Paulo University is undertaking the automation of the meridian circle and astrolabe installed at the Abrahão de Moraes Observatory at Valinhos. This automation, consist initially, to replace the present visual micrometers by a CCD detectors. Another aspect concerns the improvement of the global reduction techniques, by considering image motion filtering (Benevides-Soares et al. 1993).

The HIPPARCOS mission is being complemented by ground based radial velocity observations. These data, together with the mission results fully describe the stellar kinematics and will have a very important role in the study of the Galactic structure.

## 5. Tycho mission

The satellite attitude control is made through the observations of a great number of stars in their transits through the star mapper. In 1981, H$\phi$g proposed to ESA the exploration of these data since they could give the scientific results that outweigh all ground-based observations of all meridian circles in the present century (H$\phi$g et al. 1992).

The experiment Tycho consists in the determination of the astrometric and photometric parameters of about one million stars brighter than B = 12 magnitudes (H$\phi$g et al. 1992).

For the brightest 500000 stars ($B \leq 10.5$) the expected astrometric precision is $0\overset{''}{.}03$ and B and V photometric precision is 0.03 magnitude.

## References

Benevides-Soares P., Teixeira R. and Réquième Y. 1993: A & A in press

ESA 1992 Bulletin 69 p. 34

Fricke W., Schwan H., Lederle T. 1988: Fifth Fundamental Catalogue (FK5), Heidelberg Veroffentlichungen Astronomisches Rechen Institut, N° 32

H$\phi$g E., Bastian U., Egret D. et al. 1992: A & A, 258, 1, 177

Kovalevsky 1979: F.V. Prochazka and R.H. Tucker (eds.), "Modern Astrometry", IAU Col. 48

Morrison L.V., Gibbs P., Helmer L., Fabricius C., Réquième Y. and Rapaport M. 1991: Ap & SS, 177,31

Perryman M.A.C. et al. 1989: ESA SP-1111 Vol. 1, 2 and 3

Réquième Y. 1993: Personal comunication. Presented results by M. Froeschelé at Arcachon (France)

Teixeira R., Réquième Y., Benevides-Soares P. and Rapaport M. 1992: A & A, 264, 307

Turon C., Gomez A., Crifo F. and Grenon M. 1989: ESA SP-1111 Vol. II p. 7

Turon C., Gomez A., Crifo F. et al. 1992: A & A, 258, 1, 74

Van der Ha. 1992: ESA Bulletin N. 69, 9

Various authors 1992: A & A, 258, No. 1

Yoshizawa 1989: Publ. National. Obs. Japan. 1, 127-176

# HIPPARCOS MISSION

R. Teixeira IAG-USP

**Abstract:** The HIPPARCOS space mission represents a very big and important step in the measurements of astronomical fundamental parameters. The HIPPARCOS satellite has just performed thousands of astrometric and photometric high precision observations to build a unique stellar catalogue with the positions, parallaxes, proper motions and magnitudes for 118000 objects. The mean error in the astrometric parameters is about $0\overset{''}{.}002$ whereas the precision can reach 0.001 mag. for the photometric measurements. The associated Tycho experiment yelds a supplementary list of position for one million stars, with precisions comparable to the best ground-based catalogues.

**Key words:** stellar position, parallax, proper motion and magnitude.

## 1. Introduction

The main objective of the HIPPARCOS mission is to build a catalogue with astrometric and photometric informations - position, parallax, proper motion and magnitude - for a very large number of objects. These parameters are being measured with extreme precision. We can find a complete description of this mission in a ESA publication (Perryman et al. 1989) and a detailed discussion and some results in a issue of Astron. Astrophys. specially devoted to the HIPPARCOS mission (various authors 1992).

In order to attain the best scientific outcome the object list was carefully selected according to some main points: 1) the scientific interest manifested by a very great number of programs proposed by the scientific world-wide community; 2) the more uniform possible distribution in the sky; 3) a very large number of the bright stars. The catalogue will be complete until magnitude 8.5 (Turon et al. 1989, 1992; Gomez et al. 1989). The last item results also from a technical need, for the satellite attitude control and data reduction.

The HIPPARCOS catalogue will contain 118000 stars and some other objects with stellar aspect - one quasar (3C273), two planetary satellites (Titan and Europe) and 48 minor planets. The stellar content includes, for example: radio- stars; variable stars; stars in open clusters; stars in the Magellanic Clouds; central stars of planetary nebulae; etc. For example of the scientific programs associated to this mission, we can mention the building of a nearly perfect reference system; the link to an inertial reference frame; stellar mass determination; mass-luminosity relation calibration; distance scales calibration; Galactic structure; etc. (Turon et al. 1989, 1992).

A catalogue such as HIPPARCOS has not a precedent in the astronomical history since it can be built only from the space. The ground-based observations are very limited by the atmosphere, by the thermal and gravitational instrumental perturbations and by the impossibility to observe the whole sky with only one instrument.

The utilization of an astrometrical satellite was a propositon of P. Lacroute in 1966, wich needed 23 years to achieve completion through the launching of the HIPPARCOS satellite in August 1989, by the European Space Agency.

Because of a failure of the apogee boost motor, the satellite remained in an eccentric transfer orbit, instead of the intended geostationary one. This new orbit causes too many problems, for example: more frequent eclipses and occultations; the degradation of the solar arrays mainly due to the crossing of the Van Allen radiation belts; the need of more than one ground tracking station. Fortunately, the initial estimated degradation rate of the solar pannels, wich ultimately defines the satellite life-time, was too pessimistic. The managing teams have been successful in revising the mission to match the whole scientific programme. For this, three new ground tracking station were employed and the results reached till now point out the total success of this mission (Van der Ha 1992). In 1992 the ESA decided to extend the HIPPARCOS mission up to the satellite death. So, the mission wich initial duration was 2.5 years, has just completed 3.5 years of observations. In this way the precision initially intended can be surpassed.

## 2. HIPPARCOS Catalogue

The expected mean accuracy before the launching was 0."002 for the positions, parallaxes and anual proper motions. The expected magnitude precision for a non variable star with the magnitude between 8 and 9 was 0.001 after 100 observations (ESA 1992).

After 18 months of observation relative to 90000 objects, aproximately, the obtained precisions are in a very good agreement with the previsions. The precisions are 0."0025 in positions, 0."0030 in parallaxes, 0."0060 in proper motions and 0.001 to the magnitude of a single and non variable stars with magnitude between 8 and 9 (Réquième 1993).

The somewhat large value of the proper motion error is due to the limited time span of the mission.

In table 1 (table 2) we can see that each spectral type interval has more than 10000 stars in the HIPPARCOS catalogue. Table 1 shows that the catalogue has more than 30000 stars inside a radius of 100 pc, that is, the parallax relative error for these stars is less than 20%.

Table 2 shows that HIPPARCOS will be a catalogue of bright stars. About 95% of its stellar content is brighter than magnitude 10.

| SP | <100 | 100-500 | 500-1000 | >1000 | Total |
|---|---|---|---|---|---|
| O-B | 170 | 6050 | 2530 | 1980 | 10730 |
| A0-A9 | 1260 | 15910 | 1330 | 270 | 18770 |
| F0-F9 | 12400 | 13150 | 110 | 250 | 25910 |
| G0-K1.5 | 14200 | 23560 | 2150 | 530 | 40440 |
| K2-M8 | 3380 | 10470 | 5500 | 900 | 20250 |

Table 1. Distribuition in heliocentric distance (pc) of the HIPPARCOS stellar content as function of spectral type (Turon et al. 1989).

| SP | < 6 | 6-8 | 8-10 | ≥10 | Total |
|---|---|---|---|---|---|
| O-B | 1080 | 4350 | 4800 | 500 | 10730 |
| A0-A9 | 1000 | 7260 | 9800 | 710 | 18770 |
| F0-F9 | 660 | 6550 | 16340 | 2360 | 25910 |
| G0-K1.5 | 1220 | 11370 | 25160 | 2690 | 40440 |
| K2-M8 | 1070 | 6060 | 10610 | 2510 | 20250 |

Table 2. Distribution in magnitude V of the HIPPARCOS stellar content as function of spectral type (Turon et al. 1989).

## 3. The present situation and the pos-HIPPARCOS prospective

A very detailed discussion about the scientific impact of the HIPPARCOS mission was presented by Kovalevsky (Kovalevsky 1979). To illustrate the scientific gain from the HIPPARCOS mission we can deal with two important aspects of the stellar astronomy.

a) Reference systems

The best reference system presently available is afforded by the fundamental catalogue FK5 (Fricke et al. 1988). The basic FK5 comprises positions and proper motions of about 1500 stars with mean precisions of 0".040 and 0".001/year respectively, for 1990. To this catalogue is associated a supplement with nearly 3000 stars, with mean precisions of 0".080 and 0".002/year and a magnitude limit of about 9.5.

In spite of its qualities, the FK5 and the FK5 Supp. together, do not satisfy some very important requirements of an ideal reference system - absence of systematic errors, availability in the whole sky and perennity.

Various authors (Morrison et al. 1991, Yoshizawa et al. 1989, Teixeira et al. 1992) have shown that the FK5 has significant systematic errors. On the other hand, the FK5 and the FK5 Supp. together, have only one star for 3° x 3°. Other more dense catalogues are, in general, less accurate, have a irregular distribution in the sky, sometimes they do

*Impresso na Seção de Ilustrações Técnicas do Instituto*
*Astronômico e Geofísico da Universidade de São Paulo.*